IntechOpen

Polymer Rheology

Edited by Luis Rivera-Armenta and Beatriz Adriana Salazar Cruz

POLYMER RHEOLOGY

Edited by **Jose Luis Rivera-Armenta**
and **Beatriz Adriana Salazar Cruz**

Polymer Rheology
http://dx.doi.org/10.5772/intechopen.72137
Edited by Jose Luis Rivera-Armenta and Beatriz Adriana Salazar Cruz

Contributors

Kulsum Jan, D C Saxena, Khalid Bashir, Shumaila Jan, Sergey Vshivkov, Ildebrando Pérez-Reyes, Rene Osvaldo Vargas-Aguilar, Samuel Perez-Vega, Alejandro Sebastian Ortiz-Perez, Nico Laufer, Harald Hansmann, Christian Boss, Stefan Ofe, Juan Ragazzo-Sanchez, Darvin Ervey Jimenez-Sánchez, Montserrat Calderón-Santoyo, Laetitia Picart-Palmade, Julio Barros-Castillo, Pedro Ulises Bautista-Rosales, Şule Celasun, Laura Romero-Zerón, Saran Banthong, Christian Kukla, Ivica Duretek, Joamin Gonzalez-Gutierrez, Clemens Holzer, Mohamed Elbadawi

Notice

Statements and opinions expressed in the chapters are these of the individual contributors and not necessarily those of the editors or publisher. No responsibility is accepted for the accuracy of information contained in the published chapters. The publisher assumes no responsibility for any damage or injury to persons or property arising out of the use of any materials, instructions, methods or ideas contained in the book.

First published in London, United Kingdom, 2018 by IntechOpen
eBook (PDF) Published by IntechOpen, 2019
IntechOpen is the global imprint of INTECHOPEN LIMITED, registered in England and Wales, registration number: 11086078, The Shard, 25th floor, 32 London Bridge Street
London, SE19SG – United Kingdom
Printed in Croatia

British Library Cataloguing-in-Publication Data
A catalogue record for this book is available from the British Library

Additional hard and PDF copies can be obtained from orders@intechopen.com

Polymer Rheology
Edited by Jose Luis Rivera-Armenta and Beatriz Adriana Salazar Cruz

p. cm.

Print ISBN 978-1-78984-001-8

Online ISBN 978-1-78984-002-5

eBook (PDF) ISBN 978-1-83881-657-5

Meet the editors

José Luis Rivera-Armenta was born in Tampico, Mexico, in 1971. He attained a BSc in Chemical Engineering in 1994, an MSc in Petroleum Technology and Petrochemicals in 1998, and a PhD in Chemical Engineering in 2002 at the Technological Institute of Madero City (ITCM). Since 2003 he has been a full-time professor in posgraduate programs at ITCM and a project manager of several developments sponsored by the National Technologic of Mexico and CONACYT. Since 2005 he has been a member of the National Research System at CONACYT level 1. His responsibilities include injection and extrusion and thermal analysis at the laboratory at the Petrochemical Research Center at ITCM. He has advised on eight PhDs, 15 master's degrees, and three bachelor theses and also supervised three posdoctorate students. He has had 48 articles and five book chapters published.

Beatriz A. Salazar Cruz attained her PhD in 2014, and has been an associate member of MATCO since 2016 and an associate professor of the Technological Institute of Madero City since 2012. From 1995 to 2008 she gained experience in the chemical process industry (Dynasol Elastomers) developing projects with SBS, SBR and SEBS polymers and characterizing and innovating the quality of products in a wide range of applications: asphalts, adhesives, and compounds. Beatriz is the author or coauthor of several scientific publications in English and Spanish, and author or coauthor of several book chapters. She has taught several rheology courses. She has also collaborated in several projects supported by the National Technologic of Mexico and CONACYT. She has advised on master's degree theses and also supervised engineering students.

Contents

Preface

Rheology is the science that studies the flow behavior of materials, whether in a solid or liquid state, under the application of a stress or deformation to obtain a response to an applied force.

Rheology has some wide application areas that include foods, textiles, personal care products, pharmaceuticals, and polymers, among others. In polymers, rheology has become an important tool to understand the behavior of polymers under processing conditions, and to help to design equipment such as injectors, extruders, and other polymer processing equipment.

In diluted suspension applications and colloidal dispersions, rheological behavior is a relevant topic mainly in concentrated materials because of its high theoretical and experimental complexity. Research work in this field is of high industrial importance especially in the design, production, and shipping phases.

Also, mathematical modeling in research work has been developed in a particular way so that the modeling of complex phenomena such as thixotropy or thinning generates an interest for a variety of problems.

Special studies in materials rheology, where it depends on the nature of the stimulus to which it responds, are those that show magnetorheological and electrorheological properties (depending on magnetics or electrical fields). These materials are created by permeable suspended particles in a medium that is either magnetic or conducting according to the case, and react to external stimuli by returning to their initial conditions. They recover their original property, repeating this process many times without deterioration; therefore, they are defined as "intelligent fluids."

Another area of application of rheology in polymers is to help understand the structure–property relationship by means of changes in molecular weight, molecular weight distribution, morphology, melt degradation, and performance under processing conditions, among others.

There are several ways to evaluate rheological behavior, but mainly it is assessed to obtain rheological curves, which can be carried out in rotational, oscillatory, or creep mode.

The present book is divided into three sections: "Advances in new rheology applications," "Polymers and biopolymers rheology," and "Suspensions, colloids and granular materials rheology," covering several application areas, interpretation of results, mathematical models, as well as determining other areas where rheology and rheological phenomena can be understood.

The first section presents work that can be regarded as a novelty, mainly trying to explain phenomena that are not often reported in rheology, in addition to developing new materials. The second section focuses on works concerning the rheology of polymers and biopoly-

mers, which can have applications for petroleum recovery, as well as applications in biochemistry. The last section shows work that explains changes in the rheological behavior of materials having suspensions, colloids, or particles in a polymer.

This book comprises research work that tries to help the reader to understand the science of rheology, presenting novel work in the polymer rheology area.

Dr. José Luis Rivera-Armenta and Dr. Beatriz Adriana Salazar-Cruz
National Technologic of Mexico (TecNM)
Technological Institute of Madero City, Mexico

Section 1

Advances in New Rheology Applications

Chapter 1

Magnetorheology of Polymer Systems

Sergey Vshivkov and Elena Rusinova

Additional information is available at the end of the chapter

http://dx.doi.org/10.5772/intechopen.75768

Abstract

The results of researches of a magnetic field effect on rheological properties of both paramagnetic, and diamagnetic polymer systems are described. Influence of intensity and the direction of power lines of the magnetic field on the viscosity of magnetic liquids and magnetorheological suspensions is analyzed. Results of theoretical researches of the magnetic field effect on the diamagnetic macromolecule orientation in solutions are discussed. The data on the influence of the magnetic field on rheological parameters of cellulose ether solutions are generalized and analyzed. The rheological parameters are compared with a change of studied system structure under magnetic field. The concentration dependences of viscosity and the sizes of supramolecular particles in solutions are compared. The rheological behavior of systems in a region of phase transitions is considered. Concentration dependences of the viscosity are described by curves with a maximum which concentration corresponds to a phase transition concentration.

Keywords: polymer systems, magnetic field, rheology, structure

1. Introduction

There are two classes of substances with various magnetic properties; paramagnetics and diamagnetics. Paramagnetic placed in a magnetic field with an intensity of H is magnetized in the direction coinciding with the direction of power lines of the field. Thus, a magnetic moment μ arises in a sample. The paramagnetism is caused by the orientation of the magnetic moments of atoms and molecules of the paramagnetic under the field. At the same time $\mu = \chi_{par}H$, where χ_{par} is a paramagnetic susceptibility, $\chi_{par} >> 0$. The paramagnetic particles distributed in the liquids are oriented along the force lines of the external field that leads to an aggregation of particles and to a viscosity growth of such systems (magnetic liquids).

An increase in the viscosity of magnetic liquids under application of a magnetic field (the magnetorheological effect [1]) was discovered experimentally in the 1950s [2] for the systems based on iron carbonyl and iron oxide. Subsequently, this phenomenon was studied in some reports [3–15]. It was found that, in resting compositions, a structure formation is observed as a result of the magnetodipole interaction of particles and orientation of anisodiametrical structural elements along magnetic force lines. As the shear rate increases, the aggregates break up. Each combination of the given parameters (the viscosity of dispersion medium, the magnetic properties of particles, the field strength, and the shear rate) is characterized by a certain set of structural elements and their mutual disposition. An important feature of the rheological properties of ferrofluids in the magnetic field is their dependence on the mutual orientation of shear and magnetic field. An increment of the effective viscosity of a medium at the perpendicular orientation substantially exceeds the effective viscosity induced by a parallel field. A strong anisotropy of rheological properties upon field orientation along the flow rate, along its gradient, and along the direction of its vortex was revealed in [15]. The new experimentally observed phenomena for ferrofluids are the Weissenberg effect [16], which was detected earlier only in polymer and liquid crystalline media, and the shear-induced reduction in the degree of anisotropy of the internal structure of ferrofluids, as was revealed by small-angle neutron scattering [17]. The effect of magnetic field and surfactants on the rheological properties of strontium ferrite suspensions was studied in [18]. It was shown that, under application of the field, the viscosity of the suspension increases. This phenomenon was explained by the formation of three-dimensional chain structures from the ferrite particles. After the field is switched off, these structures do not decompose fully, and this circumstance is responsible for the hysteresis of suspension viscosity. After introduction of polyelectrolytes into a suspension, its viscosity decreases both in the field and after its switching off. This is caused by a decrease in the interparticle friction and weakening of the strength of three-dimensional structures owing to the formation of a double electrical layer on the surface of particles. In [19], the magnetoviscous properties of two types of magnetic fluids based on iron oxide Fe_3O_4 were compared: the first one included oleic acid as a surfactant, and in the second one, the surfactant was tetramethylammonium hydroxide. It was shown that the type of surfactant strongly affects the fluid behavior in the magnetic field: in the presence of oleic acid, a change in viscosity under application of the magnetic field occurs more rapidly than that in the presence of tetramethylammonium hydroxide. The rheological properties of magnetic fluids ferroparticles-poly(α-olefins)-polyurethane, ferroparticles-*n*-octyl-pyrrolidone-butyl acrylate, and ferroparticles-*n*-octylpyrrolidone-pentafluorostyrene were studied in [20]. Recent advances in the field of magnetic fluids were highlighted in reviews [1, 21–26].

To understand the internal physical nature of the magnetoviscous effect, new data on the effect of magnetic field and deforming flow on the dynamics of these systems are required. For example, up to now, the data on the effect of concentration of a magnetic fluid and the rate of its deformation on the magnetorheological effect have been scarce. Papers [24, 25, 27, 28] deal with the concentration dependence of the effect of a constant magnetic field on the viscosity of aqueous and water-glycerol magnetic fluids based on iron and iron oxide nanoparticles. It was shown that the magnetic field enhances the fluid viscosity by 20–80 times. The concentration dependence of the relative viscosity η/η_0 (η and η_0 are the viscosities in the field and in its

absence, respectively) is described by a curve with a maximum. This is explained by the transition from chain aggregates of nanoparticles to drop-shaped ones. The magnetic field with force lines oriented perpendicularly to the rotor rotation axis increases the viscosity of systems to a much higher extent than upon parallel orientation. However the data on magnetorheological properties of the paramagnetic systems containing polymers are not numerous [20, 29].

Diamagnetism is an appearance in substance of a magnetic moment directed toward to the external field, at the same time $\chi_{diam}<<0$. Molecules (atoms) of diamagnetic substances have not any unpaired electrons. The theoretical and experimental investigations of interaction of diamagnetic macromolecules with a magnetic field are currently under development [30–64]. It was found experimentally that application of a magnetic field leads to an orientation of macromolecules and their associates along the force lines, to the increase in phase transition temperatures, causes a formation of domains in solutions.

If an anisotropic macromolecule is placed in a magnetic field, then a force acts on it and causes its rotation. The magnetic anisotropy of chemical bonds is responsible for the magnetic anisotropy of the molecule. In polymer systems, the amount of contacts between macromolecules is high; therefore, an orientation of polymer chains proceeds cooperatively. The effect of the field consists in the rotation (orientation) of macromolecular domains in a certain predominant direction that depends on the sign of diamagnetic susceptibility anisotropy $\Delta\chi^M$ for this polymer. Domains are taken to mean the anisotropic associates of macromolecules or mesophase regions. The diamagnetic moment appearing at the domain under magnetic field can be written as [32, 34]:

$$\mu = \frac{\Delta\chi^M}{2\mu_0} B^2 V \sin 2\xi \tag{1}$$

where V is domain volume, μ_0 is a magnetic constant of vacuum, B is a vector of magnetic induction, ξ is an angle between the direction **B** and the domain axis.

Interaction of external magnetic field with the domain having the magnetic moment μ increases energy of magnetic field by value of E_{mag} [31]:

$$E_{mag} = -(1/2)V\chi_{\perp}^{M}\mu_0^{-1}B^2 - (1/2)V\Delta\chi^M \mu_0^{-1} B^2 \cos^2\xi \tag{2}$$

where $\chi_{\perp}^{M}$ diamagnetic susceptibility in the direction perpendicular to domain axis.

Magnetic orientation is observed when E_{mag} exceeds the value of thermal energy (k_BT), k_B is the Boltzmann's constant, T represents the absolute temperature. From here it follows [31]:

$$V > \frac{2k_B T\mu_0}{|\Delta\chi^M|B^2} \tag{3}$$

This equation determines the minimal critical volume capable to orientation.

The rotational moment of the domain (N) is expressed as [35]:

$$N = V\Delta\chi^M \mu_0^{-1} B^2 \sin\xi \cos\xi \, \omega \tag{4}$$

ω is normal vector to **B** and domain axis.

Therefore, it is necessary for the orientation of a diamagnetic particle to satisfy the following conditions: a particle must be anisodiametric; the particle volume must be higher than the corresponding critical value V_{cr}; and the medium must be low-viscosity. The particles can also be microfibers, crystallites, liquid crystals and other heterogeneous particles suspended in a liquid medium.

In the 1960s, the effect of a magnetic field on liquid crystals was theoretically studied by de Gennes and Meuer [65, 66]. It was shown that, at the critical magnetic field strength, the complete transition of a cholesteric liquid crystal to a nematic one is realized. Experimentally, this was confirmed for liquid crystals of rigid-chain polymer poly(γ-benzyl-L-glutamate) in a number of solvents in the 1970s [67, 68]. This phenomenon was explained by the orientation of liquid crystal molecules relative to force lines of the magnetic field.

Since 2006, researchers of the Chair of Macromolecular Compounds, Ural State University (since 2011 Ural Federal University), have been involved in systematic investigations of the effect of magnetic field on the phase transitions, structure, and rheological properties of liquid crystalline solutions of cellulose ethers. It was found [57–64] that application of a magnetic field leads to a change in the type of liquid crystals from cholesteric to nematic, causes formation of domains in solutions, and entails a substantial (by tens of degrees) increase in the temperature of formation of liquid crystalline phases. As the molecular mass of a polymer is increased, the ability of its molecules to orientate in the magnetic field is reduced. The solutions of cellulose ethers represent memory systems: after termination of magnetic field exposure, the orientation of macromolecules and the increased phase-transition temperature are preserved for many hours. The magnetic field leads to an increase in the sizes of associates of rigid-chain macromolecules and in the viscosity of solutions.

It should be noted that up to now there is only one theoretical [69] and some experimental works [70–76] in which an influence of the magnetic field on rheological properties of polymer solutions is considered. Note that practically no information is available on the relaxation character of the rheological behavior of polymer solutions in the magnetic field.

Therefore, the main aim of this study is to investigate the magnetorheological properties of paramagnetic and diamagnetic polymer systems

2. Results and discussion

2.1. Materials and methods

The magnetically sensitive systems (suspensions of aerosil and iron nanoparticles) in poly (ethylene glycol) (PEG) and poly(dimethylsiloxane) (PDMS) have been studied. The nanodispersed iron powder (d_w = 150 nm), nanodispersed aerosil (d_w = 250 nm), PEG with

M_n = 400 and PDMS with $M_\eta = 3.4 \times 10^4$ were used. The suspensions were prepared by mixing of PEG and PDMS with aerosil nanoparticles (systems 1 and 2, respectively). The concentrations of aerosil were 4.2 and 2.0 wt% in systems 1 and 2, respectively. The magnetic fluids have been produced by addition of iron nanoparticles to basic suspensions.

Hydroxypropyl cellulose samples with $M_w = 1 \times 10^5$ and a degree of substitution of α = 3.2 (HPC1), with $M_w = 1.6 \times 10^5$ and $\alpha = 3.6$ (HPC2), ethyl cellulose (EC) sample with $M_\eta = 2.6 \times 10^4$ and α = 2.6 have been investigated. Dimethylformamide (DMF), dimethyl sulfoxide (DMSO), ethanol and ethylene glycol were used as solvents. The purities of the solvents were confirmed by their refractive indexes. Polymer solutions were prepared in sealed ampoules for several weeks at 368 K (in DMSO), 333 K (in ethanol), 353 K (in DMF) and 363 K (in ethylene glycol).

The phase state of solutions was estimated with the use of an OLYMPUS BX-51 polarization microscope. The radii of supramolecular particles, r, in moderately concentrated and concentrated solutions were determined via the method of the turbidity spectrum, which was suggested by Heller et al. [77–79] and developed by Klenin et al. [80]. Optical density A of solutions was measured with Helios spectrophotometers. The said method is based on the Angstrom eq $A \sim \lambda^{-n}$, where λ is the wavelength of light passing through a solution and n is a composite function that depends on the relative refractive index of a solution, m_{rel}, and coefficient α related to dimensions of light-scattering particles:

$$n = \frac{d\ln A}{d\ln\lambda} \tag{5}$$

For every solution, relationships $\ln A$ versus $\ln\lambda$ were plotted, and the value of n was calculated from the slope of the straight line. The relative refractive index was calculated through the equation $m_{rel} = n_{D\ pol}/n_{D\ sol}$, where $n_{D\ pol}$ and $n_{D\ sol}$ are the refractive indexes of a polymer and solvent, respectively. With the use of the tabulated data from [80], parameter α was determined for the found values of m_{rel} and n. Parameter α is related to average weighed radius r_w of scattering particles via the expression:

$$\alpha = \frac{2\pi r_w}{\lambda_{av}} \tag{6}$$

In this expression, the wavelength of light passing through a solution is $\lambda_{av} = \lambda_{av}/n_{D\ sol}$, where λ_{av} is the wavelength of light in vacuum corresponding to the midpoint of the linear portion of the $\ln A$–$\ln\lambda$ plot.

Solution viscosities under a magnetic field and in its absence were measured on a Rheotest RN 4.1 rheometer modified by us (**Figure 1**).

Rheometer was equipped with a coaxial-cylindrical operating unit made of a poorly magnetic substance, brass. Two magnets were used: the first producing a magnetic field with an intensity of 3.7 kOe and lines of force perpendicular to the rotor-rotation axis and the second one producing a magnetic field with an intensity of 3.6 kOe and lines of force parallel to the rotor-rotation axis. A metallic rotor rotating in a magnetic field can be considered as a current generator closed upon itself [81].The working generator produces

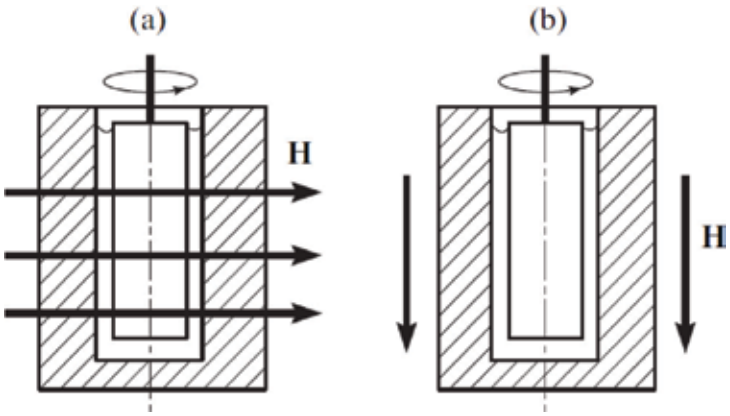

Figure 1. Schematic representation of viscosity determination with field lines directed (a) perpendicularly and (b) parallel to the rotor-rotation axis.

a braking torque. To take into account this torque, a correction dependence of shear stress on shear rate in the working unit filled with air between the cylinder surfaces was plotted. The true shear stress for solutions was obtained as the difference between the measured value and the correction value at the same shear rate. The relaxation character of rheological behavior of polymer solutions was studied via two-stage measurements: during an increase in shear rate from 0 to 13 s^{-1} (loading) for 10 min followed by a decrease in shear rate from 13 to 0 s^{-1} (unloading) for 10 min.

2.2. Magnetorheological properties of paramagnetic systems containing polymers

The dependences of viscosities of PEG-aerosil and PDMS-aerosil suspensions on the shear rate in the magnetic field and in its absence are depicted in **Figure 2**.

As the shear rate increases, the viscosity of the suspensions decreases. This fact provides evidence for the destruction of the initial structure of systems. The magnetic field has almost no effect on the viscosity of the suspensions of oligomeric PEG-aerosil upon either parallel or perpendicular orientation of magnetic force lines relative to the rotor rotation axis. An analogous phenomenon was observed for the glycerol-aerosil system [24]. However, the viscosity of the PDMS-aerosil system in the field grows substantially, although the viscosity of PDMS does not change in a magnetic field. An increase in the viscosity of polymer solutions under application of a magnetic field is observed for a series of cellulose ether-solvent systems, i.e., for the polymers with the moderate chain rigidity [70–76]. According to the developed theory of interaction between diamagnetic macromolecules and their associates with the magnetic field [31–33], the effect of the field can manifest itself under the following conditions: a particle must be anisodiametrical; the particle volume must be higher than the corresponding critical value Vcr; and the medium must be low-viscosity. The aggregates of aerosil particles bound by PDMS macromolecules may correspond to the first two conditions, so the viscosity of the PDMS-aerosil system in the field grows substantially, in conformity with the latter condition.

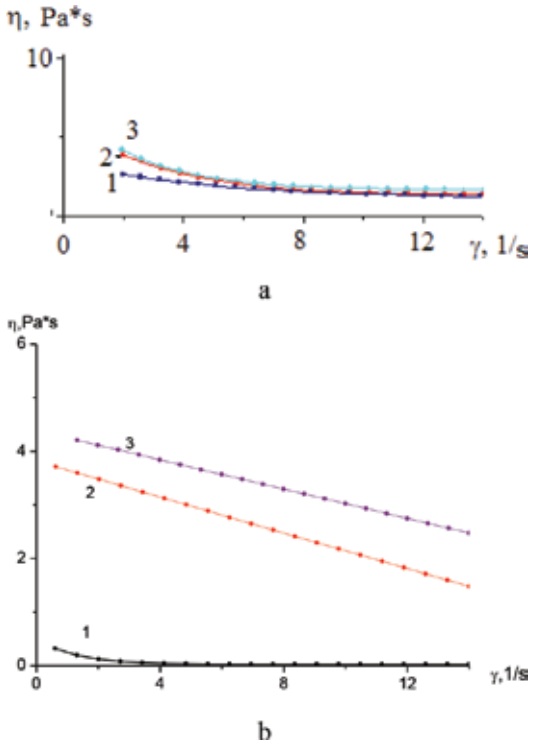

Figure 2. Dependences of the viscosity on the shear rate for the (a) PEG-aerosil and (b) PDMS-aerosil suspensions. H = 0 (1), $H_{\perp}$ = 3.7 (2), and (3) H_{II} = 3.6 kOe (3).

Figure 3 shows the dependences of the viscosity on γ for suspensions with the concentrations of iron nanoparticles of 7.4 wt % (system 1) and 5.7 wt % (system 2) in the magnetic field and in its absence.

An analogous dependence was obtained for all other explored suspensions with ferroparticles. Under application of the magnetic field, the aggregates of iron nanoparticles are formed. This leads to a substantial increase in viscosity at low shear rates ($\gamma < 1\ s^{-1}$). As the shear rate increases from 1 to 14 s^{-1}, the aggregate destruction and the nanoparticle orientation occur; as a result, the viscosity decreases. In this respect, further analysis of the field effect on the properties of the system was carried out using the viscosity data obtained at low values of γ. The dependences of suspension viscosity on the concentration of iron nanoparticles in the magnetic field are demonstrated in **Figure 4**.

From this figures, it follows that the suspension viscosity substantially increases with the growth of ferroparticle concentration. The viscosity in the transverse field is higher than that in the longitudinal one.

Figure 5 shows the dependence of relative viscosity η/η_0 of suspensions on the concentration of ferroparticles (η and η_0 are the viscosities in the field and in its absence, respectively).

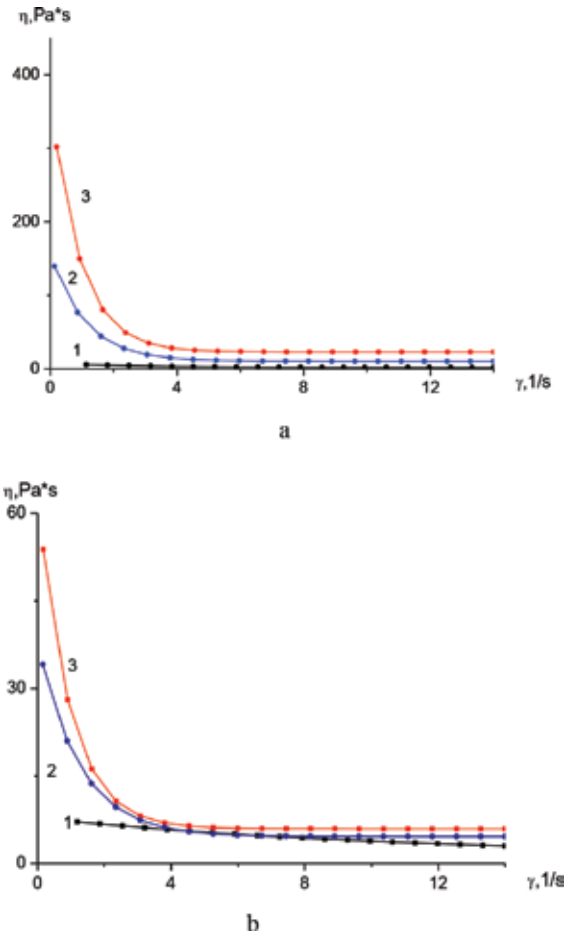

Figure 3. Dependences of the viscosity on the shear rate for (a) PEG-Aerosol-Iron nanoparticle and (b) PDMS-Aerosol-Iron nanoparticle suspensions. ω_2 = (a) 7.4 and (b) 5.7 wt %. (1) H = 0, (2) H_{II} = 3.6 and (3) $H_{\perp}$ = 3.7 kOe.

The relative viscosity reflects the effect of the magnetic field on the orientation and aggregation of iron nanoparticles. It is obvious that an increase in the concentration of iron nanoparticles, which are able to orient in the field, leads to an increase in viscosity by 18–35 times (system 1) and 120–300 times (system 2). The viscosity of the suspensions in the transverse magnetic field is almost two times higher than that in the longitudinal field. To analyze this phenomenon, let us consider the flow processes of ferrofluids using the schemes presented in **Figure 6**.

If the direction of force lines is perpendicular to the rotor-rotation axis (**Figure 6a**), the orientation of iron nanoparticle aggregates in quadrants I and III coincides with the direction of flow, and the viscosity can decrease. In quadrants II and IV, the orientation of nanoparticles and their aggregates is perpendicular to the direction of flow, and the viscosity must increase. Apparently, in the general case, the viscosity can both decrease and increase. When the direction of force lines

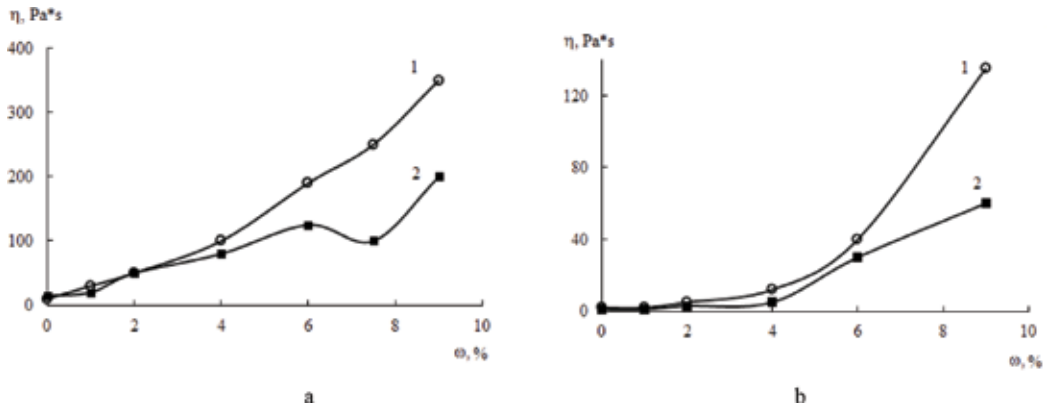

Figure 4. Concentration dependences of the viscosity of (a) PEG-Aerosol-Iron nanoparticle and (b) PDMS-Aerosol-Iron nanoparticle suspensions on the concentration of ferroparticles. (1) $H_{\perp} = 3.7$ and (2) $H_{II} = 3.6$ kOe. γ = (a) 0.4 and (b) 0.5 s^{-1}.

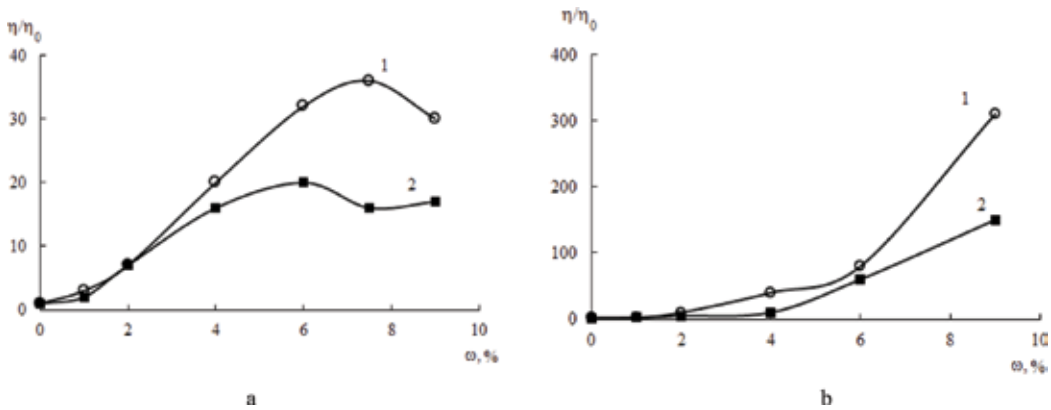

Figure 5. Dependences of the relative viscosity of (a) PEG-Aerosil-Iron nanoparticle and (b) PDMS-Aerosil-Iron nanoparticle suspensions on the ferroparticle concentration. (1) $H_{\perp} = 3.7$ and (2) $H_{II} = 3.6$ kOe; γ = (a) 0.4 and (b) 0.5 s^{-1}.

is parallel to the rotor rotation axis (in the longitudinal field) (**Figure 6b**) the aggregates of iron nanoparticles orient by their long axis along the rotor-rotation axis, i.e. layer-by-layer. In this case, an increase in viscosity caused by the aggregation of particles in the magnetic field can be compensated by reduction in the forces of viscous friction owing to the layer-by-layer arrangement of the particles. On the whole, the experiments show that, in the transverse field, the viscosity of suspensions increases to a higher extent that in the longitudinal field.

An initial increase in the effect of the magnetic field on viscosity (**Figure 5**) is connected with growth in the number of particles capable of orientation and subsequent aggregation in the field. However, upon further increase in the concentration of particles, the growth of suspension viscosity now hampers the orientation processes and the effect of the magnetic field becomes weaker. A maximum arises on curves $\eta/\eta_0 = f(\gamma)$ (**Figure 5a**).

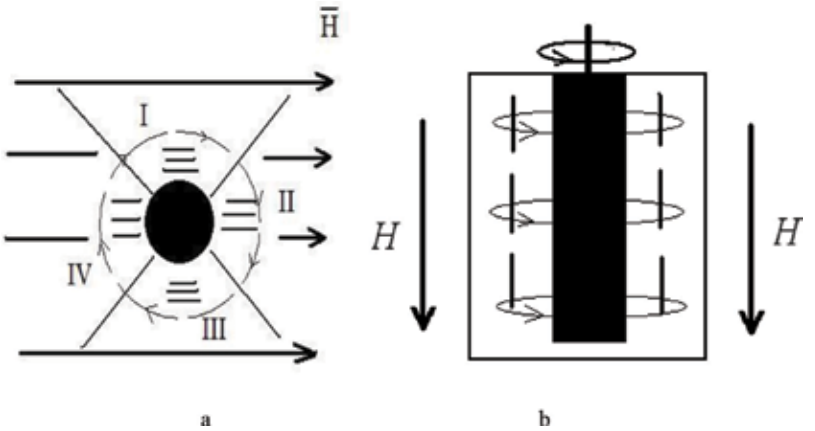

Figure 6. Schemes of suspension flow in the magnetic field at (a) perpendicular and (b) parallel directions of force lines relative to the rotor-rotation axis.

2.3. Magnetorheological properties and structure of diamagnetic polymer systems

Figure 7 shows the concentration dependences of the diameters (D = 2r) of supramolecular particles in the systems: HPC1-ethylene glycol (1), HPC1-water (2) and EC-DMF (3).

The mean-square distance between chain ends of a macromolecule was calculated via the equations $h^2 = LA$ (L is contour length) and $(h^2)^{1/2} = (LA)^{1/2}$. In calculations of macromolecule size, the Kuhn segment values A = 21.4 nm for HPC and 16 nm for EC [82], the length of a cellobiose residue of 1.03 nm, and the unit length of a cellulose ether macromolecule of 0.5 nm were used. The contour length of a macromolecule was calculated through eq. $L = 0.5n$, where n is the degree of polymerization. Calculated contour length L of HPC1 macromolecules and the mean-square distance between chain ends $(h^2)^{1/2}$ were 164 and 60 nm, respectively, 216 and 68 nm for HPC2 and 56 and 30 nm for EC. From **Figure 7**, it follows that, in solutions with

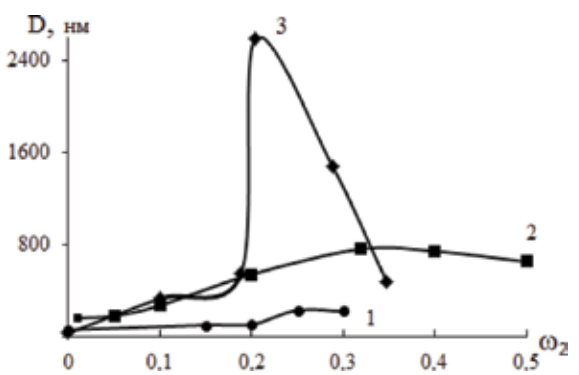

Figure 7. Concentration dependences of the diameters of supramolecular particles in the systems: HPC1-Ethylene glycol (1), HPC1-Water (2) and EC-DMF (3).

concentrations $\omega_2 > 0.05$, there are no isolated macromolecules and their associates (supramolecular particle involving a great number of macromolecules) are present, with the sizes of supramolecular particles in EC solutions being 4–10 times larger than those in HPC solutions. This can be caused by a strong interchain interaction and a higher packing density of EC relatively HPC macromolecules. Indeed, the linear ethyl radicals in the polymeric units of neighboring EC macromolecules can produce a denser packing with each other than the branched hydroxypropyl radicals of HPC.

The concentration dependences of *D* are described by curves with maxima. The concentrations of solutions with the maximum particle size coincide with the region of the transition from an isotropic solution to an anisotropic solution. In isotropic solutions, macromolecules and their associates are not oriented relative to each other. With an increase in polymer concentration, they form large particles as a result of the intensification of the interchain interaction. The formed large particles do not have a dense packing; i.e., they may contain abundant solvent. During the transition to the LC state with a further increase in the polymer concentration, the emerged orientation of macromolecules and supramolecular particles toward each other leads to increase in interchain interaction. This phenomenon may result in the squeezing out of the solvent from supramolecular particles, an event that is manifested in a decrease in their size. The such phenomenon is revealed for other systems in [83–85].

Figure 8 shows the micrographs of HPC solutions after their treatment with the magnetic field. As is seen, the streaky structure manifests itself, thus indicating formation of large domains in the course of orientation. Similar data were obtained for HPC1 solutions in ethylene glycol.

The our data of researches of a surface relief for the films HPC1 prepared from solutions in ethylene glycol under magnetic field and in its absence are given in **Figure 9** and in a **Table 1**.

Figure 9 and the **Table 1** show that heterogeneity of the surface relief of HPC1 film is more after processing by magnetic field, than before processing. At the same time on the surface of the film received in the magnetic field an orientation of strips of one height is observed. Therefore the magnetic field causes the orientation processes in solutions, at the same time the domain structure arising in solutions is fixed after evaporation of a solvent and shown in orientation of strips of the film relief.

The application of the magnetic field leads to development of the domain structure as a result of additional orientation of macromolecules in the field. Similar data were obtained for other systems having liquid crystalline transitions [57, 58, 62, 70, 71, 73, 75, 76]. In accordance with [32, 86, 87], macromolecules orient in the magnetic field with their long chains arranged parallel to the force lines. This orientation is related to the molecular diamagnetic anisotropy of macromolecules. As a consequence, supramolecular particles are formed, especially in the vicinity of the LC phase transition [57, 58, 62]. During treatment of solutions with a magnetic field, the particle size grows owing to additional orientation of macromolecules and supramolecular particles relative to the field lines of force and an increase in the interchain interaction.

The concentration dependences of diameters D = 2r of light scattering particles are depicted in **Figure 10**.

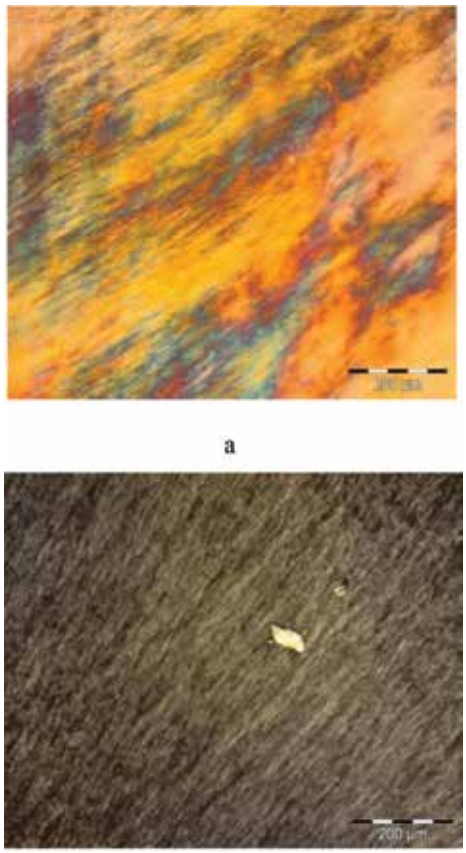

Figure 8. Micrographs of solutions under crossed polaroids after their treatment with the magnetic field. a) HPC2-Ethanol, $\omega_2 = 0.55$; b) HPC2-DMSO, $\omega_2 = 0.50$. $H = 3.7$ кЭ.

The concentration dependences of D are described by curves with maxima. The concentrations of solutions with the maximum particle size coincide with the region of the transition from an isotropic solution to an anisotropic solution.

A concentration dependence of relative size r/r_0 of supramolecular particles (where r_0 and r are the radii of light-scattering particles before and after magnetic-field treatment of solutions, respectively) was found (**Figure 11**).

Note that the solution concentration with the maximum relative size of particles for the EC-DMF system is 2.5 times lower than that for the HPC-ethylene glycol system, an outcome that is due to the larger sizes of supramolecular particles in EC solutions. These dependences reflect the effect of a magnetic field on the orientation of macromolecules and supramolecular particles in solutions. An increasing number of magnetically sensitive macromolecules and supramolecular particles, leads to the intensification of the orientation processes in the field. However, with a further increase in the polymer concentration, the increasing density of the fluctuation network of entanglements begins to hinder the orientation processes and the

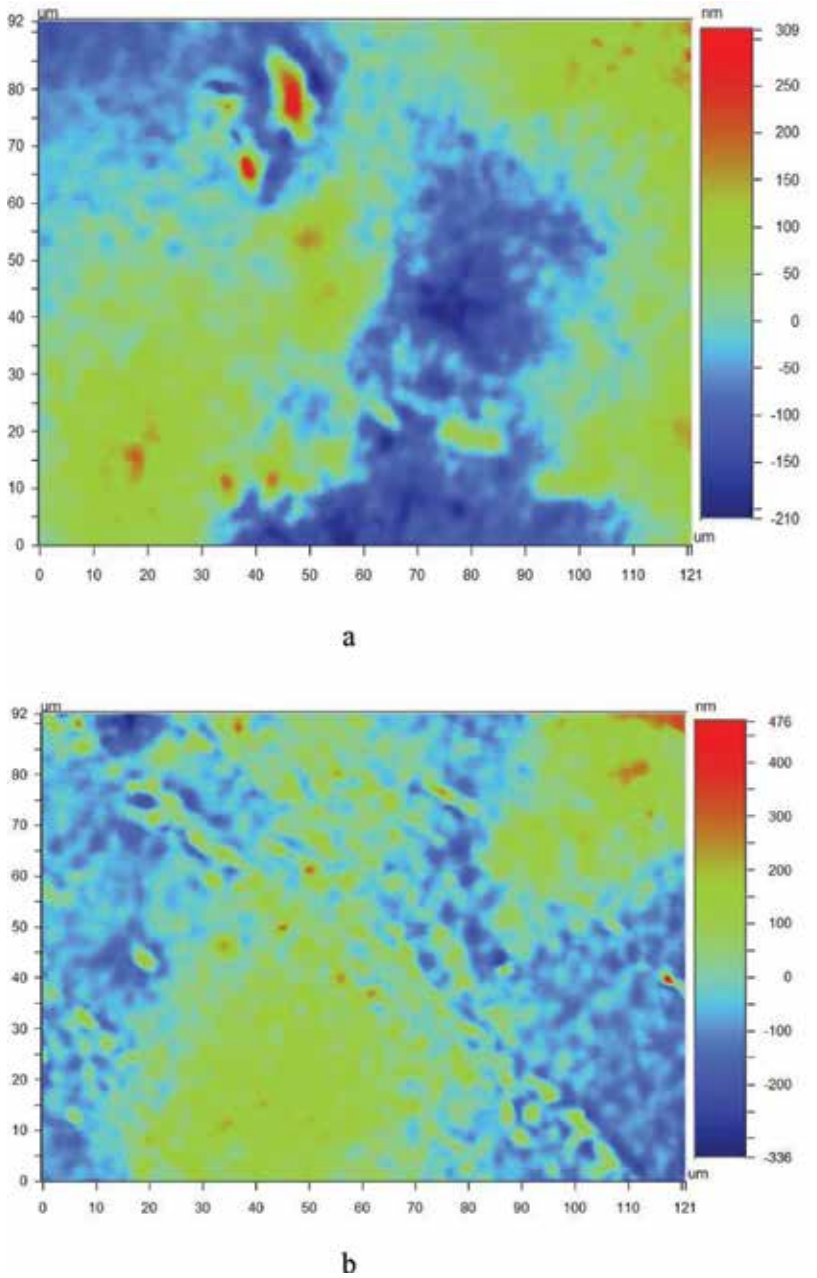

Figure 9. The micrographs of the surface relief of HPC1 films obtained by a method of an optical interferometry. H = 0 (a), H = 3.6 kOe (b).

influence of the field on the properties of solutions decreases. The similar dependences have been found for the HEC-DMF and EC-DMAA systems earlier [72].

Typical dependences of viscosity of HPC solution on shear rate are presented in **Figures 12** and **13**.

Parameters of the surface relief	Ra	Rq	Rz
Size, nм H=0 kOe	59.47	72.69	480.05
Size, nм H=3.6 kOe	71.99	86.99	629.76

Ra is an arithmetic average of absolute values of deviations of a surface profile, Rq is an average quadratic absolute values of deviations of a surface profile, Rz is a height of roughnesses of a surface profile

Table 1. Parameters of the surface relief for the films HPC1 prepared from solutions in ethylene glycol in magnetic field and in its absence.

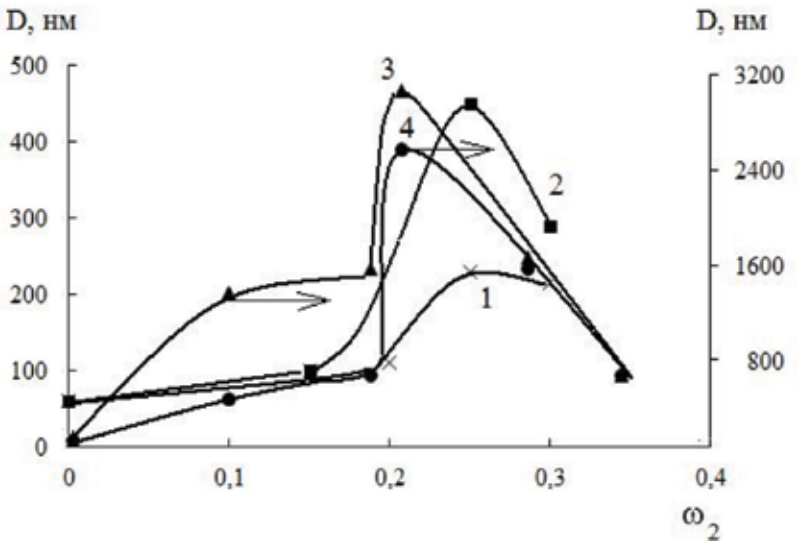

Figure 10. Concentration dependences of the diameters of supramolecular particles in the systems: HPC1-ethylene glycol, H = 0 (1) и 9.0 kOe (2) and EC-DMF, H = 0 (4) и 9.0 kOe (3). T = 298 K.

The solutions of HPC are non-Newtonian liquids, as manifested by a reduction in viscosity with an increase in shear rate. This result is in agreement with the data available for other liquid crystalline systems [70–76] and indicates that the initial structuring of polymer solutions is destroyed and that macromolecules and their associates orient along the direction of flow in the course of shearing. In addition, **Figure 11** shows that application of the magnetic field increases the viscosities of isotropic solutions. As it has been stated above it is connected with orientation of macromolecules in magnetic field. Such an orientation is related to the molecular diamagnetic anisotropy of macromolecules. As a result, supramolecular particles are formed, especially in the vicinity of the LC phase transition, and viscosity grows. But the magnetic field decreases the viscosities of anisotropic solutions (**Figure 12**). It is caused by easier orientation of macromolecules and supramolecular particles of anisotropic solutions in the magnetic field and also by the reduction of the particle sizes.

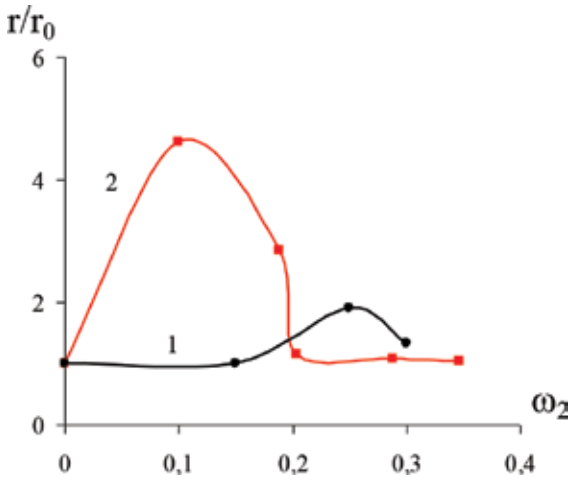

Figure 11. Concentration dependence of relative size r/r_0 of supramolecular particles for systems: HPC1-ethylene glycol (1) and EC-DMF (2).

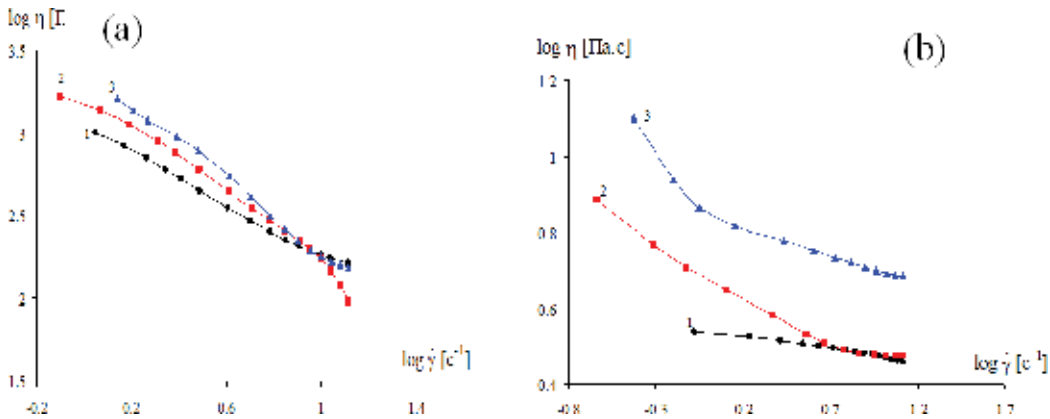

Figure 12. Dependences of viscosity on shear rate of isotropic solutions HPC1 in ethylene glycol: $\omega_2 = 0.15$ (a), HPC2 in ethanol, $\omega_2 = 0.15$ (b).

The above data were used to construct the concentration dependence of viscosity. In this case, the values of viscosity measured at a small shear rate 2.5 s^{-1} were chosen because, as was shown in [88–94], the concentration dependence of viscosity measured at precisely low shear rates is typical for anisotropic solutions. These dependences are described by curves with maxima for all studied systems. As the concentration of polymers is increased, the interchain interaction becomes stronger; as a consequence, supramolecular particles enlarge and viscosity increases. However, in the anisotropic region, viscosity decreases, in agreement with the literature data available for other systems having liquid crystalline transitions [88–94], and is related to the easier orientation of macromolecules and supramolecular particles along the direction of flow and to the reduction of the particle sizes. The magnetic field causes an increase in the viscosities of polymers solutions owing to the above-mentioned causes.

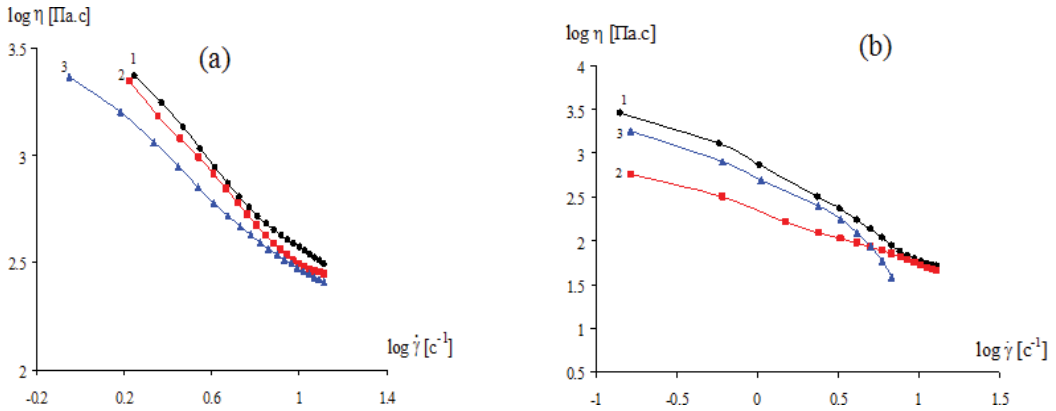

Figure 13. Dependences of viscosity on shear rate of anisotropic solutions HPC1 in ethylene glycol: $\omega_2 = 0.30$ (a), HPC2 in ethanol, $\omega_2 = 0.56$ (b).

Processes occurring during the flow of solutions in the magnetic field may be represented by the scheme (**Figure 6**). In quadrants I and III, the orientation of macromolecules coincides with the direction of flow and viscosity may decrease. In quadrants II and IV, the orientation of macromolecules is perpendicular to the direction of flow and viscosity should increase. Apparently, in this case, viscosity may either decrease or increase. When the force lines are directed parallel to the rotor-rotation axis (**Figure 6b**), macromolecules orient with their long axes along the axis of rotor rotation, that is, perpendicular to the direction of flow; as a result, viscosity may increase. Moreover, the macromolecules and supramolecular particles orient by their long axis along the rotor-rotation axis, i.e. layer-by-layer. In this case, an increase in viscosity can be compensated by reduction in the forces of viscous friction owing to the layer-by-layer arrangement of the macromolecules and particles.

The data were used to plot the concentration dependence of relative viscosity η/η_0 (**Figure 14**), which reflects the effect of a magnetic field on the orientation of macromolecules and supramolecular particles in solutions (η and η_0 are the viscosities in the presence of the magnetic field and in its absence, respectively).

As can be seen, the concentration dependences of η/η_0 are described by curves with maxima. Analogous data for other systems involving liquid crystalline transitions (HPC-dimethyl sulfoxide, EC-DMF, hydroxyethyl cellulose-DMF, EC-DMAA, HEC-DMAA, HPC-DMF), were presented in some works [70–76]. The initial increase in η/η_0 with concentration is related to an increasing number of magnetically sensitive macromolecules and supramolecular particles, a situation that results in intensification of the orientation processes in the field. However, with a further increase in the polymer concentration, the increasing density of the fluctuation network of entanglements begins to hinder the orientation processes and the influence of the field on the properties of solutions decreases. An analogous concentration dependence of relative size r/r_0 of supramolecular particles (where r_0 and r are the radii of light-scattering particles before and after magnetic field treatment of solutions, respectively) was found (**Figure 11**).

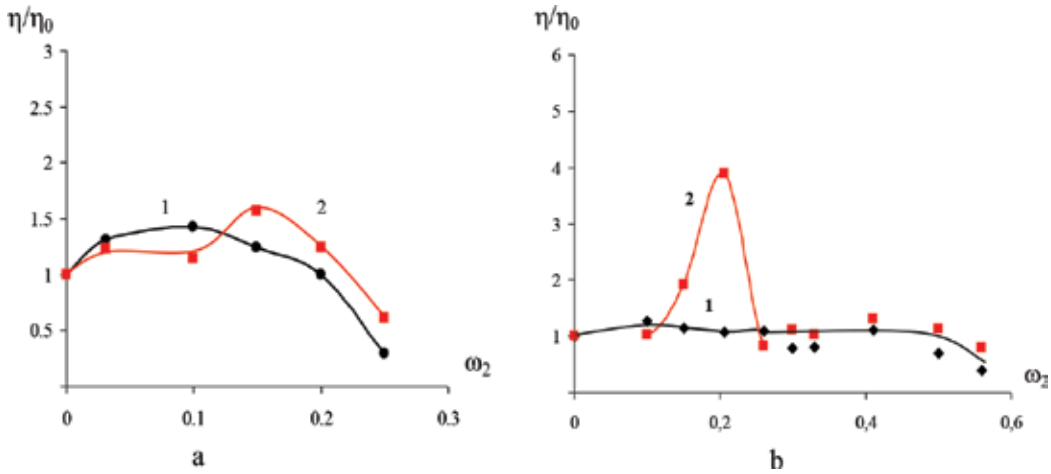

Figure 14. Concentration dependences of η/η_o for systems: (a) HPC1-ethylene glycol and (b) HPC2-ethanol. $H_{||}$ = 3.6 kOe (1) and $H_{\perp}$ = 3.7 kOe (2) $\dot{\gamma}$=2.5 c^{-1}.

2.4. The relaxation character of the rheological behavior of hydroxypropyl cellulose in ethylene glycol

The study of the viscosities of diluted and moderately concentrated solutions of HPC in ethanol and DMSO under the application of the magnetic field and in its absence showed that the loading and unloading curves coincide; that is, the hysteresis loop is absent. This result testifies that the structuring of the given solutions has time to recover after deformation. **Figure 15** presents the rheological properties of the concentrated isotropic solutions of HPC in ethanol under loading and unloading. The same dependences are typical for more concentrated isotropic and anisotropic solutions of HPC in DMSO.

The loading and unloading curves do not coincide, and the hysteresis loop is present. This fact indicates that, in the concentrated solutions of HPC, the structuring of solutions has no time to recover after deformation. In fact, an increase in the concentration of a solution

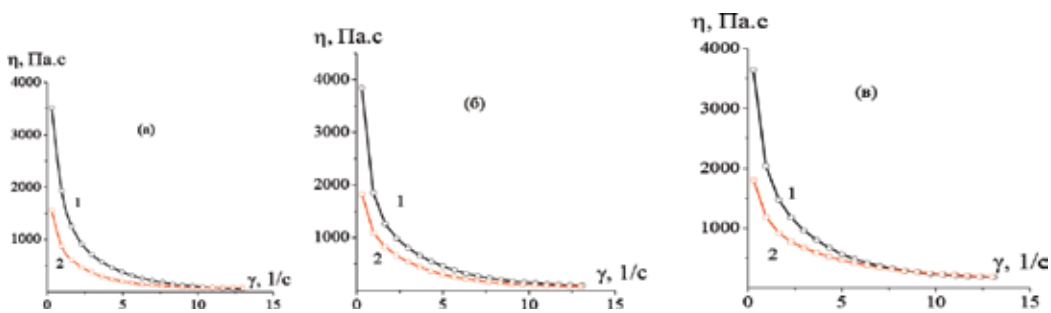

Figure 15. Dependence of viscosity on shear rate for the HPC2 solution in ethanol: ω_2 = 0.41 with (*1*) an increase and (*2*) a decrease in shear rate; (a) H = 0, (b) H_{II} = 3.6 and (c) $H_{\perp}$ = 3.7 kOe.

entails an increase in viscosity, which is related to relaxation time τ via the following relationship [95]: $\eta = E\tau$, where E is the shear modulus. For solutions with concentrations up to $\omega_2 < 0.25$ (the HPC-ethanol system) and up to $\omega_2 < 0.30$ (system HPC-DMSO), viscosities and relaxation times are smaller than those for more concentrated systems, the structuring of solutions has time to rearrange under the desired regime of change in the direction and value of shear rate, and the hysteresis loop is absent. However, for more concentrated solutions, the values of η and τ are high enough; therefore, the structuring of systems has no time to recover and the loading and unloading curves do not coincide. In this case, the hysteresis loop is observed; its area characterizes the part of mechanical energy ΔE irreversibly converting into heat energy, that is, mechanical losses in the unit volume of the sample per loading-unloading cycle.

Figure 16 shows the concentration dependences of mechanical losses for studied systems. These dependences are described by curves with maxima. Maximum mechanical losses are seen in the vicinity of the isotropic - anisotropic transition of solutions. The same dependence is typical for the concentration dependence of viscosity of HPC solutions. In fact, as the concentration of HPC is increased, the interchain interaction becomes stronger; as a result, the sizes of supramolecular particles increase and viscosity grows. This situation hinders the orientation of macromolecules and supramolecular particles along the direction of flow, and, as a consequence, mechanical losses increase. However, in the anisotropic region, viscosity decreases because of the easier orientation of macromolecules and supramolecular particles along the direction of flow; as a result, mechanical losses decrease.

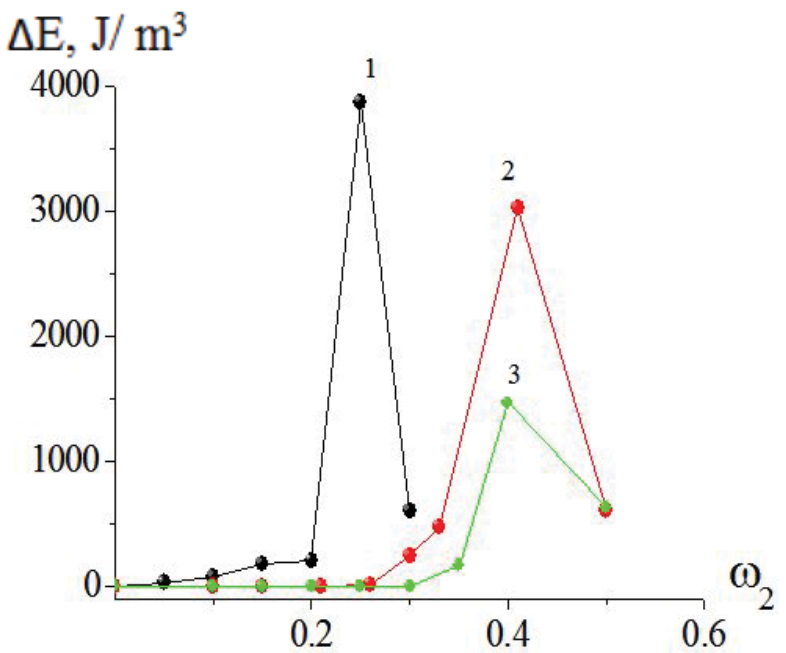

Figure 16. Concentration dependences of mechanical losses for the systems: (1) HPC1-ethylene glycol, (2) HPC2-ethanol and (3) HPC2-DMSO.

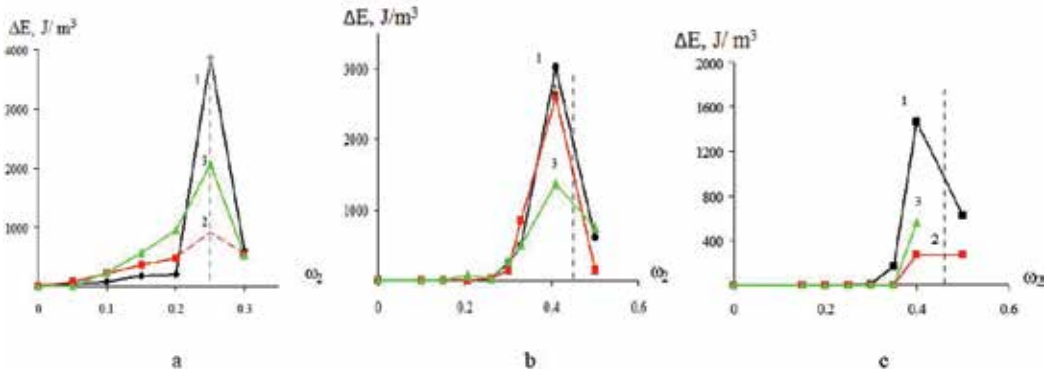

Figure 17. Concentration dependences of mechanical losses for the systems: (a) HPC1-ethylene glycol, (b) HPC2-ethanol and (c) HPC2-DMSO. H = 0 (1), $H_{||}$=3.6 (2) и $H_{\perp}$=3.7 (3). Dashed lines divide isotropic and anisotropic regions.

The similar dependences have been determined also for HPC solutions under magnetic field (**Figure 17**).

It is shown that the maximum of losses is observed in the concentration region near phase transition isotropic solution – anisotropic solution for the reasons described above.

3. Conclusion

The effect of a magnetic field on the viscosity of poly(ethylene glycol)-aerosol-iron nanoparticle and poly(dimethylsiloxane)-aerosol-iron nanoparticle magnetorheological suspensions is studied. The magnetic field leads to an increase in the viscosity of the suspensions by a factor of 20–300. The concentration dependence of the effect of magnetic field on the relative viscosity of the systems is described by a curve with a maximum.

The rheological properties, phase transitions, and structure of the hydroxypropyl cellulose-ethanol, hydroxypropyl cellulose-dimethyl sulfoxide, hydroxypropyl cellulose-ethylene glycol and ethyl cellulose-dimethylformamide systems have been studied in the presence and in the absence of a magnetic field. The regions of existence of isotropic and anisotropic phases and the concentration dependence of the sizes of supramolecular particles are determined. It is found that a magnetic field increases the viscosities of solutions. The concentration dependences of viscosity and particle size are described by curves with maxima. Loading and unloading curves do not coincide for solutions with the polymer concentrations $\omega_2 > 0.25$ (the HPC-ethanol system), $\omega_2 > 0.30$ (the HPC-DMSO system) and $\omega_2 > 0.10$ (HPC1-ethylene glycol). The hysteresis loop is observed; its area characterizes the part of mechanical energy transformed into heat energy, i.e., mechanical losses. The concentration dependences of mechanical losses for studied systems are described by curves with maxima. The maximum mechanical losses are detected in the vicinity of the isotropic-anisotropic transition of solutions.

Author details

Sergey Vshivkov* and Elena Rusinova

*Address all correspondence to: sergey.vshivkov@urfu.ru

Ural Federal University, Ekaterinburg, Russia

References

[1] Odenbach S. Recent progress in magnetic fluid research. Journal of Physics. Condensed Matter. 2004;**16**:1135-1150. DOI: 10.1088/0953-8984/16/32/R02

[2] Harvey ENJ. Effect of magnetic fields on the rheology of ferromagnetic dispersions. Journal of Colloidal Science. 1953;**8**:543-547. DOI: 10.1016/0095-8522(53)90060-9

[3] McTague JP. Magnetoviscosity of magnetic colloids. The Journal of Chemical Physics. 1969;**51**:133-136. DOI: 10.1063/1.1671697

[4] Shliomis MI. Effective viscosity of magnetic suspensions. JETP. 1972;**34**:1291-1294

[5] Demchuk SA, Kordonskii VI, Shul'man ZP. Magnetorheological characteristics of ferromagnetic suspensions. Magnetohydrodynamics 1977;**13**:153-156

[6] Bibik EE. Particles interaction in ferrofluids. In: Physical Properties and Hydrodynamics of Dispersed Ferrromagnetic Materials. Articles. UNTs AN SSSR: Sverdlovsk; 1977. p. 3-19. [in Russian]

[7] Shul'man ZP, Kordonskii VI, Zaltsgendler EA. Measurement of the magnetorheological characteristics of ferromagnetic suspensions. Magn. Gidrodinam. 1979;**15**:31-34

[8] Shul'man ZP, Kordonskii VI, Zaltsgendler EA, Prokhotov IV, Khusidand BM, Demchuk SA. Structure and magnetic and rheological characteristics of a ferrosuspension. Magn. Gidrodinam. 1984;**20**:223-229

[9] Varlamov YD, Kaplun AB. Measurement of viscosity of weakly clustering magnetic liquids. Magn. Gidrodinam. 1986;**22**:43-49

[10] Varlamov YD, Kaplun AB. Agglomeration processes in magnetofluids. Magn. Gidrodinam. 1983;**19**:25-30

[11] Kolomentsev AV, Kordonskii VI, Protasevich NA, Prokhorov IV. Hydrodynamic demagnetization and its effect on the flow of a magnetorheological suspension in a plane channel. Magn. Gidrodinam. 1988;**24**:414-416

[12] Kashevskii BE, Kordonskii VI, Prokhorov IV. Magnetorheological effect in a suspension with an active carrier fluid. Magn. Gidrodinam. 1988;**24**:30-35

[13] Kordonskii VI, Gorodkin SR, Protasevich NA. Orientation effects in the flow of a magnetorheological suspension in a magnetic field. Magn. Gidrodinam. 1989;**25**:261-263

[14] Kashevskii BE, Kordonskii VI, Prokhorov IV, Demchuk SA, Gorodkin SR. Relaxation of viscous stresses in magnetorheological suspension. Magn. Gidrodinam. 1990;**26**:140-143

[15] Grants A, Irbītis KG, Maiorov MM. Rheological properties of magnetite magnetic fluid. Journal of Magnetism and Magnetic Materials. 1990;**85**:129-132. DOI: 10.1016/0304-8853(90)90035-O

[16] Odenbach S, Rylewicz T, Rath H. Investigation of Weissenberg effect in suspensions of magnetic nanoparticles. Physics of Fluids. 1999;**11**:2901-2905. DOI: 10.1063/1.870148

[17] Pop LM, Odenbach S, Wiedenmann A, Matoussevitch N, Bonnemann H. Microstructure and rheology of ferrofluids. Journal of Magnetism and Magnetic Materials. 2005;**289**:303-306. DOI: 10.1016/j.jmmm.2004.11.086

[18] Letyuk LM, Andreev VG, Gonchar AV, Strygin AA. Magnetic-field effect on the rheological properties of strontium ferrite suspensions. Inorganic Materials. 2006;**42**:423-426. DOI: 10.1134/S0020168506040157

[19] Devi M, Mohanta D. Rheological properties of Iron oxide based ferrofluids. AIP Conf. Proc. 2009;**1147**:495-501

[20] Mantripragada S, Wang X, Gordaninejad F, Hu B, Fuchs A. Rheological properties of novel magnetorheological fluids. International Journal of Modern Physics B. 2007;**21**:4849-4857. DOI: 10.1142/S021797920704575X

[21] Vshivkov SA, Zubarev AY, Safronov AP. Self-Organization, Phase Transitions and Properties of Anisotropic Media in Magnetic and Mechanical Fields. Yekaterinburg [in Russian]: AMB; 2011. p. 384

[22] Odenbach S. Editors. Lecture Notes in Physics. Ferrofluids: Magnetically Controllable Liquids and their Applications. Berlin: Springer; 2002. 256 p

[23] Avdeev MV, Aksenov VL. Small-angle neutron scattering in structure research of magnetic fluids. Uspekhi Fizicheskikh Nauk. 2010;**180**:1009-1034. DOI: 10.3367/UFNr.0180.201010a.1009

[24] Vshivkov SA, Galyas AG, Oznobikhin AY. The effect of a magnetic field on the rheological properties of iron-aerosil-glycerol suspensions. Colloid Journal. 2014;**76**:292-299. DOI: 10.1134/S1061933X1402015X

[25] Vshivkov SA, Rusinova EV, Galyas AG. Effect of a magnetic field on the rheological properties of iron oxide – Water – Glycerol system. Rheologica Acta. 2016;**55**:155-161. DOI: 10.1007/s00397-016-0909-8

[26] Zubarev AY, Iskakova LY. On the theory of rheological properties of magnetic suspensions. Physica A. 2007;**382**:378-388. DOI: doi.org/10.1016/jphysa.2007.04.061

[27] Vshivkov SA, Galyas AG, Oznobikhin AY. The effect of a magnetic field on the rheological properties of iron – Aerosol - glycerol suspensions. Annual Transactions of the Nordic Rheology Society. 2017;**25**:389-391

[28] Vshivkov SA, Rusinova EV, Safronov AP, Galyas AG, Terziyan TV. Effect of a magnetic field on the rheological properties of magnetic liquids based Ob iron oxides. Russian Journal of Physical Chemistry A. 2015;**89**:327-330. DOI: 10.1134/S0036024415020375

[29] Vshivkov SA, Avvakumova AS. Effect of a magnetic field on the rheological properties of poly(ethylene glycol) and poly(dimethylsiloxane) mixtures with aerosil and iron nanoparticles. Polymer Science A. 2017;**59**:734-741. DOI: 10.1134/S0965545X17050170

[30] Maret G, Dransfeld K. Biomolecules and polymers in high steady magnetic fields. In: Herlach F, editor. Strong and Ultrastrong Magnetic Fields and their Applications. Springer-Verlag: Berlin; Heidelberg; New York; Tokyo; 1985. p. 143-204

[31] Kimura T. Study on the effect of magnetic field on polymeric materials and its application. Polymer Journal. 2003;**35**:823-843

[32] Moore JS, Stupp SI. Orientation dynamics of main-chain liquid crystal polymers. 2. Structure and kinetics in a magnetic field. Macromolecules. 1987;**20**:282-293. DOI: 10.1021/ma00168a009

[33] Kestel'man VN. Physical Methods of Modification of Polymer Materials. Moscow: Khimiya; 1980. p. 224 [in Russian]

[34] Mikelson AE, Kh KY. Control of crystallization processes by means of magnetic fields. Journal of Crystal Growth. 1981;**52**:524-529. DOI: 10.1016/0022-0248(81)90333-X

[35] Kimura T, Yoshino M, Yamane T, Yamato M, Tobita M. Uniaxial alignment of the smallest diamagnetic susceptibility axis using time-dependent magnetic fields. Langmuir. 2004;**20**: 5669-5672. DOI: 10.1021/la049347w

[36] Kimura T, Yamato M, Koshimizu W, Koike M, Kawai T. Magnetic orientation of polymer fibers in suspension. Langmuir. 2000;**16**:858-861. DOI: 10.1021/la990761j

[37] Yamagishi A, Takeuchi T, Higashi T, Date M. Diamagnetic orientation of polymerized molecules under high magnetic field. Journal of Physical Society Japan. 1989;**58**:2280-2283 doi.org/10.1143/JPSJ.58.2280

[38] Kawai T, Kimura T. Magnetic orientation of isotactic polypropylene. Polymer. 2000;**41**: 155-159. DOI: doi.org/10.1016/S0032-3861(99)00150-0

[39] Ezure H, Kimura T, Ogawa S, Ito E. Magnetic orientation of isotactic polystyrene. Macromolecules. 1997;**30**:3600-3605. DOI: 10.1021/ma970077g

[40] Kimura T, Kawai T, Sakamoto Y. Magnetic orientation of poly(ethylene terephthalate). Polymer Communication. 2000;**41**:809-812. DOI: doi.org/10.1016/S0032-3861(99)00451-6

[41] Sata H, Kimura T, Ogawa S, Yamato M, Ito E. Magnetic orientation of poly(ethylene-2,6-naphthalate). Polymer. 1996;**37**:1879-1882. DOI: doi.org/10.1016/0032-3861(96)87304-6

[42] Sata H, Kimura T, Ogawa S, Ito E. Magnetic orientation of poly(ethylene-2,6-naphthalate) during crystallization from melt. Polymer. 1998;**39**:6325-6330. DOI: doi.org/10.1016/S0032-3861(97)10073-8

[43] Guo C, Kaufman LJ. Flow and magnetic field induced collagen alignment. Biomaterials. 2007;**28**:1105-1114. DOI: 10.1016/j.biomaterials.2006.10.010

[44] Kimura T. Study on the effect of magnetic fields on polymeric materials and its application. Polymer Journal. 2003;**35**:823-843. DOI: 10.1295/polymj.35.823

[45] Kawamura Y, Sakurai I, Ikegami A, Iwayanagi S. Magneto-orientation of phospholipids. Molecular Crystals and Liquid Crystals. 1981;**67**:77-87

[46] Kimura T. Phase transformation of polymeric materials in high magnetic field. Materials Transactions. 2003;**44**:2520-2523

[47] Kimura T. Orientation-dependent Magneto-Clapeyron equation. Japanese Journal of Applied Physics. 2001;**40**:6818-6820

[48] Ebert F, Thurn-Albrecht T. Controlling the orientation of Semicrystalline polymers by crystallization in magnetic fields. Macromolecules. 2003;**36**:8685-8694. DOI: org/doi/abs/10.1021/ma034760g

[49] Yamato M, Kimura T. Relationship between magnetic alignment and the crystallization condition of isotactic polystyrene. Science and Technology Advanced Materials. 2006;**7**: g-341. doi/pdf/10.1016/j.stam.2006.01.013

[50] Naga N, Saito Y, Noguchi K, Takahash K, Watanabe K, Yamato M. Magnetic-field-induced alignment of syndiotactic polystyrene. Polymer Journal. 2016;**48**:709-714

[51] Naga N, Ishikawa G, Noguchi K, Takahashi K, Watanabe K, Yamato M. Magnetic-field-induced alignment of low molecular weight polyethylene. Polymer. 2013;**54**:784-790. DOI: doi.org/10.1016/j.polymer.2012.12.016

[52] Al-Haik MS, Hussaini MY. Molecular dynamics simulation of reorientation of polyethylene chains under a high magnetic field. Molecular Simulation. 2006;**32**(8):601-608. DOI: 10.1080/08927020600887781

[53] Garrido L. Magnetic orientation of diamagnetic amorphous polymers. Journal of Polymer Science Part B: Polymer Physics. 2010;**48**:1009-1015. DOI: 10.1002/polb.21989

[54] Kimura F, Kimura T, Tamura M, Hirai A, Ikuno M, Hori F. Magnetic alignment of the chiral nematic phase of a cellulose microfibril suspension. Langmuir. 2005;**21**:2034-2041. DOI: 10.1021/la0475728

[55] Sugiyama J, Chanzy H, Maret G. Orientation of cellulose microcrystals by strong magnetic field. Macromolecules. 1992;**25**:4232-4234. DOI: 10.1021/ma00042a032

[56] Revol JF, Godbout L, Dong XM, Gray DG, Chanzy H, Maret G. Chiral nematic suspensions of cellulose crystallites; phase separation and magnetic field orientation. Liquid Crystals. 1994;**16**:127-134. doi.org/10.1080/02678299408036525

[57] Vshivkov SA, Galyas AG, Kutsenko LI, Tyukova IS, Terziyan TV, Shepetun AV. Self-organization of macromolecules and liquid-crystalline phase transitions in solutions of cellulose ethers. Polymer Science A. 2011;**53**:1-5. DOI: 10.1134/S0965545X1101010X

[58] Vshivkov SA, Galyas AG. Mechanism of self-assembly of rigid–chain macromolecules of cellulose ethers in solutions. Polymer Science A. 2011;**53**:1032-1039. DOI: 10.1134/S0965545X11100130

[59] Vshivkov SA, Rusinova EV, Kudrevatykh NV, Galyas AG, Alekseeva MS, Kuznetsov DK. Phase transitions of hydroxypropyl cellulose liquid-crystalline solutions in magnetic field. Polymer Science A. 2006;**48**:1115-1119. DOI: 10.1134/S0965545X06100142

[60] Vshivkov SA, Rusinova EV, Kutsenko LI, Galyas AG. Phase transitions in liquid-crystalline cyanoethyl cellulose solutions in magnetic field. Polymer Science B. 2007;**49**: 200-202. DOI: 10.1134/S156009040707007X

[61] Vshivkov SA. Phase Transitions of Polymer Systems in External Fields. Ekaterinburg: AMB Press; 2015 324 p

[62] Vshivkov SA. Effect of magnetic and mechanical fields on phase liquid crystalline transitions in solutions of cellulose derivatives. In: Dr. Juan Carlos Moreno PirajÃ¡n, editor. Thermodynamics-Physical Chemistry of Aqueous Systems. Croatia: InTech. 2011. p. 407-434. DOI: 10.5772/20996

[63] Vshivkov SA, Rusinova EV. Effect of magnetic fields oh phase transitions in solutions of cellulose derivatives. Polymer Science A. 2008;**50**:725-732. DOI: 10.1134/S0965545X08070018

[64] Vshivkov SA, Zhernov IV, Nadol'skii AL, Mizyov AS. Effect of magnetic field on phase transitions in solutions and melts of flexible polymers. Polymer Science A. 2017;**59**:465-472. DOI: 10.1134/S0965545X17040149

[65] de Gennes PG. Calcul de la distorsion d'une structure cholesterique par un champ magnetique. Solid State Communication. 1968;**6**:163-165. doi.org/10.1016/0038-1098(68)90024-0

[66] Meuer RB. Distortion of a cholesteric structure by a magnetic field. Applied Physics Letters. 1969;**14**:208-212. DOI: doi.org/10.1063/1.1652780

[67] DuPre DB, Duke RW. Temperature, concentration, and molecular weight dependence of the twist elastic constant of cholesteric poly-γ-benzyl-L-glutamate. The Journal of Chemical Physics. 1975;**63**:143-148. DOI: doi/abs/10.1063/1.431066

[68] Duke RW, DuPre DB, Hines WA, Samulski ET. Poly(γ-benzyl L-glutamate) helix-coil transition. Pretransition phenomena in the liquid crystal phase. Journal of the American Chemical Society. 1976;**98**:3094-3101

[69] Hamza SEE. MHD flow of cellulose derivatives and dilute suspensions Rheology of its Nanocrystals. American Journal of Fluid Dynamics. 2017;**7**:23-40. DOI: 10.5923/j.ajfd.20170701.03

[70] Vshivkov SA, Rusinova EV, Galyas AG. Effect of a magnetic field on the rheological properties of cellulose ether solutions. Journal of Composites and Biodegradable Polymers. 2014;**2**:31-35

[71] Vshivkov SA, Rusinova EV, Galyas AG. Phase diagrams and rheological properties of cellulose ether solutions in magnetic field. European Polymer Journal. 2014;**59**:326-332. DOI: doi.org/10.1016/j.eurpolymj.2014.07.042

[72] Vshivkov SA, Rusinova EV, Galyas AG. Effect of a magnetic field on the rheological properties of the rheological properties of cellulose ether solutions. Polymer Science A. 2012;**54**:827-832. DOI: 10.1134/S0965545X1211003X

[73] Vshivkov SA, Byzov AA. Phase equilibrium, structure, and rheological properties of the carboxymethyl cellulose – Water system. Polymer Science A. 2013;**55**:102-106. DOI: 10.1134/S0965545X13020107

[74] Vshivkov SA, Rusinova E. V,Galyas a G. Relaxation character of the rheological behavior of cellulose ether solutions in a magnetic field. Russian Journal of Applied Chemistry. 2014;**87**:1140-1145. DOI: 10.1134/S1070427214080217

[75] Vshivkov SA, Soliman TS. Effect of a magnetic field on the rheological properties of the systems hydroxypropyl cellulose – Ethanol and hydroxypropyl cellulose – Dimethyl sulfoxide. Polymer Science A. 2016;**58**:307-314. DOI: 10.1134/S0965545X16030184

[76] Vshivkov SA, Soliman TS. Phase transitions, structures, and rheological properties of hydroxypropyl cellulose – Ethylene glycol and ethyl cellulose – Dimethylformamide systems in the presence and in the absence of a magnetic field. Polymer Science A. 2016; **58**:499-505. DOI: 10.1134/S0965545X16040143

[77] Heller W, Bhathagar HL, Nakagaki M. Theoretical investigations on the light scattering of spheres. XIII. The "wavelength exponent" of differential turbidity spectra. The Journal of Chemical Physics. 1962;**36**:1163-1170. DOI: doi/abs/10.1063/1.1732710

[78] Heller W, Pangonis WL. Theoretical investigations on the light scattering of colloidal spheres. I. The specific turbidity. The Journal of Chemical Physics. 1957;**26**:498-505. DOI: doi/abs/10.1063/1.1743332

[79] Heller W. Theoretical investigations on the light scattering of spheres. XV. The wavelength exponents at small α values. The Journal of Chemical Physics. 1964;**40**:2700-2704. https://doi.org/10.1063/1.1725583

[80] Klenin VI, Shchegolev SYu, Lavrushin VL. Characteristic Functions of Light Scattering from Disperse Systems. Saratov: Saratovsk. Gos. Univ.; 1977. 177 p. [in Russian]

[81] Sivuhin DV. Obshchj kurs fiziki. 4th ed. Moscow: Fizmatlit; 2004. 656 p. [in Russian]

[82] Kulichikhin VG, Golova LK. Liquid crystalline state of cellulose and their derivatives. Khim. Drev. 1985;**3**:9-27

[83] Panar M, Bestel F. Structure of poly (1, 4-benzamide) solutions. American Chemical Society Polymer Preprints. 1976;**17**:65-68

[84] Iovleva MM, Prozorova GE, Smirnova VN, Papkov SP. About a peculiar role of the solvent role in some systems on the basis of aromatic polyamides. Vysokomolek. Soedin. A. 1981;**23**:2092-2098

[85] Panfilova AA, Platonov VA, Kulichikhin VG, Kalmikova BD, Papkov SP. Change of a surface tension of PBA solutions during their transition to a liquid crystal state. Colloid Journal. 1975;**37**:210-211

[86] Anwer A, Windle AH. Magnetic orientation and microstructure of main-chain thermotropic copolyesters. Polymer. 1993;**34**:3347-3357 https://doi.org/10.1016/0032-3861(93)90459-N

[87] Anwer A, Windle AH. Orientation kinetics of thermotropic main-chain liquid-crystalline polymers in a magnetic field. Polymer. 1991;**32**:103-108. https://doi.org/10.1016/0032-3861(91)90569-5

[88] Malkin AY, Isaev AI. Rheology Concepts, Methods and Applications. 2nd ed. Toronto - Canada: ChemTec Publishing; 2011. p. 528

[89] Yang JT. Non-Newtonian viscosity of poly-γ-benzyl-L-glutamate solutions. Journal of the American Chemical Society 1958;**80**:1783-1788

[90] Wissbrun KF. Rheology of rod-like polymers in liquid crystalline state. Journal of Rheology. 1981;**25**:619-662. DOI: doi.org/10.1122/1.549634

[91] Kulichikhin VG, Malkin AY, Papkov SP. Rheological properties of liquid crystalline polymer systems. Polymer Science U.S.S.R. 1984;**26**:499-524

[92] Hermans J. The viscosity of concentrated solutions of rigid rod-like molecules poly (γ-benzyl-L-glutamate) in m-cresol. Colloid Science. 1962;**17**:638-648

[93] Yang JT. Factors affecting the non-Newtonian viscosity of rigid particles. Journal of the American Chemical Society. 1959;**81**:3902-3907

[94] Papkov SP, Kulichikhin VG, Kalmykova VD, Malkin AY. Rheological properties of anisotropic poly (Para-benzamide) solutions. Journal of Polymer Science: Polymer Physics Edition. 1974;**12**:1753-1770. DOI: 10.1002/pol.1974.180120903

[95] Tager A. Physical Chemistry of Polymers. 2nd ed. Moscow: Mir Publisher; 1978. 653 p

Chapter 2

Applications of Viscoelastic Fluids Involving Hydrodynamic Stability and Heat Transfer

Ildebrando Pérez-Reyes,
René Osvaldo Vargas-Aguilar,
Samuel Bernardo Pérez-Vega and
Alejandro Sebastián Ortiz-Pérez

Additional information is available at the end of the chapter

http://dx.doi.org/10.5772/intechopen.76122

Abstract

Rayleigh and Marangoni convection and rheology are linked in the thermal convection of viscoelastic fluids to some recent technological applications. Such technology developments as the ones presented here undoubtedly shall be based on interdisciplinary projects involving not only rheology or fluid mechanics but several other disciplines. Three practical applications which use Rayleigh or Marangoni convection in their working principle are presented along with some technical details. This contribution focus mainly on the physical mechanism and the involved hydrodynamics of some lab and industrial applications. Finally, a short discussion on the role play by the convective mechanisms is given in order to provide integration of the exposed ideas.

Keywords: viscoelastic fluid, convection, hydrodynamics

1. Introduction

Viscoelastic fluids are common in very important applications [1, 2]. Many of these are so common that people usually do not pay attention to its importance. Paints are a very good example since almost all buildings are painted with a combination of a polymer and a solvent, for different reasons. More complex applications involving polymeric solutions and some kind of process may exist.

On the other hand, not all viscoelastic fluids are paints and some of these may have biological nature or even may be intended for some optical application or the like. Also, viscoelastic fluids may be so different to each other that a reasonable number of constitutive equations have been developed to model their behavior. At the same time, some applications involving viscoelastic fluids may require physical mechanisms for proper working, like natural convection. Such is the case of deoxyribonucleic acid (DNA) replication and the fabrication of corrugated surfaces, for example. Viscoelasticity is then at the same level of importance than natural convection.

The present contribution is devoted to exposed the link between viscoelasticity and Rayleigh and/or Marangoni convection and how these fit in lab or industrial applications. In fact, this is also a different point of view for polymer rheology applications. In this case some examples involving viscoelastic fluids and hydrodynamic stability can be addressed to show another connection of rheology with fluid mechanics. These type of applications are only a few years old and remain relevant.

The author has been working in similar theoretical problems and is trying to make experimental contributions that would finally improve applications like these. Hopefully, this proposal could show the link between rheology and other subjects in new multidisciplinary research topics and developments. The aim of this contribution is to call the attention of researchers and graduate students to interdisciplinary subjects were important technological advances are awaiting to be discovered. Hydrodynamic stability and rheology are both matured topics with interesting theoretical and experimental findings.

The chapter is organized as follows. In Section 2, general comments on viscoelasticity are given so that a connection with thermal hydrodynamic stability in Section 3 can be made. In Section 3 a summary of the physics of thermal convection in Newtonian and viscoelastic fluids is presented too. A brief presentation of the methods used to study the thermal hydrodynamics in viscoelastic fluids is given in Section 4. Next in Section 5 interesting application examples that use thermoconvection are given. Finally, a short discussion on the role played by thermal convection in the example applications is given.

2. About viscoelastic fluids

Viscoelastic fluids are a type of non-Newtonian fluid formed by a viscous component and an elastic one. For short, viscoelastic fluids are the blend of a solvent and some polymer. Examples of these are paints, DNA suspensions, some biological fluids and others from the chemical industry. A number of features make the viscoelastic fluids very interesting and of industrial importance: polymers are almost everywhere. Take for example the case of paints whose annual production generates several USD millions. Proper understanding of viscoelasticity is key for industrial applications.

Polymeric suspensions show viscoelastic behavior but its stress - deformation relationship is not easily represented by a single model. In rheology these models are called constitutive equations and for which the books of Bird et al. [3] and Macosko [4] are two very good classic readings on this subject.

2.1. Some models

Modeling viscoelasticity is a complicated matter since viscoelastic fluids may show, for example, linear and non-linear behavior. On the other hand, some features of the polymeric component may have too much importance to be explicitly introduced in these models. Such is the case for thixotropic behavior in viscoelastic micellar solutions and liquid crystalline dispersions [5]. Some of the constitutive equations of common usage and interest in the academic and industrial community are

- the viscoelastic Maxwell fluid,
- the viscoelastic Jeffreys fluid,
- the viscoelastic Oldroyd fluid,
- the viscoelastic Carreau fluid,
- the viscoelastic "ordered" fluids
- and the viscoelastic KBZ fluid,
- among others.

The readers may find more details on the viscoelastic fluids in the papers of Larson [6, 7] and the textbook of Phan-Thien [8]. For thermal convective instabilities problems the constitutive equations for the viscoelastic Maxwell [9, 10], Jeffreys [11, 12] and second order [13, 14] fluids has some popularity. Several investigations has used these models to study the hydrodynamics of viscoelastic fluids heated from below. Also, these results are the foundation of a number of applications [15–17] like those presented in this contribution.

As a common and widely constitutive equation consider the case of Jeffreys viscoelastic fluids represented by the following expression

$$\left(\frac{\partial}{\partial t}+\lambda_1\right)\tau=-\eta_0\left(\frac{\partial}{\partial t}+\lambda_2\right)\dot{\gamma} \tag{1}$$

where τ is the stress tensor, $\dot{\gamma}$ is the rate of strain tensor, η_0 is the zero shear rate viscosity, λ_1 is the stress relaxation time and λ_2 is the stress retardation time. An important feature of Eq. (1) is that it reduces to the model for viscoelastic Maxwell fluids when $\lambda_2 = 0$, and to the constitutive equation for Newtonian fluids when $\lambda_1 = \lambda_2 = 0$. Several investigations dealing with Rayleigh and Marangoni convection has to do with this type of constitutive equations because of the previously mentioned feature.

3. Thermoconvection hydrodynamics

Thermal convection is of interest for the applications described below but mainly Rayleigh and Marangoni convection. A particular feature of these is the secondary flow generated solely by

a thermal gradient. Also, Rayleigh and Marangoni convection form regular patterns which is related to the heat transfer across the fluid.

The problem of thermal convection in incompressible fluids is not new and several geometrical configurations have been considered. Also, the orientation of the thermal gradient and nature of the thermal source has been subjected to different arrangements. This has been driven mainly for potential industrial and/or lab applications [18, 19]. the following cases are of interest for the present contribution: Rayleigh and Marangoni convection in horizontal fluid layers and in vertical cylinders. Pattern formation and heat transfer are key for the proper understanding of the technological developments described below.

3.1. Convection in Newtonian fluids

For Newtonian fluids the physics behind these two classical problems of fluid mechanics is as follows. In horizontal fluid layers heated from below and cooled from above (see **Figure 1a**), near the bottom where the heating source is located the fluid changes its density by becoming lighter. At the same time the fluid near the top is heavy since because of the top cooling. This is an unstable arrangement of the fluid since portions of fluid with higher density tend to fall pushing portions of lower density fluid to the top (see **Figure 1b**). Next, the movement of the fluid occurs only if a critical temperature is achieved. This is called Rayleigh convection and investigation of the critical conditions at which the convective motions are set is key [20].

For the case of Marangoni convection the physical mechanism is quite different since the surface tension variations with temperature, at the surface, trigger fluid motions. This type of thermal convection occurs in very thin fluid layers or in low gravity conditions. Briefly, as the fluid layer is heated from below the energy is transferred by diffusion to the fluid surface. As the fluid surface tension depends on temperature, in hot surface spots the fluid moves away to cooler surface regions. Next, the convective motions take place.

Both, Rayleigh and Marangoni convection are connected and this has been demonstrated theoretical and experimentally. Most important is that the physical mechanisms has been studied and can be identified not only in the examples shown here but in other engineering areas.

Figure 1 only shows the beginning of the convective motion in the core of the fluid layer. As the process is reinforced, the motions become ordered in a periodical fashion. These convective

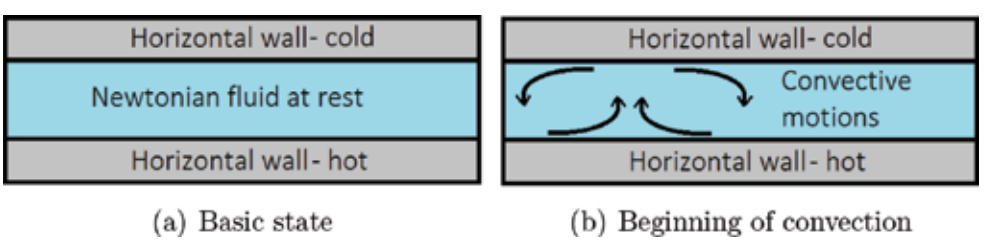

Figure 1. Schematics of the physical mechanism of thermal convection in a Newtonian fluid layer heated from below. (a) Basic state (b) Beginning of convection.

Rayleigh number	Wavenumber	Walls
1708.6	3.12	Conductors [9, 20]
720	0	Insulators [9, 21]
Marangoni number	**Wavenumber**	**Walls**
48	0	Insulators [22]

Table 1. List of critical values for the onset of convection of Newtonian fluids in horizontal fluid layers heated from below. These data correspond to perfect thermal conducting or insulating bounding horizontal walls. For viscoelastic fluids these critical numbers change.

motions are called convective cells. One important fact is that the problem of Rayleigh convection has been widely studied so that for certain cases the critical conditions at which convective motions set are well known as it is shown in **Table 1**. For the case convection of Newtonian fluids in horizontal fluid layers heated from below the critical conditions of perfect thermal conducting and thermal insulators are a common result. From these two cases, that of bounding perfect thermal conductors has been widely studied because it fits better with lab and industrial applications.

The Rayleigh number and the wavenumber are dimensionless parameters featuring the hydrodynamic stability of the fluid layer. As these two parameters achieve critical values thermal convection sets in. Otherwise the fluid motions eventually stop.

3.2. Convection in viscoelastic fluids

Convection in viscoelastic fluids has been widely studied too [9–12, 14, 16]. The discussion in this section shall be restricted to viscoelastic Maxwell and Jeffreys fluids. Then, the physical mechanisms is completely changed due to the introduction of two parameters featuring viscoelasticity as shown in Eq. (1)

- stress relaxation time λ_1,
- stress retardation time λ_2.

Also, convection may be set starting as oscillatory motions. Fortunately, a number of investigators have been working on this subject and the hydrodynamics is well known for some cases. For viscoelastic Maxwell and Jeffreys fluids physics is known to some extent with both the relaxation and the retardation time featuring its behavior. Rayleigh and Marangoni convection in viscoelastic fluids appear in industrial applications and are of interest because the industry of polymers generates millions of USD per year.

4. Methods

Research on hydrodynamics of viscoelastic fluids involves two different approaches. Theoretical and experimental studies are to be linked in order to improve practical applications, which are explained later in this chapter. The aim in hydrodynamic stability studies is to find the

critical conditions that defined the onset of convection and later the formed patterns. In Section 5 the previously mentioned critical conditions make sense through the brief explanation of the physical mechanisms of each application.

4.1. Theoretical approach

The theoretical approach uses the common mathematical techniques of hydrodynamic stability for linear and non-linear problems. In either, Rayleigh or Marangoni convection these techniques are used since both are eigenvalue problems. In linear Rayleigh convection the analysis in made to find critical values of the Rayleigh number (*Ra*), and those of the Marangoni number (*Ma*) in linear Marangoni convection. As the mathematical procedure for different geometrical and heat source orientation, for example, are different only that for the convection in a fluid layer heated from below shall be presented.

Consider a horizontal Maxwell viscoelastic fluid layer heated from below and bounded by two horizontal solid walls which are very good thermal conductors. The physical arrangement is very similar to that shown in **Figure 1** with a Maxwell viscoelastic fluid instead of a Newtonian fluid. If the thermal convection in this system is to be studied then the momentum, the continuity, the heat conduction and a constitutive equations should be considered. These are,

$$(1 + Fi\omega)\left[\frac{i\omega}{\mathrm{Pr}}\left(\frac{d^2}{dz^2} - k^2\right)W - Rk^2\theta\right] = \left(\frac{d^2}{dz^2} - k^2\right)^2 W \tag{2}$$

$$\left[i\omega - \left(\frac{d^2}{dz^2} - k^2\right)W\right]\theta = W \tag{3}$$

subjected to the following boundary conditions

$$W = \frac{dW}{dz} = \theta = 0 \ \text{ at } \ z = 0, 1 \tag{4}$$

The system of differential Eqs. (2-4) is an eigenvalue problem for the Rayleigh number *Ra*. In Eqs. (2)–(4) Pr is the Prandtl number, ω is the frequency of oscillation, W is the vertical fluid velocity, θ is the temperature and k is the wavenumber. This eigenvalue problem can be analytically approached with the Galerkin method without fully solving for W and θ.

For short, as inputs, the Galerkin method needs approximated W and θ which are obtained as functions satisfying the corresponding boundary conditions. Then as the approximated functions are used to calculate the residual and find an analytical expression or numerical value of the Rayleigh number. This is a brief explanation of the solution process and further details can be found in Refs. [9, 10], for example. Then, the Rayleigh number *Ra*, the wavenumber k and the frequency of oscillation ω are obtained as outputs of the Galerkin method, for fixed values of Pr and F, as shown in the following **Table 2**

4.2. Experimental techniques

As the working fluids are viscoelastic, these should be characterized. In the case of Maxwell viscoelastic fluids a rheological study is necessary in order to find the corresponding relaxation

Ra	*k*	*ω*	Pr	*F*
226.7151	7.26	76.2593	10	0.1
0.04623	3.44	1.9625	10	100

Table 2. List of critical values for the onset of convection of viscoelastic Maxwell fluids in horizontal fluid layers heated from below. These data correspond to perfect thermal conducting horizontal walls. These are shown here as representative values [9].

time. Certain polymeric suspensions may fit the Maxwell viscoelastic fluid model. With the working fluid relaxation time F the theoretical methodology may help to find the corresponding critical conditions for the onset of convection.

Also, experiments in thermal hydrodynamics of convection in fluids are mainly based on visual techniques like Schlieren and shadowgraph. Some authors have also used particle image velocimetry to study the flow field of convective motions. Here, the shadowgraph techniques is considered because the evolution of the convective patterns is key. Besides, the temperature difference and the geometrical dimensions are sufficient for a discussion on the physics of this phenomena.

The experimental setup considered is sketched in **Figure 2**. The shadowgraph technique is very suitable for this type of investigations because it outputs important results at very low costs and time. It is based in the fact that fluid density changes also modify how the light is reflected by it. Then, an optical arrangement is built in ordered to detect light reflexion variations.

The aim of the experimental tests is to help find the real critical conditions at which a given convective pattern is formed. This is of paramount importance for improvement of existent and potential applications.

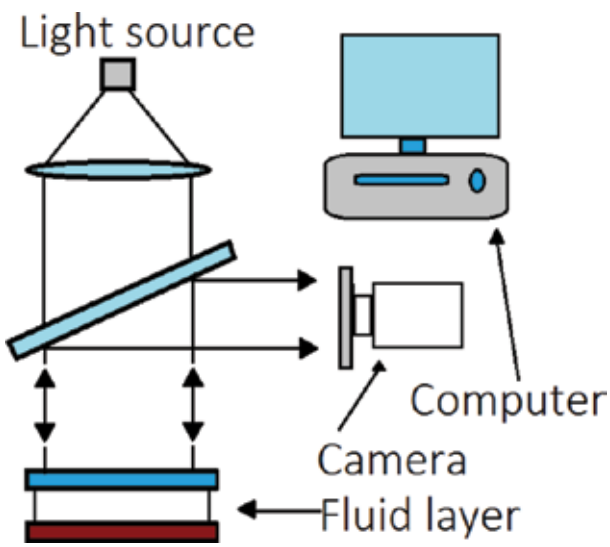

Figure 2. Experimental setup for the shadowgraph technique applied on the convection in a viscoelastic Maxwell fluid layer heated from below.

The theoretical results for Ra, k and ω are linked to the experimental observations as follows. The critical value of the Rayleigh number predicts the critical temperature difference at which the convective motions set and the critical value of the wavenumber indicates the number of formed convective cells. Then the theoretical results help for tuning the lab experiments and to control the formation of patterns in the fluid.

At this point both, theory and experiments are connected for the formation of convective patterns in viscoelastic fluids. As explain in the next section, this background is the foundation that makes it possible.

5. Some applications

The purpose of this section is to introduce two key example applications of thermal hydrodynamic instabilities in viscoelastic fluids. It is important to mention that these applications were selected because thermal convection is at the core of its working principles. In other words, proper understanding of the hydrodynamic stability in the convection of viscoelastic fluids would improve those applications.

A remarkable fact of the applications described here is that these are placed at the frontier of at least two research topics. The fabrication of corrugated surfaces involved knowledge of hydrodynamics, rheology, heat transfer, optics and polymer chemistry. On the other hand, appliances for DNA replication may need knowledge of genetics, hydrodynamics, heat transfer and rheology.

5.1. Corrugated surfaces

In optics and some electronic appliances [1, 2, 23], it is necessary to print regular patterns over a surface. In fact, there are already technologies that print the mentioned patterns. However, redundant techniques are important for a number of reasons: for reduction of costs and production time, for special cases for which traditional techniques do not work, etc. [1, 2] (**Figure 3**).

The pattern printed over a surface is in fact a corrugated surface. Precisely, natural convection in thin films of viscoelastic suspensions is used to produced this type of corrugated surfaces. The fabrication process of these corrugated surfaces briefly includes

1. preparation of the polymeric suspension,
2. application of the suspension in a plate surface,
3. heating from below of the plate
4. thermal control of the convection process in order to achieve and maintain the critical conditions,
5. formation of the desired pattern in the polymeric suspension,
6. evaporation of the solvent and deposition of the polymeric pattern.

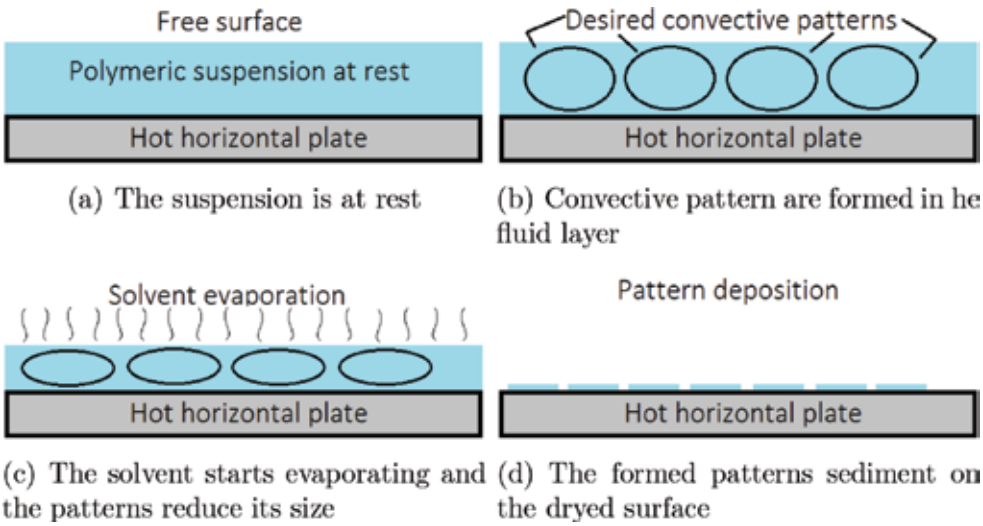

Figure 3. Brief schematics for the fabrication of corrugated surfaces based on thermal convection. Notice that at the beginning Rayleigh convection dominates the process but at certain fluid layer thickness the Marangoni convection rules the process until the solvent evaporates completely. (a) The suspension is at rest (b) Convective pattern are formed in the fluid layer (c) The solvent starts evaporating and the patterns reduce its size (d) The formed patterns sediment on the dried surface.

Steps 4 to 6 in the above are tightly related to thermal convection. As the viscoelastic fluid is heated from below the critical conditions for the onset of convection may be achieved or not. It all depend on the control of the heating source, on the plate thermal and geometrical properties, on the fluid properties [9] and on the desired pattern. This is not an easy task and may resemble a craft work. However very good improvements on this technique has been made so that good quality can be achieved.

Several researchers have made advances on this matter which become hot topic with the paper by Nie and Kumacheva [2]. In fact, in 1998 Mitov and Kumacheva [17] reported instability induced patterning as printing technique for the fabrication of corrugated surfaces. More recently, other researchers have made findings on how the theory of Marangoni convection is coupled with the deposition of regular patterns on a surface.

Further work is needed for the improvement of the experimental technique. For example, it is known that thickness of the fluid layer decreases in time so that both Rayleigh and Marangoni convection may appear in the fluid. Also, as the fluid layer decreases may be the viscoelastic properties may change and in turn modify the formed patterns. In the literature can be found a few papers dealing with the evaporation rate. On the other hand, thermal control should be robust in order that the fluid layer may sustain the formed patterns. Also, several authors have reported new findings for the proportional and proportional integral control of Rayleigh convection. Although more isolated advances can be done in different fields interesting integrating work remains for this type of applications.

5.2. DNA replication

DNA technologies have attracted special attention, first because DNA suspensions are considered viscoelastic fluids because these are a combination of an aqueous solvent and a kind of polymer in the form of DNA chains. Second, hydrodynamics of biological fluids has become a subject of growing interest in recent decades because of its link to a biochemical reaction. For short, DNA replication needs a temperature gradient and an enzyme to be done so that possibly convective motions are involved. DNA replication is common task for geneticists and biotechnologists which also is an important tool for research and development in biotechnology, medicine, molecular biology and other important subjects.

In DNA replication a very expensive apparatus is involved. The thermocycler is small specialized piece of equipment that has become an indispensable tool for research laboratories for industry and academy. However, thermocyclers work is based on the physical mechanism of thermal convection. This is, the equipment creates a temperature gradient by heating from below small tubes and mixes the fluid by producing soft horizontal motions. Several years ago the process followed by the thermocycler was identified as thermal convection in a vertical cylinder [24] and a number of more simple and cheaper thermocyclers were prototyped [25].

The complicated DNA replication process can now be very briefly outlined. The steps given below should be taken as a general picture and the reader is encouraged to search specialized literature for more details on this matter. **Figure 4** shows a very simplified scheme of the thermoconvective motions that take place in this type of biological viscoelastic fluids. Thus, the process is as follows

1. an aqueous dilute suspension of a DNA fragments and the polymerase enzyme is prepared,
2. the suspension is placed in nearly cylindrical containers called vials,

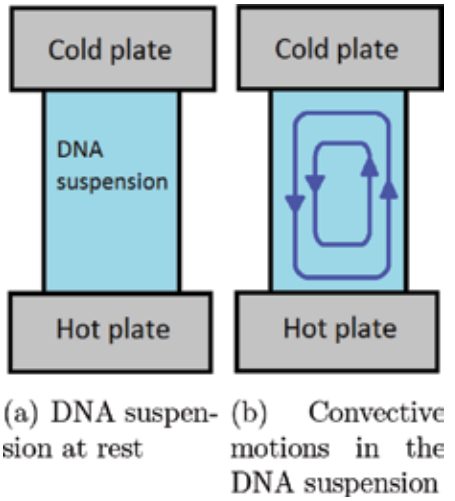

Figure 4. Brief schematics for thermal convection in a DNA suspension confined in a vertical cylinder. Notice that convection cannot be set if a proper critical Rayleigh number is not achieved. (a) DNA suspension at rest (b) Convective motions in the DNA suspension.

3. a thermal gradient is set vertically in the vial,
4. a temperature of 95°C is maintain in order that the polymerase chain reaction (PCR) takes place,
5. DNA replication.

The above given steps lack of some biochemical details but the aim is to show that a physical phenomenon involving thermal gradients and fluid motions is implied. As before, thermal convection is at the core of this appliance and it has been demonstrated the feasibility of cheaper and not too complicated thermocyclers [26]. The lab experiments conducted by Muddu et al. [26] with a very simple cycler prototype based on thermal convection are very important since these are based on the Rayleigh convection.

DNA replication is not the only application involving Rayleigh convection. Some other uses in molecular biology have been found like trapping of DNA with help of thermophoresis or the Soret effect [24]. The Soret effect and the Rayleigh and/or Marangoni convection are related, and for short it is mass transfer assisted by heat transfer and vice versa. This is, DNA material can be concentrated in suitable spot for further recovery.

6. Discussion

Some applications mainly based on Rayleigh and Marangoni thermal convection were briefly presented. These technologies were developed by researchers working on the frontier of various subjects which, from the authors point of view, is the perfect spot for human advances. Several complicated theories have a similar way finding unexpected common technological applications for most humans.

Thermal convection in its general sense has found practical applications in a number of other fields. For example, geology and volcanology use the theory of Rayleigh convection in fluids confined between insulating walls and many industrial equipments for heat transfer use the theory of convection too. On the other hand and to the best knowledge of the authors there are very few new technologies using Rayleigh or Marangoni convection as the ones presented here. It is remarkable that the physical mechanisms of these phenomena are at the core of the above presented technologies and what makes them work is the vast results reported since several decades.

Hopefully, researchers working on interdisciplinary projects could take advantage of the large amount of reported results on Rayleigh and Marangoni convection.

7. Conclusions

Here, an interesting connection between rheology and thermal hydrodynamics is presented through some applications. The theoretical approach is linked to an experimental setup by using dimensionless parameters like the Rayleigh number and the wavenumber. Already

existent applications are then presented as the result a strong understanding of the physics involved. It can be concluded that for applications involving viscoelastic fluids rheology is intrinsically related to the thermal hydrodynamics. This is, pattern formation and heat transfer cannot be controlled if adequate constitutive model are not used. The rheological behavior of the fluid is key for these applications since relaxation time actually favors the heat transfer. It can be also concluded that robust control strategies, on the fluid rheology and heat transfer, may be needed for some applications as such is the fabrication of corrugated surfaces case. In this case the solvent is evaporated, so that viscoelasticity and then heat transfer change, which is not taken into account. Finally, it is shown that further investigation in this branch of rheology is needed.

Acknowledgements

I. Pérez-Reyes would like to thank the financial support from CONACyT through the project Ciencia Básica - 255,839.

Author details

Ildebrando Pérez-Reyes[1]*, René Osvaldo Vargas-Aguilar[2], Samuel Bernardo Pérez-Vega[1] and Alejandro Sebastián Ortiz-Pérez[3]

*Address all correspondence to: ildebrando3@gmail.com

1 Chemical Sciences Faculty, Autonomous University of Chihuahua, New University Campus, University Circuit, Chihuahua, Chih., Mexico

2 SEPI ESIME Azcapotzalco, National Polytechnic Institute, Santa Catarina, Azcapotzalco, Mexico City, Mexico

3 Engineering Faculty, Autonomous University of Baja California, Mexicali, Mexico

References

[1] Xue L, Zhang J, Han H. Phase separation induced ordered patterns in thin polymer blend films. Progress in Polymer Science. Apr 2012;**37**(4):564-594

[2] Nie Z, Kumacheva E. Patterning surfaces with functional polymers. Nature Materials. 2008;**7**(4):277-290

[3] Bird RB, Curtiss CF, Armstrong RC, Hassager O. Dynamics of Polymeric Liquids (Volume 1). United States: Wiley-Interscience; 1987

[4] Macosko CW. Rheology: Principles, Measurements, and Applications. Advances in interfacial engineering series. New York: Wiley-VCH; 1994

[5] Bautista F, de Santos jM, Puig JE, Manero O. Understanding thixotropic and antithixotropic behavior of viscoelastic micellar solutions and liquid crystalline dispersions. i. The model. Journal of Non-Newtonian Fluid Mechanics. 1999;**80**(2–3):93-113

[6] Larson RG. Constitutive equations for thixotropic fluids. Journal of Rheology. 2015;**59**(3): 595-611

[7] Larson RG. Instabilities in viscoelastic flows. Rheologica Acta. 1992;**31**(3):213-263

[8] Phan-Thien N, Mai-Duy N. Understanding Viscoelasticity: An Introduction to Rheology. Graduate Texts in Physics. Berlin: Springer International Publishing; 2017

[9] Pérez-Reyes I, Dávalos-Orozco LA. Effect of thermal conductivity and thickness of the walls in the convection of a viscoelastic Maxwell fluid layer. International Journal of Heat and Mass Transfer. 2011;**54**:5020-5029

[10] Vest CM, Arpaci VS. Overstability of a viscoelastic fluid layer heated from below. Journal of Fluid Mechanics. 1969;**36**:613-623

[11] Pérez-Reyes I, Dávalos-Orozco LA. Vorticity effects in the non-linear long wavelength convective instability of a viscoelastic fluid layer. Journal of Non-Newtonian Fluid Mechanics. jun 2014;**208-209**:18-26

[12] Takashima M. Thermal instability in a viscoelastic fluid layer. I. Journal of the Physical Society of Japan. 1972;**33**(2):511-518

[13] Nagouda SS, Pranesh S. Rayleigh-bñnard convection in a second-order fluid with Maxwell-cattaneo law. The Bulletin of Society for Mathematical Services and Standards. 2012;**2**:24-32

[14] Dávalos-Orozco LA, Manero O. Thermoconvective instability of a second-order fluid. Journal of the Physical Society of Japan. 1986;**55**(2):442-445

[15] Braun D. PCR by thermal convection. Modern Physics Letters B. 2004;**18**(16):775-784

[16] Kolodner P. Oscillatory convection in viscoelastic DNA suspensions. Journal of Non-Newtonian Fluid Mechanics. 1998;**75**:167-192

[17] Mitov Z, Kumacheva E. Convection-induced patterns in phase-separating polymeric fluids. Physical Review Letters. Oct 1998;**81**(1|6):3427-3430

[18] Bari A, Zarco-Pernia E, Garca de Mara J-M. A review on natural convection in enclosures for engineering applications. The particular case of the parallelogrammic diode cavity. Applied Thermal Engineering. 2014;**63**(1):304-322

[19] Ostrach S. Natural convection in enclosures. Journal of Heat Transfer. 1988;**110**(4b):1175

[20] Chandrasekhar S. Hydrodynamic and Hydromagnetic Stability. 180 Varick Street, New York, N. Y: Dover Publications, Inc.; 1981. p. 10014

[21] Gershuni GZ, Zhukovitskii EM. Convective Instability of Incompressible Fluids. Jerusalem: Keter Publications; 1976

[22] Pearson JRA. On convection cells induced by surface tension. Journal of Fluid Mechanics. 1958;**4**:489-500

[23] Bassou N, Rharbi Y. Role of Bénard - Marangoni instabilities during solvent evaporation in polymer surface corrugations. Langmuir. 2009;**25**(1):624-632

[24] Braun D, Libchaber A. Trapping of DNA by thermophoretic depletion and convection. Physical Review Letters. 2002;**89**(18)

[25] Agrawal N. Design and Characterization of Convective Thermal Cyclers for High-Speed DNA Analysis. PhD thesis. Texas, USA: Texas A& M; 2006

[26] Muddu R, Hassan YA, Ugaz VM. Rapid PCR thermocycling using microscale thermal convection. Journal of Visualized Experiments. mar 2011;**49**

Chapter 3

Polymeric Additive Manufacturing: The Necessity and Utility of Rheology

Mohammed Elbadawi

Additional information is available at the end of the chapter

http://dx.doi.org/10.5772/intechopen.77074

Abstract

Additive manufacturing techniques have recently seen an explosive growth across a myriad of fields, partly galvanised by their advantages over traditional fabrication techniques. As with most fabrication processes, maximising efficiency is a requisite, particularly if commercialisation is sought-after. Understanding how the material behaves during additive manufacturing is necessary to accomplishing said task. Accordingly, the chapter herein collates examples of where rheology is applicable in polymer-based additive manufacturing techniques, thereby demonstrating the necessity and utility thereto. The main focus herein will be fused deposition modelling and stereolithography additive manufacturing techniques, with examples of how both capillary and rotational rheometers can be utilised.

Keywords: additive manufacturing, 3D printing, fused deposition modelling, stereolithography, rheology

1. Introduction

Additive manufacturing (AM), also referred to as solid freeform fabrication, rapid prototyping and three-dimensional (3D) printing, is ostensibly a transformative manufacturing technique that will play a vital role in the next Industrial Revolution. AM entails the fabrication of 3D structures with both geometrical complexities and spatial resolution beyond the capacity of traditional fabrication techniques. The ubiquity of AM, from the automotive and aerospace industry, to tissue engineering and drug delivery, unequivocally demonstrates the rising appeal of the technology. From a research perspective, AM allows for rapid prototyping and integration with other technologies, that again, seldom observed in traditional routes.

Furthermore, there are several polymeric AM technologies available for purchase by consumers that will allow manufacturing of goods to be achieved at home. However, despite the vast progression made, the technology is still in its infancy. Therefore, to make AM an essential instrument, further research is needed, including new material formulations.

Rheology is a necessity for all polymer fabrication techniques. The characterisation can deliver extensive and reliable material information. The data is subsequently correlated to the process to maximise productivity. Rheology will further be a key component as new materials are formulated to advance the versatility of AM. In spite of this, rheology remains an underutilised tool. Thus, a chapter into how rheology can be utilised to help maximise AM efficiency is warranted. The chapter presents two of the commonly-used AM techniques in the field of polymers: fused deposition modelling (FDM) and stereolithography (SLA); and demonstrates the necessity of rheology thereto. As detailed herein, both technologies form 3D structures through disparate means, and albeit different, rheology is still an indispensable tool for both technologies. The chapter will conclude with a brief description of other AM techniques and how rheology is still relevant.

2. Fused deposition modelling

Fused deposition modelling (FDM) is one of the most common polymer additive manufacturing techniques. FDM is an extension of hot melt extrusion (HME), which is an already established technique in the field, whereby thermoplastics are heated to their semi-molten state and extruded through a given orifice. However, HME can only be used to fabricate basic geometries, whereas FDM utilises a gantry system that allows a nozzle to move and extrude the semi-molten polymer in three-dimensions until a 3D print is fabricated.

The similarities between FDM and HME are that both use high heat to achieve a semi-molten thermoplastic polymer, and that it is then forced through an orifice[1]. Hence, high temperature rheology and the shearing effect at the orifice, respectively, are of interest to both. Upon exiting the orifice, the thermoplastic is cooled until solidification, which again, is rheologically relevant. The rheological events of FDM are delineated in **Figure 1**.

2.1. Nozzle flow and viscosity

2.1.1. Determining the shear rate from FDM parameters

Knowing the ideal viscosity range can help in predicting whether the new melt formulation is extrudable. Said knowledge will prevent time-consuming and costly empirical trials, as well as mitigating nozzle blockage and consequently machine downtime. A straightforward approach is to compare the viscosity of the new formulation to that of a successfully extruded formulation (e.g. a commercial filament) using a rheometer. A dissimilar viscosity profile may not necessarily equate to an unextrudable melt, provided that they possess comparable viscosity at the operating shear rate; hence the shear rate of interest will need to be identified. Unlike HMEs,

[1]For HME, the orifice is typically called a die; for FDM it is the nozzle.

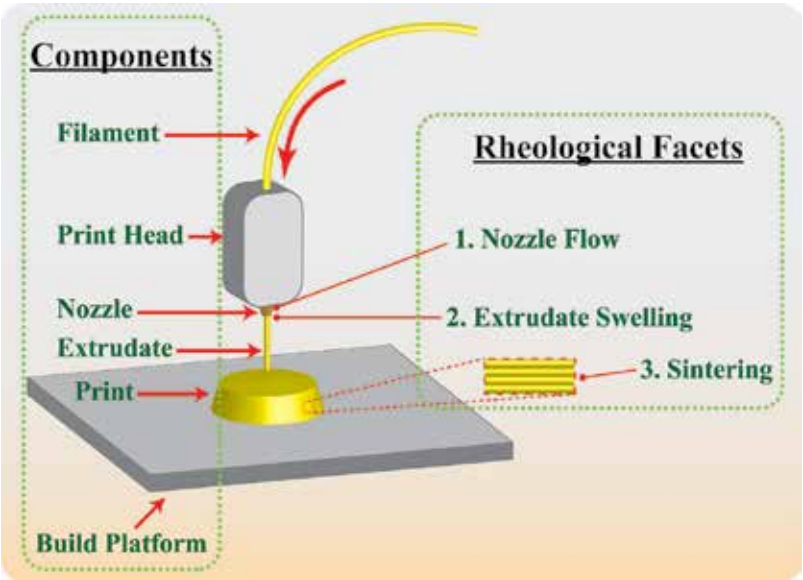

Figure 1. Schematic of fused deposition modelling. The figure lists the components involved in the fabrication process, as well as the rheological facets of interest measurable by rheometers.

however, most FDMs are not equipped with a transducer, and thus the shear rate will need to be determined semi-empirically. This can be achieved by: (i) performing an initial shear-rate viscosity measurement of the melt to obtain the power law index; (ii) knowing the speed of printing and nozzle diameter; and (iii) applying the rheological equations (Eqs. (1)–(4)).

The apparent shear rate $\dot{\gamma}_{app}$ of the nozzle can be semi-empirically determined using the following equation [1]:

$$\dot{\gamma}_{app} = \frac{4Q}{\pi r^3} \tag{1}$$

where Q is the volume flow rate, determined from the exit nozzle radius r and the speed of extrusion v (i.e. printing speed) [1]:

$$Q = \pi r^2 v \tag{2}$$

For example, a printing speed of 50 mm/s and a nozzle diameter of 0.2 mm equates to a flow rate of 6.3 mm^3/s and consequently an apparent shear rate of ~1000 s^{-1}. The apparent shear rate $\dot{\gamma}_{app}$ provides a relatable shear rate that is then examined using the rheometer, which is typically in the order of 10^2 to 10^3 s^{-1} [2]. Thus, a capillary rheometer is best suited for such analysis, as 10^3 s^{-1} is above the attainable shear rate performed by a rotational rheometer [3]. For the true shear rate $\dot{\gamma}$, the following equation should be used [4–6]:

$$\dot{\gamma} = \dot{\gamma}_{app}\left(\frac{(3n+1)}{4n}\right) \tag{3}$$

whereby n is the power law index obtained using the power law model from a viscosity-shear rate test:

$$\eta = k\,\dot{\gamma}^{n-1} \tag{4}$$

The best fit[2] to the data gives the power law index n, which is a dimensionless value between 0 and 1[3]. From the above equations, the true shear rate at the nozzle wall can be obtained, and therefore, viscosity-shear rate tests can be performed at the relatable shear rate range.

Although a capillary rheometer covers the ideal shear rate found in FDM, and exhibits the same flow behaviour to that found within the nozzle (i.e. Poiseuille flow), a rotational rheometer can be used if a capillary rheometer is not accessible. A shear rate test can be performed up to the instrument's shear rate limit, and the experimental data can then be fitted with a rheological model to predict the viscosity at higher shear rates. Examples of curve fitting models include the power law model, Williamson model, Cross model and Carreau-Yasuda model. Note that the oscillatory mode extends the shear rate limit of the rotational mode, however, the former provides the complex viscosity. If the Cox-Merz rule [7] is upheld for the melt formulation, then the complex viscosity can be converted into the steady-state viscosity, and subsequently curve fitted.

In addition to the above rotational rheometer analysis, large amplitude oscillatory shear (LAOS) measurements can be conducted to investigate the performance of the formulation. LOAS is regarded as a more complex analysis, however, it can be more revealing than its counterparts: small amplitude oscillatory shear (SAOS) and medium amplitude oscillatory shear (MAOS). In the former, the sample measured is subjected to large deformations, which is more reflective of the deformation polymers sustain during most polymer processing techniques; and the analysis is more sensitive to polymer architecture and consequently deformation. LAOS has been used to predict wall slip [8, 9] and polymer morphology, with regards to orientation, during extrusion [10]. Such an approach is a subject of interest for the author, and is currently under investigation.

2.1.2. Filament buckling

An additional consideration with too high a viscosity is filament buckling. The filament acts as the piston that drives the extrusion process. If the filament is not extruded at the desired rate it can apply backpressure to the ensuing filament, and in turn causes it to buckle. A critical stress limit σ_c exists that the filament can be subjected to, of which above this value the filament will buckle, and consequently rendered inadequate. Hence, the critical stress must be greater than the pressure P imparted thereupon to drive the extrusion process.

The pressure required to drive the filament through the nozzle needs to be greater than the filament critical stress by a factor of 1.1 [11], as depicted in **Figure 2**.

The factor of 1.1 accounts for the difference between the nozzle and the filament diameter. The dependence of pressure on viscosity is given in the following equation for an ideal flow:

[2]Typically performed by taking the slope from a double-log plot (i.e. log Viscosity vs log Shear Rate).
[3]Note that since n is between 0 and 1, the true shear rate is greater than the apparent shear rate.

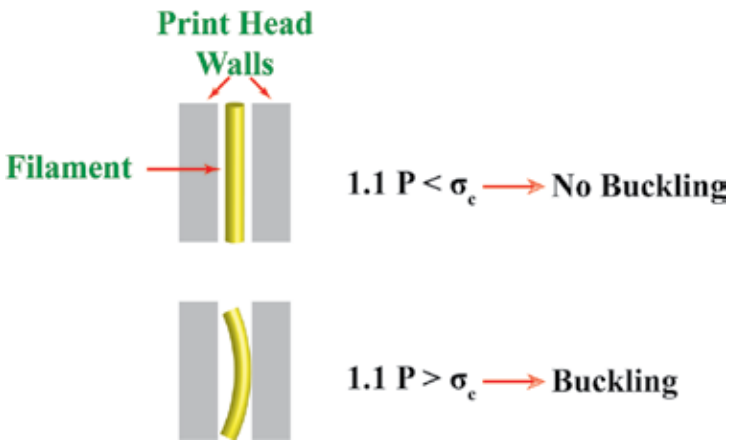

Figure 2. Illustration depicting buckling and no buckling conditions.

$$\mathbf{P} = \frac{2l\eta\,\dot{\gamma}_w}{r} \tag{5}$$

where l is the length of the tube flown through, r is the filament radius, and γ_w is the wall shear rate. Thus, as the pressure is proportional to viscosity and shear rate, reducing the two rheological factors can help mitigate filament buckling; and thereby demonstrating the necessity of rheology once-more.

2.1.3. Further considerations

Prior to extruding, the nozzle is heated to the desired printing temperature, wherein a portion of the filament is housed. The filament should exhibit an appreciable yield strength, whereby flow is resisted at high temperatures until the designated pressure is applied; and thereby preventing 'premature extrusion'. For this reason, the melt should exhibit shear-thinning characteristics at elevated temperatures, whereby the viscosity is high at low shear rates and resists, for example, gravity; but decreases with increasing shear rate. Conversely, a melt with Newtonian flow characteristics possesses no yield strength, and consequently will prematurely extrude, which can result in print failure if not addressed promptly. Therefore, it is necessary to perform viscosity-shear rate measurements and confirm whether the new formulation is shear-thinning in order to avoid premature extrusion.

2.2. Extrudate swelling and viscoelasticity

Extrudate swelling is a frequently encountered phenomenon, and of great interest in polymer processing. The phenomenon occurs in contemporary processes such as hot melt extrusion [12], injection moulding [13] and electrospinning [14], and also reported for fused deposition modelling [15]. Extrudate swell, or die swell, occurs when polymers pass through an orifice with a smaller diameter. The polymer is constrained with energy that is elastically stored as it enters the nozzle, whereafter the energy is released upon exiting the nozzle, leading to a

radial expansion of the melt that consequently results in an extrudate diameter greater than that of the nozzle (**Figure 3**). This event is significant to FDM as it affects print resolution [16]. In addition, it affects print surface topography, which in the case of tissue engineering may influence biological properties. Thus, predicting the degree of extrudate swelling can help to avoid undesirable prints. The size of extrudate swelling is positively affected by shear rate and pressure, and exhibits a negative correlation to temperature and nozzle length. As these are FDM parameters that can be controlled, they can be exploited to minimise extrudate swelling once their effects thereto have been elucidated.

A capillary rheometer is the simplest method of predicting the degree of swelling. The material is extrudate through a capillary die with a similar configuration to that of the FDM nozzle, and the swell ratio B is defined as the ration between extrudate diameter D_{ext} and die diameter D_{die} [17]:

$$B = \frac{D_{ext}}{D_{die}} \tag{6}$$

The swelling phenomenon can also be predicted using a rotational rheometer. Tanner et al. demonstrated that the above equation is correlated to both the wall shear stress and zero-shear viscosity [18]:

$$\frac{D_{ext}}{D_{die}} = \left[1 + \frac{\tau_w^2}{2\,G_0^2}\right]^{1/6} \tag{7}$$

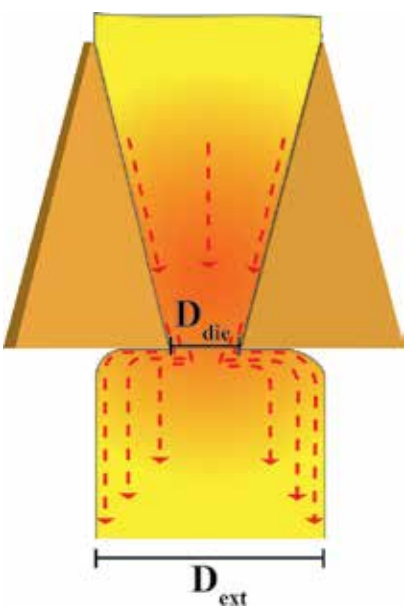

Figure 3. Cross-sectional view of the nozzle portraying extrudate swelling. The schematic illustrates that the extrudate diameter (D_{ext}) is greater than the diameter of the die (or nozzle) (D_{die}) once the melt exits the orifice.

where τ_w is the wall shear stress; and $G_0 = \eta_0/\lambda$, where λ is the relaxation time and η_0 is the zero-shear viscosity. The zero-shear viscosity can be determined by a rheological mathematical model (for example the Williamson or Cross Model) following a viscosity-shear rate test. In a modified FDM, the wall shear stress was acknowledged to induce swelling, and accordingly a lower extrusion speed was opted for to limit extrudate swell [19]. This corresponded with another study that found increasing the extrusion speed increased the filament diameter, again due to extrudate swelling, but also due to time-dependent deformation [20]. Similarly, a slower hot melt extrusion rate is once-more favoured for fabricating filaments suitable for FDM [21], given the latter's low diameter tolerance.

The relaxation time λ is another rheologically-derived parameter that has been proven to correlate well to extrudate swelling. The relaxation time can be obtained through various rheological tests, including from a steady shear rate measurement and curve fitting the data to the Carreau model; or by performing an oscillatory frequency sweep [22, 23]. The relaxation time is directly proportional to the ratio of extrudate swell, therefore, a shorter relaxation time is indicative of improved melt stability and of a polymer that is less susceptible to extrudate swelling [24–27]. Furthermore, the lower the relaxation time in contrast to the deformation time (e.g. time spent deformed in the die or nozzle) then extrudate swelling will be of less concern [13].

2.2.1. Analysing extrudate swelling through creep recovery

Creep and creep recovery experiments are two-halves of an experiment. First, a constant stress σ_0 is applied to the sample and the shear deformation is measured. The stress is then removed at t_1 and the recovery of the deformation is observed in creep recovery. In an elastic material, the strain generated, and the strain recovery is instantaneous to the application and removal of the stress, respectively. However, polymeric materials, which display viscoelastic deformation, convey a different response. Under the constant stress, part of the polymer strains instantly, whereas another part of the polymer deforms at a slower rate under the action of the stress; hence the term 'creep'. Similarly, in the recovery phase, a part of the material recovers instantly, another slowly recovers, and a final part does not recover completely, and hence, the polymer remains permanently deformed [28] (**Figure 4**).

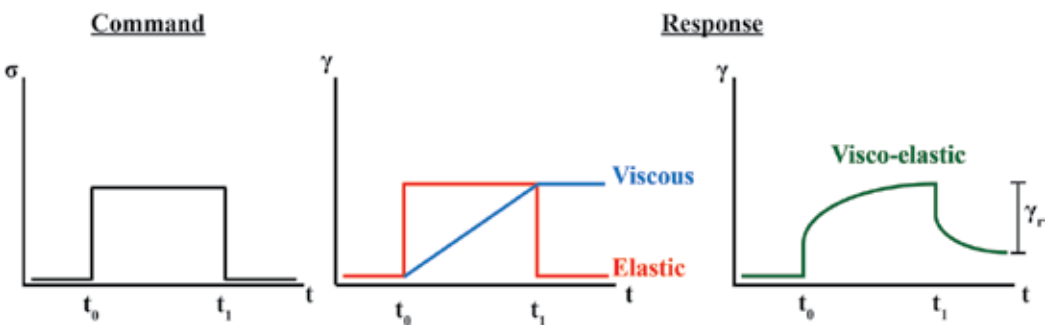

Figure 4. Schematic delineating the possible material responses to a creep test. (t- time; t_0- onset of stress; t_1 _ Endpoint of stress; σ - stress; γ- strain; γ_r recoverable strain).

In the context of extrudate swelling, a creep and creep recovery experiment is analogous to the events that result therein, hence, the test is more closely related to extrudate swell than any other test measurable in a standard rheometer [29]. From a qualitative perspective, a polymer that displays a larger recovery following removal of the stress will indicate a tendency to exhibit a larger extrudate swelling. Conversely, little or no strain recovery is attributed to damping of the applied load [30].

For an experimental quantification in predicting extrudate swelling using a creep recovery test: typically the recoverable compliance J_r is determined, which is positively correlated to extrudate swelling [29, 31, 32]. After the stress is removed, the ratio between recoverable strain γ_r as a function of recovery time t_r, and stress applied σ_0 gives the recoverable compliance [33]:

$$J_r(\sigma_0, t_0, t_r) = \gamma_r(\sigma_0, t_0, t_r)/\sigma_0 \tag{8}$$

2.2.2. Analysing extrudate swelling through stress relaxation

Stress relaxation is another rheological test that can be employed to understand melt viscoelasticity, and verily the effects of stress relaxation characteristics on extrudate swell have been investigated [34–37]. A stress relaxation experiment entails applying a strain to a previously stress-free material and measuring the stress decay at this fixed strain (**Figure 5**). This test is used to determine whether the stress will dissipate within the processing technique time scale. In addition to extrudate swelling, stress relaxation may also help to explain flow warpage[4] [38], and other flow distortions.

Stress relaxation measurements can be made using step-strain rheology. Here, the molten polymer is subjected to an abrupt strain γ at time t_0, typically in the order of 20 ms, and the stress σ needed to keep this deformation is recorded as a function of time [39] (**Figure 5**). The strain applied should be in the linear-viscoelastic region. The relaxation modulus G can be simply determined from this measurement:

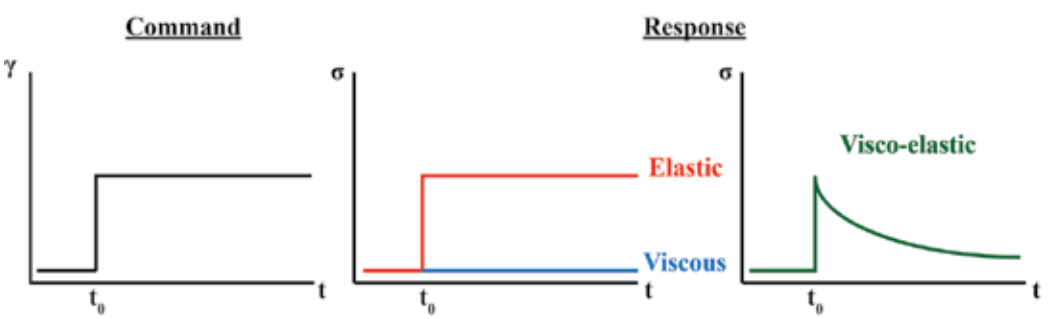

Figure 5. Schematic delineating the stress response to a stress-relaxation test.

[4]This is referred to as 'flow warpage' to differentiate it from 'drying warpage', where the former results in warped (i.e. bent) extrudates; whereas the latter results in a warped print due to inhomogeneous cooling.

$$G(t) = \sigma(t)/\gamma \tag{9}$$

Computational studies experimentally determine the relaxation modulus G(t) to obtain the damping function [40–42] for their numerical swell predictions. The damping function has been found to correspond well with swell results empirically determined by a capillary rheometer [34, 43]. Transferring these computational studies, from extrusion dies to FDM nozzles, will indeed enhance FDM productivity. Additionally, determining damping behaviour of polymers is of general interest as it provides insight into the molecular structure thereof [44, 45]; which is not only helpful in understanding polymer behaviour under deformation, and thereby relevant to many fabrication techniques, but also can help in understanding, for example, polymer disintegration in a solvent medium. Therefore, rheological analysis delivers information that will be of interest beyond the FDM processing stage.

2.3. Filament deposition: layer bonding and cooling

The final stage of the FDM process is the layer-by-layer deposition of the filament. In this stage, the first layer is deposited and adheres onto the build platform. Subsequent layers are deposited thereupon, whereby adjacent layers adhere together until the 3D print is completed. The bonding quality determines the final properties of the 3D print; for example, poorly adhered layers exhibit weak mechanical properties. The layer bonding is referred to as sintering, which in polymers is driven by viscous sintering. Hence, viscosity plays another key role at this stage. There are numerical models used for predicting filament coalescence between two layers using viscosity measurements [46, 47], however, depending on the material used or printing parameters, the theoretical model may underestimate the neck growth achieved between adjacent models [48] (**Figure 6**).

Most FDM printers have the option of controlling the temperature of the build platform. Ideally, the temperature should be high enough to ensure that viscous sintering can be achieved, and thereby adhesion. Below a critical sintering temperature sintering is negligible [46]. Equally, the build plate temperature should also ensure that the material possesses sufficient strength to maintain its structural integrity, particularly as layers are deposited above. Thus, a dynamic cooling ramp, via a rotational rheometer, can be utilised to examine the cooling evolution of the newly formulated material, and compared to that of an already successfully printed melt. Such a test can be incorporated to directly follow either a steady- or dynamic-shear test to determine whether shearing influences the solidification process, due to polymer chain dis-entanglement.

Finally, as adherence plays a vital role in FDM, and the printing parameters can affect polymer adhesive properties [49], this presents a potential to perform a tack test. Although not strictly rheology, a tack test allows one to determine the tack, or 'stickiness', properties of a material, which can be performed at elevated temperatures on some rotational rheometers. Information such as pull-off force, and mode of failure (i.e. cohesive failure, adhesive failure, or both) can be obtained. Furthermore, a tack test can be preceded by a shearing test, where the effects of shearing on tack properties can be measured [50].

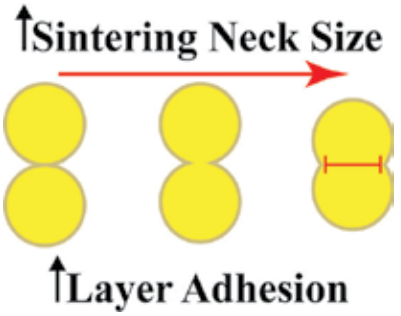

Figure 6. Schematic depicting the evolution of neck size during polymer sintering. The larger the sintering neck size formed the better the adhesion between adjacent layers.

3. Stereolithography

Stereolithography (SLA) is a widely used additive manufacturing technique in the field of polymers, as well as ceramics (**Figure 7**). Here, a monomer resin is polymerised by a laser, layer-by-layer, until a 3D print is fabricated. Hence it differs from fused deposition modelling and other additive manufacturing techniques as it does not involve the use of a nozzle. Such light-curable resins are referred to as photopolymers. In its simplest form, the resin will include the photopolymer and a photoinitiator: the compounds needed to initiate cross-linking of the monomers. However, other additives can be incorporated to modify the properties, such as modifying the mechanical properties of the final product, or the viscosity of the pre-cured resin [51]. Additionally, the resin is a suitable binder for fashioning metal, ceramic and glass materials; and in conjunction with the spatial resolution obtainable, makes SLA an attractive technique for fabricating complex three-dimensional structures.

SLA has been used in the field of structural, tissue engineering, electronics and pneumatically-actuated soft robots [52, 53], and ergo, demonstrating its wide applicability. There are many advantages to this technique over FDM, including printing can be achieved without high temperatures, higher spatial resolution, and nozzle clogging is not of concern. SLA is predominantly Couette flow, thus only rotational rheometry is pertinent here. Furthermore, the dynamic aspect of rotational rheometers can be used for photorheology, which will be described in Section 3.2.

3.1. Viscosity measurements

In comparison to FDM, both the operating viscosity and shear rates are considerably smaller. The viscosity of the photopolymer should be under 5 Pa.s at 30 s^{-1} [54, 55], which ensures that the photopolymer is free-flowing, and capable of forming a new layer (i.e. recoating) ready for polymerisation. However, this value depends on the SLA printer, as others require, for example, a viscosity below 10 Pa.s at 100 s^{-1} [56]. This will ultimately depend on the settings of the SLA printer, but nonetheless, one should consider the maximum operable viscosity prior to printing.

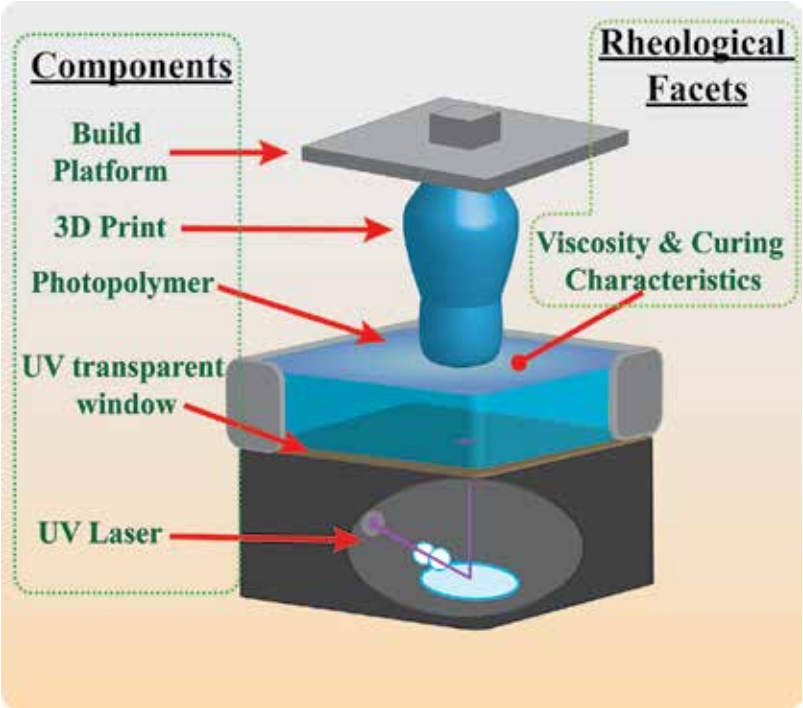

Figure 7. Representative schematic of a stereolithography printer. The figure includes the components that comprise the printer, and the rheological facet of interest.

The viscosity measurement is achieved by performing a steady-shear rate test on the resin free from curable light source(s). The test can be performed at the SLA's functioning shear rate, whether it be 30 s^{-1}, 100 s^{-1} or any other value, and ensuring the viscosity is below the effective threshold[5]; but the test is more commonly performed at a wider shear rate range as more information can be attained. Alternatively, a repeated cycle of LAOS and SAOS can be used; whereby LAOS for reflecting the deformation imparted during the submergence and withdrawal (**Figure 8**); and SAOS to investigate the viscoelastic recovery [57]. At the initial position during SLA printing, the build platform is lowered until submersion thereof is achieved. The platform is thereafter withdrawn, before being submerged again. During withdrawal, the resin should possess a low viscosity to attain complete recoating. Otherwise, a resin with high viscosity, the platform will be lowered with an incomplete recoating. A repeated cycle of LAOS and SAOS can be informative as to whether the structure can recover following deformation by the submersion of the build platform.

Measuring the viscosity over a range of shear rates rather than at a single point would be of particular interest to those formulating a UV-curable suspension, as parameters such as degree of shear-thinning and yield stress are of importance. The yield stress is correlated to the stability

[5]If working with a commercial printer whose supplier produces their own photopolymer resin, then one can measure the viscosity thereof, and attempt to closely match it.

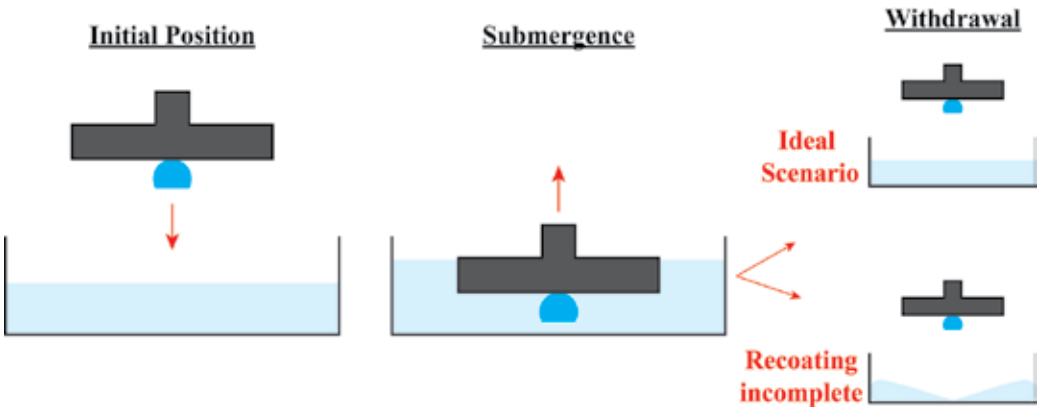

Figure 8. Illustration depicting SLA sequence of events.

of the suspension, which would provide insight into the stability of the suspension over time, and the tendency of the particles to sediment. Particle sedimentation is indeed undesirable as it results in an inhomogeneous print. Other rheological analysis performed to elucidate the degree of sedimentation in suspensions include determining the tan δ from oscillatory tests, creep-recovery tests and stress relaxation tests [58]. Note that if suspensions are to be measured using a rotational rheometer, then one has to use a plate-plate geometry configuration as a cone-plate configuration is susceptible to erroneous measurement due to the particles.

If a UV-curable emulsion has been formulated, and syneresis (i.e. phase separation between the two solvents) is of concern, then a frequency sweep is advisable. Using this test, a storage modulus G' of comparable magnitude, or superior, to the loss modulus G'', at the low frequency (i.e. longer periods) suggests the emulsion is less likely to exhibit syneresis. In other words, a high tan δ indicates a higher tendency to exhibit syneresis [59].

A minimum viscosity limit on the other hand appears to be less discussed, as this is less problematic for most researchers. One author inferred a minimum of 2 Pa.s [55], albeit successful SLA prints were achieved with a viscosity between 0.1 and 1 Pa.s [53, 60].

The low viscosities make SLA desirable as a binder for powder metallurgy, as more of the inorganic powder can be suspended therein. Both metal and ceramic structures have been fabricated using SLA, wherein the inorganic particles are suspended therein; cured into the desirable 3D structure, and subsequently thermally de-bound, leaving behind only the inorganic material [61] elbadawi et al. The material is then sintered to achieve permanence. To achieve a green body that is mechanically sound, at least 40 vol% solids loading is needed, and as expected, this produces a substantial increase in viscosity, above the operating range. However, through the incorporation of dispersants and diluents, the viscosity can be lowered, and hence rheological analysis is key to identifying the minimum dispersant concentration needed to produce a suitable resin.

If working with a photopolymer resin that is not liquid at room temperature, then a viscosity test of importance will be to perform a temperature ramp. Elomaa et al. (2011) opted to

formulate a solvent-free photopolymer comprising of polycaprolactone, in which heating was needed to achieve the operable viscosity [62]. If such an approach is pursued, then performing a temperature ramp will help to identify the minimum temperature without needing to use an unnecessarily high value.

3.2. Photorheology: dynamic mechanical analysis

Aside from viscosity measurement, a rheometer is an indispensable tool for SLA as it can be used to measure the cross-linking characteristic of the resin. As mentioned, the monomer transforms from a liquid to a solid upon UV contact, which can be measured by a rotational rheometer. The transition from resin to solid manifest itself in a tremendous increase to both the storage and loss modulus, with values such as a curing time and material stiffness extracted. This entails the use of an oscillatory time ramp, whereby both the storage and loss modulus are recorded over time (**Figure 9**). The test is allowed to run until a baseline value for the resin is obtained, whereafter a UV source is activated, and the solidification behaviour is observed. Both the time to achieving solidification and the shear modulus of the solid can be quantified. The former is necessary to predict the scanning speed of the UV laser needed to achieve a solid structure; whereas the latter provides a strong correlation to the mechanical properties of the 3D print, namely Young's Modulus [63]. Such a test saves both time and cost.

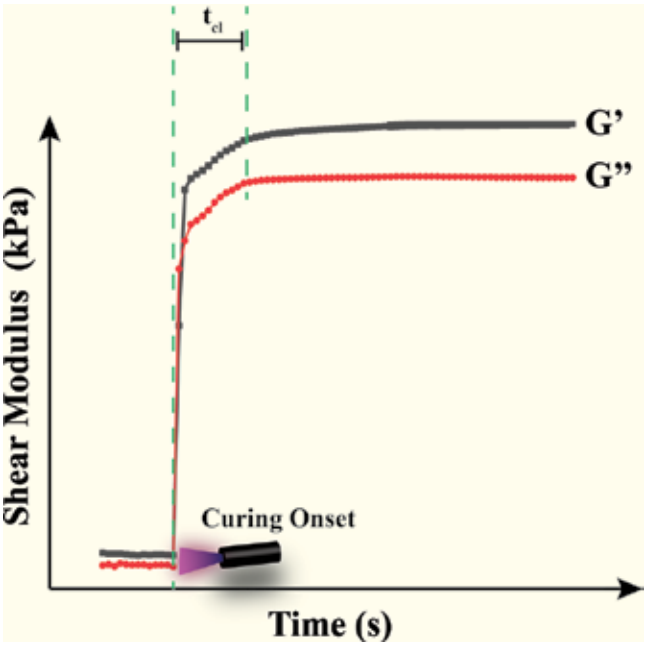

Figure 9. Representative dynamic mechanical analysis curve for measuring the crosslinking characteristics of a UV-curable formulation.

The shrinkage of the material can also be measured by exploiting the rheometer's[6] axial movement, and the upper plate geometry can be adjusted to move in-line with the shrinkage that occurs with cross-linking. As **Figure 10** demonstrates, a minimum compressive force is

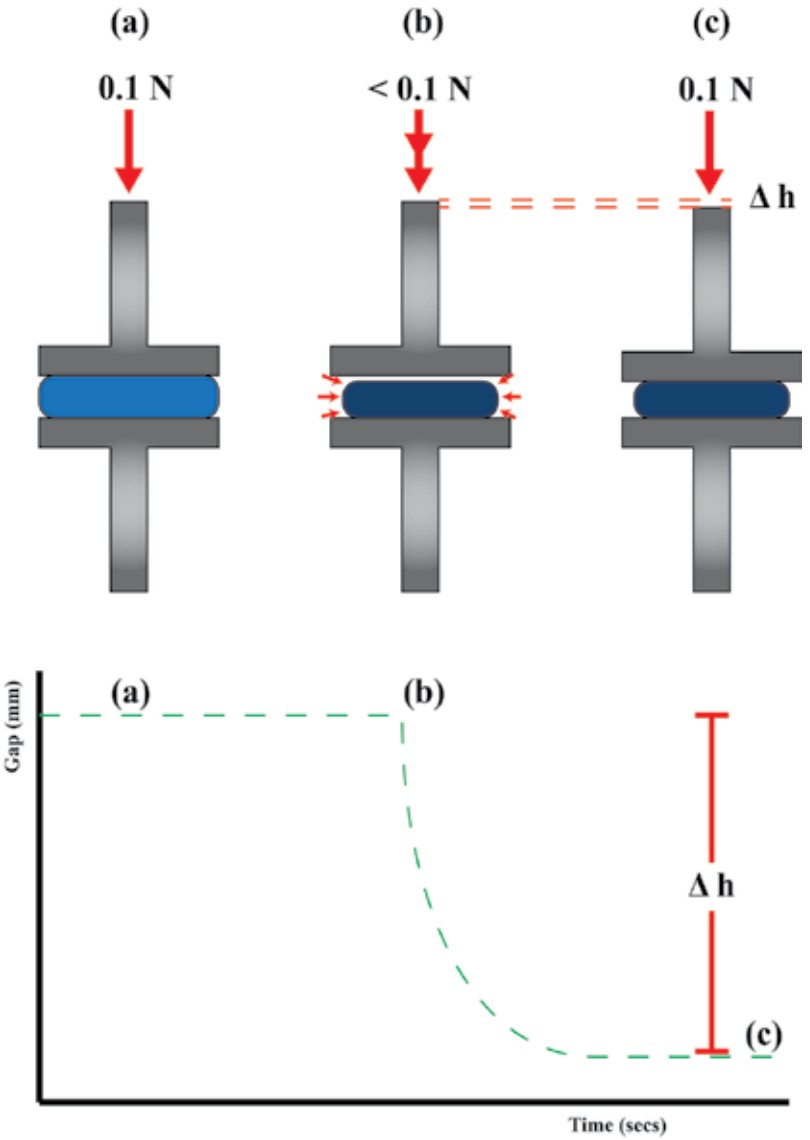

Figure 10. Schematic illustrating the events occurring when measuring shrinkage due to UV-curing. (a) at first the rheometer plate establishes a baseline by applying a prescribed axial force (0.1 N). As the sample is cured it shrinks (b) causing a decrease in the force, and subsequently the rheometer moves axially until the prescribed force is re-established (c). Such movements allow the simultaneous measurement of the gap decrease(Δh).

[6]For Example TA Instruments Discovery Hybrid Series rheometers, which can measure both tensile and compressive forces up to 50 N.

applied to the sample during oscillatory measurements, which if not registered will cause the upper plate to move until the compressive force is re-established. Therefore, in addition to measuring the crosslinking properties of the photopolymers, a rotational rheometer can be incorporated to offer insight into the material's shrinkage characteristics.

4. Other techniques

Given the success and ubiquity of FDM, similar extrusion-based additive manufacturing techniques exists. Examples include bioprinters, where hydrogels and cells are extruded; robocasting, where a ceramic, metallic, or glass powder enveloped by a polymeric binder is extruded; and inkjet printing, where polymeric inks are ejected. Said techniques differ to FDM with respect to their printing conditions. For example, bioprinters and robocasting can be performed at room temperature, and hence high-temperature rheology is of less interest. Another example is the solidification process post-extrusion: where FDM relies in cooling for the material post-extrusion to maintain its structural integrity, cold-extrusion techniques require shear-thinning materials that can rapidly restore their structural integrity following shearing [63]. Moreover, each of the aforementioned techniques have their unique desirable rheological properties, with respect to viscosity ranges, flow characteristics and dynamic mechanical properties. These are just a few of the common extrusion-based AM techniques, and as the field progresses, alternative derivatives are anticipated. Hence, the desirable rheological properties will evolve accordingly, and it is for this reason, that rheology will need to be a habitual characterisation technique in polymer AM fabrication.

A brief mention of selective laser sintering (SLS) is merited. Distinctly different from other techniques, SLS utilises a laser to sinter adjacent polymer powders laterally, such as nylon, and subsequently layer-by-layer to fashion a 3D print. After each layer is fully sintered, a new powder layer is deposited, prior to sintering. The ability of the powder to flow, as well as its packing performance and distribution behaviour, are of interest; and where powder rheology can be employed for elucidation thereof. Measurements performed using a powder rheometer include powder flow, particle-particle interaction during flow, compressibility, and adhesivity. Furthermore, the sintering behaviour discussed in Section 2.3 are applicable herein. Thus, despite SLS possessing a dissimilar mode of operation, rheology is still a relevant technique.

5. Concluding remarks

The chapter has demonstrated the necessity and utility of rheological characterisation techniques for polymer-based additive manufacturing, irrespective of the technique. For fused deposition modelling, rheologically characterisation are performed to obtain the true shear rate at the nozzle wall, the ideal viscosity for material flow, the critical buckling stress, extrudate swelling and sintering characteristics. For stereolithography, a contrasting AM technique, rheology is a requisite for ensuring the resin possesses the ideal viscosity, as well as attaining information regarding the curing characteristics and mechanical properties of the cured resin.

Author details

Mohammed Elbadawi

Address all correspondence to: elbadawi.moe@gmail.com

Pharmaceutical Science and Biomaterials Research Group, Division of Medical Sciences, Department of Health Sciences, Luleå University of Technology, Luleå, Sweden

References

[1] Son Y. Determination of shear viscosity and shear rate from pressure drop and flow rate relationship in a rectangular channel. Polymer (Guildf) [Internet]. 2007;**48**(2):632-637. DOI: 10.1016/j.polymer.2006.11.048

[2] Boetker J, Water JJ, Aho J, Arnfast L, Bohr A, Rantanen J. Modifying release characteristics from 3D printed drug-eluting products. European Journal of Pharmaceutical Sciences. 2016;**90**:47-52. DOI: 10.1016/j.ejps.2016.03.013

[3] Aho J, Boetker JP, Baldursdottir S, Rantanen J. Rheology as a tool for evaluation of melt processability of innovative dosage forms. International Journal of Pharmaceutics [Internet]. 2015;**494**(2):623-642. DOI: 10.1016/j.ijpharm.2015.02.009

[4] Ren X, Shao H, Lin T, Zheng H. 3D gel-printing—An additive manufacturing method for producing complex shape parts. Material Design [Internet]. 2016;**101**:80-87. DOI: 10.1016/j.matdes.2016.03.152

[5] Giovanni P, Gabriele N, Gianmarco G, Marinella L, Stefano T. UV-assisted three-dimensional printing of polymer nanocomposites based on inorganic fillers. Polymer Composition [Internet]. 2017 Aug 8;**38**(8):1662-1670. DOI: 10.1002/pc.23735

[6] Lobe VM, White JL. An experimental study of the influence of carbon black on the rheological properties of a polystyrene melt. Polymer Engineering and Science [Internet]. 2004 Aug 25;**19**(9):617-624. DOI: 10.1002/pen.760190905

[7] Cox WP, Merz EH. Correlation of dynamic and steady flow viscosities. Journal of Polymer Science [Internet]. 1958 Apr 1;**28**(118):619-622. DOI: 10.1002/pol.1958.1202811812

[8] Coblas D, Broboana D, Balan C. Correlation between large amplitude oscillatory shear (LAOS) and steady shear of soft solids at the onset of the fluid rheological behavior. Polymer (Guildf) [Internet]. 2016;**104**:215-226. DOI: 10.1016/j.polymer.2016.06.003

[9] Graham MD. Wall slip and the nonlinear dynamics of large amplitude oscillatory shear flows. Journal of Rheology (N Y N Y) [Internet]. 1995;**39**(4):697-712. DOI: 10.1122/1.550652

[10] Hyun K, Wilhelm M, Klein CO, Cho KS, Nam JG, Ahn KH, et al. A review of nonlinear oscillatory shear tests: Analysis and application of large amplitude oscillatory shear

(LAOS). Progress in Polymer Science [Internet]. 2011;**36**(12):1697-1753. DOI: 10.1016/j.progpolymsci.2011.02.002

[11] Sriram R, Gang Q, Natesan V, Ahmad S, DS C. Powder processing, rheology, and mechanical properties of feedstock for fused deposition of Si_3N_4 ceramics. Journal of American Ceramic Society [Internet]. 2004 Dec 20;**83**(7):1663-1669. DOI: 10.1111/j.1151-2916.2000.tb01446.x

[12] Zhang F, McGinity JW. Properties of sustained-release tablets prepared by hot-melt extrusion. Pharmaceutical Development and Technology [Internet]. 1999 Jan 1;**4**(2):241-250. DOI: 10.1081/PDT-100101358

[13] Smallman RE, Bishop RJ. Chapter 11 - Plastics and Composites BT - Modern Physical Metallurgy and Materials Engineering. 6th ed. Oxford: Butterworth-Heinemann; 1999. pp. 351-375. DOI: 10.1016/B978-075064564-5/50011-2

[14] Diban N, Haimi S, Bolhuis-Versteeg L, Teixeira S, Miettinen S, Poot A, et al. Development and characterization of poly(ε-caprolactone) hollow fiber membranes for vascular tissue engineering. Journal of Membrane Science [Internet]. 2013;**438**:29-37. DOI: 10.1016/j.memsci.2013.03.024

[15] Monzón MD, Gibson I, Benítez AN, Lorenzo L, Hernández PM, Marrero MD. Process and material behavior modeling for a new design of micro-additive fused deposition. International Journal of Advanced Manufacture Technology [Internet]. 2013 Aug;**67**(9):2717-2726. DOI: 10.1007/s00170-012-4686-y

[16] Rimington RP, Capel AJ, Christie SDR, Lewis MP. Biocompatible 3D printed polymers via fused deposition modelling direct C2C12 cellular phenotype in vitro. Lab Chip [Internet]. 2017;**17**(17):2982-2993. DOI: 10.1039/C7LC00577F

[17] Gomes ACO, Soares BG, Oliveira MG, Pessan LA, Paranhos CM. Influence of compatibilizer content on PA/NBR blends properties: Unusual characterization and evaluation methods. Journal of Applied Polymer Science [Internet]. 2013 Feb 5;**127**(3):2192-2200. DOI: 10.1002/app.37792

[18] Tanner RI. A theory of die-swell. Journal of Polymer Science Part A-2 Polymer Physics [Internet]. 1970 Dec 1;**8**(12):2067-2078. DOI: 10.1002/pol.1970.160081203

[19] Lu X, Lee Y, Yang S, Hao Y, Evans JRG, Parini CG. Fine lattice structures fabricated by extrusion freeforming: Process variables. Journal of Material Processing Technology [Internet]. 2009;**209**(10):4654-4661. DOI: 10.1016/j.jmatprotec.2008.11.039

[20] Lu X, Lee Y, Yang S, Hao Y, Evans J, Parini C. Extrusion freeforming of millimeter wave electromagnetic bandgap (EBG) structures. Rapid Prototype Journal [Internet]. 2009 Jan 16;**15**(1):42-51. DOI: 0.1108/13552540910925054

[21] Murphy CA, Collins MN. Microcrystalline cellulose reinforced polylactic acid biocomposite filaments for 3D printing. Polymer Composite [Internet]. 2016 May 1;**n**(a-n):a. DOI: 10.1002/pc.24069

[22] Mackley MR, Marshall RTJ, Smeulders JBAF, Zhao FD. The rheological characterization of polymeric and colloidal fluids. Chemical Engineering Science [Internet]. 1994;**49**(16): 2551-2565. DOI: 10.1016/0009-2509(94)E0082-2

[23] Banerjee SS, Kumar KD, Bhowmick AK. Distinct melt Viscoelastic properties of novel nanostructured and microstructured thermoplastic elastomeric blends from polyamide 6 and fluoroelastomer. Macromolecular Material Engineering [Internet]. **300**(3):283-290. DOI: 10.1002/mame.201400264

[24] Threepopnatkul P, Teppinta W, Sombatsompop N. Effect of co-monomer content on rheological property of sawdust/ABS composites. Advanced Material Research [Internet]. 2010;**93-94**:611-614. DOI: 10.4028/www.scientific.net/AMR.93-94.611

[25] Yang Q, Chung T-S, Weber M, Wollny K. Rheological investigations of linear and hyperbranched polyethersulfone towards their as-spun phase inversion membranes' differences. Polymer (Guildf) [Internet]. 2009;**50**(2):524-533. DOI: 10.1016/j.polymer.2008.11.039

[26] Koopmans RJ. Extrudate swell of high density polyethylene. Part II: Time dependency and effects of cooling and sagging. Polymer Engineering Science [Internet]. 1992 Dec 1;**32**(23):1750-1754. DOI: 10.1002/pen.760322303

[27] Aho J, Boetker J, Baldursdottir S. Rheology as a tool for evaluation of melt processability of innovative dosage forms. International Journal of Pharmaceutics [Internet]. 2015 Oct 30 [cited 2017 Oct 20];**494**(2):623-642. DOI: 10.1016/j.ijpharm.2015.02.009

[28] Münstedt H, Schwarzl FR. Linear viscoelastic deformation behavior in simple shear. In: Deformation and Flow of Polymeric Materials [Internet]. Berlin, Heidelberg: Springer Berlin Heidelberg; 2014. pp. 121-187. DOI: 10.1007/978-3-642-55409-4_5

[29] den Doelder CFJ, Koopmans RJ. The effect of molar mass distribution on extrudate swell of linear polymers. Journal of Nonnewtonian Fluid Mechanics [Internet]. 2008;**152**(1):195-202. DOI: 10.1016/j.jnnfm.2007.04.005

[30] Zheng H, Wang G, Zhou C, Yu W, Zhang H. Computer-aided optimization of the extrusion process of automobile rubber seal. Journal of Macromolecular Science Part A [Internet]. 2007 Mar 1;**44**(5):509-516. DOI: 10.1080/10601320701235552

[31] Münstedt H, Schwarzl FR. Rheological properties and molecular structure. In: Deformation and Flow of Polymeric Materials [Internet]. Berlin, Heidelberg: Springer Berlin Heidelberg; 2014. pp. 419-452. DOI: 10.1007/978-3-642-55409-4_13

[32] Handge UA, Zeiler R, Dijkstra DJ, Meyer H, Altstädt V. On the determination of elastic properties of composites of polycarbonate and multi-wall carbon nanotubes in the melt. Rheologica Acta [internet]. 2011 Jun;**50**(5):503. DOI: 10.1007/s00397-011-0558-x

[33] Münstedt H, Schwarzl FR. Shear rheology. In: Deformation and Flow of Polymeric Materials [Internet]. Berlin, Heidelberg: Springer Berlin Heidelberg; 2014. p. 363-386. ADOI: 10.1007/978-3-642-55409-4_11

[34] Huang SX, Lu CJ. Stress relaxation characteristics and extrudate swell of the IUPAC-LDPE melt. Journal of Nonnewtonian Fluid Mechanics [Internet]. 2006;**136**(2):147-156. DOI: 10.1016/j.jnnfm.2006.03.013

[35] Konaganti VK, Ansari M, Mitsoulis E, Hatzikiriakos SG. The effect of damping function on extrudate swell. Journal of Nonnewtonian Fluid Mechanics [Internet]. 2016;**236**:73-82. DOI: 10.1016/j.jnnfm.2016.08.007

[36] Kiriakidis DG, Park HJ, Mitsoulis E, Vergnes B, Agassant J-F. A study of stress distribution in contraction flows of an LLDPE melt. Journal of Nonnewtonian Fluid Mechanics [Internet]. 1993;**47**:339-356. DOI: 10.1016/0377-0257(93)80057-I

[37] Guillet J, Seriai M. Quantitative evaluation of extrudate swell from viscoelastic properties of polystyrene. Rheologica Acta [Internet]. 1991;**30**(6):540-548. DOI: 10.1007/BF00444372

[38] Rosato D, Rosato D. 2 - Design Optimization BT - Plastics Engineered Product Design. In Amsterdam: Elsevier Science; 2003. pp. 46-160. DOI: 10.1016/B978-185617416-9/50003-X

[39] Kamath VM, Mackley MR. The determination of polymer relaxation moduli and memory functions using integral transforms. Journal of Nonnewtonian Fluid Mechanics [Internet]. 1989;**32**(2):119-144. DOI: 10.1016/0377-0257(89)85032-3

[40] Porter D. Combining molecular and continuum mechanics concepts for constitutive equations of polymer melt flow. Journal of Nonnewtonian Fluid Mechanics [Internet]. 1997;**68**(2):141-152. DOI: 10.1016/S0377-0257(96)01516-9

[41] Garcia-Rejon A, DiRaddo RW, Ryan ME. Effect of die geometry and flow characteristics on viscoelastic annular swell. Journal of Nonnewtonian Fluid Mechanics [Internet]. 1995;**60**(2):107-128. DOI: 10.1016/0377-0257(95)01384-X

[42] Polacco G, Stastna J, Biondi D, Zanzotto L. Relation between polymer architecture and nonlinear viscoelastic behavior of modified asphalts. Current Opinion in Colloidal Interface Science [Internet]. 2006;**11**(4):230-245. DOI: 10.1016/j.cocis.2006.09.001

[43] Ganvir V, Gautham BP, Pol H, Bhamla MS, Sclesi L, Thaokar R, et al. Extrudate swell of linear and branched polyethylenes: ALE simulations and comparison with experiments. Journal of Nonnewtonian Fluid Mechanics [Internet]. 2011;**166**(1):12-24. DOI: 10.1016/j.jnnfm.2010.10.001

[44] Tam KC, Ng WK, Jenkins RD. Non-linear shear deformation of hydrophobically modified polyelectrolyte systems. Polymer (Guildf) [Internet]. 2006;**47**(19):6731-6737. DOI: 10.1016/j.polymer.2006.07.051

[45] Osaki K. On the damping function of shear relaxation modulus for entangled polymers. Rheologica Acta [Internet]. 1993 Sep;**32**(5):429-437. DOI: 10.1007/BF00396173

[46] Bellehumeur C, Li L, Sun Q, Gu P. Modeling of bond formation between polymer filaments in the fused deposition modeling process. Journal of Manufacturing Processes [Internet]. 2004;**6**(2):170-178. DOI: 10.1016/S1526-6125(04)70071-7

[47] Cole DP, Riddick JC, Iftekhar Jaim HM, Strawhecker, KE, Zander NW. Interfacial mechanical behavior of 3D printed ABS. Journal of Applied Polymer Science [Internet]. 2016 Apr;**133**(30):20. DOI: 10.1002/app.43671

[48] Sun Q, Rizvi GM, Bellehumeur CT, Gu P. Effect of processing conditions on the bonding quality of FDM polymer filaments. Rapid Prototype Journal [Internet]. 2008 Mar 28;**14**(2):72-80. DOI: 10.1108/13552540810862028

[49] Hashemi Sanatgar R, Campagne C, Nierstrasz V. Investigation of the adhesion properties of direct 3D printing of polymers and nanocomposites on textiles: Effect of FDM printing process parameters. Applied Surface Science [Internet]. 2017;**403**:551-563. DOI: 10.1016/j.apsusc.2017.01.112

[50] Landa M, Fernandez M, Munoz ME, Santamaria A. The effect of flow on the physical properties of polyurethane/carbon nanotubes nanocomposites: Repercussions on their use as electrically conductive hot-melt adhesives. Polymer Composition [Internet]. 2014 Mar 29;**36**(4):704-712. DOI: 10.1002/pc.22989

[51] Hinczewski C, Corbel S, Chartier T. Stereolithography for the fabrication of ceramic three- dimensional parts. Rapid Prototype Journal [Internet]. 1998 Sep 1;**4**(3):104-111. DOI: 10.1108/13552549810222867

[52] PD K, Hosein SA, Michael L, Biao Z, Qi G, Shlomo M. Highly stretchable and UV curable Elastomers for digital light processing based 3D printing. Advanced Material [Internet]. 2017 Feb 7;**29**(15):1606000. DOI: 10.1002/adma.201606000

[53] Shepherd BNP, TJW, HZ, RF. 3D printing antagonistic systems of artificial muscle using projection stereolithography. Bioinspiration and Biomimetics [Internet]. 2015; **10**(5):55003. DOI: 10.1088/1748-3190/10/5/055003

[54] Wu H, Cheng Y, Liu W, He R, Zhou M, Wu S, et al. Effect of the particle size and the debinding process on the density of alumina ceramics fabricated by 3D printing based on stereolithography. Ceramics International [Internet]. 2016;**42**(15):17290-17294. DOI: 10.1016/j.ceramint.2016.08.024

[55] Thavornyutikarn B, Tesavibul P, Sitthiseripratip K, Chatarapanich N, Feltis B, Wright PFA, et al. Porous 45S5 bioglass®-based scaffolds using stereolithography: Effect of partial pre-sintering on structural and mechanical properties of scaffolds. Materials Science and Engineering: C. 2017;**75**:1281-1288. DOI: 10.1016/j.msec.2017.03.001

[56] Hsiao LC, Badruddoza AZM, Cheng L-C, Doyle PS. 3D printing of self-assembling thermoresponsive nanoemulsions into hierarchical mesostructured hydrogels. Soft Matter [Internet]. 2017;**13**(5):921-929. DOI: 10.1039/C6SM02208A

[57] Faers MA, Choudhury TH, Lau B, McAllister K, Luckham PF. Syneresis and rheology of weak colloidal particle gels. Colloids Surfaces A Physicochemical Engineering Aspects [Internet]. 2006;**288**(1):170-179. DOI: 10.1016/j.colsurfa.2006.03.031

[58] van Vliet T, van Dijk HJM, Zoon P, Walstra P. Relation between syneresis and rheological properties of particle gels. Colloidal Polymer Science [Internet]. 1991 Jun;**269**(6):620-627. DOI: 10.1007/BF00659917

[59] Esposito CC, Mariaenrica F, Domenico A. Rheological characterization of UV-curable epoxy systems: Effects of o-Boehmite nanofillers and a hyperbranched polymeric modifier. Journal of Applied Polymer Science [Internet]. 2009 Jan 30;**112**(3):1302-1310. DOI: 10.1002/app.29603

[60] Elbadawi M, Meredith J, Hopkins L, Reaney I. Progress in bioactive metal and, ceramic implants for load- bearing application. Advanced Techniques in Bone Regeneration [Internet]. Chapter 10. 2016 Aug 31:195-219. DOI: 10.5772/62598

[61] Elomaa L, Teixeira S, Hakala R, Korhonen H, Grijpma DW, Seppälä JV. Preparation of poly(ε-caprolactone)-based tissue engineering scaffolds by stereolithography. Acta Biomaterilia [Internet]. 2011;**7**(11):3850-3856. DOI: 10.1016/j.actbio.2011.06.039

[62] Killion JA, Geever LM, Devine DM, Kennedy JE, Higginbotham CL. Mechanical properties and thermal behaviour of PEGDMA hydrogels for potential bone regeneration application. Journal of Mechanical Behavior of Biomedical Materials [Internet]. 2011;**4**(7):1219-1227. DOI: 10.1016/j.jmbbm.2011.04.004

[63] Elbadawi M, Mosalagae M, Reaney IM, Meredith J. Guar gum: A novel binder for ceramic extrusion. Ceramics International. 2017;**43**:16727-16735. DOI: 10.1016/j.ceramint.2017.09.066

Chapter 4

Particle Settling in a Non-Newtonian Fluid Medium Processed by Using the CEF Model

Şule Celasun

Additional information is available at the end of the chapter

http://dx.doi.org/10.5772/intechopen.75977

Abstract

In this study, the settling of small particles in a non-Newtonian fluid medium is considered. The simulation of this problem according to the fluid mechanics principles may be realized by the flow of a non-Newtonian fluid around a sphere falling along the centerline of a cylindrical tube. The knowledge of the rate of settling of particles in practice is particularly significant in determining the shelf life of materials such as foodstuffs, cleaning materials and many others. Thus, this problem has great importance in many natural and physical processes and in a large number of industrial applications such as chemical, genetic and biomedical engineering operations. The majority of the theoretical, experimental and numerical studies available in the literature deal with Newtonian fluids. Conversely, for non-Newtonian fluids the problem is considerably more complex. It is well-recognized that extensional behaviour in non-Newtonian fluids plays a major role in complex flows. Most non-Newtonian fluids such as polymeric solutions and melts exhibit shear-thinning behaviour. In this study it is aimed to determine the equations governing this process and some important conclusions about the properties of polymeric liquids related to their viscoelastic constitution are drawn. Effectively, it is found that for polymeric liquids, the elastic behaviour characterized by the normal stress coefficients, implies relatively increased normal stresses with respect to the generalized Newtonian fluids, whereas the shear stresses tend to decrease, thus changing somewhat the category of the flow from shear-flow into extensional flow in a small rate. Hence, the viscoelastic property of the polymeric liquids must be stressed by their constitutive equation choice, which led us to the CEF model.

Keywords: non-Newtonian fluids, CEF equation, shear strain-rate, particle settling, FEM, optimization, optimization techniques, elastic behaviour

1. Introduction

As an example to the application of Criminale-Ericksen-Filbey (CEF) fluid, we can consider the settling of small particles in a non-Newtonian fluid medium. The geometry of the problem: schematic diagram of a sphere falling through a fluid in a cylinder is shown in (**Figure 1**). Due to axisymmetry the problem can be considered as 2-D.

This problem has great importance in a large number of industrial applications. Because these materials are rather polymeric and consequently viscoelastic, it is obligatory to include the elastic behaviour in the analysis. The notations are the usual ones.

The quantities of interest are the stresses: we must consider the effects of the normal stress in addition to those of the shear stresses and to use a constitutive equation which includes normal stress coefficients, υ_1 and υ_2 as well as viscosity coefficient η, while taking into account their shear-thinning variation [1–3].

1.1. The non-Newtonian fluid chosen

Many constitutive equations developed from the continuum mechanics or microstructural viewpoints, are used to describe the behaviour of non-Newtonian fluids. Among them the second-order Rivlin-Ericksen model is generally preferred because it describes the real behaviour of the fluids with sufficient accuracy and also because its application is not very

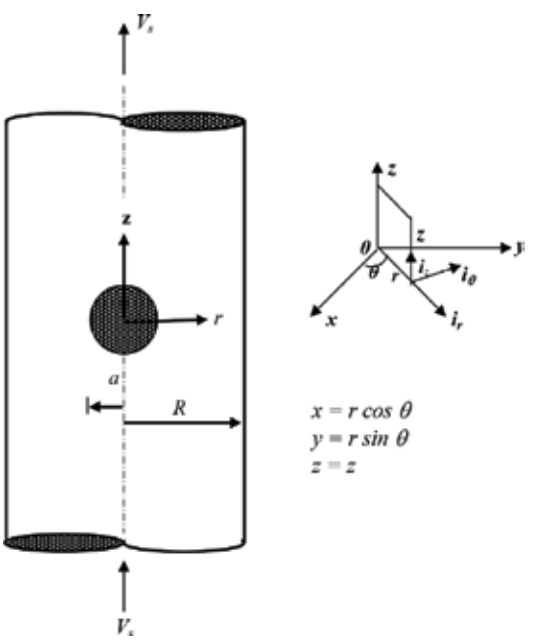

Figure 1. Schematic diagram of a sphere falling through a fluid in a cylinder.

cumbersome. On the other hand, the material coefficients used being constant, it is not in good agreement with experimental results in case the shear strain-rate is not very small. The CEF constitutive equation removes this draw-back by taking these coefficients variable and dependent of the shear strain-rate. That is why this model is used in the study of the settling of small particles in a non-Newtonian fluid medium.

1.1.1. The CEF equation

The constitutive equation of the CEF fluid is:

$$\boldsymbol{\tau} = -p\,\boldsymbol{I} + \eta\,\boldsymbol{A_1} + (\upsilon_1 + \upsilon_2)\,\boldsymbol{A_1}^2 - \frac{1}{2}\upsilon_1\,\boldsymbol{A}_2 \tag{1}$$

The merit of CEF constitutive equation is that it stresses the dependence of the viscosity coefficient on shear strain-rate, that is, it takes into account the shear thinning (or shear-thickening) effects, and those of normal stresses which are also dependent on the shear strain-rate. In steady-state shear flow an extremely wide class of viscoelastic constitutive equations simplifies to CEF equation. The first term of the CEF equation for τ is just $\eta(\dot{\gamma})\dot{\gamma}$; the other two terms, containing υ_1 and υ_2, describe the elastic effects associated with the normal stresses [4].

The Rivlin-Ericksen tensors involved in the CEF equation are [5]:

$$\begin{aligned} \boldsymbol{A_1} &= 2\boldsymbol{d} = \nabla \boldsymbol{V} \;\; + \nabla \boldsymbol{V}^T \\ \boldsymbol{A_1}^2 &= 4\boldsymbol{d}^2 \\ \boldsymbol{A_2} &= \nabla \boldsymbol{a} + \nabla \boldsymbol{a}^T + \boldsymbol{2}\,\nabla \boldsymbol{V}\,\nabla \boldsymbol{V}^T \end{aligned} \tag{2}$$

The first invariant of $\boldsymbol{d}$ is null

$$I_d = 0 \tag{3}$$

The shear strain-rate in term of the second invariant II_d is [6]

$$\dot{\gamma} = 2\sqrt{\mathrm{II_d}} = \sqrt{\frac{1}{2}\mathrm{tr}\boldsymbol{A}_1^2} = \sqrt{\frac{1}{2}\mathrm{tr}\boldsymbol{A}_2} \tag{4}$$

The velocity gradients of $\boldsymbol{A}_1$, A_1^2, $\boldsymbol{A}_2$ appearing in Eq. (1) are given in extenso.

1.1.1.1. Material functions in steady-state shear flows

At high shear rates, the viscosity of most polymeric liquids decreases with increasing shear rate (**Figure 2**). For many engineering applications this is the most important property of polymeric fluids.

An especially useful form has been described by Carreau [4] for the viscosity coefficient (n = 0.364).

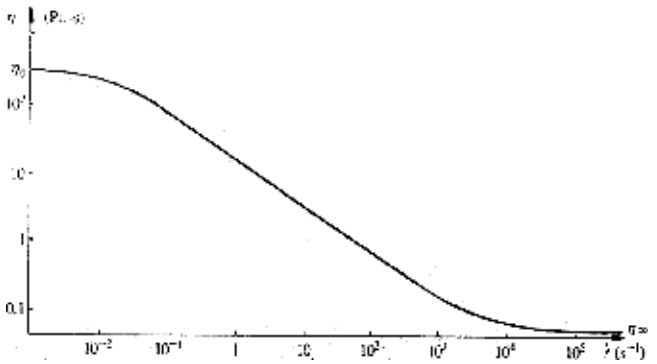

Figure 2. Shear-thinning in a typical non-Newtonian fluid.

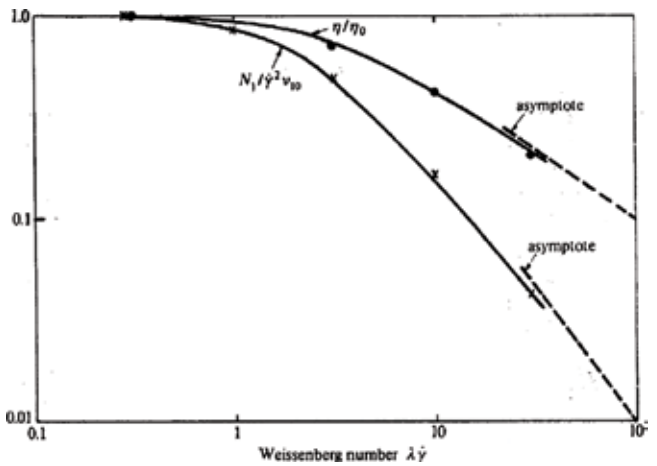

Figure 3. Non-linear results.

$$\eta = \eta_0\left(1 + 32.32 \cdot tr \cdot A_1^2\right)^{-0.318} \tag{5}$$

The normal stress coefficients may be handled as below:

If $\eta = \eta_o$ and $\upsilon_1 = \upsilon_{10}$ for $\dot{\gamma} = 0$, according to $\lambda\dot{\gamma}$ Weissenberg number, η/η_o and $\frac{N_1}{\dot{\gamma}^2 \upsilon_{10}} = \frac{\upsilon_1}{\upsilon_{10}}$ curves may be displayed as in the **Figure 3** [7]. Elastic effects are observable in a steady simple-shear flow through normal stress effects. This is demonstrated in **Figure 4** [8].

Treating the curve in the **Figure 4** by the least square method, the formula below can be found for the first normal stress coefficient υ_1:

$$\frac{\upsilon_1}{\eta} \approx 10^{\left[-0.169\left(\log_{10}\dot{\gamma}\right)^2 - 0.76\log_{10}\dot{\gamma} - 0.821\right]} \tag{6}$$

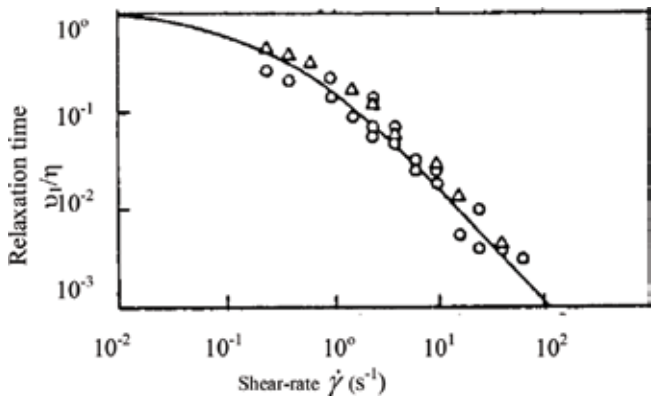

Figure 4. The relaxation time (defined as $\frac{N_1}{\tau\dot{\gamma}} = \frac{\upsilon_1}{\eta}$) is plotted against the shear-rate.

The most important points to note about υ_2 are that its magnitude is much smaller than υ_1, usually about 10–20% of υ_1, and that it is negative [4].

Hence, we shall take

$$\upsilon_2 = -0.15\upsilon_1 \tag{7}$$

Consequently

$$\upsilon_1 + \upsilon_2 = 0.85\upsilon_1 \tag{8}$$

The choice of Carreau formula is justified by the behaviour similarity of inelastic and viscoelastic fluids concerning the viscosity, and that of the formula about the normal stress coefficients by the fact that the particle settling problem has characteristics close to dilute suspensions.

2. An example to CEF fluid application

As an example to the application of the CEF fluid, we can consider the settling of small particles in a non-Newtonian fluid medium. The simulation of this problem according to the fluid mechanics principles may be realized by the flow of a non-Newtonian fluid around a sphere falling along the centerline of a cylindrical tube [9–14].

The knowledge of the rate of settling of particles in practice is particularly significant in determining the shelf life of materials such as foodstuffs, cleaning materials and many others. Also, in oil and gas drilling it is important to understand the distribution of loose material, removed by the drill bit and carried to the surface by the drilling mud. Thus, this problem has great importance in many natural and physical processes and in a large number of industrial applications such as chemical, genetic and biomedical engineering operations. The cylindrical tube is considered as stationary. The drag coefficient must be calculated. The equations determining

the motion of a sphere in an incompressible fluid under isothermal conditions will be given for a non-Newtonian viscous fluid exhibiting shear-thinning and using cylindrical coordinates [15]. As this study is the simulation of the slow motion of small particles, we can suppose the flow irrotational. Furthermore, due to the data of the considered problem, the motion may be assumed steady, axisymmetric and the fluid incompressible. The global cylindrical coordinate system (r, θ, z) is shown in **Figure 1**, cited firstly in the introduction section showing schematic diagram of the problem studied. The local area coordinates are L_1, L_2, and L_3.

Due to the lack of analytical solutions, one will have to resort to numerical methods. The finite element method (FEM) will be used for this purpose.

2.1. Governing equations

Continuity equation

$$\nabla.\boldsymbol{V} = \frac{\partial v_r}{\partial r} + \frac{\partial v_z}{\partial z} + \frac{v_r}{r} = 0 \tag{9}$$

Motion equations

$$\rho \frac{D\boldsymbol{V}}{Dt} = \nabla.\boldsymbol{\tau} \tag{10}$$

They have two projections in the axisymmetric problem considered. Hence, there are overall three equations. Unknowns are v_r, v_z, p. Supposing a creeping flow, the left-hand side may be taken null, and the motion equations reduce to

$$\nabla.\boldsymbol{\tau} = 0 \tag{11}$$

According to the assumptions of steady, axisymmetric, incompressible and irrotational flow properties above mentioned, we can write

$$\frac{\partial}{\partial t} = 0 \ \frac{\partial}{\partial \theta} = 0 \ \nabla.\ \boldsymbol{V} = 0 \ \nu_\theta = 0 \tag{12}$$

2.2. Nondimensionalization

Nondimensional variables and scales are introduced as

$$r^* = \frac{r}{a} \quad z^* = \frac{z}{a} \quad {v_r}^* = \frac{v_r}{V_s} \quad {v_\theta}^* = \frac{v_\theta}{V_s} \quad {v_z}^* = \frac{v_z}{V_s}$$

$$p^* = p\frac{a}{V_s \eta_o} \ t^* == t\frac{\eta_o}{a^2\rho} \ \eta^* = \frac{\eta}{\eta_o} \ {v_1}^* = \frac{v_1}{v_{10}} \ {v_2}^* = \frac{v_2}{v_{20}} \ D^* = \frac{D}{\eta_0 a V_s}$$

$$(A_1)^* = (A_1)\frac{a}{V_s} \qquad \left(A_1^2\right)^* = \left(A_1^2\right)\left(\frac{a}{V_s}\right)^2 \qquad (A_2)^* = (A_2)\left(\frac{a}{V_s}\right)^2 \qquad \psi^* = \frac{\psi}{a_2 V_s} \tag{13}$$

For brevity * notation will be elected by implication.

2.3. Explicit expressions of the dimensionless governing equations

Continuity equation

$$\frac{\partial v_r}{\partial r}+\frac{\partial v_z}{\partial z}+\frac{v_r}{r}=0 \tag{14}$$

Projection of the motion equation on the r axis

$$\begin{aligned}&-\frac{\partial p}{\partial r}+\frac{\partial \eta}{\partial r}(A_1)_{rr}+\frac{\partial \eta}{\partial z}(A_1)_{zr}+\eta\left[\frac{\partial (A_1)_{rr}}{\partial r}+\frac{\partial (A_1)_{zr}}{\partial z}+\frac{(A_1)_{rr}-(A_1)_{\theta\theta}}{r}\right]+\\&+0.85K\left\{\frac{\partial v_1}{\partial r}\left(A_1^2\right)_{rr}+\frac{\partial v_1}{\partial z}\left(A_1^2\right)_{zr}+v_1\left[\frac{\partial \left(A_1^2\right)_{rr}}{\partial r}+\frac{\partial \left(A_1^2\right)_{zr}}{\partial z}+\frac{\left(A_1^2\right)_{rr}-\left(A_1^2\right)_{\theta\theta}}{r}\right]\right\}-\\&-\frac{1}{2}K\left\{\frac{\partial v_1}{\partial r}(A_2)_{rr}+\frac{\partial v_1}{\partial z}(A_2)_{zr}+v_1\left[\frac{\partial (A_2)_{rr}}{\partial r}+\frac{\partial (A_2)_{zr}}{\partial z}+\frac{(A_2)_{rr}-(A_2)_{\theta\theta}}{r}\right]\right\}=0\end{aligned} \tag{15}$$

Projection of the motion equation on the z axis

$$\begin{aligned}&-\frac{\partial p}{\partial z}+\frac{\partial \eta}{\partial r}(A_1)_{rz}+\frac{\partial \eta}{\partial z}(A_1)_{zz}+\eta\left[\frac{\partial (A_1)_{rz}}{\partial r}+\frac{\partial (A_1)_{zz}}{\partial z}+\frac{(A_1)_{rz}}{r}\right]+\\&+0.85K\left\{\frac{\partial v_1}{\partial r}\left(A_1^2\right)_{rz}+\frac{\partial v_1}{\partial z}\left(A_1^2\right)_{zz}+v_1\left[\frac{\partial \left(A_1^2\right)_{rz}}{\partial r}+\frac{\partial \left(A_1^2\right)_{zz}}{\partial z}+\frac{\left(A_1^2\right)_{rz}}{r}\right]\right\}-\\&-\frac{1}{2}K\left\{\frac{\partial v_1}{\partial r}(A_2)_{rz}+\frac{\partial v_1}{\partial z}(A_2)_{zz}+v_1\left[\frac{\partial (A_2)_{rz}}{\partial r}+\frac{\partial (A_2)_{zz}}{\partial z}+\frac{(A_2)_{rz}}{r}\right]\right\}=0\end{aligned} \tag{16}$$

where K is the normalization coefficient.

Taking as numerical example

$a/R = 0.2$, $a = 0.05$ m, and $V_s = 0.016$ m/s, and because for $\dot{\gamma} \to 0$, we have $\frac{v_1}{\eta} \to \frac{v_{10}}{\eta_0} = 1$

which ensues

$$K=\frac{v_{10}}{\eta_o}\frac{V_s}{a}=0.32 \tag{17}$$

The coefficient K is the special case for $\dot{\gamma} = 0$ of the Weissenberg number. It is worthwhile to notice that for $K = 0$ we go back to the generalized Newtonian fluid.

2.3.1. Stream function

$$\psi=\text{constant}-\int_0^r rv_z dr\approx\pi-\int_0^r rv_z dr \tag{18}$$

2.3.2. Boundary conditions (dimensionless)

At the inlet of the flow: $v_r = 0$ $v_z = 1$.

Along the cylindrical tube ($r = R$): $v_r = 0$ $v_z = 1$.

Along the centerline of the cylindrical tube ($r = 0$): $v_r = 0\ \frac{\partial v_z}{\partial r} = 0$

On the surface of the sphere: $v_r = v_z = 0$.

At the outlet of the flow: $v_r = 0\ \frac{\partial v_z}{\partial r} = 0$.

$$p = 0\ (\text{atmospheric pressure}) \tag{19}$$

2.4. Dimensionless stress components

Introducing $K = \frac{\upsilon_{10}}{\eta_0}\frac{V_s}{a}$ in the CEF constitutive equation Eq. (1), using Eq.(13) nondimensional formulas and Eq. (7), $\tau^* = \tau\ \frac{a}{V_s \eta_o}$ stress tensor components can be written electing the * notation by implication as follows:

$$\begin{aligned}
\tau_{rr} &= -p + \eta(A_1)_{rr} + K\left[0.85\upsilon_1\left(A_1^2\right)_{rr} - \frac{1}{2}\upsilon_1(A_2)_{rr}\right] \\
\tau_{rz} &= \eta(A_1)_{rz} + K\left[0.85\upsilon_1\left(A_1^2\right)_{rz} - \frac{1}{2}\upsilon_1(A_2)_{rz}\right] \\
\tau_{\theta\theta} &= -p + \eta(A_1)_{\theta\theta} + K\left[0.85\upsilon_1\left(A_1^2\right)_{\theta\theta} - \frac{1}{2}\upsilon_1(A_2)_{\theta\theta}\right] \\
\tau_{zz} &= -p + \eta(A_1)_{zz} + K\left[0.85\upsilon_1\left(A_1^2\right)_{zz} - \frac{1}{2}\upsilon_1(A_2)_{zz}\right]
\end{aligned} \tag{20}$$

3. Application of the finite element method to fluids

Due to the assumptions Eq. (12), only v_r, v_z velocity components and pressure p are chosen as primitive variables.

All stress variables are expressed in terms of the velocities and the pressures and the stresses are then back-calculated after finding the velocities v_r, v_z and the pressure p.

For stability the pressure field must be interpolated with a polynomial one order lower than the velocity terms. Here we have chosen linear pressure and quadratic velocity fields over the element.

A quadratic triangle for velocities with six nodes, three on the vertices and the three others on mid-sides, and a linear triangle for pressures, both processed with area coordinates (**Figure 5**).

In our problem gravitational and inertial forces are neglected and the motion is obtained as in the first Stokes problem by drawing the cylinder opposite to the sphere displacement with a constant, upward V_s velocity. To solve the nonlinear equations iterative optimization techniques are used.

3.1. Linear and quadratic triangles

The $\{N^e\}$ shape functions for velocities corresponding to the three vertice nodes and three mid-side nodes (*1, 2, …, 6*) are respectively using the well-known area coordinates L_1, L_2, L_3.

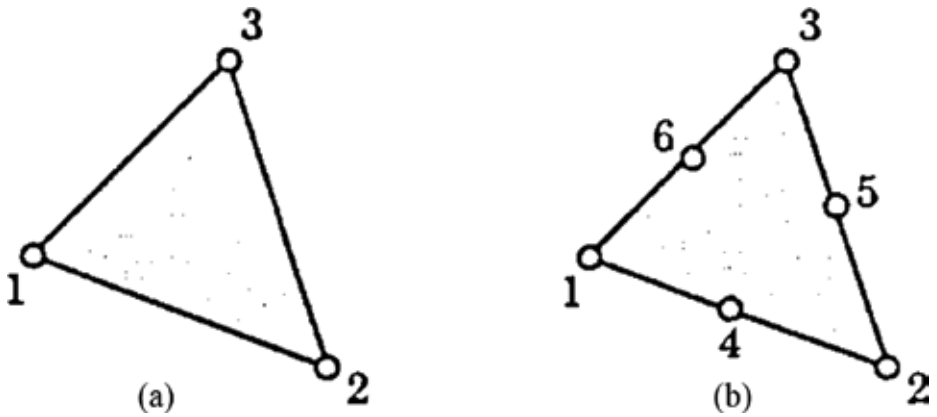

Figure 5. (a) A linear triangular element; and (b) a quadratic triangular element.

$$L_1(2\,L_{1-1});\, L_2\,(2\,L_{2-1});\, L_3(2\,L_{3-1});\, 4L_1L_2;\, 4L_2L_3;\, 4L_3L_1 \tag{21}$$

and those concerning the pressure for nodes *1, 2, 3* are L_1, L_2, L_3, (**Figure 6**).

The element shown satisfies the LBB condition and thus gives reliable and convergent solutions for velocity and pressure fields [16].

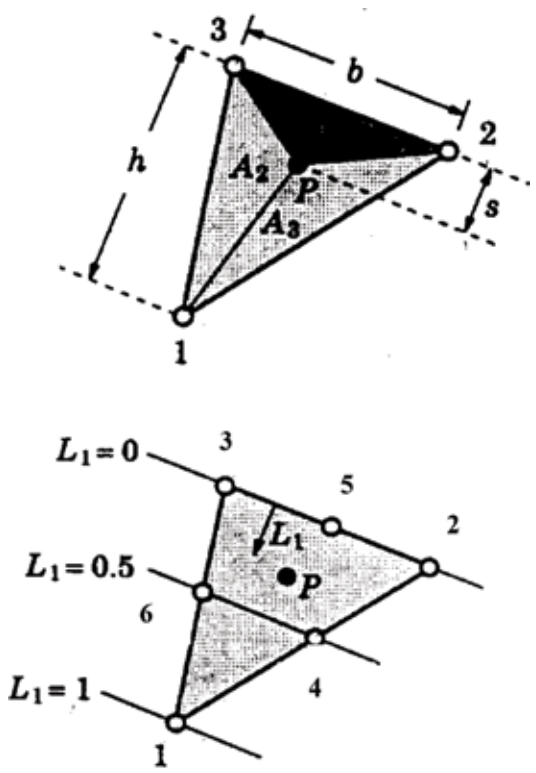

Figure 6. Area coordinates.

The derivatives of the interpolation functions with respect to the global coordinates are of the form

$$\begin{Bmatrix} \dfrac{\partial N_i^e}{\partial r} \\ \dfrac{\partial N_i^e}{\partial z} \end{Bmatrix} = J^{-1} \begin{Bmatrix} \dfrac{\partial N_i^e}{\partial L_1} \\ \dfrac{\partial N_i^e}{\partial L_2} \end{Bmatrix} \tag{22}$$

with the Jacobian matrix of transformation

$$J = \begin{vmatrix} \dfrac{\partial r}{\partial L_1} & \dfrac{\partial z}{\partial L_1} \\ \dfrac{\partial r}{\partial L_2} & \dfrac{\partial z}{\partial L_2} \end{vmatrix}$$

The element area

$$drdz = \frac{1}{2} \det J dL_1 dL_2 \tag{23}$$

The integration must be carried out over the elemental volume of the axisymmetric geometry $rdrd\theta dz$. Since the solution is independent of the θ coordinate, the integration with respect to θ yields a multiplicative constant 2π. (**Table 1**) [17].

3.2. Interpolation formulas

According to the constraint

$$L_1 + L_2 + L_3 = 1$$

Number of integration points	Degree of polynomial Order of the residual	Location of integration points				
		L_1	L_2	L_3	W	Geometric locations
1 (Pressures)	1 $O(h^2)$	1/3	1/3	1/3	1	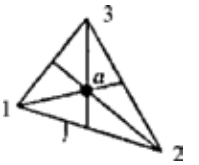
3 (Velocities)	2 $O(h^3)$	1/2 0 1/2	0 1/2 1/2	1/2 1/2 0	1/3	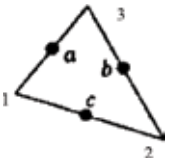

Table 1. Quadrature weights and points for triangular elements.

we eliminate the dependent variable $L3$ for the sake of simplicity. Thus, we have

$$\begin{aligned} v_r = {} & \left(-L_1 + 2L_1^2\right)v_{r1} + \left(-L_2 + 2L_2^2\right)v_{r2} + (1 - 3L_1 - \\ & - 3L_2 + 2L_1^2 + 4L_1L_2 + 2L_2^2)v_{r3} + 4L_1L_2v_{r4} + \\ & + 4\left(L_2 - L_1L_2 - L_2^2\right)v_{r5} + 4\left(L_1 - L_1L_2 - L_1^2\right)v_{r6} \end{aligned}$$

$$\begin{aligned} v_z = {} & \left(-L_1 + 2L_1^2\right)v_{z1} + \left(-L_2 + 2L_2^2\right)v_{z2} + (1 - 3L_1 - \\ & - 3L_2 + 2L_1^2 + 4L_1L_2 + 2L_2^2)v_{z3} + 4L_1L_2v_{z4} + \\ & + 4\left(L_2 - L_1L_2 - L_2^2\right)v_{z5} + 4\left(L_1 - L_1L_2 - L_1^2\right)v_{z6} \end{aligned}$$

$$p = L_1\left(p_1 - p_3\right) + L_2\left(p_2 - p_3\right) + p_3 \tag{24}$$

3.3. Basis of application

The flow domain is meshed using linear and quadratic triangular elements [9]. Three unstructured meshes are generated by an adaptive mesh generator, as given in **Table 2** and shown in **Figure 7**. Independent unknown variables are, due to axisymmetry vr, vz and p. The continuity equation being interpreted as an additional relation among the velocity components, i.e., a constraint satisfied in an approximate least squares sense [18], it may be omitted in the effective area consideration around the mid-side nodes, in order to keep the balance between the equation and unknown variable numbers. Resolving the global equation system obtained while taking into account the boundary conditions and integrating numerically by means of Gauss quadrature over the effective area around each node, the values of the variables are found [19, 20].

As a typical numerical example after [9], the values below are processed:

$$a = 0.05\ \mathrm{m} \quad a/R = 0.2 \quad Vs = 0.016\ \mathrm{m/s}$$

3.3.1. Comparison and contour patterns

In order to provide a basis for a comparison, and to pose the behavioral difference between inelastic and viscoelastic fluids, an example taken from the literature [9], for the simpler case $\upsilon_1 = 0$, gives contours of streamfunction, velocity, stress, pressure and viscosity at parameter settings of n = 0.5 and We = Weissenberg number = 2.5 (**Figure 8**). As it can be seen in the **Figure 8**, the flow accelerates as the fluid approaches the sphere.

The extrema contour levels for the inelastic fluid are again shown in a table (**Table 3**).

Mesh	Sphere surface nodes	Elements	Nodes
AM1	21	644	1401
AM2	31	948	2035
AM3	41	1242	2645

Table 2. Summary of finite element meshes.

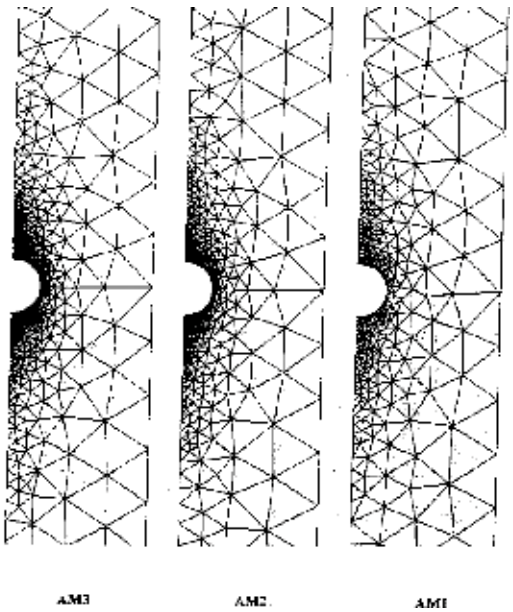

Figure 7. Mesh patterns around sphere, $a/R = 0.2$.

3.3.2. The attempt of getting $\upsilon_1 = \upsilon_2 = 0$ *condition as a special case*

The reasons why the results obtained by Townsend [9] cannot be achieved for the generalized fluid by replacing $\upsilon_1 = \upsilon_2 = 0$ in our equations given above for the generalized condition are explained by Kaloni [21] in the literature.

Nonetheless, we think that is beneficial to make a comparison with Townsend [9] solutions.

3.3.3. Mesh-independent results

The model used in this study, which is called as Mesh#1, was obtained as a result of a three-stage optimization. In the "Initmesh" stage, an "adaptive mesh" was formed. In the second stage number of triangles was increased with the "refinemesh" function to obtain an improvement in this first mesh. Finally, at the third stage, an optimization was achieved with the "jigglemesh" function. Therefore, Mesh#1 is an optimal mesh, and it can be considered sufficient in terms of "mesh independence" alone. Mesh#2 is an adaptive mesh, and the number of triangles in this mesh, was increased considerably with respect to Mesh#1 (**Figure 9** and **Table 4**).

Because the subject of this study is based on the fact that the elastic effect in polymeric fluids cannot be neglected, Mesh#1 and Mesh#2 results in **Table 5** were presented as comparison of the normal stresses. In this table, the average difference between each mesh is approximately 2%. Because the results of two very different meshes mostly overlap, the results obtained are proven to be independent from mesh configuration, i.e., "mesh independence" is achieved. The generated mesh is improved according to the initmesh, refine mesh and jigglemesh MATLAB programs and the mesh independence is tested and ensured.

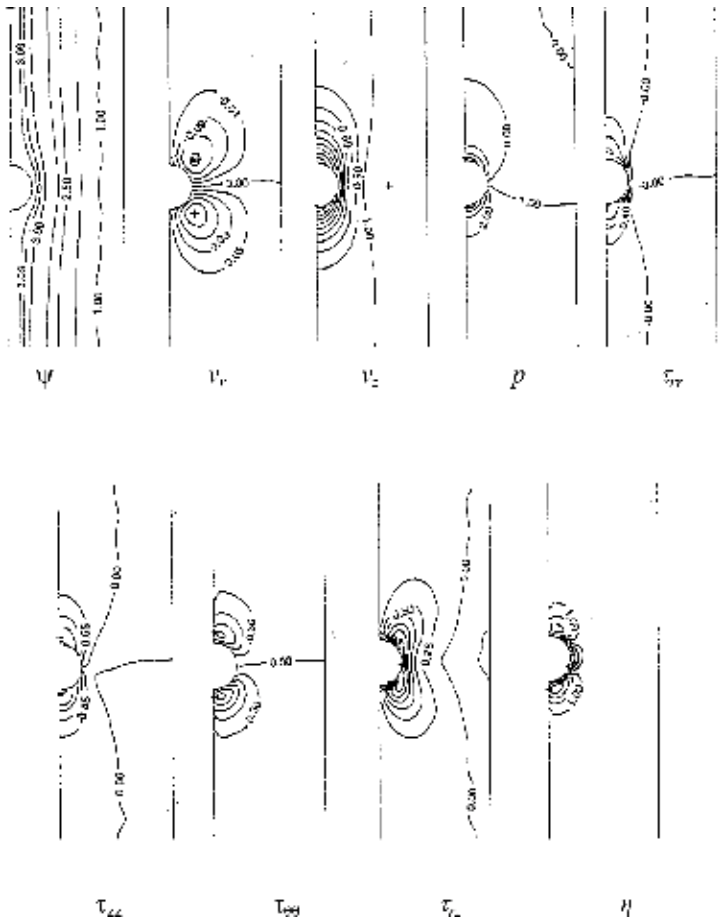

Figure 8. Contours of streamfunction (ψ), radial velocity (v_r), axial velocity (v_z), pressure (p), stress components (τ_{rr}, τ_{zz}, $\tau_{\theta\theta}$, τ_{rz}), and viscosity (η); $a/R = 0.2$, We = 2.5, and $n = 0.5$.

3.4. Explanatory flow characteristics remarks and results of our the theoretical problem solved numerically, cited before the sections findings and discussion and conclusions to better find out the problem studied

3.4.1. Explanatory remarks

The starting example of "Settling of Small Particles in Fluid Medium" problem in the literature which has important applications in many fields such as the shelf life of foodstuffs etc., is given for "generalized Newtonian fluid" medium [9]. As is known, the motion equation is Navier-Stokes in this case, and viscosity coefficient η is function of the shear-rate $\dot{\gamma}$. Although this paper contains useful information, especially for velocity and stress contours, the elastic effects should not be neglected because in practice the fluids encountered in this field are non-Newtonian. This study is to cover this difference. Thus, CEF model was taken as fluid, and for emphasizing the elastic effect, the normal stress coefficients υ_1 and υ_2 was included. The simulation model is in

Flow domain	Minimum	Maximum
ψ	0.0000	3.1250
v_r	−0.1933	0.2171
v_θ	—	—
v_z	0.0000	1.1249
P	−4.9296	7.8010
τ_{rr}	−2.6545	3.1418
$\tau_{\theta\theta}$	−1.4139	1.8356
τ_{rz}	−1.3276	2.9703
τ_{zz}	−3.6693	2.8291
η	0.244	1.4672

Table 3. Extrema contour levels.

the form of the flow of a non-Newtonian fluid around a sphere falling along the centerline of a cylindrical tube. The problem was tried to be solved numerically by writing continuity and motion equations and using FEM. The partial differential equation system obtained was transformed into a set of simultaneous, nonlinear, algebraic equations. Here, we chose linear triangular elements for pressures and quadratic triangular elements for velocities.

Because of the boundary conditions, the equations are "overdetermined." The problem is axisymmetric, the global coordinates r, z were transformed into local coordinates $L1$, $L2$, $L3$; and Gauss quadrature was used for integrating numerically over the effective area around each node. In the solution of the algebraic equation system, naturally optimized formulation with the aid of (MATLAB-Optim set f-solve) function was used instead of the methods like "weak form."

It is useful to give following explanatory remarks:

Although the differential equation is third order, the shape functions are chosen as linear for pressures and quadratic (2nd degree) polynomials for velocities. The degree difference between pressures and velocities is compulsory for stability. These are thought to be sufficient in the literature examples. Using third order polynomial would extend the problem extremely, and make the solution unreachable. Considering the elastic effect (υ_1, υ_2 coefficients) made the problem already harder compared to the generalized Newtonian fluid example [9]. Zienkiewicz especially stresses that FEM application of very refined and sophisticated models does not always yield better solutions [19].

Because the motion is relative, the sphere was taken constant in the problem; however, a motion from bottom to top with a constant Vs velocity was introduced to the cylinder, as done in the 1st Stokes problem. In this case, the inlet is through the bottom surface, while the outlet is through the top surface of the cylinder.

As an example to viscoelastic fluid, Carreau type Separan 30 was chosen [7]. The coefficient λ = 8.04 s was taken from the table given by Tanner [7]. This fluid was used frequently in experiments, and detailed information about its properties is given in the literature [4].

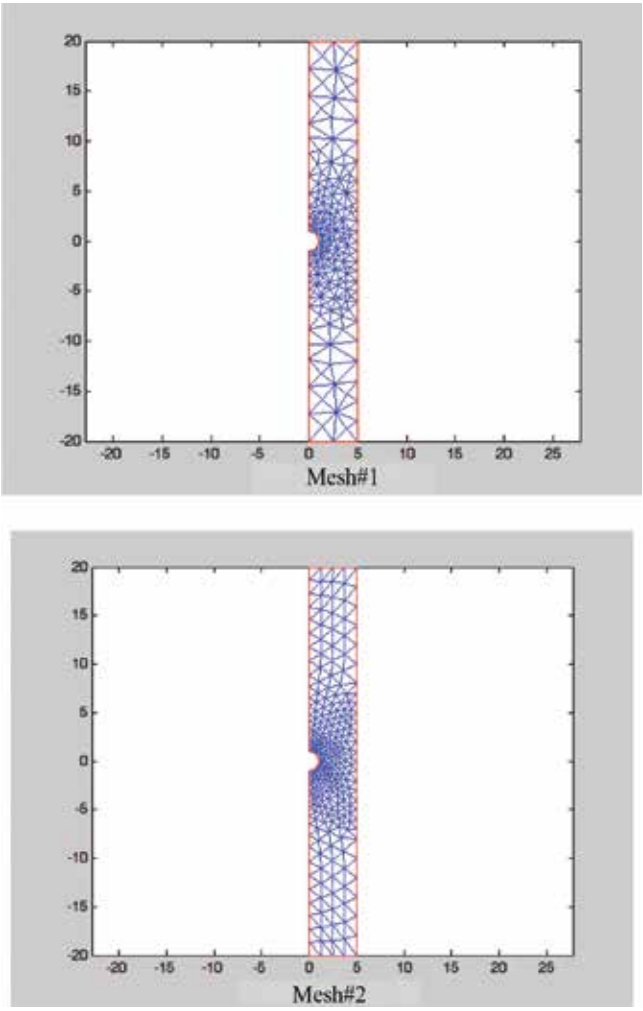

Figure 9. Mesh#1 and Mesh#2.

Definition	Matrices for points P	Matrices for edges E	Matrices for triangles T	Vector of nodal values V
Mesh#1	2 / 205	7 / 62	4/346	1/1715
Mesh#2	2 / 311	7 /84	4/536	1/2625

Table 4. Mesh comparison.

The boundary conditions are generally the conditions at the inlet and outlet, and—for velocities—the no slip conditions at the sphere surface and cylinder wall. It was assumed that $vr = 0$ $vz = 0$ at sphere surface and $vr = 0$ $vz = 1$ (i.e., Vs) at cylinder wall. These values are observed clearly on the contours (**Figures 10** and **11**).

Stresses	τ_{rr}		$\tau_{\theta\theta}$		τ_{zz}	
Extreme values	**Min**	**Max**	**Min**	**Max**	**Min**	**Max**
Mesh#1	−6.0019	3.3792	−6.0115	3.4000	−6.1339	3.7165
Mesh#2	−5.9810	3.2325	−5.8722	3.4022	−6.3396	3.8825

Table 5. Comparison of normal stresses.

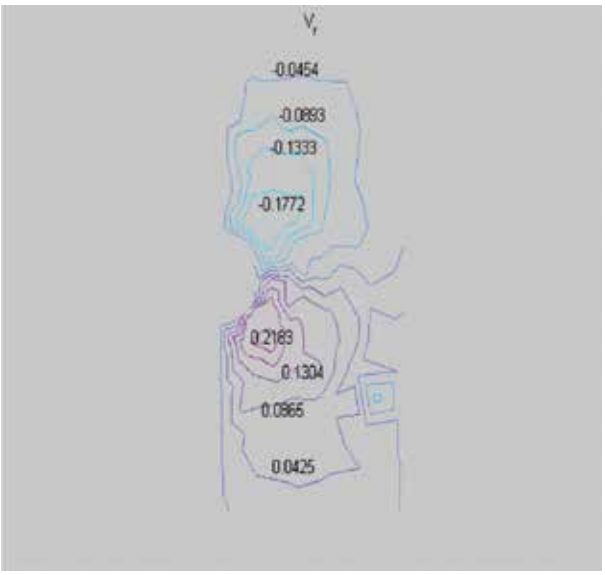

Figure 10. Radial velocity (v_r) [−0.1772 −0.1333 −0.0893 −0.0454 −0.0014 0.0425 0.0865 0.1304 0.1743 0.2183].

Contour values were found by dividing the space between the max and min contours by ten, and were written on the figures without covering them up. That is why contour labels are generally fractional. If an integer contour (e.g., zero) is to be drawn, it can be shown with linear interpolation on the figure.

As seen in pressure (p) contours (**Figure 12**), similarly to the example Rameshwaran, Townsend [9], max and min values are on the "stagnation" points on the sphere (at the vicinity of the vertical axis). Here $vr = vz = 0$; since the total energy is constant (Bernoulli at inviscid flow), if the kinetic energy is zero, potential energy is an extremum, i.e., the pressure is at its extremum value. This is what is seen perspectively in the 3-D surf (surface) drawing (**Figure 13**).

The extreme values concerning the contours are gathered in **Table 6**. The flow is not uniform: the existence of the sphere at the center, the wall effect of cylinder (drag) and the boundary conditions prevent the flow from being uniform. Thus, max and min values are obtained.

In the adaptive "mesh" drawn, there are 755 nodes. At these nodes vr, vz, p values are taken as unknowns and they were determined as a result of calculations. Because the contours followed the nodes, zigzag course was obtained instead of a smooth curve. If the number of nodes had

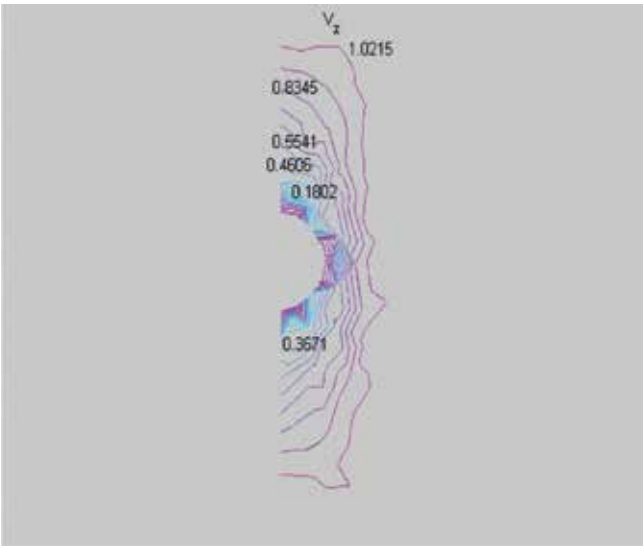

Figure 11. Axial velocity (v_z) [0.0000 0.1802 0.2737 0.3671 0.4606 0.5541 0.6476 0.7411 0.8345 0.9280 1.0215].

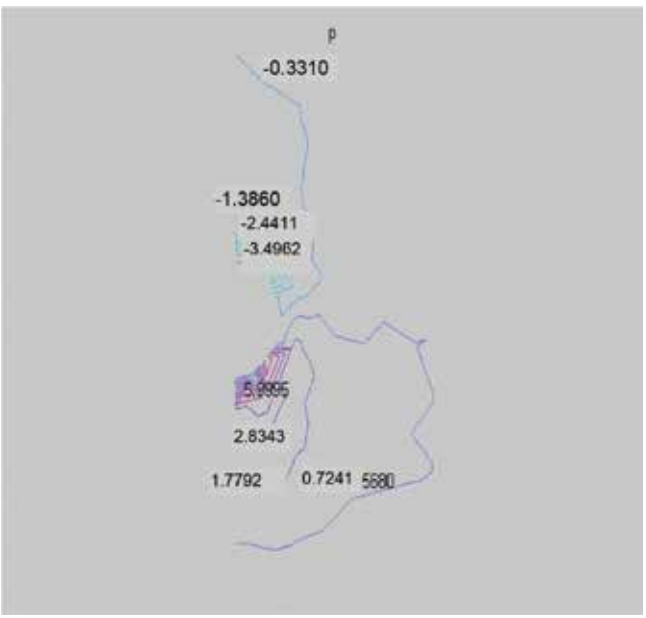

Figure 12. Pressure (p) [−3.4962 −2.4411 −1.3860 −0.3310 0.7241 1.7792 2.8343 3.8893 4.9444 5.9995].

been increased extremely, we could have got curves instead of the zigzag course. This is not a drawback in terms of the results. 10 contours were drawn by dividing space between the max and min values into 10 fragments. Contours are the geometric milieu of the nodes which have the same value of the related independent variable. Horizontal projections of the curves

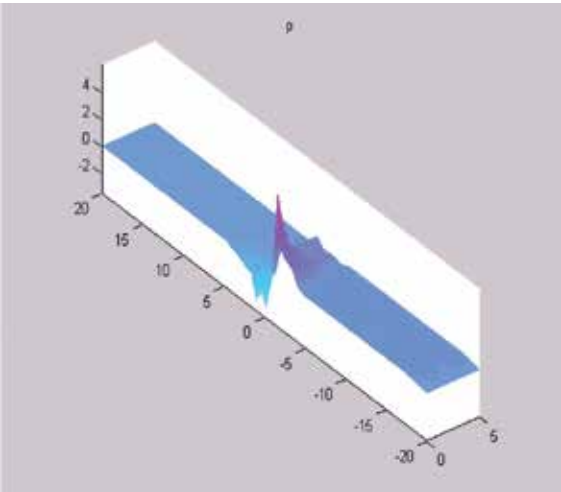

Figure 13. 3-D surf drawing of pressure.

Flow domain	Minimum	Maximum
ψ	0.0000	3.1416
v_r	−0.1772	0.2183
v_z	0.0000	1.0215
p	−3.4962	5.9995
τ_{rr}	−6.0019	3.3792
τ_{zz}	−6.1339	3.7165
$\tau_{\theta\theta}$	−6.0115	3.4000
τ_{rz}	−0.3701	0.8390
η	0.0845	1.0000
v_1	0.0029	0.9981

Table 6. Extrema contour levels.

(level curves) that are obtained by intersecting the surface shown in 3D in the surf drawing with the horizontal planes yield the contours. Contours were drawn with the pdecont, pdemesh, pdesurf commands at MATLAB. These 10 values, below the contours are given separately.

3.4.2. Technical details for the solution of the equation system

We transformed the partial equation system with the aid of FEM to nonlinear overdetermined algebraic equation system. As we have numerous simultaneous and highly nonlinear

Average error	0.1004
Standard Deviation	0.1820
η_avg	0.1104
C	1.6502

Table 7. Error computation, standard deviation, the average of η values at sphere surface (η_avg) and drag coefficient (C).

Error spaces	0–0.5	0.5–1.0	1.0–1.5	1.5–2.0	2.0–2.5
Equation number	1637	66	11	1	0
Percentage (%)	95.4519	3.8484	0.6414	0.0583	0

Table 8. Histogram results concerning equation errors; 1715 equations were used in total.

Min., Max. and Norms:	**Min(F)**	**Max(F)**	$\|\|F\|\|_2$	$\|\|F\|\|_\infty$
	−1.3449	1.6251	8.6075	1.6251

Table 9. Euclidean and infinite norms and minimum and maximum values of the minimized equation vector F.

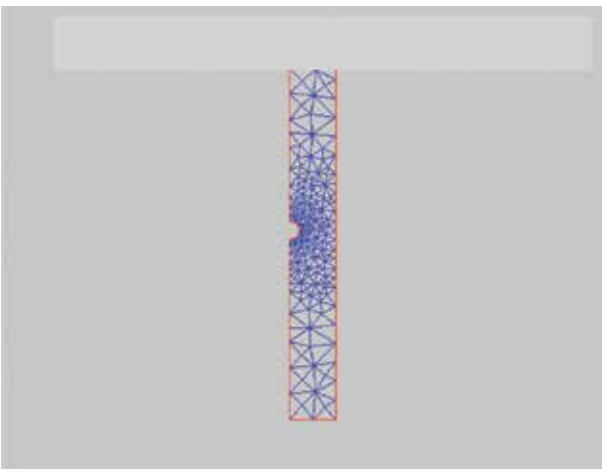

Figure 14. Mesh scheme for $a/R = 0.2$.

equations, which moreover are overdetermined due to the existence of the boundary conditions, we were compelled to resort to the optimization techniques to resolve the equation system [22].

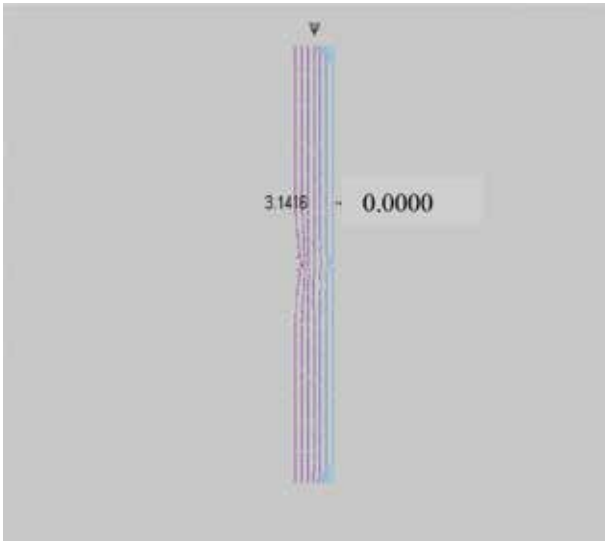

Figure 15. Stream function (Ψ) [0.00 0.01 0.05 0.20 0.44 0.77 1.25 1.88 2.67 3.14].

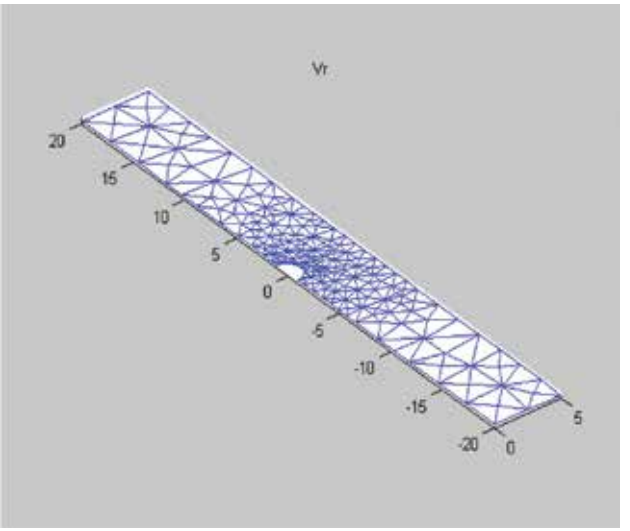

Figure 16. 3-D mesh drawing of radial velocity.

The end of the iterative optimization process is determined according to the fulfillment of the Error computation, Standard deviation, Histogram and minimum and maximum values of the minimized equation vector ***F***, Euclidean norm and Infinite norm (**Tables 7–9**). We determined that the results are in the acceptable order. We used the (Optim set f-solve) function in MATLAB for iterative optimization. The basis of the method is based on "least squares method."

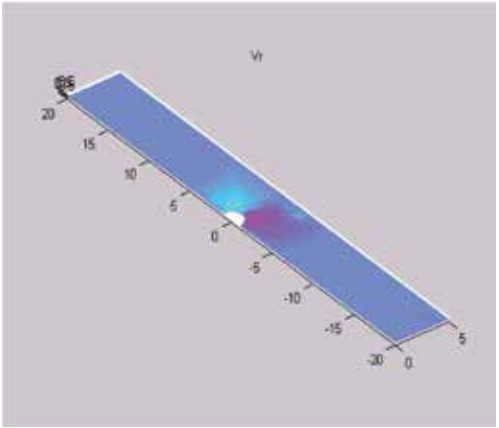

Figure 17. 3-D surf drawing of radial velocity.

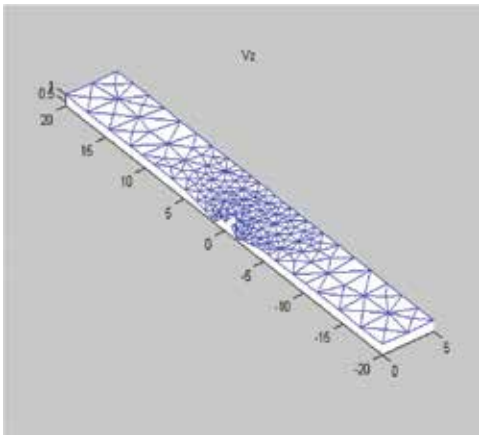

Figure 18. 3-D mesh drawing of axial velocity.

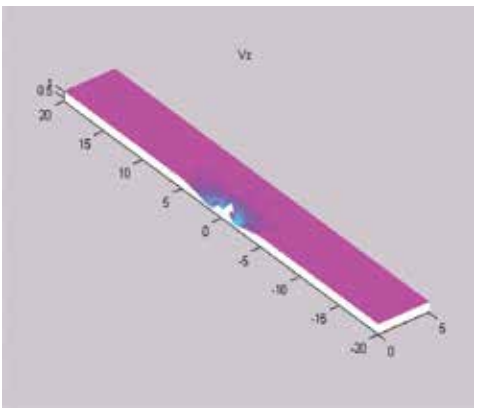

Figure 19. 3-D surf drawing of axial velocity.

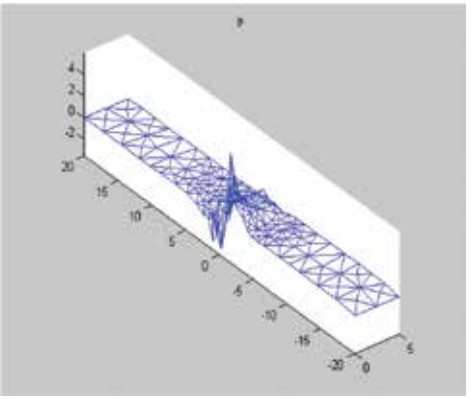

Figure 20. 3-D mesh drawing of pressure.

Figure 21. Normal stress (τ_{rr}) [−6.0019 −4.9595 −3.9172 −2.8748 −1.8325 −0.7902 0.2522 1.2945 2.3369 3.3792].

Figure 22. Axial stress (τ_{zz}) [−6.1339 −5.0394 −3.9449 −2.8504 −1.7560 −0.6615 0.4330 1.5275 2.6220 3.7165].

Figure 23. Azimuthal stress ($\tau_{\theta\theta}$) [−6.0115 −4.9658 −3.9200 −2.8743 −1.8286 −0.7829 0.2628 1.3086 2.3543 3.4000].

Figure 24. Shear stress (τ_{rz}) [−0.3701 −0.2358 −0.1014 0.0329 0.1673 0.3016 0.4360 0.5703 0.7047 0.8390].

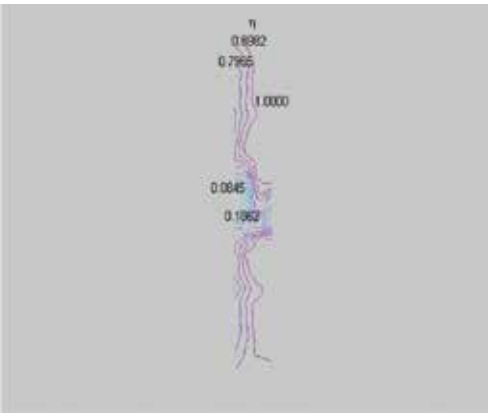

Figure 25. Viscosity coefficient (η) [0.0845 0.1862 0.2879 0.3896 0.4914 0.5931 0.6948 0.7965 0.8982 1.0000].

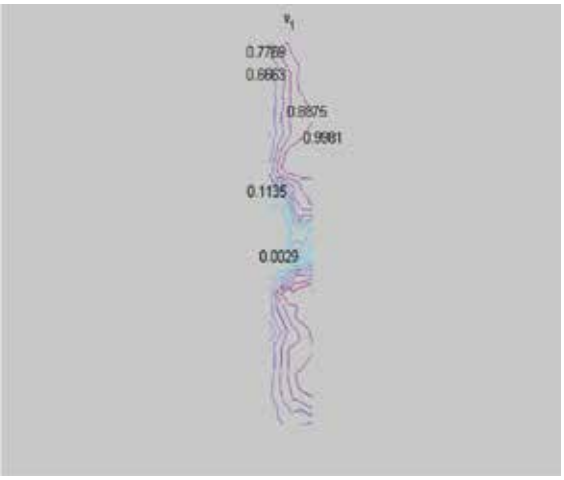

Figure 26. Normal stress coefficient (υ_1) [0.0029 0.1135 0.2241 0.3346 0.4452 0.5558 0.6663 0.7769 0.8875 0.9981].

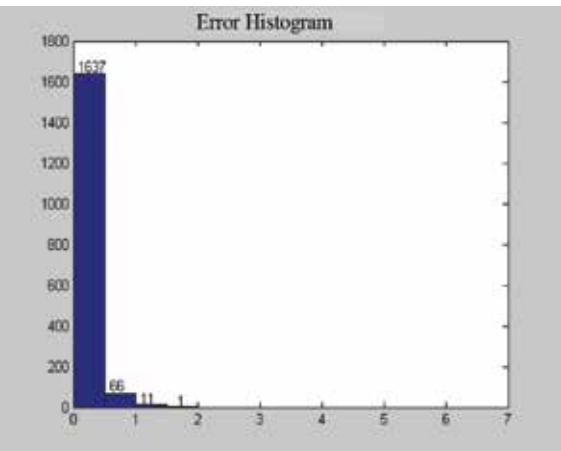

Figure 27. Equation numbers producing error are shown on the vertical axis.

3.4.3. Numerical solution

Obtained mesh configuration contains (linear and quadratic) 755 nodes in total (**Figure 14**). Totally, 1715 equations are used. Extrema contour levels are given in **Table 6**. Error computation, Standard deviation, Drag coefficient in **Table 7** and Histogram results about equation errors are given in **Table 8**. Minimum and maximum values of the minimized equation vector F, Euclidean and Infinite norms are shown in **Table 9**.

Stream function ψ, radial velocity vr, axial velocity vz, pressure p, normal stress τ_{rr}, axial stress τ_{zz}, axisymmetric stress $\tau_{\theta\theta}$, shear stress τ_{rz}, viscosity coefficient η, normal stress coefficient $v1$ contours and error histogram are given in **Figures 10–13** and in **Figures 15–27**.

4. Findings and discussion

In order to make a comparison and to compare the findings given in the literature in connection with settling of small particles for inelastic fluids with the behaviour of viscoelastic non-Newtonian fluids having variable material coefficient that show shear-thinning due to being mostly polymeric and viscoelastic nature of aforementioned materials; based on an example given by Rameshwaran et al. [9] for generalized Newtonian fluid, results of a typical example (CEF fluid) discussed in this study are compared visually with stream function, velocities, pressures and stresses with contour curves, and numerically with extrema tables. For both fluids the contour curves are shown in **Figure 8** and in **Figures 10–13** and in **Figures 15–27**, and the contour levels are shown numerically in **Table 3** and **6**. The contours are drawn for the ψ stream function, vr, vz velocities, p pressure, τ_{rr}, $\tau_{\theta\theta}$, τ_{zz}, and τ_{rz} stresses, η viscosity coefficient, $\upsilon 1$ normal stress coefficient (**Figures 10–13**, **15–27**). These contours and their extrema are compared with the generalized Newtonian fluid given in the literature [9].

As explained above, although the transition from system we used to a simpler example in the literature taking $\upsilon 1$ as equal to 0 is not completely possible, this comparison was very useful in general terms and allowed for new findings.

This comparison results can be explained as follows:

ψ stream function contours are completely similar for each two fluids. The extreme values match up with each other. vr radial velocity contours are also in complete harmony to each other. Although max values being 0.2171 and 0.2183 are approximately equal, there is small difference between minimums, −0.1933 and −0.1772. At vz contours, harmony is perfect, extreme values are respectively 0.00/0.00 and 1.1249/1.0215. Because $vz = 1$ must be at cylinder wall as a boundary condition, the value we found is more realistic. The courses of p contours are similar. The contour given in the literature is not very detailed, however our contour is completely detailed and also it gives a better idea as it is colorful. What attracts attention is that max and min values of each contour are at the same place at source and sink points of the sphere surface. Extreme values are −4.9296/−3.4962 and 7.8010/5.9995. The pressure drops for the fluids between sphere's front and back faces caused by sphere motion, which settles along the cylinder axis are $7.8 - 4.93 = 2.87$ and $5.9995 - 3.4962 \approx 2.50$, respectively. The small difference between the pressure drops can be explained by the elastic effect.

The viscosity coefficient (η) contours are harmonic. The contour given by us is colorful and detailed, and it continues throughout the cylinder. Shear-thinning in this contour obviously manifests itself. In the vicinity of the sphere where the shear-rate $\dot{\gamma}$ is very large, η coefficient becomes smaller and approaches to zero. Extreme values are respectively 0.244/0.0845 and 1.4672/1.0000. For both fluids Carreau equation and shear-thinning curve is used, and according to this extreme values given for the generalized Newtonian fluid seem to be exaggerated. The contour of the first normal stress coefficient $\upsilon 1$ properly illustrates the formula it was derived from and shows a course parallel to contour η. In conformity to the relaxation time curve $\frac{\upsilon_1}{\eta}$ given by Barnes et al. [8], this ratio approaches to 1 for small values of $\dot{\gamma}$ and goes

Stresses	τ_{rr}		$\tau_{\theta\theta}$		τ_{zz}		τ_{rz}	
Extreme values	**Min**	**Max**	**Min**	**Max**	**Min**	**Max**	**Min**	**Max**
Inelastic	−2.6545	3.1418	−1.4139	1.8356	−3.6693	2.8291	−1.3276	2.9703
Viscoelastic	−6.0019	3.3792	−6.0115	3.400	−6.1339	3.7165	−0.3701	0.8390

Table 10. Comparison of the normal and shear stresses.

to zero for large values. Extrema values are 0.0029/0.9981. Likewise ratio of the $\upsilon 1$ and η extreme values is 0.9981/1.0000 ≈ 1.0 for small $\dot{\gamma}$ and 0.0029/0.0845 ≈ 0.034 for large $\dot{\gamma}$.

The main differences are at the stresses. These support our expectations. The magnitudes of normal stresses $\tau_{rr}, \tau_{\theta\theta}, \tau_{zz}$ in absolute values are increased considerably. Thus, elastic effect appeared by inclusion of $\upsilon 1$ in our equations. In spite of this, the shear stress τ_{rz} in absolute value decreased.

So, the shear effect decreased relatively, while the extensional effect increased. The category of the flow slightly changed from shear flow toward extensional flow (**Table 10**).

5. Conclusions

Since the materials under consideration are rather polymeric and consequently viscoelastic, it is compulsory to include the elastic behaviour in the analysis by taking the effects of the normal stress into account in addition to those of the shear stresses and to use a constitutive equation appropriate to this. In this study, this point of view is tried to be ensured, and in order not to neglect the viscoelastic effect, a constitutive equation such as CEF, which includes normal stress coefficients, $\upsilon 1$, $\upsilon 2$, is used.

The results of the analysis, as expressed above in the findings and discussion section, confirms this idea. Comparison of the normal and shear stresses given in **Table 10** exposed an increase which reaches 3 times in absolute value in the normal stresses and in parallel a decrease which reaches 4 times in the shear stresses. This table reveals that elastic effect in polymeric fluids cannot be neglected. In this manner a fact has been emphasized, and an important point in fluid literature has been clarified.

Author details

Şule Celasun

Address all correspondence to: celasuns@itu.edu.tr

Department of Mechanics, Mechanical Engineering Faculty, Istanbul Technical University, Taksim, Istanbul, Turkey

References

[1] Celasun Ş, Öztürk Y. CEF model in the industrial application of non-Newtonian fluids. Proceedings of the Parallel CFD Conference, Kyoto, Japan. May 2002. 20-22

[2] Celasun Ş, Öztürk Y. An example to the numerical processing of nonisothermal flow of non-Newtonian fluids. Proceedings of the Parallel CFD Conference, Moscow, Russia. May 2003

[3] Celasun Ş. Flow of Newtonian and non-Newtonian fluids. European International Journal of Science and Technology. 2014;**3**:3

[4] Bird RB, Armstrong RC, Hassager O. Dynamics of Polymeric Liquids. Vol. 1, Fluid Mechanics. U.S.A: John Wiley; 1987

[5] Accurate solution of steady and rotational motion of Rivlin-Ericksen fluid in between two coaxial, porous, rotating cylinders [thesis]. Öztürk Yılmaz: I.T.U. Department of Mechanical Engineering, 1975

[6] Huilgol RR. Continuum Mechanics of Viscoelastic Liquids. New York: John Wiley & Sons Inc; 1975

[7] Tanner RI. Engineering Rheology. Oxford: Clarendon Press; 1988

[8] Barnes HA, Hutton JF, Walters K. An Introduction to Rheology. New York: Elsevier; 1989

[9] Rameshwaran P, Townsend P, Webster MF. Simulation of particle settling in rotating and non-rotating flows of non-Newtonian fluids. International Journal of Numerical Method Fluids. 1998;**26**, 851-874, Swansea, U.K.

[10] Bohlin T. On the drag on a rigid sphere moving in a viscous fluid inside a cylindrical tube. Transactions of Royal,Institute of Technology (Stockholm). 1960:155

[11] Dennis SC, Ingham R, Singh SN. The slow translation of a sphere in a rotating viscous fluid. Journal of Fluid Mechanics. 1982;**117**:251-267

[12] Haberman WL, Sayre RM. Motion of rigid and fluid spheres in stationary and moving liquids inside cylindrical tubes. Hydromechanics Laboratory, Research and Development Report, No.1143, Department of the Navy, David Taylor Model Basın, 1958

[13] Maxworthy T. An experimental determination of the slow motion of a sphere in a rotating viscous fluid. Journal of Fluid Mechanics. 1965;**23**:373-384

[14] Manogg GJ, Townsend P, Webster MF. Numerical simulation of multilayer injection moulding. Journal of Non-Newtonian Fluid Mechanics. 1997;**68**:153-167

[15] Yuan SW. Foundations of Fluid Mechanics. New Delhi: Prentice – Hall; 1969

[16] Oden JT, Carey GF. Finite Elements, Mathematical Aspects. Vol. Vol. IV. New Jersey: Prentice Hall; 1983

[17] Cowper GR. Gaussian Quadrature Formulas for Triangles. Ottowa: National Research Council of Canada; 2007

[18] Reddy JN, Gartling DK. The Finite Element Method in Heat Transfer and Fluid Dynamics (Second Edition). New York: CRC Press; 2001

[19] Zienkiewicz OC, Taylor RL. The Finite Element Method (Fourth Edition). Vol. 1. London: Mc Graw – Hill; 1994

[20] Celasun Ş. Three-dimensional lubrication theory in viscoelastic short-bearing. Industrial Lubrication and Tribology. 2013;**65**(6):pp.357-368. Emerald Group Publishing Limited

[21] Kaloni PN. Some remarks on useful theorems for the second order fluid. Journal of Non-Newtonian Fluid Mechanics. 1989;**31**:115-120

[22] Adolph T, Schönauer W, Koch R, Knoll G. High Performance Computing in Science and Engineering. Münich: Garching; 2009

Section 2

Polymers and Biopolymers Rheology

Chapter 5

Viscoelasticity of a Supramolecular Polymer Network and its Relevance for Enhanced Oil Recovery

Laura Romero-Zerón and Saran Banthong

Additional information is available at the end of the chapter

http://dx.doi.org/10.5772/intechopen.77277

Abstract

Supramolecular polymer networks are built up by combining multiple noncovalent interactions among macromolecules, resulting in the formation of materials with versatile functionality. This chapter describes an exploratory research focused on the formulation of a supramolecular polymer network based on reversible interactions among the main- and side chains of a mixture of xanthan gum, partly hydrolyzed polyacrylamide (HPAM), and a hydrophobically modified polyacrylamide (HMPAM) in brine solutions relevant for applications in enhanced oil recovery (EOR). The formation and characterization of the supramolecular network system was carried out through oscillatory rheology.

Keywords: supramolecular polymers, self-assembling, self-association, polymer flooding, heavy oil recovery, salt tolerance, mechanical stability, thermal stability

1. Introduction

Self-organization of molecular structures refers to the spontaneous assembly of individual building blocks into ordered and thermodynamically stable nanostructures by noncovalent interactions, resulting in the formation of dynamic and responsive materials. The noncovalent (reversible) interactions include electrostatic attractions, metal/ligand complexes, π/π-stacking, ionic interactions, hydrogen bonding, or hydrophobic effects without the application of external energy. Therefore, self-assembly is a low-cost and high-yield process [1–6] that can be activated by external stimuli, which involves changes in temperature, pH, ionic strength, radiation, the addition of other molecules, or their combination [2, 7–9].

Supramolecular polymer networks can be formed by polymer blends (PBs) in which the reversible and highly directional noncovalent interactions are randomly distributed across the polymer chains [6]. The resulting supramolecular structure displays polymeric properties in dilute and concentrated solutions that follow well-established theories of polymer physics [9]. These networks exhibit enhanced material properties compared to the individual polymers [1], and the reversibility of noncovalent interactions provides self-healing properties to these materials [6, 10].

This study focuses on the formulation and characterization of a supramolecular polymer network based on reversible interactions among the main- and side chains of a mixture of xanthan gum, HPAM, and HMPAM or associating polymer (AP) in brine. Xanthan gum and HPAM are the most commonly used polymers in the field for enhanced oil recovery (EOR) [11]. **Figure 1** displays the chemical structures of these polymers.

Xanthan gum is a high-molecular weight (≈2–3 × 10^6 g/mol) anionic polysaccharide derived from the fermentation of the bacterium *Xanthomonas campestris*. Its chemical structure contains a cellulose backbone consisting of five monosaccharides to form a pentasaccharide repeating unit. The cellulosic backbone is substituted at C-3 on alternate β-1,4-D-glucopyranosyl residues with charged trisaccharide side chains of β-D-rhamnopyranosyl β-1,4-D-glucuronopyranosyl, and α-1,2-D-mannopyranosyl. The two charged functional groups, COO^-, are found in the α-Manp and β-GlcAp residues (**Figure 1(a)**) [8, 11–25].

Xanthan gum is a stereoregular polymer and displays order–disorder transition in solution that depends on polymer concentration, ionic strength, and temperature [11–14, 17, 19, 24, 26]. A high polymer concentration and an increased ionic strength support ordered structures, while elevated temperatures favor disorder structures [11]; therefore, xanthan gum is a thermally responsive biopolymer [27]. At low temperatures, the native state of xanthan gum shows an ordered and rigid conformation as a single helical or a double-strand helix stabilized by inter- and intramolecular hydrogen bonds. The ordered conformation of the xanthan molecule is semi-flexible with a hydrodynamic length ranging from 600 to 2000 nm and a hydrodynamic diameter of 2 nm [20]. At elevated temperatures (≥60°C) [12, 16, 24] and low ionic strength, the native state, which displays an order state, transitions to a more flexible disordered-denatured state [13]. Optical rotation measurements have demonstrated that xanthan gum dissolved in distilled water at 25°C displayed the nonordered conformation [24]. However, a decrease in temperature (<40°C) [16, 24, 28] and the simultaneous increase in the ionic strength cause

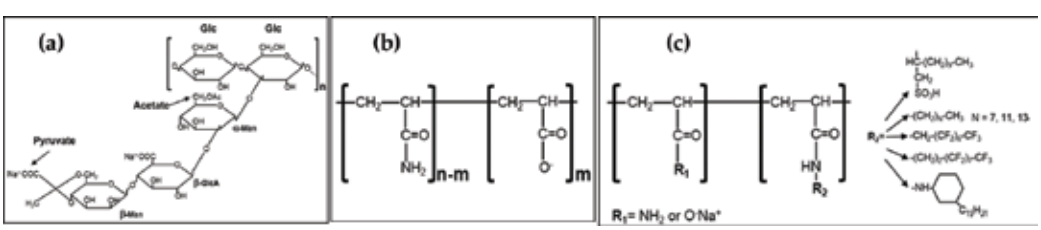

Figure 1. Generic chemical structures of (a) xanthan gum, (b) HPAM, and (c) associating polymers (**Figure 1(a)** was adapted from reference [12] and **Figure 1(b)** and **(c)** were adapted from reference [13]).

conformation reversal to a reordered-renatured state [11–19, 21–23, 27, 29, 30]. In saline solutions, monovalent or divalent cations (e.g., Na^+ and Ca^{2+}) condense on the ionized carboxyl moieties on the xanthan trisaccharide side chains, reducing repulsive forces between polymer chains. The side chains collapse down to the backbone causing conformation transition to a rigid rod-like shape of reduced hydrodynamic size stabilized by hydrogen bonding [23]. This conformation increases the intra- and intermolecular attraction and the xanthan chains tend to adopt a more rigid ordered conformation [13, 14]. The stability of xanthan gum is attributed to its ordered conformation which is stabilized by salts. Thus, the optimum functionality of xanthan gum requires the addition of salt [17].

Xanthan gum is prone to self-association at low concentrations and has been used as a building block to generate self-assembled structures [24, 25]. The onset of macromolecular self-organization has been reported at concentrations ≥0.1 wt% [8]. Parallel packing or side-by-side associations stabilized by hydrogen bonds facilitate the formation of three-dimensional networks [8, 19, 26]. Previous research has also demonstrated the self-organization of xanthan gum through polyelectrolyte complexation with other polysaccharides, such as chitosan-xanthan, β-lactoglobulin-xanthan, α-galactosidase-modified guar gum-xanthan, and sodium caseinate-xanthan, among many others [8, 26, 31]. Another example of self-aggregation through hydrophobic interactions is the intermolecular binding of xanthan gum-carob gum. These self-organizations take place in both the ordered and disordered conformations of the xanthan macromolecule depending on the ionic strength [8, 20, 32, 33].

Advantages of xanthan gum include non-toxicity, high water solubility, salinity tolerance, stability over a broad range of pH values, thermal stability against hydrolysis provided by its ordered conformation, high shear stability, high viscosities but a significant shear-thinning behavior on shearing at a low concentration, slight variations in viscosity with changes in temperature, availability, the ease of processing, and low manufacturing costs [11, 17, 18, 22, 26, 34, 35]. The main downside of xanthan gum is high sensitivity to microbial attack. Salt-tolerant aerobic and anaerobic microorganisms can degrade the xanthan gum chains leading to loss in solution viscosity. In practical applications, biocides are added to the xanthan gum solution to suppress the growth of degrading microorganisms [11, 17, 36].

Partially hydrolyzed polyacrylamides, HPAMs (**Figure 1(b)**), with degree of hydrolysis ranging from 25 to 35%, are the most used polymers for enhanced oil recovery (EOR) [35, 37]. HPAM is highly sensitive to mono- and divalent cation environments because of the shielding effect of the negative charges on the polymer backbone. Thus, the static repulsion between the HPAM lateral groups fades and the polymer structure collapses, which drastically reduces the viscosity of the polymer solution [35]. Divalent cations (e.g., Ca^{2+}) can also induce the self-aggregation of HPAM through polyion-cation complexation and depending on the concentration of Ca^{2+} inter- and intrachain complexation takes place [36]. The molecular conformation and viscosity of HPAM solutions are also affected by the degree of hydrolysis, pH, temperature, molecular weight, pressure, and solvent quality [35, 36]. HPAM is susceptible to mechanical degradation under high shear due to chain scission reducing the polymer chain size and molecular weight, which in turns reduces the viscosity of the polymer solution. Advantages of HPAM are low manufacturing costs and resistance to bacterial attack [36].

Hydrophobically modified polyacrylamides (HMPAMs) are water-soluble polymers containing both hydrophobic groups (e.g., methyl or ethyl acrylates, alkyl vinyl ethers, styrene comonomers, or alkyl acrylamides) and weakly charged pendant groups (e.g., carboxylic acid pendant groups) directly attached to the polymer backbone (**Figure 1(c)**). The hydrophobic groups can be distributed in a block-like fashion, randomly, or discretely distributed along the backbone. In aqueous solutions, these hydrophobic groups aggregate through intra- and intermolecular associations that increase the hydrodynamic volume of the polymer, which increases the viscosity of the polymer solution [36, 38]. The alkyl chain length and charge density determine the hydrophobicity of these polymers [39]. The presence of counter-ions in the aqueous media reduces the repulsion between charged groups within the polymer chain, which favors inter- and intrachain hydrophobic interactions [39, 40]. Benefits of HMPAM include salt tolerance and the enhancement in solution viscosity in the presence of low-molecular-weight electrolytes because of the shielding of intramolecular Coulombic attractions rather than the intermolecular hydrophobic interactions [36]. The inter- and intramolecular hydrophobic interactions are dynamic and reversible. Therefore, under high shear rate, these associations are interrupted and the viscosity of the solution decreases, but as soon as the high mechanical shear is removed, the hydrophobic groups re-associate and the viscosity of the solution returns to its original value [36].

The goal of this exploratory research was to formulate a supramolecular polymer network with enhanced properties (i.e., viscoelasticity, mechanical stability, salt tolerance, and thermal stability), taking advantage of the synergistic combination of the beneficial properties of the individual polymers in the blend. The formation and characterization of the supramolecular polymer network was demonstrated through frequency (time) and temperature-dependent oscillatory rheology [4, 5]; the use of other analytical techniques for structural characterization of the supramolecular system is beyond the scope of this work.

In this chapter, the formulation and characterization of the supramolecular self-assembled polymer network (SAP) is first described, and then the effect of ionic strength on the viscoelastic behavior of the SAP is discussed. The next section describes the structural strength of the SAP through dynamic mechanical analysis (DMA), followed by the evaluation of the SAP thermal stability by dynamic mechanical thermo-analysis (DMTA). In the following section, the long-term thermal stability of the SAP prepared in brines having different ionic strengths is discussed. Finally, the performance of the SAP in displacing heavy oil employing conventional sad-pack displacement tests at simulated oil reservoir conditions is presented.

2. Formulation of the self-assembled polymer network (SAP)

Several types of polymers commercially available were evaluated for the formulation of the SAP network with enhanced viscoelastic flow behavior. Xanthan gum (B), commercial food grade (Groupe Maison Cannelle Inc. (Richmond, QC, Canada)), a partly hydrolyzed polyacrylamide, HPAM, with a degree of hydrolysis ranging from 5 to 10 mol% and a molecular weight of approximately 5×10^6 daltons [41] (GelTech, Midland, TX, USA), and AP of low anionicity, low-molecular weight (8–12 million Dalton), and a high hydrophobic content [42–44] (SNF Floerger, Riceboro, GA, USA). Baseline polymers and polymer blends were initially prepared in brine solution of 2.1 wt% concentration (see **Table 1**). Polymer solutions

were mixed using a magnetic stirrer under strong mixing conditions to prevent the formation of lumps (e.g., fish eyes) at room temperature. The viscoelastic behavior, DMA, and DTMA of the baseline polymers and SAP were characterized through oscillatory rheology at 25°C using a Bohlin Geminin HR Nano Rheometer manufactured by Malvern (Worcestershire, UK) equipped with a parallel-plate measuring geometry (gap: 1000 μm) and a solvent trap to prevent drying effects during measurements. The amplitude sweep was performed in the strain range from 1 to 1000% at a fixed frequency of 1 rad/s, while the frequency sweep was run from 0.01 to 100 rad/s at fixed strain within the linear viscoelastic (LVE) range as determined from the preceding amplitude sweep.

Figure 2 displays the frequency sweeps as the curve functions of the loss factor (tanδ), storage modulus (G'), loss modulus (G''), and complex viscosity ($|\eta^*|$) for the baseline polymers B, HPAM, and AP at concentrations of 0.2, 0.2, and 0.1 wt%, respectively, prepared in 2.1 wt% brine.

The frequency sweeps (**Figure 2**) demonstrate that all polymers follow the characteristic shear-thinning flow behavior of polymers, thus viscosity decreases with increasing shear rate. At the same salinity (2.1 wt% brine), temperature, and angular frequency range, polymer B at 0.2 wt% solution concentration shows a significantly higher viscoelasticity than the HPAM at 0.2 wt% solution and the AP at 0.1 wt% solution. The behavior of polymer B (i.e., xanthan gum) results from its molecular-ordered aggregation behavior in saline solutions.

Regarding the loss factor (tanδ), which is useful to describe the viscoelastic behavior of materials in the low shear range ($\omega \leq 1\ s^{-1}$) [12, 45]; **Figure 2** shows that polymer B behaves different from the HPAM and AP polymer solutions. Polymer B exhibits a flow transition from a viscoelastic liquid behavior (tan$\delta > 1$) to a viscoelastic weak-gel behavior (tan$\delta < 1$) as angular frequency increases. At low angular frequencies (i.e., $\omega \leq 1$ rad/s), the polysaccharide molecules are entangled with neighboring macromolecules forming aggregates stabilized

Salts	Brine compositions (wt%)		
	2.1	**4.2**	**8.4**
NaCl	1.72	3.45	6.9
$MgCl_2$	0.04	0.09	0.18
$CaCl_2$	0.33	0.65	1.30
Na_2SO_4	0.01	0.02	0.04

Table 1. Brine compositions (wt%).

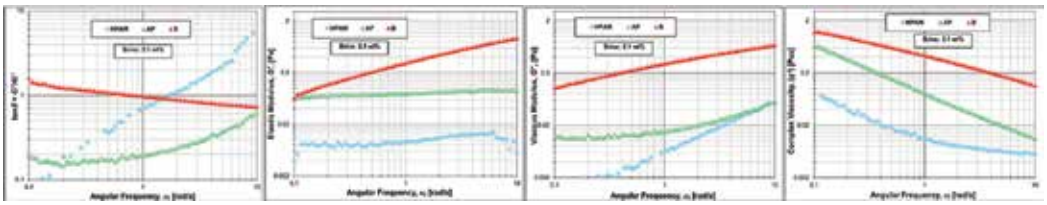

Figure 2. Frequency sweeps as curve functions of tanδ, G', G', and $|\eta^*|$for baseline polymers prepared in 2.1 wt% brine.

by hydrogen bonds and intermolecular associations through acetate residues [15] that resist flow and therefore viscous behavior dominates [13, 14, 17, 19, 45]. As the angular frequency increases, progressive disentanglement of the macromolecules takes place aligning the molecules in the direction of shear and shear gradient, which offer less resistance to flow, and the viscoelastic flow behavior of polymer B solution transitions to an elastic-dominated state [11, 12, 17, 20, 45, 46]. This flow behavior at rest and/or low shear is different from the typical flow behavior of common polymer solutions [15–17, 19, 29].

The polymer blends (PBs) and respective concentrations evaluated were as follows:

PB#**1**:**B**[0.2 wt%] ↔ HPAM [0.2 wt%]—— PB#**2** : **B** [0.2 wt%] ↔ AP [0.1 wt%]

PB#**3**:HPAM[0.2 wt%] ↔ AP [0.1 wt%]—— PB#**4**:**B**[0.2 wt%] ↔ HPAM[0.2 wt%] ↔ AP [0.1 wt%].

All polymer blend solutions were homogeneous as such phase separation was not observed. The dynamic rheological properties of PB #1, #2, and #4 (**Figure 3**) suggest polymer interactions with an enhanced viscoelasticity relative to the baseline polymers, except for PB # 3 (**HPAM** [0.2 wt%]↔**AP** [0.1 wt%]) that resulted in far inferior viscoelasticity (data not shown) and was rejected. Besides, it seems that polymer B directs the interactions among the main- and side chains of the blended polymers because PB # 1, # 2, and # 4 assume the rheological behavior of the baseline polymer B (see **Figures 2** and **3**).

Polymer blend # 4 -**B** [0.2 wt%]↔**HPAM** [0.2 wt%]↔**AP** [0.1 wt%] showed the highest elasticity and viscosity gain (**Figure 3**). At the angular frequency (ω) of 7.055 rad/s, the percentage increase in $\Delta G'$ was 43%, $\Delta G''$ was 41%, and $\Delta|\eta^*|$ was 42% relative to polymer B baseline. $\Delta G,'$ $\Delta G''$, and $\Delta|\eta^*|$increase by more than an order of magnitude relative to the baseline of the HPAM and AP polymers at the same ω = 7.055 rad/s. Furthermore, the low loss factor, tanδ < 1, with $G' > G''$ in the entire range of angular frequency; corresponds to a flow behavior that is characteristic of stable dispersions in the form of network-like structures built up through inter- and intramolecular interactions [3, 9, 45, 47–51]. Furthermore, the storage modulus, G', kept increasing at high angular frequencies, which "[verifies] the dynamic nature of the bonds within the network" [5]. This rheological behavior demonstrates that interchain self-association among the blended polymers forms a stronger polymer network of a larger hydrodynamic volume showing an enhanced solution viscosity. **Figure 3** also shows that PB # 1 displays the second larger gain in G', G'', and $|\eta^*|$relative to their individual polymer constituents.

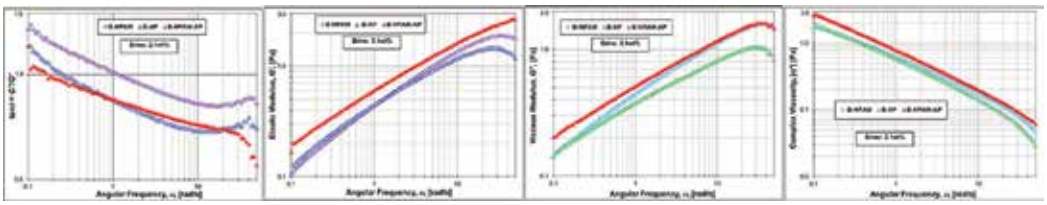

Figure 3. Frequency sweeps as curve functions of tanδ, G', G'', and $|\eta^*|$for the polymer blends prepared in 2.1 wt% brine.

Supramolecular systems can be formed via electrostatic interactions due to the high solubility of charged groups in water. Previous research has demonstrated that xanthan gum and HPAM form physical networks through ionic cross-linking using divalent cations (e.g., Ca^{2+}) [2, 26]. More examples of network systems built up through electrostatic interactions are reported in Ref. [6]. Specifically, Ca^{2+} is an efficient binder for carboxylic acids that induce aggregation in aqueous polymer solutions through the formation of polyion/cation complexes. In these systems, "the focal point is the carboxylate moiety [that is an] excellent ligand" [52].

In this work, the anionic polymers were mixed in brine containing 3300 ppm of $CaCl_2$ (see **Table 1**, brine 2.1 wt%). In this system, self-assembling is dominated by rapid cooperative electrostatic interactions in which the divalent cations, Ca^{2+}, bridge the negative charges (i.e., carboxylic groups) in the polymer macromolecules causing complexation of a mixture of anionic polymers. In this case, the divalent cations act as the physical crosslink among the anionic polymer chains [6, 8]. The interpolymer associations driven by electrostatic interactions decrease the intra- and interpolymer electrostatic repulsion promoting the intra- and intermolecular hydrophobic interactions (i.e., van der Waals interactions) among the hydrophobic segments of the macromolecules forming a stronger network structure [36]. Therefore, the screening of the charged groups by divalent cations reduces the steric hindrance among polymer chains and aids the interpolymer association via hydrogen bonding and hydrophobic interactions [53]. Hydrogen bonding among side chains (e.g., carboxylic acids and amide groups) of polymers B, HPAM, and AP takes place, as previously demonstrated between HPAM and xanthan gum side groups [35, 51]. In solution, supramolecular networks are commonly controlled by strong intra- and intermolecular hydrogen bonds. "The double hydrogen bonding of two or more amides can work in a cooperative manner to drive the formation of many ordered supramolecular architectures" [54].

Figure 4 displays the frequency sweep rheometry data that shows the effect of varying the concentration of polymer B in PB # 1 and # 4 from 0.1 to 0.3 wt%, while maintaining the concentrations of HPAM and AP fixed at 0.2 and 0.1 wt%, respectively.

Increasing the concentration of polymer B significantly increases the elasticity and viscosity of both blends. However, the largest gain in viscoelasticity is shown by PB # 4. The rheological data suggest that increasing the concentration of polymer B encourages more intra- and interpolymer chain associations through cation bridging, hydrophobic interactions, and hydrogen bonding, which enhances the structural strength and viscosity of the SAP without compromising its solubility in brine solution [36]. Furthermore, PB # 4 exhibits the lowest

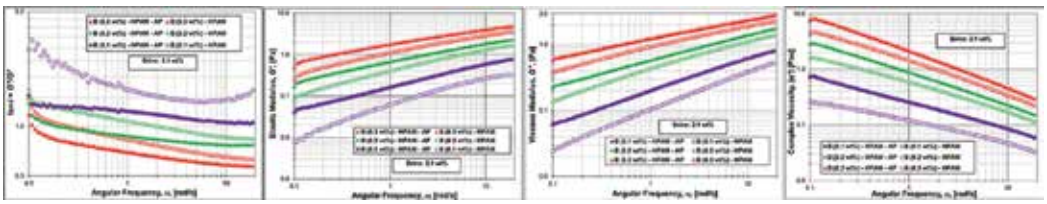

Figure 4. Frequency sweeps as curve functions of tanδ, G', G'', and $|\eta^*|$for PB # 1 and PB # 4 in 2.1 wt% brine using different concentrations of polymer B in the blends.

crossover point ($G' = G''$ and $\tan\delta < 1$ at $\omega = 0.1$ rad/s), which indicates the formation of a more stable supramolecular system [4]. For this reason, PB # 4 was selected as the optimum SAP formulation. Hereafter, PB # 4 is designated as SAP, while PB # 1 is designated as the baseline system for comparison purposes.

On the basis of the results obtained from oscillatory rheology in this exploratory research, a hypothetical structure of the optimum supramolecular polymer network is proposed in **Figure 5**, which shows the plausible reversible interactions taking place during self-aggregation of the SAP network.

Forthcoming research will characterize the structure of the optimum SAP system in depth, employing several analytical techniques (i.e., ^{1}H Nuclear Magnetic Resonance (^{1}H-NMR), Scanning Electron Microscopy (SEM), Fourier Transform Infrared Spectrometry (FTIR), and Size Exclusion Chromatography, among others) to test the proposed hypothetical SAP structure shown in **Figure 5**. In the succeeding section, a qualitative characterization of the polymers and SAP morphologies was conducted through optical microscopy. However, a more comprehensive characterization of these systems is required. This information will be provided in the upcoming work, which is beyond the scope of this chapter.

The morphology of the baseline polymers samples and the optimum SAP was observed using a polarized light optical microscope (Olympus model GX41), equipped with an M Plan N 10×/0.25 ∞/-FN22n objective (Olympus), digital camera, and image analysis software (Lumenera model Infinity 2-2C). **Figure 6(a)** and **(b)** display the micrographs of the baseline polymers and SAP dissolved in distilled water and in brine (8.4 wt%), respectively. In these micrographs, **Figures 1–4** correspond to polymers AP, B, HPAM, and SAP respectively.

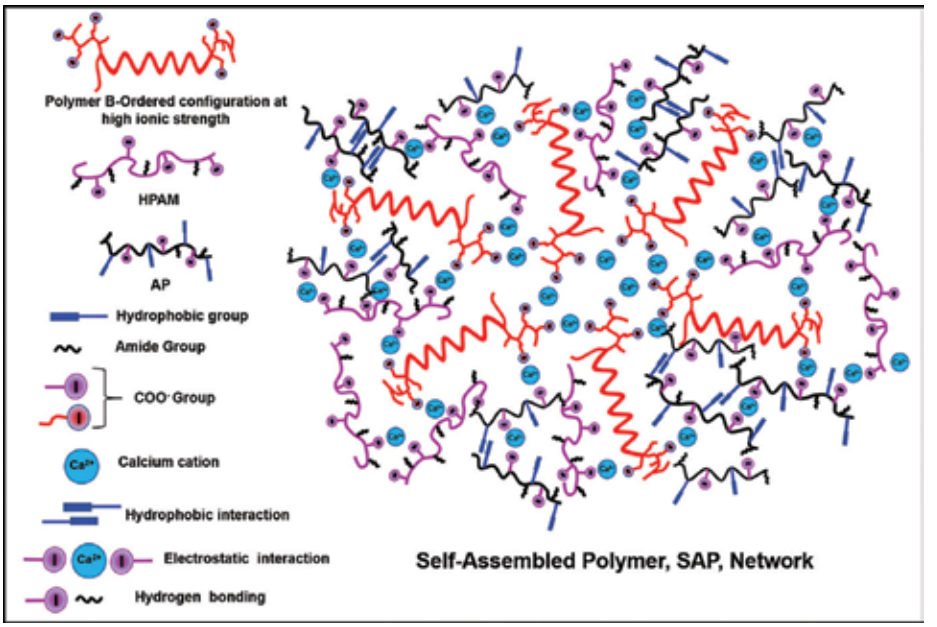

Figure 5. Proposed hypothetical structure of the SAP network.

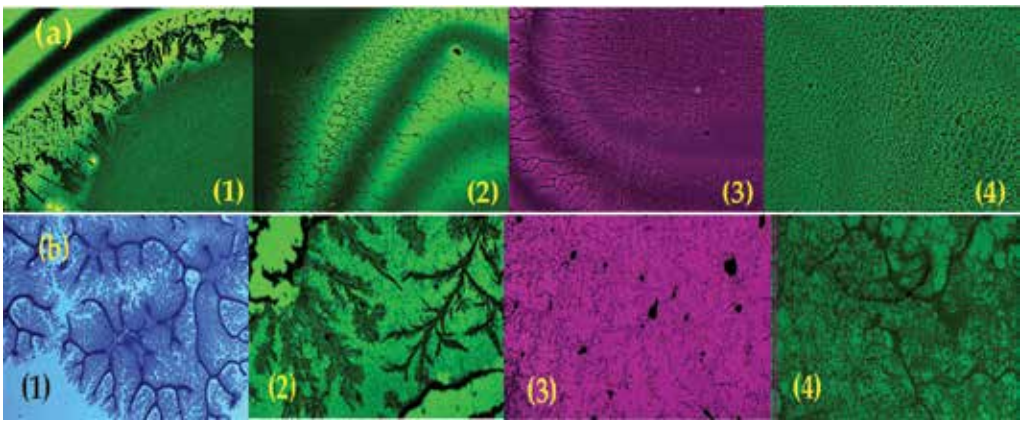

Figure 6. Polarized light micrographs of samples of baseline polymers and SAP system. (a) in distilled water and (b) in brine (8.4 wt%). Micrographs (1)–(4) correspond to polymers AP, B, HPAM, and the SAP system, respectively.

In the photomicrographs presented in **Figure 6(a)** is possible to qualitatively observe the morphology of the different polymer systems despite light interference [55]. The micrograph of the AP polymer in distilled water (**Figure 6(a1)**) reveals well-separated ramifications of aggregated macromolecules or clusters as previously reported for hydrophobically modified polyacrylamides [6, 40], while polymer B (**Figure 6(a2)**), HPAM (**Figure 6(a3)**), and the SAP (**Figure 6(a4)**) display extended macromolecular configurations. The polymer blend in **Figure 6(a4)** exhibits a more dense, well-aligned, and extended configuration of polymer structures. This macromolecular configuration results from the reciprocal charge repulsion among the anionic polymers stretching out the chains, which occupy a larger hydrodynamic volume because, minimum interchain interactions take place in distilled water [13, 26].

Figure 6(b1)–(b4) demonstrate that in brine solution, the screening of the negative charges in the polymer chains causes the increase of intra- and interchain interactions among the anionic polymers. For instance, dense intra- and interchain hydrophobic interactions are visible for the associating polymer, AP, in **Figure 6(b1)**, in the form of a dense network that was not observed in distilled water (**Figure 6(a1)**). Micrographs in **Figure 6(b2)** and **(b3)** display branch-like fractal structures for polymer B and HPAM, which agree with previous research [56]. The screening of the negative charges in the polymer side chains causes the coiling/folding of the polymer chains that decreases the hydrodynamic volume of the macromolecules and the viscosity of the polymer solutions [13, 26]. By contrast, **Figure 6(b4)** exposes a network of fully entangled macromolecules. This high-density thread-like net reveals a homogeneous web of intra- and interchain interactions among the anionic polymers.

3. Effect of ionic strength on the viscoelasticity of the SAP system

Three brine concentrations 2.1, 4.2, and 8.4 wt% (see **Table 1**) were employed to establish the effect of ionic strength on the viscoelasticity of the SAP system. **Figure 7** presents the frequency sweep of the SAP and baseline solutions in different brine concentrations in terms of the curve functions of tanδ, G', G'', and $|\eta^*|$.

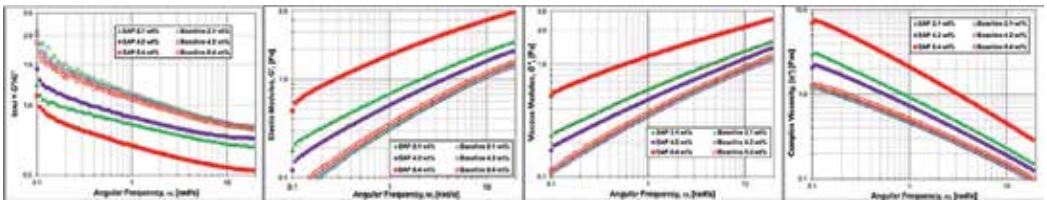

Figure 7. Curves of tanδ, G', G'', and $|\eta^*|$ versus ω and brine concentration.

Figure 7 demonstrates the significant effect of ionic strength on the SAP system. At the highest ionic strength (i.e., brine 8.4 wt%), the SAP system displays the highest elasticity and viscosity. The curves in **Figure 7** show G' values that are markedly larger than G'' at all frequencies. A tanδ < 1 in the entire range of angular frequency is consistent with a gel (physical network)-like behavior [45]. **Figure 7** also reveals a negligible effect of ionic strength on the viscoelasticity of the baseline or PB # 1, which consists of a mixture of 0.2 wt% polymer **B and at 0.2 wt% of HPAM.**

These rheological data indicate that the higher the ionic strength the higher the suppression of the electrostatic repulsion among polymer chains through cation bridging (i.e., Ca^{2+}), which results in more and stronger intra- and specially interpolymer complexations and associations that reinforce the polymer network and enhances the viscosity of the solution [36]. Previous research has also demonstrated that the addition of inorganic salts to interpolymer mixtures (e.g., anionic and nonionic polymers) in aqueous solutions deteriorates the thermodynamic quality of the solvent (e.g., water) with respect to the polymers, which promotes the strengthening of the interchain complexation through hydrophobic interactions and hydrogen bonding [57].

The main difference between the SAP system and the baseline shown in **Figure 7** is that the SAP system contains 0.1 wt% of AP polymer (i.e., hydrophobically modified polymer); therefore, the addition of inorganic salts shelters the charged groups in the associating polymer side chains and uncovers the hydrophobic moieties, making these associating groups more accessible for intra- and interpolymer hydrophobic interactions [31, 36]. These observations agree with previous work [51].

These experimental findings indicate that the viscoelastic functionality of the SAP formulation is improved as the ionic strength in the aqueous solution increases. This performance makes the SAP system suitable for EOR applications involving brines containing high salinity and hardness concentrations.

4. Dynamic mechanical analysis (DMA)

The structural strength of a material is usually determined through the reestablishment of the storage modulus, G', of the disrupted network after the shear deformation driven by high shear rates has been lifted [5, 45]. In this study, the structural strength of the SAP system was established through thixotropic behavior analysis by applying an oscillatory rheological test consisting of three steps, each one at constant dynamic mechanical conditions, as recommended in Ref. [45]. The first or *reference* step is carried out at low-shear conditions

(strain = 20%, ω = 6.283 rad/s, time ≈ 960 s) within the LVE range. The G'-value at the end of the first step is taken as the reference value of G'-at-rest to be compared to the G'-value occurring at the end of the third step [45]. The second or *high shear* step is conducted at high shear conditions (strain = 1000%, ω = 6.283 rad/s, time ≈ 480 s) outside the LVE range with the purpose of breaking the internal structure of the sample. The third or *regeneration* step is performed at the same shear conditions (strain = 20%, ω = 6.283 rad/s, time ≈ 960 s) of the first step within the LVE range to facilitate the regeneration of the sample's structure. The percentage of structural regeneration is calculated by taking the G'-value at the end of the third step in relation to the reference value of G'-at-rest of the first step [45].

Figure 8 displays the curves of G' and G'' as a function of time [s], brine concentration (2.1 and 8.4 wt%), and polymer systems for the *reference* step (step 1) and for the *regeneration* step (step 3).

Figure 8 shows that at low salinity (i.e., brine 2.1 wt%), the baseline displays a complete structural regeneration (i.e., thixotropic behavior), while the SAP system exhibits a 5% increase in the structural strength relative to the reference value of G' obtained from step 1. The G'-values (empty square symbols) gathered during the regeneration step are consistently higher than the G'-values (solid square symbols) obtained during the reference step. Furthermore, **Figure 8** indicates that the structural regeneration of both systems takes place immediately after the high shear step ends. The corresponding G''-curves for both systems show a similar behavior. The mechanical response for both systems is dominated by G' ($\tan\delta < 1$) during the entire testing period, thus displaying a network-like character. The upsurge in the structural strength exhibited by the SAP network is due to the increase in the number and strength of noncovalent interchain associations that reconnect the polymer chains in the network very quickly, causing the rapid regain and enhancement of the mechanical structural strength and solution viscosity [3, 5, 36, 45].

At high brine concentration (i.e., 8.4 wt%), the baseline does not show complete structural regeneration (**Figure 8**). The G'-values obtained in step 3 are below the G'-values obtained in step 1 during the entire testing period. The decrease in the structural strength might be related to the weakening of the interchain noncovalent interactions for this system. On the contrary, the SAP system demonstrates full recovery after extension under load. The G'-values in step 3 show an immediate 100% structural strength regeneration. Again, for the SAP system, $G' > G''$ showing network-like properties during the total testing period.

These results verify the reversibility of the interpolymer interactions of the SAP system involving the instant recovery of the noncovalent associations following shear thinning [58]. This demonstrates the self-healing advantage of supramolecular polymer networks due to the reversibility of the physical associations and high-chain mobility in water [3, 6, 58].

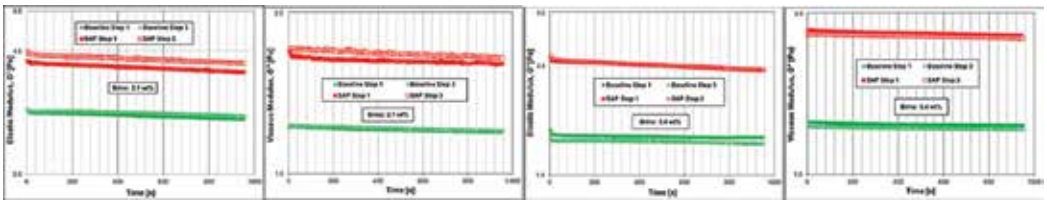

Figure 8. Thixotropic analysis: G' and G'' as a function of time.

5. Dynamic mechanical thermo-analysis (DMTA)

Dynamic mechanical thermo-analysis was conducted by performing upwards temperature ramps from 282.5 (9°C) to 353.5 K (80°C) at a linear heating rate of 9 K/min and downwards temperature ramps from 353.5 (80°C) to 282.5 K (9°C) at a linear cooling rate of 7 K/min at a constant frequency (1 Hz) and % strain (20%) within the LVE range. **Figure 9** displays the oscillatory upward and downward temperature sweeps showing the G'- and G''-curves of the baseline and SAP network at low- and high salinity.

The upward heating curves (**Figure 9**) show that for both systems (i.e., baseline and SAP network), the G'- and G''-values decrease as the temperature increases with the G'-values showing steeper curves. Similarly, the downward cooling curves show the reverse process; however, the G'- and G''-curves show hysteresis upon cooling. As temperature increases during the heating process, the motion and friction between the polymer chains increase, producing frictional heat. A fraction of this frictional heat may heat up the sample and another part may be lost to the surrounding environment; therefore, these materials exhibit irreversible deformation behavior [45] due to heat transfer. **Figure 9** also shows that hysteresis is less pronounced for both systems at higher salinities, which suggests the formation of supramolecular networks that are more rigid, stronger, and more stable at elevated temperatures.

Figure 10 shows that the baseline system reaches the gel transition temperature (T_{gel}) at approximately 334 K (60.5°C) for both brine salinities: 2.1 and 8.4 wt%. As temperature increases, the interchain interactions undergo faster rates of dissociation-association up to the vicinity of the gel transition temperature at which the rate of dissociation is much higher than the rate of association. At $T_{gel,}$ disruption of the network takes place and the system transitions from a gel-like flow behavior to a fluid-like flow behavior [9, 58]. Likewise, during the cooling process as temperature decreases, the rate of interchain dissociation-association decreases and chain interactions get progressively stronger and the material becomes more elastic until $G' = G''$ at the crossover point, the flow gel-like behavior is regained and $G' > G''$ at lower temperatures [45].

The SAP system displays a different behavior as shown in **Figure 10**. In both brine salinities (2.1 and 8.4 wt%), the heating curves do not reach the gel transition temperatures. At low salinity, the cooling curve just reaches the crossover point ($G' = G''$ and $\tan\delta = 1$) at the highest testing temperature and then rapidly transitions to a viscoelastic gel behavior upon cooling. The SAP cooling curve at a high salinity never reaches the transition temperature ($G' = G''$). These observations suggest that the SAP network exhibits more rigid and stronger polymer

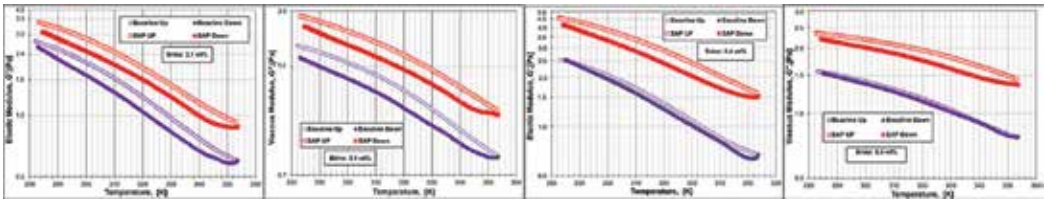

Figure 9. Temperature-dependent functions of G' and G'' of baseline and SAP network.

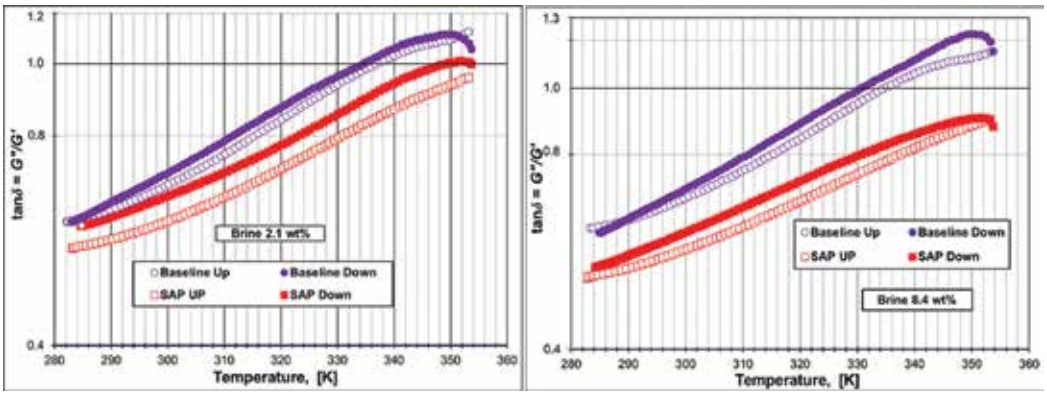

Figure 10. Temperature-dependent function of tanδ of the baseline and SAP system.

chain interactions, which are capable of maintaining the stability of the supramolecular polymer network and the behavior of a viscoelastic gel ($G' > G''$) in the range of temperature evaluated. Therefore, the interchain associations are stable and network disruption was not observed in the temperature range from 282.5 (9°C) to 353.5 K (80°C) [45, 58].

6. Extended thermal stability

The extended thermal stability evaluation was performed at 90°C for a period of 8 weeks. **Figure 11** displays the G′- and G″-curves versus angular frequency and time of the baseline and SAP system at low- and high-salinity brines.

The G'- and G''-curves (**Figure 11**) indicate that after the second week (Week # 2) of testing, the elasticity and viscosity of the baseline and the SAP network are significantly affected. At low-salinity brine (2.1 wt%), the baseline displays a more stable performance than the SAP network during the testing period; however, this behavior is reversed at high-salinity brine concentration (8.4 wt%), in which the SAP system is noticeably more stable, particularly at week # 8, than the baseline system. Furthermore, the direct observation of the samples reveals the onset of fine solid precipitation from week # 2 for both systems and brine concentrations. Some of the samples became turbid with testing time.

The thermal deterioration of the viscoelasticity of both systems as a function of time could be attributed in part to the autohydrolysis of the amide moieties (i.e., acrylamide groups) and hydrophobic functional groups forming additional acrylate moieties at elevated temperatures (i.e., >85°C). These acrylate structures rapidly associate with divalent cations (i.e., Ca^{2+}) causing the precipitation of polymer from the bulk of the solution, which becomes turbid. More detailed information on autohydrolysis of polymers at elevated temperature and ionic strength is provided elsewhere [43, 59]. Thermal degradation of the polymer samples can also be attributed to the induced breaking of the acrylic backbone trigger via free-radical reactions, which reduces the molecular weight of the polymer chains [59].

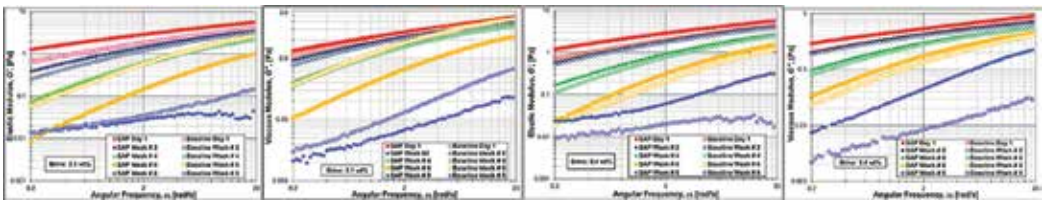

Figure 11. *G′*- and *G″*-curves as a function of angular frequency and time.

Although this extended thermal stability evaluation demonstrates the significant effect of temperature and time on the viscoelastic **flow** behavior of both systems, these results further confirm that the functionality of the SAP system is increased at higher ionic strengths due to the formation of stronger intra- and interpolymer associations that enhances its stability at 90°C.

7. Heavy oil recovery

The performance of the baseline and the SAP system as mobility control agents in displacing and mobilizing heavy oil was carried out through conventional sand-pack displacement tests. The heavy oil that was provided by Husky Energy Inc. (Calgary, AB, Canada) had an initial viscosity of 68,728 cP at 25°C that was adjusted to 3000 cP at 25°C by dilution with natural condensate (density: 0.9 g/ml) provided by Corridor Resources Inc. (McCully field, Sussex, NB, Canada). A Temco DCHH-series core holder (Temco Inc., Tulsa, OK, USA) was employed to perform the displacement tests. The core holder's rubber sleeve was packed with sand (QUIKRETE® Premium Play Sand®, No. 1113, 100% quartz) of effective size: D10 = 180 μm and a uniformity coefficient: D60/D10 = 2.44 determined by sieve analysis (ASTM C136/C136M-14) [60] employing woven wire brass sieves (Endecotts Limited, London, UK). The packed sleeve was sealed using the floating distribution plug and inserted into the core holder body. An overburden pressure of 500 psi was applied by filling the annulus between the outer diameter of the sleeve and the inner diameter of the core holder body with distilled water. CFR-series transfer vessels (Temco Inc., Tulsa, OK, USA) were used to store heavy oil, brine, and polymer that were pumped to the sand pack by a Teledyne ISCO Syringe pump, model 100DX (Teledyne Isco Inc., Lincoln, NE, USA). Pressure gauges (Omega, Laval, QC, Canada) with an accuracy of 0.5% (FS) were installed in different sections of the sand-pack displacement setup (**Figure 12**).

Four displacement tests were carried out at 25°C. Two displacement tests evaluated the performance of the baseline system and the other two tests the performance of the SAP network. The unconsolidated porous media were characterized by determining the pore volume (PV), porosity (φ), and permeability (k) following standard procedures described in Ref. [61]; at this stage, the sand packs were 100% saturated with brine (8.4 wt%). **Table 2** summarizes the properties of each of the sand packs employed during the flooding tests.

The fluid injection sequence was carried out in four steps as follows. The first step was the injection of heavy oil into the brine-saturated porous media until no more brine was produced from the sand pack that corresponded to approximately two pore volumes (2PV), followed by

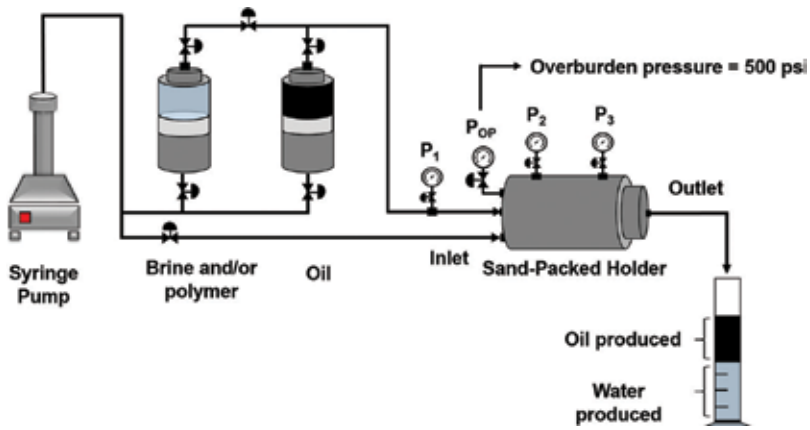

Figure 12. Experimental setup sand-pack displacement test.

Flooding test #	Pore volume, PV (cm^3)	Porosity, ϕ (%)	Permeability, k (mD)
Baseline # 1	208	29	10,049
Baseline # 2	206	29	8667
SAP # 1	204	29	8109
SAP # 2	187	26	4700

Table 2. Sand-pack properties.

the second step of brine (8.4 wt%) injection to displace heavy oil (i.e., water flooding) until the production of oil stopped, which corresponded on average to the injection of 6 PVs of brine. The third step consisted of the injection of 1 PV of baseline and/or the SAP system as EOR mobility control agents to further displace and recover oil. The fourth and final step was the post-polymer brine (8.4 wt%) injection as a chaser to displace the baseline polymer and/or the SAP system through the sand pack. On average, 6PV of post-polymer brine was injected. The average injection flow rate was 0.76 ml/min that corresponds to a linear velocity of 0.77 ft./day. During each injection step, the volume of fluid injected, the volume of fluid produced, injection time, and pressures at the inlet, at the sand-pack pressure ports, and outlet of the sand-pack holder were recorded. Material balance of each injection step was carried out to determine the sand-pack fluid saturation and oil recovery. More details on the experimental procedure employed during these routine sand-pack displacement tests are provided in Ref. [62].

The performance of the baseline and the SAP network as mobility control agents in porous media was analyzed by plotting the effective viscosity or resistance factor (RF) [63–68] of the polymer system during flow through porous media as a function of the volume of fluid injected expressed as a fraction of pore volume (PV), which was normalized for porosity and permeability to compare the displacement tests on the same reference. The capillary bundle parameter model was applied for data normalization [66, 69–71].

Polymer retention in porous media after the post-polymer brine injection was determined by the residual resistance factor, RRF [59, 62–65, 67, 68, 70–74]. RF and RRF are significant parameters because they provide reliable information on the propagation and effectiveness of polymeric systems as mobility control agents through porous media. **Figure 13** displays the average RF and RRF as a function of the volume of fluid injected normalized for porosity and permeability of the baseline and the SAP system sand-pack displacement tests.

The RF curves reveal that the SAP system offers a higher end value of effective viscosity, RF (61%), during flow in porous media relative to the baseline. The SAP RF curve also shows a tendency to level off as a function of the volume of fluid injected, which indicates an appropriate propagation of the SAP network through the unconsolidated porous media. Therefore, the SAP network displays a better performance as mobility control agent compared with the baseline system.

The RRF curves indicate a larger retention of the SAP system along the sand pack with an end RRF value that stabilizes at around 2.8, while the end RRF value induced by the baseline levels off at approximately 1.3. Therefore, the permeability of the unconsolidated sand packs was further reduced by the SAP system, which aids the displacement and mobilization of heavy oil by further reducing the relative permeability to water [70, 75].

Figure 14 shows cumulative oil recovery as the percentage of the original oil in place (OOIP) recovered, the ratio of the remaining oil saturation to the initial oil saturation (S_{or}/S_{oi}), and the water to oil ratio (WOR) as a function of the volume of fluid injected for the water-flooding stage, polymer-flooding stage, and post-polymer water-flooding stage. Water flooding as a secondary oil recovery process on average recovers between 20 and 30% of the original oil in place [76, 77], which agree with our results.

Polymer-flooding and the post-polymer water-flooding steps rendered an overall percentage of cumulative oil recovery of 41% for the baseline system and 51% for the SAP network. Therefore, the SAP system rendered a 10% higher incremental oil recovery relative to the baseline. In field applications of polymer flooding, an incremental oil recovery of 5% is considered successful [44].

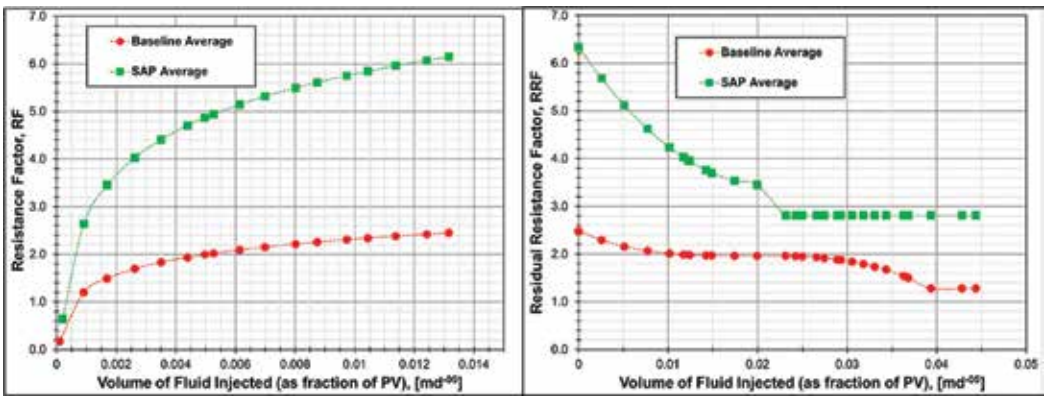

Figure 13. RF and RRF versus volume of fluid injected.

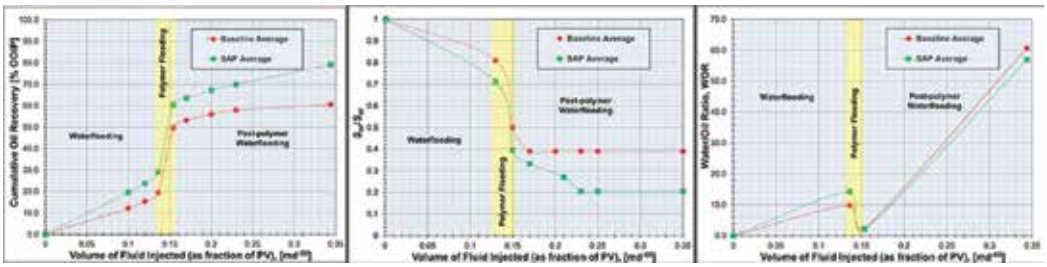

Figure 14. Cumulative oil recovery, S_{or}/S_{oi}, and WOR versus volume of fluid injected.

The superior performance of the SAP network in displacing heavy oil is attributed to an enhanced effective viscosity during flow in porous media, which generates a more stable displacement front that increases the volumetric sweep efficiency accelerating the production of oil. Besides, both systems—the baseline and the SAP network—show to be very efficient in controlling WOR during the polymer-flooding stage. However, as soon as the post-polymer water flooding is initiated, the water to oil ratio, WOR, increases very rapidly, due to the uncontrollable channeling of brine toward the production end caused by viscous fingering [63].

8. Conclusions

A stable supramolecular system was formulated based on the self-assembling of xanthan gum, HPAM, and HMPAM driven by electrostatic interactions through divalent cation (i.e., Ca^{2+}) bridges, which reduce the steric hindrance among anionic polymer chains promoting strong and stable intra- and interpolymer associations via hydrophobic interactions and hydrogen bonding. The viscoelastic functionality of the SAP system is enhanced in high ionic strength aqueous solutions. This performance makes the SAP system suitable for EOR applications involving brines containing high salinity and hardness concentrations.

The SAP system shows a high structural strength, mechanical stability, and self-healing capabilities. The supramolecular polymer network exhibits instant recovery of the interpolymer noncovalent interactions and even the increase in structural strength following the lifting of high-shear conditions (i.e., severe shear thinning).

In the temperature range from 282.5 (9°C) to 353.5 K (80°C), the SAP network exhibits thermal stability. In this temperature range, the strong and stable intra- and interchain interactions maintain the integrity of the supramolecular polymer and its flow viscoelastic behavior. Likewise, the SAP system demonstrated an enhanced thermal stability after 8 weeks at 90°C in high-salinity brine (8.4 wt%) compared with the thermal performance of the baseline. This further confirms that the functionality of the SAP system is upgraded at higher ionic strengths due to the formation of stronger intra- and interpolymer associations.

The SAP system rendered a 10% higher incremental oil recovery relative to the baseline system. The superior performance of the SAP network in displacing heavy oil is attributed to better mobility control properties, to the generation of a stable displacement front, the

efficient and rapid control of the WOR, and an improved volumetric sweep efficiency that accelerates the production of oil. Overall, the SAP system is a straightforward formulation that offers several advantages relevant to EOR such as enhanced viscoelastic flow behavior, increased functionality in high ionic strength environments, stability to mechanical shear, and an improved thermal stability.

Acknowledgements

The authors would like to extend their appreciation to Dr. Chutima Kongvarhodom, Department of Chemical Engineering, Faculty of Engineering, King Mongkut's University of Technology Thonburi (KMUTT), Thoongkru, Bangkok, Thailand, for leading the academic exchange program between KMUTT and the University of New Brunswick (UNB). Likewise, the authors gratefully acknowledge GelTech, SNF Floerger, Husky Energy, and Corridor Resources Inc. for providing samples of polymers, heavy oil, and condensate. The authors would like to acknowledge financial support from the UNB through the Sabbatical Research Grant and the Canada Foundation for Innovation, CFI, research grant.

Author details

Laura Romero-Zerón[1]* and Saran Banthong[2]

*Address all correspondence to: laurarz@unb.ca

1 Chemical Engineering Department, Faculty of Engineering, University of New Brunswick, Fredericton, New Brunswick, Canada

2 Chemical Engineering Department, Faculty of Engineering, King Mongkut's University of Technology Thonburi, Bangkok, Thailand

References

[1] Zhang C. Flow enabled self assembly of polymers [Doctoral dissertation]. Georgia Institute of Technology: Atlanta; 2016

[2] Lowe AB, McCormick CL. Stimuli responsive water-soluble and amphiphilic (co)polymers. In: McCormick CL, editor. Stimuli–Responsive Water Soluble and Amphiphilic Polymers. Washington: American Chemical Society; 2001. pp. 1-13. DOI: 10.1021/bk-2001-0780

[3] Aida T, Meijer EW, Stupp SI. Functional supramolecular polymers. Science. 2012; **335**:813-817

[4] Chen S, Döhler D, Binder WH. Rheology of hydrogen-bonded dendritic supramolecular polymer networks in the melt state. Polymer. 2016;**107**:466-473

[5] Yan T, Schröter K, Herbst F, Binder WH, Thurn-Albrecht T. Unveiling the molecular mechanism of self-healing in a telechelic, supramolecular polymer network. Scientific Reports. 2016;**6**:32356

[6] Voorhaar L, Hoogenboom R. Supramolecular polymer networks: Hydrogels and bulk materials. Chemical Society Reviews. 2016;**45**(14):4013-4031

[7] Mendes AC, Baran ET, Reis RL, Azevedo HS. Fabrication of phospholipid–xanthan microcapsules by combining microfluidics with self-assembly. Acta Biomaterialia. 2013;**9**(5): 6675-6685

[8] Shchipunov Y, Sarin S, Kim I, Ha CS. Hydrogels formed through regulated self-organization of gradually charging chitosan in solution of xanthan. Green Chemistry. 2010; **12**(7):1187-1195

[9] Brunsveld L, Folmer BJ, Meijer EW, Sijbesma RP. Supramolecular polymers. Chemical Reviews. 2001;**101**(12):4071-4098

[10] Gyarmati B, Pukánszky B. Natural polymers and bio-inspired macromolecular materials. European Polymer Journal. 2017;**93**:612-617

[11] Xu L, Xu G, Liu T, Chen Y, Gong H. The comparison of rheological properties of aqueous welan gum and xanthan gum solutions. Carbohydrate Polymers. 2013;**92**(01):516-522

[12] Cunha RL, Maialle KG, Menegalli FC. Evaluation of the drying process in spouted bed and spout fluidized bed of xanthan gum: Focus on product quality. Powder Technology. 2000;**7**(03):234-242

[13] Baumgartner S, Pavli M, Kristl J. Effect of calcium ions on the gelling and drug release characteristics of xanthan matrix tablets. European Journal of Pharmaceutics and Biopharmaceutics. 2008;**69**(02):698-707

[14] Sereno NM, Hill SE, Mitchell JR. Impact of the extrusion process on xanthan gum behaviour. Carbohydrate Research. 2007;**342**(10):1333-1342

[15] Song KW, Kim YS, Chang GS. Rheology of concentrated xanthan gum solutions: Steady shear flow behavior. Fibers and Polymers. 2006;**7**(02):129-138

[16] Garcıa-Ochoa F, Santos VE, Casas JA, Gomez E. Xanthan gum: Production, recovery, and properties. Biotechnology Advances. 2000;**18**(7):549-579

[17] Katzbauer B. Properties and applications of xanthan gum. Polymer Degradation and Stability. 1998;**59**(1-3):81-84

[18] Casas JA, Santos VE, Garcıa-Ochoa F. Xanthan gum production under several operational conditions: Molecular structure and rheological properties. Enzyme and Microbial Technology. 2000;**26**(2-4):282-291

[19] Cuvelier G, Launay B. Concentration regimes in xanthan gum solutions deduced from flow and viscoelastic properties. Carbohydrate Polymers. 1986;**6**(5):321-333

[20] Rodd AB, Dunstan DE, Boger DV. Characterisation of xanthan gum solutions using dynamic light scattering and rheology. Carbohydrate Polymers. 2000;**42**(02):159-174

[21] Holzwarth G. Molecular weight of xanthan polysaccharide. Carbohydrate Research. 1978; **66**(01):173-186

[22] Boyd MJ, Hampson FC, Jolliffe IG, Dettmar PW, Mitchell JR, Melia CD. Strand-like phase separation in mixtures of xanthan gum with anionic polyelectrolytes. Food Hydrocolloids. 2009;**23**(08):2458-2467

[23] Viebke C. Order-disorder conformational transition of xanthan gum. In: Dumitriu S, editor. Polysaccharides: Structural Diversity and Functional Versatility. 2nd ed. New York: CRC press; 2004. 1189 p

[24] Mendes AC, Strohmenger T, Goycoolea F, Chronakis IS. Electrostatic self-assembly of polysaccharides into nanofibers. Colloids and Surfaces, A: Physicochemical and Engineering Aspects. 2017;**531**:182-188

[25] Merino-González A, Kozina A. Influence of aggregation on characterization of dilute xanthan solutions. International Journal of Biological Macromolecules. 2017;**105**:834-842

[26] Kumar A, Rao KM, Han SS. Application of xanthan gum as polysaccharide in tissue engineering: A review. Carbohydrate Polymers. 2018;**180**:128-144

[27] Pastuszka MK, MacKay JA. Engineering structure and function using thermoresponsive biopolymers. Nanomedicine and Nanobiotechnology. 2016;**8**(01):123-138

[28] Kim J, Hwang J, Kang H, Choi J. Chlorhexidine-loaded xanthan gum-based biopolymers for targeted, sustained release of antiseptic agent. Journal of Industrial and Engineering Chemistry. 2015;**32**:44-48

[29] Milas M, Rinaudo M, Knipper M, Schuppiser JL. Flow and viscoelastic properties of xanthan gum solutions. Macromolecules. 1990;**23**(09):2506-2511

[30] Camesano TA, Wilkinson KJ. Single molecule study of xanthan conformation using atomic force microscopy. Biomacromolecules. 2001;**2**(04):1184-1191

[31] Hidalgo ME, Armendariz M, Wagner JR, Risso PH. Effect of xanthan gum on the rheological behavior and microstructure of sodium caseinate acid gels. Gels. 2016;**2**(03):23

[32] Williams PA, Day DH, Langdon MJ, Phillips GO, Nishinari K. Synergistic interaction of xanthan gum with glucomannans and galactomannans. Food Hydrocolloids. 1991;**4**(06):489-493

[33] Cairns P, Miles MJ, Morris V. Intermolecular binding of xanthan gum and carob gum. Nature. 1986;**322**:89

[34] Becker A, Katzen F, Pühler A, Ielpi L. Xanthan gum biosynthesis and application: A biochemical/genetic perspective. Applied Microbiology and Biotechnology. 1998;**50**(02): 145-152

[35] Cai S, He X, Liu K, Rodrigues AM, Zhang R. Macromolecular interactions and synergy in xanthan/HPAM aqueous solutions. RSC Advances. 2017;**7**(66):41630-41639

[36] Wever DA, Picchioni F, Broekhuis AA. Polymers for enhanced oil recovery: A paradigm for structure–property relationship in aqueous solution. Progress in Polymer Science. 2011;**36**(11):1558-1628

[37] Xin X, Xu G, Gong H, Bai Y, Tan Y. Interaction between sodium oleate and partially hydrolyzed polyacrylamide: A rheological study. Colloids and Surfaces, A: Physicochemical and Engineering Aspects. 2008;**326**(1-2):1-9

[38] Semenov AN, Rubinstein M. Dynamics of entangled associating polymers with large aggregates. Macromolecules. 2002;**35**(12):4821-4837

[39] Tonge SR, Tighe BJ. Responsive hydrophobically associating polymers: A review of structure and properties. Advanced Drug Delivery Reviews. 2001;**53**(01):109-122

[40] Yang ZL, Gao BY, Li CX, Yue QY, Liu B. Synthesis and characterization of hydrophobically associating cationic polyacrylamide. Chemical Engineering Journal. 2010;**161**(1-2):27-33

[41] Seright RS. Gel propagation through fractures. SPE Production & Facilities. 2001;**16**(04): 225-231

[42] SNF Floerger. Enhancing Polymer Flooding Performance. 30 years of Experience in EOR [Internet]. 2018. Available from: http://www.snfoil.com/images/ phocagallery /brochures/SNF _in_chemical_enhanced_oil_recovery.pdf. [Accessed: 2018-01-29]

[43] Levitt D, Pope GA. Selection and screening of polymers for enhanced-oil recovery. In: SPE Symposium on Improved Oil Recovery; 19-23 April 2008; Tulsa. Oklahoma: SPE; 2008. pp. 1-18

[44] Perttamo EK. Characterization of Associating Polymer (AP) Solutions. Influences on flow behavior by the degree of hydrophobicity and salinity [thesis]. The University of Bergen; 2013

[45] Mezger TG. The Rheology Handbook. 4th ed. Vincentz Network: Hanover; 2014

[46] Talukdar MM, Vinckier I, Moldenaers P, Kinget R. Rheological characterization of xanthan gum and hydroxypropylmethyl cellulose with respect to controlled-release drug delivery. Journal of Pharmaceutical Sciences. 1996;**85**(05):537-540

[47] Clausen TM, Vinson PK, Minter JR, Davis HT, Talmon Y, Miller WG. Viscoelastic micellar solutions: Microscopy and rheology. Physical Chemistry. 1992;**96**(01):474-484

[48] Kitazawa Y, Ueki T, McIntosh LD, Tamura S, Niitsuma K, Imaizumi S, Lodge TP, Watanabe M. Hierarchical sol-gel transition induced by thermosensitive self-assembly of an ABC triblock polymer in an ionic liquid. Macromolecules. 2016;**49**(04):1414-1423

[49] Herrera MP, Vasanthan T. Rheological characterization of gum and starch nanoparticle blends. Food Chemistry. 2018;**243**:43-49

[50] Wang Y, Zhong M, Park JV, Zhukhovitskiy AV, Shi W, Johnson JA. Block co-polyMOCs by stepwise self-assembly. Journal of the American Chemical Society. 2016;**138**(33): 10708-10715

[51] Lewis CL, Stewart K, Anthamatten M. The influence of hydrogen bonding side-groups on viscoelastic behavior of linear and network polymers. Macromolecules. 2014; **47**(02):729-740

[52] Steed JW, Atwood JL. Supramolecular Chemistry. John Wiley & Sons; 2013

[53] Chen S, Binder WH. Dynamic ordering and phase segregation in hydrogen-bonded polymers. Accounts of Chemical Research. 2016;**49**(7, 07):1409-1420

[54] Zhang D-W, Wang H, Li Z-T. Hydrogen bonding motifs: New progresses. In: Wu L-Z, Li Z-T, editors. Hydrogen Bonded Supramolecular Structures. New York: Springer Heidelberg; 2015. p. 350

[55] Carlton RA. Polarized Light Microscopy. Pharmaceutical Microscopy. New York: Springer; 2011. pp. 7-64

[56] Chen YL, Yuan JH, Yang WH, Huang DH, Tan H, Fei Q. Self-assembly fractal microstructures of HPAM/chromium acetate and HPAM/phenolic aldehyde colloidal dispersion gel. Journal of Dispersion Science and Technology. 2003;**24**(01):113-121

[57] Khutoryanskiy VV, Mun GA, Nurkeeva ZS, Dubolazov AV. pH and salt effects on interpolymer complexation via hydrogen bonding in aqueous solutions. Polymer International. 2004;**53**(09):1382-1387

[58] Yu X, Chen X, Chai Q, Ayres N. Synthesis of polymer organogelators using hydrogen bonding as physical cross-links. Colloid & Polymer Science. 2016;**294**(01):59-68

[59] Levitt D-B. The optimal use of enhanced oil recovery polymers under hostile conditions [Doctoral dissertation]. Austin: The University of Texas; 2009

[60] University, The Ohio State. Sand Size Analysis for Omsite Wastewater Treatment Systems. Determination of Sand Effective Size and Uniformity Coefficient [Internet]. Available from: https://ohioline.osu.edu/factsheet/aex-757. [Accessed: August 18, 2017]

[61] McPhee C, Reed J, Zubizarreta I. Core Analysis: A Best Practice Guide. Waltham: Elsevier; 2015

[62] Riahinezhad M, Romero-Zerón L, McManus N, Penlidis A. Evaluating the performance of tailor-made water-soluble copolymers for enhanced oil recovery polymer flooding applications. Fuel. 2017;**203**:269-278

[63] Seright RS. How much polymer should be injected during a polymer flood? Review of previous and current practices. SPE Journal. 2017;**22**(01):1-8

[64] Dupuis G, Rousseau D, Tabary R, Grassl B. Flow of Hydrophobically modified water-soluble polymers in porous media: Controlled resistance factors vs. flow-induced gelation in the Semidilute regime. SPE Journal. 2012;**17**(04):1196-1206

[65] Pancharoen M, Thiele MR, Kovscek AR. Inaccessible pore volume of associative polymer floods. In: SPE Improved Oil Recovery Symposium; 24-28 April, 2010. Tulsa, Oklahoma: SPE; 2010. pp. 1-15

[66] Seright RS, Fan T, Wavrik K, Wan H, Gaillard N, Favéro C. Rheology of a new sulfonic associative polymer in porous media. SPE Reservoir Evaluation & Engineering. 2011;**14**(06):726-734

[67] Kazempour M, Sundstrom EA, Alvarado V. Effect of alkalinity on oil recovery during polymer floods in sandstone. SPE Reservoir Evaluation & Engineering. 2012;**15**(02):195-209

[68] Manichand RN, Seright R. Field vs. laboratory polymer-retention values for a polymer flood in the tambaredjo field. SPE Reservoir Evaluation & Engineering. 2014;**17**(03):314-325

[69] Civan F. Porous Media Transport Phenomena. John Wiley & Sons; 2011

[70] Seright RS. Use of Polymers to Recover Viscous Oil from Unconventional Reservoirs. US Department of Energy. Final Report. Contract No. DE-NT0006555; 2011

[71] Taylor KC, Nasr-El-Din HA. Water-soluble hydrophobically associating polymers for improved oil recovery: A literature review. Journal of Petroleum Science and Engineering. 1998;**19**(03):265-280

[72] Li K, Sun W, Li F, Qu Y, Yang Y. Novel method for characterizing single-phase polymer flooding. SPE Journal. 2014;**19**(04):695-702

[73] Lotfollahi M, Farajzadeh R, Delshad M, Al-Abri AK, Wassing BM, Al-Mjeni R, Awan K, Bedrikovetsky P. Mechanistic simulation of polymer injectivity in field tests. SPE Journal. 2016;**21**(04):1178-1191

[74] Quadri SM, Shoaib M, AM AS, Alhassan SM. Screening of polymers for EOR in high temperature, high salinity and carbonate reservoir conditions. In: International Petroleum Technology Conference; 6-9 December, 2015; Doha, Qatar. Vol. 2015. pp. 1-30

[75] Sheng JJ, Leonhardt B, Azri N. Status of polymer-flooding technology. Journal of Canadian Petroleum Technology. 2015;**54**(02):116-126

[76] Satter A, Iqbal GM, Buchwalter JL. Practical Enhanced Reservoir Engineering: Assisted with Simulation Software. Tulsa: Pennwell Books; 2007

[77] Levitt D, Pope GA. Selection and screening of polymers for enhanced-oil recovery. In: SPE Symposium on Improved Oil Recovery; 19-23 April 2008. Tulsa, Oklahoma: SPE; 2008. pp. 1-18

Chapter 6

Effect of Maltodextrin Reduction and Native Agave Fructans Addition on the Rheological Behavior of Spray-Dried Juices

Darvin Ervey Jimenez-Sánchez,
Montserrat Calderón-Santoyo,
Laetitia Picart-Palmade,
Pedro Ulises Bautista Rosales,
Julio Cesar Barros-Castillo and
Juan Arturo Ragazzo-Sánchez

Additional information is available at the end of the chapter

http://dx.doi.org/10.5772/intechopen.75758

Abstract

Agave fructans have thermal protective and encapsulating properties as well as technological functions as stabilizers. The effect of the combination of maltodextrin 10% [w/v] and native agave fructans in concentrations of 0, 2, and 4% [w/v] on the rheological properties and microstructure, of spray-dried chayote, carrot, mango and pineapple powders was evaluated. The flow behavior was analyzed in a simple shear flow and low-cutting speed in the range of 5–200 s^{-1}. The experimental data of fresh or reconstituted juices were fitted to different flow models such as Newtonian, Bingham, and Ostwald-de-Waele. The flow behavior of all juices can be described by the Bingham model with low plastic viscosities; the addition of fructans and the step of spray drying had no significant influence on the plastic viscosity of juices as compared to fresh juices.

Keywords: fructans, spray drying, rheology, microstructure, Newtonian fluid

1. Introduction

Pineapple, mango, carrot and chayote are highly regarded due to their taste and nutritional value. All these fruits are recognized because of their high content in antioxidants such as

polyphenols, carotenoids and vitamin C. Chayote is also an important source of folic acid. There is an increasing interest in highly nutritious and instant foods, which is why the concentrated juice powder of these fruits could be an excellent and profitable option for consumption. In this way, chayote is mainly produced in Mexico and unknown in most countries. Due to the physical characteristics of the different types of fruit and the environmental conditions in the growing regions, large amounts of the harvested fruits fall short of the minimum quality standards for direct use and result in significant losses.

In recent years, new processes have been under development in order to achieve commercialization for fruit that fails to meet quality standards—the idea is to create products higher in quality and with greater added value. In this sense, the production of fruit juice powders is a better alternative for the use of raw material that fails to meet quality standards for exportation. In the processing of fruit juice, many variables exist that can lead to changes in the final product quality [1]. Rheological properties play an important role in the handling and processing, quality control and sensory evaluation of various foods [2]. The determination of rheological properties such as viscosity is of great importance in the prediction of heat and mass coefficients as well as for the design or development of heat transfer equipment and mass in the fruit juice industry [3]. Operational effects, such as concentration by evaporation, reverse osmosis, pumping and homogenization, are due to variations in viscosity [3]. In addition, factors such as the variety or maturity of the fruit and the treatment applied to fruit juice affect the viscosity of a reconstituted juice, so that the preference and acceptability of the consumer will be influenced by these factors [1, 4, 5]. Spray-drying is an alternative process for products which are sensitive to heat and has been used successfully in fruit juices [6]; the result is a product that has acceptable sensory characteristics and stability for storage.

In order to increase the glass transition temperature (Tg), the addition of thermoprotective additives such as maltodextrin is necessary to guarantee an adequate control of the spray drying process in fruit juices and the quality of the products obtained. The average aggregate amount has been reported between 30% and 75% (w/v); however, an excess of these generates increases in viscosity [7, 8], which stands in function of the total solids content of the particular juice to be processed. Carrier agent usually used in spray drying of fruit juices are carbohydrate based, such as maltodextrins and gums, mainly due to their high solubility, low viscosity, which are important conditions for the spray-drying process [9]. The production of fruit powders presents a challenge in the reduction of the viscosity of the juice of feeding, for the improvement of the drying, handling and storage. The presence of fructose, glucose and sucrose which are low molecular weight sugars as well as some organic acids in the fruit have changes in the viscosity of the fruit powder and the reconstituted.

Recent studies have attributed agave fructans with thermal protective and encapsulating properties, as well as technological functions as stabilizers [10]. Fructans are rich in fructose polymers with a terminal glucose and are composed of fructose units and terminal glucose unit linked by β-(2 → 1) and β-(2 → 6) links [11]. The most common inulin type fructans are from chicory roots (*Cichorium intybus*). On the other hand, levan-type fructans are present in grasses and cereals as well as those produced by bacteria [12]; however, this levan fructans are

rarely commercially available. At the same time, inulin-type fructans are widely used as food ingredients because of their gelling and thickening capacity, its ability for replace fat by up to 100% [13] as well as substitute of other carbohydrates to reduce the calories of some foods such as ice creams, dairy products and baked goods [11, 14].

Fructans are widely distributed in plants. They perform similar functions as dietary fiber and indigestible in the gastro-intestinal tract. As polymers, they have high molecular weight, increase amount of solids, provide no flavor or color, in general, they have functional properties that are excellent candidates as carrier agents. Botrel et al. [15] demonstrated that fructans have favorable effects on the microencapsulation of fish oil when used as carrier agents, favoring the reduction of particle size, high efficiency in microencapsulation and a decrease in bulk density. Chávez et al. [16] concluded that the thermal stability of agave fructans during the spray-drying process gives them the ability to be used as carrier agents.

Linear fructans show the tendency to form gels while branched fructans promote the formation of solutions [10]. In this sense, it has been reported that levan-type fructans interact with the membranes of phospholipids, which causes the properties of the surface of the acid mixtures to be strongly affected [17].

The reconstituted powders are fluids that can be classified according to their response to deformation in the linear (LVR) and non-linear viscoelastic (n-LVR) region. In particular, large amplitude oscillatory shear (LAOS) deformation permits varying experiments depending on whether suitable conditions for examining the material response within LVR are present and to obtain additional information in n-LVR. LVR is related to the structural arrangement, while n-LVR is associated with the mechanical response when food structure has been mostly deformed [18]. The n-LVR is more related to consumer perception than LVR [19].

Currently, few reports on the use of agave fructans as additives in the spray-drying process of fruit, or their use in the reduction of conventionally used materials, such as MD exist. In this sense, the objective of this study was to evaluate the effect of adding agave fructans and maltodextrin DE 10 on rheology in spray-dried chayote (*Sechium edule*), pineapple (*Ananas comosus*), carrot (*Daucus carota*) and mango (*Mangifera indica*) juices.

2. Fruit powder rheology

2.1. Raw materials

Chayote, carrot, mango and pineapple fruit in consumption degree of ripeness were obtained in Tepic, Nayarit and subsequently washed and disinfected in a sodium hypochlorite solution (NaClO) at 200 ppm (0.02%). Then, they were peeled, and the juice of these fruits was obtained using a conventional extractor. Maltodextrin DE10 or native agave fructans were added by homogenization using an electric laboratory homogenizer (PRO Scientific. Inc. 300 PC) at 350 rpm during 15 min and filtered in a No. 50 filter sieve. One liter of homogenized juice was used for each test.

2.2. Spray drying

A pilot dryer (model LPG-5, CIMA Industries Inc.) equipped with a rotatory nozzle was used for the spray-drying process with a feed rate of 15 mL.min^{-1}, 2.5 bar, a juice feed temperature of 25°C, air inlet rate of 9.4 m/s and temperature of 120°C. Maltodextrin was added to reach a final concentration of 10% (m/v). Fructans were added to a concentration of 0.2% or 4%. The inlet temperature and maltodextrin concentrations were determined in preliminary studies. Total solids were determined in fresh chayote, carrot, mango and pineapple juices; these parameters were taken as a reference for rehydration. A mass balance was performed to determinate the quantity of water necessary to reconstitute the powder with total solids content similar (TSS) to fresh juice.

2.3. Rheological properties of juices

The rheometric measurements were carried out with a controlled stress rheometer (Model AR-G2 TA Instruments with Software Trios v4.0.1) using concentric cylinder geometry [exterior cylinder diameter 21.96 mm, interior cylinder diameter 20.38 mm, height 59.50 mm], gap 500 μm, a constant temperature of 25°C, maintained in a circulating water bath and a AG2 heater. The flow behavior was analyzed in a simple shear flow, low cutting speed in a range of 5–200 s^{-1}. Juices were reconstituted based on the total soluble solids of the fresh juice. The experimental data of fresh or reconstituted juices were fitted to different flow models such as Newtonian (Eq. 1), Bingham (Eq. 2) and Ostwald-de-Waele Power Law model (Eq. 3).

$$\tau = \eta \dot{\gamma} \tag{1}$$

$$\tau - \tau_0 = \eta' \dot{\gamma} \tag{2}$$

$$\tau = K \dot{\gamma}^{\eta} \tag{3}$$

where τ is the shear stress [Pa], $\dot{\gamma}$ is the shear rate [s^{-1}], η is the viscosity (Pa.s), η′ is the plastic viscosity (Pa.s), τ_0 is the yield stress (Pa), K is the consistency index (Pa$^{1/2}$ s^{n}) and n is the flow behavior index.

The best rheological model for describing the flow behavior of juices was selected by comparing the value of correlation coefficient, R^2.

2.4. Rheological analysis

Figure 1 represents the flow curve of reconstituted juices containing three different concentrations of native agave fructans 0.2 and 4%. As can be observed from the figure, the flow curves at the three concentrations demonstrate an initial yield stress, indicating the presence of entangled rehydrated powders which prevents the free flow of the juices at zero shear rates. Similar flow curves were observed in the three concentrations of fructans. **Figure 1** shows

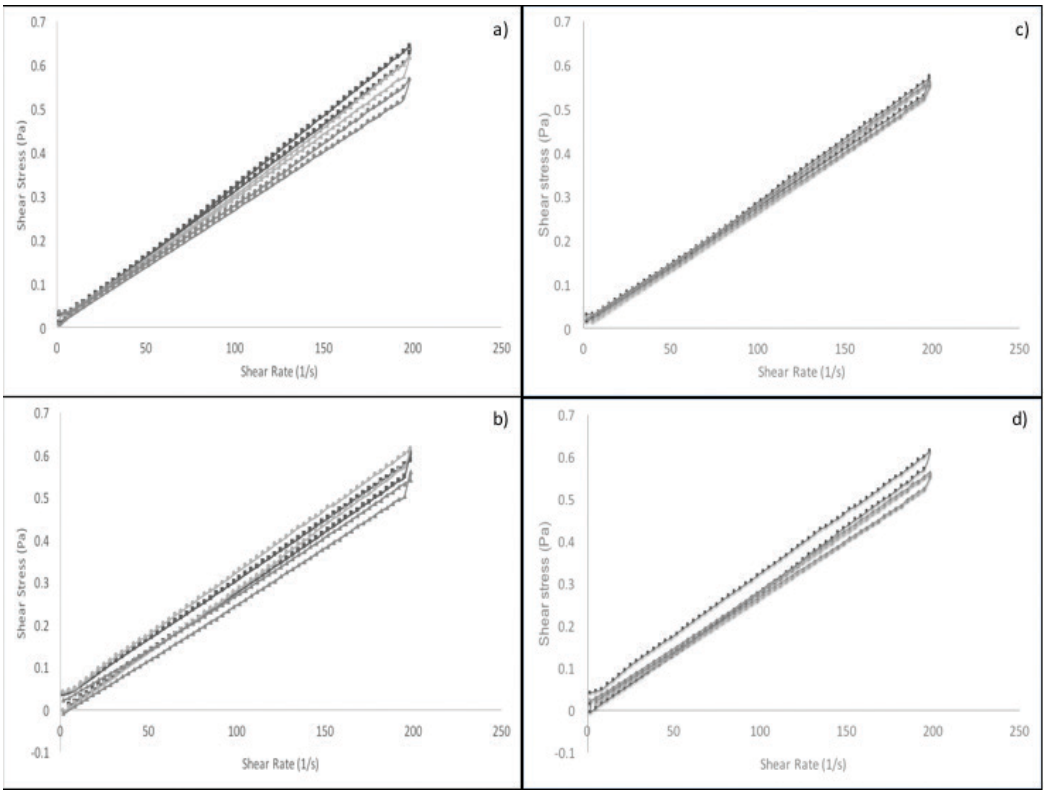

Figure 1. Flow behavior index curves of reconstituted chayote (a), pineapple (b), carrot (c), and mango (d) powders [■] 0% FT, [●] 2% FT, [▲] 4% FT. FT: Fructanos.

in the curves flow a Newtonian behavior (viscosity independent of the shear rate) for all the concentrations of fructans studied. In this sense, shear thinning behavior is characterized for a viscosity decrease with the shear rate due to structure destruction or a new structure formation. In this study, the concentrations of fructans were below 5%, so it is important to mention that for $C_{fructan} \leq 30\%$ [w/v] [which were measured in a double wall Couette geometry], and at shear rates smaller than 70 s^{-1} shear thinning was detected followed by shear thickening at shear rates higher than 270 s^{-1} in accordance with Ponce et al. [20].

Arvidson et al. [12] found shear thinning for aqueous levan polysaccharide solutions of 30% [w/v] and were measured at 20°C. The double wall Couette-type geometry presents secondary flow formation or Taylor vortices at higher shear rates, behaving turbulently as a flow type. The observed shear thickening behavior at high shear rates is attributed to the formation of instabilities of hydrodynamic flow [21, 22].

This phenomenon has been studied predicting the stress near to the wall with the theoretical analysis of Stuart [22, 23]. Others authors have reported hydrodynamic instabilities such as Taylor-Couette Vortices in Newtonian fluids [23] and viscoelastics fluids [24, 25]. Macias et al. [26] observed flow instabilities at shear rates higher than 250 s^{-1} for water in Double

wall Couette-type geometry. The shear thinning observed at low fructans concentration ($C_{fructans} \leq 30\%$ [w/v]) could be due to these flow instabilities, since the viscosity of agave solutions is near to the water viscosity.

The increase in viscosity is explained based on the transition of non-entangled fructan chains, however, an increase in the fructans concentration produce a greater amount of entanglements. The two slope changes they present themselves at medium concentration regimen at $C_{fructans} = 35\%$ [w/v] which are related to the overlap chains concentration. At higher concentrations at $C_{fructans} = 70\%$ [w/v], the solution behaves like a weak gel where high entanglements between fructan chains are detected. In solutions of linear polymers diluted with good solvents the dependence of η0 with concentration should be $\eta \approx C_{fructans}$ 4.7 [27]. Nevertheless, an increase in the concentration of polysaccharides causes the addition in the values of the exponent in the law of viscosity scale. Therefore, the value of the power law generates a screen in the understanding of the structure of the solution.

At 30°C, the agave fructan solutions exhibit a Newtonian behavior, this for samples with concentrations ≤80% [w/v]. In higher concentrations, the formation of a highly viscous solution is observed, so that the system at temperatures between 25 and 30°C shows a shearing dilution behavior; however, at high temperatures, there is a shear thickening [20]. The effect of fructan concentration on viscosity was similar to that of fructose or sucrose solutions. This confirms that the dependence of rheology on fructan concentration is closer to that of low molecular weight monosaccharides than to that of high molecular weight polysaccharides, as was proposed by Martínez-Padilla [28].

Table 1 shows the fitted parameters of the Newtonian, Bingham and Power Law rheological models for chayote, carrot, mango and pineapple fresh or reconstituted juices with different content of fructans. For all the reconstituted juices, the best adjustment of flow data was obtained with the Bingham model, values of R^2 ranged between 0.9992 and .9999. These results are in agreement with those of Shamsudin et al. [29] who found that the flow curves of Yankee pineapple juices were described by the Bingham model.

FT: fructans, N/A: no additives. All samples contain 10% maltodextrin. Note: similar letters no significant differences. Different letters significant differences ($p > 0.05$).

Bingham model describes plastic fluid that behaves as a rigid body at low stresses but flows as a viscous fluid at high stress. Then this type of fluid is characterized by a yield stress and a plastic viscosity. These parameters were statistically compared in **Table 2** for each formulation of juices. Whether for pineapple, carrot, mango or chayote juices, the addition of maltodextrin (10% [w/v]) and fructans (0–4% [w/v]) and the step of spray-drying had no significant influence on the plastic viscosity of juices as compared to fresh juices. Moreover, all the considered juices (**Table 1**) presented a low plastic viscosity that ranged from 0.0026 to 0.0030 Pa.s at 25°C. In contrast, yield stresses were impacted by the addition of maltodextrin, fructans or by the step of spray drying. Yield stress values were correlated to the presence and the degree of entanglement of colloids in fluids. For chayote and carrot juices, the addition of maltodextrin decreases significantly the value of the yield stress

http://dx.doi.org/10.5772/intechopen.75758

Sample		Newtonian		Bingham			Power Law		
		η	R^2	τ_0	η'	R^2	n	K	R^2
Chayote juice									
Fresh	N/A	0.0030	0.9974	0.0158[a]	0.0028	0.9996	0.8225	0.0069	0.9815
	0% FT	0.0029	0.9996	0.0028[b]	0.0029	0.9997	0.8981	0.0046	0.9890
	2% FT	0.0028	0.9992	0.0064[c]	0.0028	0.9996	0.8903	0.0047	0.9924
	4% FT	0.0029	0.9991	0.0082[c]	0.0028	0.9997	0.8794	0.0050	0.9913
Reconstituted	0% FT	0.0032	0.9995	0.0041[b]	0.0032	0.9997	0.9393	0.0043	0.9967
	2% FT	0.0031	0.9991	0.0040[b]	0.0030	0.9992	0.9260	0.0043	0.9961
	4% FT	0.0028	0.9985	0.0094[c]	0.0027	0.9994	0.8965	0.0046	0.9953
Pineapple juice									
Fresh	N/A	0.0030	0.9940	0.0252[a]	0.0028	0.9999	0.9961	0.0029	0.9997
	0% FT	0.0031	0.9912	0.0306[b]	0.0028	0.9999	0.7795	0.0088	0.9878
	2% FT	0.0031	0.9875	0.0366[b]	0.0028	0.9999	0.7516	0.0103	0.9849
	4% FT	0.0032	0.9819	0.0441[b]	0.0028	0.9999	0.7211	0.0121	0.9815
Reconstituted	0% FT	0.0030	0.9945	0.0237[a]	0.0028	0.9999	0.8430	0.0064	0.9960
	2% FT	0.0032	0.9920	0.0302[b]	0.0029	0.9999	0.8305	0.0072	0.9968
	4% FT	0.0027	0.9988	0.0073[c]	0.0027	0.9994	0.9309	0.0037	0.9955
Carrot juice									
Fresh	N/A	0.0032	0.9921	0.0174[a]	0.0030	0.9932	0.8125	0.0078	0.9918
	0% FT	0.0029	0.9913	0.0045[b]	0.0032	0.9897	0.8811	0.0055	0.9812
	2% FT	0.0027	0.9991	0.0056[c]	0.0030	0.9846	0.8845	0.0048	0.9829
	4% FT	0.0028	0.9956	0.0072[c]	0.0031	0.9911	0.8867	0.0053	0.9943

Reconstituted	0% FT	0.0035	0.9993	0.0054[b]	0.0041	0.9992	0.9478	0.0052	0.9973
	2% FT	0.0031	0.9984	0.0045[b]	0.0035	0.9981	0.9130	0.0054	0.9923
	4% FT	0.0025	0.9967	0.0091[c]	0.0029	0.9989	0.8977	0.0057	0.9891
Mango juice									
Fresh	N/A	0.0031	0.9935	0.0215[a]	0.0028	0.9965	0.9046	0.0055	0.9968
	0% FT	0.0030	0.9915	0.0177[b]	0.0031	0.9943	0.8311	0.0078	0.9875
	2% FT	0.0029	0.9937	0.0217[b]	0.0029	0.9931	0.8197	0.0081	0.9849
	4% FT	0.0030	0.9889	0.0256[b]	0.0032	0.9963	0.8049	0.0087	0.9983
Reconstituted	0% FT	0.0033	0.9965	0.0149[a]	0.0036	0.9989	0.8953	0.0067	0.9923
	2% FT	0.0032	0.9952	0.0173[b]	0.0033	0.9973	0.8875	0.0054	0.9957
	4% FT	0.0026	0.9976	0.0083[c]	0.0027	0.9995	0.9143	0.0049	0.9997

FT: Fructans, N/A: no additives. All samples contain 10% maltodextrin.
Note: Group means with the same letters in a column are significantly different at 5% level of significant by Tukey test.

Table 1. Experimental data fitted to parameters of rheological models (Newtonian, Bingham and Power Law).

from 0.0145 Pa (fresh juice) to 0.0029 Pa. The addition of maltodextrin to chayote and carrot juice induces a significant decrease of the yield stress of juice. This effect may be attributed to the interactions between the maltodextrin and the other polysaccharides, which do not allow these polysaccharides to fully extend in solution [30]. According to Grabowski et al. 2008 who studied the rheological properties of spray-dried sweet potato-maltodextrin powders, maltodextrin polysaccharide interactions could induce a decrease of the viscosity, since longer molecules have a larger hydrodynamic volume, which increases solution viscosity.

The additional supplementation of fructans up to 4% induced a slight but significant increase of the yield stress of fresh chayote juice up to 0.0078 Pa. Furthermore, spray drying did not seem to deeply impact the rheological behavior of chayote juices (**Table 1**). Pineapple juices presented higher yield stresses than chayote, while they had the same plastic viscosity. These findings could be because fruit juices contain colloidal systems. These colloids are part of the fruit itself or may be formed by microorganisms during fruit ripening. Most of the colloids come from the plant itself. The amount of colloids present in fruit juice is in the range of 100–1000 mg/L. An examination of colloids in the juice after pressing shows that they are basically polysaccharides such as pectins and starch [31, 32]. In this sense, the pineapple contains

Sample		Flow parameters	
		τ_0	η'
Fresh Chayote	N/A	0.0145 ± 0.0017[a]	0.0030 ± 0.0003[a]
	0% FT	0.0029 ± 0.0002[b]	0.0032 ± 0.0004[a]
	2% FT	0.0062 ± 0.0002[c]	0.0033 ± 0.0008[a]
	4% FT	0.0078 ± 0.0006[c]	0.0032 ± 0.0007[a]
Reconstituted Chayote	0% FT	0.0039 ± 0.0002[b]	0.0029 ± 0.0004[a]
	2% FT	0.0042 ± 0.0003[b]	0.0029 ± 0.0001[a]
	4% FT	0.0091 ± 0.0004[d]	0.0029 ± 0.0003[a]
Fresh Pineapple	N/A	0.0266 ± 0.0021[a]	0.0026 ± 0.0002[a]
	0% FT	0.0301 ± 0.0006[b]	0.0029 ± 0.0002[a]
	2% FT	0.0354 ± 0.0017[b]	0.0029 ± 0.0001[a]
	4% FT	0.0432 ± 0.0013[c]	0.0027 ± 0.0001[a]
Reconstituted Pineapple	0% FT	0.0216 ± 0.0028[a]	0.0026 ± 0.0002[a]
	2% FT	0.0310 ± 0.0011[b]	0.0027 ± 0.0003[a]
	4% FT	0.0087 ± 0.0025[d]	0.0028 ± 0.0001[a]
Fresh Carrot	N/A	0.0152 ± 0.0010[a]	0.0035 ± 0.0005[a]
	0% FT	0.0036 ± 0.0012[b]	0.0037 ± 0.0004[a]
	2% FT	0.0075 ± 0.0009[c]	0.0036 ± 0.0006[a]
	4% FT	0.0082 ± 0.0005[c]	0.0031 ± 0.0011[a]
Reconstituted Carrot	0% FT	0.0042 ± 0.0003[b]	0.0031 ± 0.0002[a]
	2% FT	0.0056 ± 0.0006[b]	0.0033 ± 0.0005[a]
	4% FT	0.0098 ± 0.0006[d]	0.0032 ± 0.0004[a]
Fresh Mango	N/A	0.0311 ± 0.0011[a]	0.0025 ± 0.0003[a]
	0% FT	0.0402 ± 0.0016[b]	0.0022 ± 0.0001[a]
	2% FT	0.0461 ± 0.0021[b]	0.0026 ± 0.0007[a]
	4% FT	0.0512 ± 0.0003[c]	0.0029 ± 0.0008[a]
Reconstituted Mango	0% FT	0.0318 ± 0.0009[a]	0.0025 ± 0.0006[a]
	2% FT	0.0223 ± 0.0012[b]	0.0029 ± 0.0005[a]
	4% FT	0.0156 ± 0.0015[d]	0.0031 ± 0.0011[a]

Note: Values follow by the same letter within the same row are notsignificantly different from each other ($p > 0.05$)

Table 2. Influence of fructans addition and spray-drying on yield stress (τ_0, pa) and plastic viscosity (η', pa.S) of juices.

more pectins than chayote, carrot and mango, and pectins are responsible for the turbidity and high viscosity of fruit juices. The addition of maltodextrin and fructans up to 4% [w/v] also induced a slight but significant increase of the yield stress of pineapple juices. However,

a decrease of this rheological parameter was observed for reconstituted juices after spray drying especially for samples with 4% of fructans, which could be due to the solubility of fructans above 95% [10].

The viscosity of agave fructans solutions (*Agave tequilana* Weber blue var.) at different concentrations and temperatures has been studied by Ponce et al. [20]. They observed that solutions with concentrations inferior to 30% [w/v] at temperatures ranging between 30 and 60°C presented a low viscosity, similar to water. Meanwhile, the viscosity of solutions with concentrations superior or equal to 30% [w/v], increased when increasing the concentration up to 70%, forming a highly viscous fluid. The results obtained in this work are in agreement with previous findings; lower plastic viscosity was observed in fructans powders with lower concentrations, this according to the flow parameters such as plastic viscosity (η') and yield stress (τ_0) obtained with Eq. 2. This shear thinning behavior at low shear rate (20 s^{-1}) followed by thickening behavior at high shear rate [300 s^{-1}] in low fructans concentrations ($C_{fructans} \leq 30\%$ in weight) could be due to flow instabilities such as vortices, since the viscosity of the samples is close to that of water [33].

The effect of adding maltodextrin on tomato pulp during spray-drying has been studied by Goula and Adamopoulos [30]. They observed that reconstituted tomato pulp from the resulting powder showed a non-Newtonian behavior with low stress, and a decrease in viscosity when the maltodextrin concentration and dextrose equivalent increase. This same effect is observed in the reconstituted chayote and pineapple powders and is attributed to the fact that the 10% maltodextrin concentration is higher in comparison to that of fructans.

Chayote, carrot, mango and pineapple juices [fresh and reconstituted] did not present the same rheological behavior [specially for the yield stress]. In this sense, studies have found that a decrease in sweet-potato solids, as well as interaction between maltodextrin and sweet-potato polysaccharides contributed to a decrease in viscosity of the reconstituted purée [34]. In general, the flow behavior of fresh and reconstituted sweet-potato solutions was different suggesting that the solids concentration being modified by the molecular changes during spray-drying. This could also explain the distinct rheological behavior for each reconstituted fruit powder in the present study.

3. Conclusions

The addition of native agave fructans contributes to a significant decrease in the mass fraction of maltodextrin added in this type of industrial products. All fresh or reconstituted juices present a flow behavior typical of plastic fluids [Bingham model]. The addition of maltodextrin [10%] and fructans [up to 4%] as well as the step of spray-drying did not change significantly the plastic viscosity of juices. Only the yield stresses, which represent the behavior of fluids at rest, were impacted by these parameters. The combination of native agave fructans with maltodextrin as a stabilizer produced spherical particles with shrinkage, lumps, and caking between them. The flow behavior as a function of concentration indicates that the agave native fructans and the fructans-maltodextrin mixtures behave similar to simple sugars but with an increase in the viscosity of the mixture.

Acknowledgements

The authors thank CONACyT [México] for their support in conducting the work throughout project number 210874 and for the scholarship granted to Jimenez-Sanchez D. E.

Author details

Darvin Ervey Jimenez-Sánchez[1], Montserrat Calderón-Santoyo[1], Laetitia Picart-Palmade[2], Pedro Ulises Bautista Rosales[3], Julio Cesar Barros-Castillo[1] and Juan Arturo Ragazzo-Sánchez[1]*

*Address all correspondence to: jragazzo@ittepic.edu.mx

1 Laboratorio Integral de Investigación en Alimentos, Tecnológico Nacional de México—Instituto Tecnológico de Tepic, Tepic, Nayarit, México

2 Université de Montpellier, UMR 1208, Ingénierie des Agropolymères et Technologies Emergentes, Place Eugène Bataillon, Montpellier, France

3 Centro de Tecnología de Alimentos, Universidad Autónoma de Nayarit, Ciudad de la Cultura "Amado Nervo", Tepic, Nayarit, México

References

[1] Juszczak L, Witczak M, Fortuna T, Solarz B. Effect of temperature and soluble solids content on the viscosity of beetroot [Beta vulgaris] juice concentrate. International Journal of Food Properties. 2010;**13**(6):1364-1372

[2] Rao A. Rheology of Fluid, Semisolid, and Solid Foods: Principles and applications. Rheology Fluid, Semisolid, Solid Foods. 2013;**19**:461

[3] Magerramov MA, Abdulagatov AI, Azizov ND, Abdulagatov IM. Effect of temperature, concentration, and pressure on the viscosity of pomegranate and pear juice concentrates. Journal of Food Engineering. 2007;**80**(2):476-489

[4] Tiziani S, Vodovotz Y. Rheological effects of soy protein addition to tomato juice. Food Hydrocolloids. 2005;**19**(1):45-52

[5] Aguiló-Aguayo I, Oms-Oliu G, Soliva-Fortuny R, Martín-Belloso O. Changes in quality attributes throughout storage of strawberry juice processed by high-intensity pulsed electric fields or heat treatments. LWT- Food Science and Technology. 2009;**42**(4):813-818

[6] Bhandari BR, Senoussi A, Dumoulin ED, Lebert A. Spray drying of concentrated fruit juices spray drying of concentrated fruit juices. An International Journal Drying Technology. 1993;**11**(55):10811092

[7] Fernandes RVB, Borges SV, Botrel DA. Influence of spray drying operating conditions on microencapsulated rosemary essential oil properties | Influência das condições operacionais da secagem por atomização nas propriedades de óleo de alecrim microencapsulado. Ciência e Tecnologia de Alimentos. 2013;**33**(SUPPL. 1):171-178

[8] Shrestha AK, Ua-Arak T, Adhikari BP, Howes T, Bhandari BR. Glass transition behavior of spray dried orange juice powder measured by differential scanning calorimetry [DSC] and thermal mechanical compression test [TMCT]. International Journal of Food Properties. 2007;**10**(3):661-673

[9] Quek SY, Chok NK, Swedlund P. The physicochemical properties of spray-dried watermelon powders. Chemical Engineering and Processing Process Intensification. 2007;**46**(5):386-392

[10] Espinosa-Andrews H, Urias-Silvas JE. Thermal properties of agave fructans [*Agave tequilana* Weber var. Azul]. Carbohydrate Polymers [Internet]. Elsevier Ltd. 2012;**87**(4): 2671-2676 Available from: http://dx.doi.org/10.1016/j.carbpol.2011.11.053

[11] Roberfroid MB, Delzenne NM. Dietary fructans. Annual Review of Nutrition. 1998;**18**: 117-143

[12] Arvidson SA, Rinehart BT, Gadala-Maria F. Concentration regimes of solutions of Levan polysaccharide from Bacillus sp. Carbohydrate Polymers. 2006;**65**(2):144-149

[13] Trumbo P, Schlicker S, Yates AA, Poos M. Dietary reference intakes for energy, carbohydrate, fiber, fat, fatty acids, cholesterol, protein and amino acids. Journal of the American Dietetic Association. 2002;**102**:1621-1630

[14] Franck A. Technological functionality of inulin and oligofructose. British Journal of Nutrition [Internet]. 2002;**87**(6):287-291 Available from: http://www.ingentaselect.com/rpsv/cgi-bin/cgi?ini=xref&body=linker&reqdoi=10.1079/BJNBJN/2002550

[15] Botrel DA, Borges SV, Fernandes RVDB, Lourenço Do Carmo E. Optimization of fish oil spray drying using a protein: Inulin system. Drying Technology. 2014;**32**(3):279-290

[16] Chávez-Rodríguez A, López-Muraira IG, Goméz-Leyva JF, Luna-Solano G, Ortíz-Basurto RI, Andrade-González I. Optimization of Agave tequilana Weber var. Azul juice spray drying process. Journal of Chemistry. 2014;**2014**

[17] Vereyken IJ, Chupin V, Demel RA, Smeekens SCM, De Kruijff B. Fructans insert between the headgroups of phospholipids. Biochimica et Biophysica Acta, Biomembranes. 2001;**1510**(1-2):307-320

[18] Harte F, Clark S, Barbosa-Cánovas GV. Yield stress for initial firmness determination on yogurt. Journal of Food Engineering. 2007;**80**(3):990-995

[19] Guggisberg D, Cuthbert-Steven J, Piccinali P, Bütikofer U, Eberhard P. Rheological, microstructural and sensory characterization of low-fat and whole milk set yoghurt as influenced by inulin addition. International Dairy Journal. 2009;**19**(2):107-115

[20] Ponce SJA, Macías BER, Soltero MJFA, Fern_andez EVV, Zúniga PV, Escalona BHB. Physical-Chemical and non-linear rheological properties of aqueous solutions of agave fructans Propiedades fisicoquímicas y reología no lineal de soluciones acuosas de fructanos de agave. 2008;**6**:1-23

[21] Soltero JFA, Alvarez-Ramírez JG, Fernández VVA, Tepale N, Bautista F, Macías ER, et al. Phase and rheological behavior of the polymerizable surfactant CTAVB and water. Journal of Colloid and Interface Science. 2007;**312**(1):130-138

[22] Donnelly RJ, Simon NJ. An empirical torque relation for supercritical flow between rotating cylinders. Journal of Fluid Mechanics. 1960;**7**(3):401-418

[23] Cole JA. Taylor-vortex instability and annulus-length effects. Journal of Fluid Mechanics. 1976;**75**(1):1-15

[24] Baumert BM, Muller SJ. Axisymmetric and non-axisymmetric elastic and inertio-elastic instabilities in Taylor-Couette flow. Journal of Non-Newtonian Fluid Mechanics. 1999; **83**(1-2):33-69

[25] Li Z, Khayat RE. Pattern formation in weakly forced Taylor-Couette flow. Phys rev E - stat physics, plasmas, fluids. Related Interdisciplinary topics. 2004;**69**(4):9

[26] Macias ER, Gonzalez A, Manero O, Gonzales-Nunez R, Soltero JFA, Attané P. Flow regimes of dilute surfactant solutions. Journal of Non-Newtonian Fluid Mechanics. 2001;**101**(1-3):149-171

[27] Raspaud E, Lairez D, Adam M. On the number of blobs per entanglement in Semidilute and good solvent solution: Melt influence. Macromolecules. 1995;**28**(4):927-933

[28] Sosa-Herrera MG, Martínez-Padilla LP, Delgado-Reyes VA, Torres-Robledo A. Effect of agave fructans on bulk and surface properties of sodium caseinate in aqueous media. Food Hydrocolloids. 2016;**60**:199-205

[29] Shamsudin R, Ling CS, Adzahan NM, Daud WRW. Rheological properties of ultra-violet-irradiated and thermally pasteurized Yankee pineapple juice. Journal of Food Engineering. 2013;**116**(2):548-553

[30] Goula AM, Adamopoulos KG. Effect of Maltodextrin Addition during Spray Drying of Tomato Pulp in Dehumidified Air: I. Drying Kinetics and Product Recovery. Dry Technology [Internet]. 2008;**26**(6):714-725 Available from: http://www.tandfonline.com/doi/abs/10.1080/07373930802046369

[31] Barros STD, Mendes ES, Peres L. Influence of depectinization in the ultrafiltration of West Indian cherry [*Malpighia glabra* L.] and pineapple [*Ananas comosus* [L.] Meer] juices. Ciência e Tecnologia de Alimentos [Internet]. 2004;**24**(2):194-201 Available from: http://search.epnet.com/login.aspx?direct=true&db=lah&an=20043117754

[32] Echavarría AP, Falguera V, Torras C, Berdún C, Pagán J, Ibarz A. Ultrafiltration and reverse osmosis for clarification and concentration of fruit juices at pilot plant scale. LWT- Food Science and Technology. 2012;**46**(1):189-195

[33] Macías-Rubalcava ML, Hernández-Bautista BE, Jiménez-Estrada M, Cruz-Ortega R, Anaya AL. Pentacyclic triterpenes with selective bioactivity from Sebastiania adenophora leaves, euphorbiaceae. Journal of Chemical Ecology. 2007;**33**(1):147-156

[34] Grabowski JA, Truong V, Daubert CR. Nutritional and rheological characterization of spray dried sweetpotato powder. 2008;**41**:206-216

Section 3

Suspensions, Colloids and Granular Materials

Chapter 7

Interparticle Interaction Effects in Polymer Suspensions

Nico Laufer, Harald Hansmann, Christian Boss and Stefan Ofe

Additional information is available at the end of the chapter

http://dx.doi.org/10.5772/intechopen.75207

Abstract

Viscosity functions of particle-filled polymer melts are shifted to higher values in comparison with those of the unfilled polymer melts. This increase is affected by a number of factors such as the volume content, size, size distribution and the aspect ratio of the suspended particles. If interparticle interactions occur, which include the formation and breaking of agglomerates as well as the migration and rotation of particles during flow, the extent of the viscosity increase of suspensions also depends on the applied shear stress. Filler with a high aspect ratio, such as fibrous and plate-like particles, exhibits a strong tendency for interparticle interactions even at low volumetric concentrations. However, depending on the polymer matrix, spherical particles can exhibit a range of negligible interparticle interactions at low filler volume concentrations. Non-negligible interactions occur at higher filler concentrations. On the basis of the *generalized interaction function*, which considers the transition from negligibly interparticle interactions to the domain of non-negligibly interactions, the flow behavior of particle-filled polymer melts can be estimated. The subject of this chapter is the application of the *generalized interaction function* for the characterization of the flow behavior of particle-filled polyolefin melts.

Keywords: interparticle interaction, generalized interaction function, interaction exponent, rheology, flow function, suspension

1. Introduction

A suspension is a heterogeneous system in which solid particles are dispersed in a liquid. An example of a suspension is a particle-filled thermoplastic polymer melt in which

the dispersed phase is characterized by the fillers and the continuous or suspending phase (matrix) by the polymer melt. The rheological properties of suspensions that are relevant to processing are influenced by a variety of factors and significantly differ from those of the matrix fluid. When the suspending medium is a Newtonian fluid, then the suspension exhibits non-Newtonian behavior with increasing filler concentration. When the suspending medium is non-Newtonian in character, the presence of solid particles magnifies the complexities of its rheological behavior [1].

Rheological investigations on particle-filled polymer melts show that the viscosity functions exhibit higher values with increasing volumetric filler concentration (**Figure 1**). The offset depends not only on the volume fraction but also on the shape, size and size distribution of the suspended particles. In the case of interaction effects, the offset also depends on the applied shear stress and shear rate.

Several theoretical and empirical relationships have been proposed to describe the viscosity of suspensions [1]. Most of these relationships describe the influence of the volumetric filler concentration on the relative viscosity, which is defined as the ratio of the viscosity of the suspension to the viscosity of the suspending liquid.

$$\eta_r = \frac{\eta_s}{\eta_0} \tag{1}$$

where

η_r = relative viscosity [−]

η_s = viscosity of the suspension [Pa s]

η_0 = viscosity of the suspending liquid [Pa s]

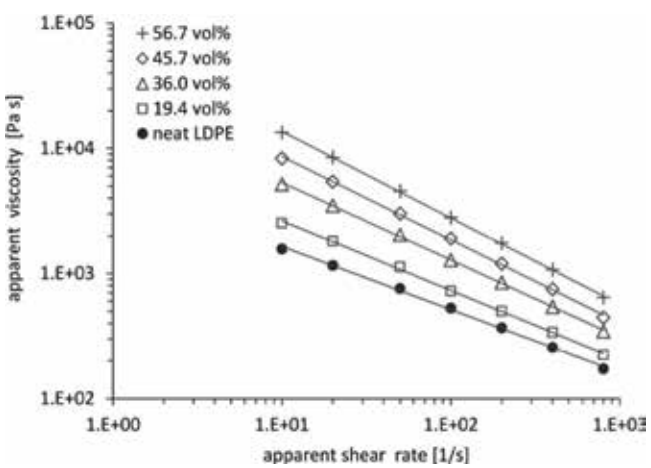

Figure 1. Viscosity functions of LDPE filled with natural graphite (d50 = 266.6 μm; median particle size of a particle analysis) with varying volume content (T = 190°C; typical processing and recommended MFI temperature – ISO 1133).

The first theoretical relationship of the relative viscosity of a Newtonian fluid in which rigid spheres are suspended was proposed in 1906 by Albert Einstein (corrected in 1911) [2, 3]. He derived an analytical solution that is valid for dilute suspensions in which no particle-particle interactions occur:

$$\eta_r = 1 + 2.5\phi \tag{2}$$

Rutgers experimentally proved that (Eq. (2)) is valid for volume fractions up to $\phi < 0.1$ [1]. For more densely filled suspensions, Einstein's equation was extended by higher order terms to mathematically describe the nonlinear relationship between relative viscosity η_r and filler volume fraction ϕ:

$$\eta_r = 1 + B\phi + B_1\phi^2 + \ldots \tag{3}$$

with B = 2.5 according to Einstein's constant and with $7.35 \leq B_1 \leq 14.1$ found by different authors [1, 4–6]. The main drawback of the polynomial function (Eq. (2)) is the poor consistency of calculated and measured values for particle volume fractions $\phi > 0.25$ [5].

Krieger & Dougherty developed an empirical equation describing the relative viscosity as a function of the filler content, taking into account the maximum packing of the filler ϕ_m (equivalent formulas or modifications by Maron-Pierce, Kitano, Queimada or Mooney) [1, 5–9]:

$$\eta_r = \left(1 - \frac{\phi}{\phi_m}\right)^{-B\phi_m} \tag{4}$$

This equation is one of the most widely used functions for fitting to experimental data, since B and ϕ_m can be used as fitting parameters for the approximation [5].

In addition to the abovementioned equations, there are a variety of other relationships for describing the flow behavior of suspensions based on the relative viscosity [1, 5–12]. Within a large number of publications, the relative viscosity as a function of the filler concentration is determined either at a constant shear rate or at a constant shear stress. However, studies on particle-filled LDPE and PP indicate that the relative viscosity (determined at both constant shear stress and constant shear rate) depends not only on the filler concentration but also on the applied shear rate (**Figure 2**).

Figure 2 (right) shows the impact of the apparent shear rate on the relative viscosity, which can be expressed by a power function. On the basis of this function, it can be shown that an increase of the shear rate by a decade leads to a reduction of the relative viscosity, determined at constant shear stress, by approximately 60%. The relative viscosity, determined at constant shear rate, is reduced by approximately 28%. This shows that the shear rate has to be taken into account for an exact prediction of the real flow behavior of particle-filled polymer melts.

Hinkelmann noted in his investigations on glass-filled SAN that a simple analytical description of the filler concentration on the relative viscosity is problematic due to the strong

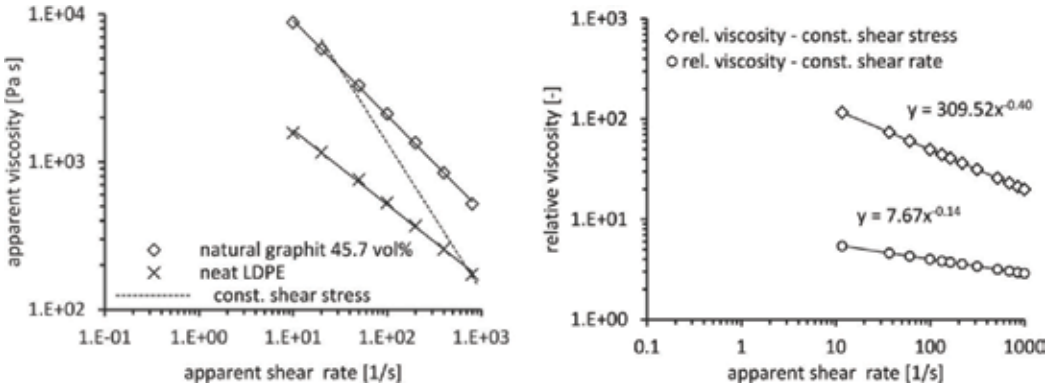

Figure 2. (left) Viscosity functions of LDPE and LDPE filled with 45.7 vol% natural graphite; (right) Relative viscosity determined at the same shear rate and shear stress, respectively.

impact of the shear rate on this value [12]. Gleißle *et al.* also pointed out in his investigations on charcoal-filled silicone oil that equations describing the relative viscosity as a function of the volume concentration cannot universally describe the increase in the viscosity of liquids by the addition of particles [13]. Alternatively, Gleißle and Baloch proposed a very vivid description to illustrate the flow behavior of suspensions based on the concept of shear-stress-equivalent shear rate.

Within this concept, the hydraulic diameter is reduced by the volume content of the particles. This leads to an increase in the shear rate of the continuous phase between these particles, the so-called inner shear rate (**Figure 3**).

The relative increase of this inner shear rate to the shear rate of the suspension (considered as a homogeneous liquid) is expressed by the shift factor B.

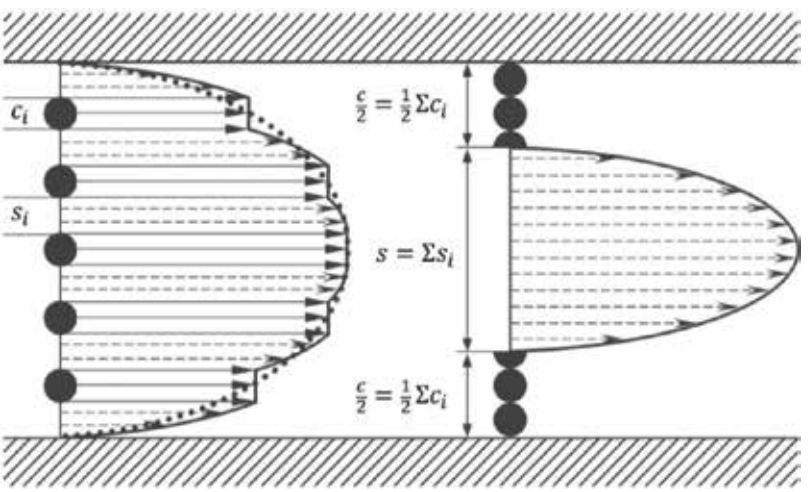

Figure 3. Idealization of Poiseuille flow (pressure-induced channel flow) processes in suspensions according to the concept of the shear-stress-equivalent shear rate.

$$B = \frac{\dot{\gamma}_c}{\dot{\gamma}_0} \tag{5}$$

where,

$\dot{\gamma}_c$ = inner shear rate [1/s]

$\dot{\gamma}_0$ = shear rate of the suspension [1/s]

In general, the flow behavior of a shear thinning fluid, such as particle-filled polymer melt, can be described by the power law (defined by consistency index K and flow behavior index n) of Ostwald/de Waele. On the basis of the power law, interaction effects can be taken into account in the calculation of the shift factor as follows [14]:

$$B(\tau)^{n_0} = \frac{K_c}{K_0^{\chi}} \cdot \tau^{(\chi-1)} \tag{6}$$

where,

K_c = consistency index (suspension) [Pa s^n]

K_0 = consistency index (polymer matrix) [Pa s^n]

τ = applied shear stress [Pa]

χ = interaction exponent $\left(\chi = \frac{n_c}{n_0}\right)$ [−]

n_c = flow behavior index (suspension) [−]

n_0 = flow behavior index (polymer matrix) [−]

Shift factor B is affected by a number of factors: interparticle interactions, the formation and breaking of particle aggregates, the solids content of the suspension, the particle size and morphology of the solid phase, the effects of surfactants, which in turn affect the viscosity of the suspension [15]. In case of negligible interparticle interactions, the flow behavior indices are the same for the flow functions of the suspension (n_c) and the matrix polymer (n_0); thus, the interaction exponent is equal to one. In this case, shift factor B is independent of the applied shear stress, and the filler content only affects the consistency index [13].

The quantitative impact of the volumetric filler concentration on the consistency index of the suspension (**Figure 4**) is expressed by the following empirical Equation [16, 17]:

$$K_c = K_0 \cdot \left(1 + A \cdot \phi_v^{\alpha} \cdot e^{\beta \cdot \phi_v}\right) \tag{7}$$

where,

ϕ_v = volumetric filler concentration [−]

The adjustable parameters A, α, β can be found by regression analysis to fit a given set of experimental data.

As already stated, in case of negligible interparticle interactions, only the consistency index of the suspension changes as a function of the volumetric filler concentration, while the

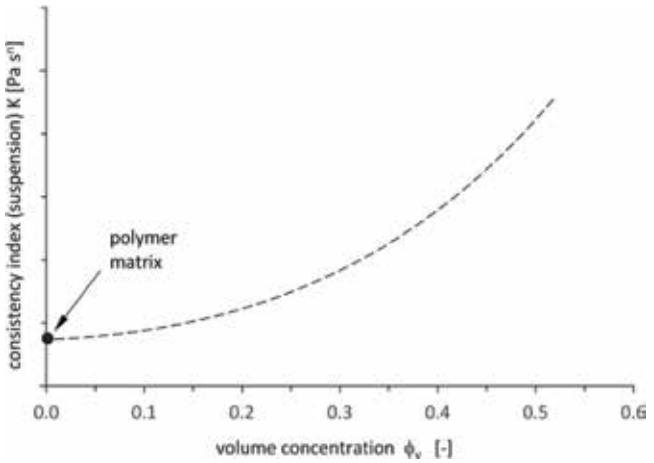

Figure 4. Typical function of the correlation between consistency index of a suspension and volumetric filler concentration.

interaction exponent remains constant at a value of one. The interaction exponent decreases only if interparticle interactions occur (**Figure 5**).

A general mathematical description of the interaction exponent over the entire range of negligible interparticle interactions with the transition to non-negligible interparticle interactions provides the following equation, which is called the *generalized interaction function* [18]:

$$\chi = \frac{1}{\left(1 + \left(\frac{K_c}{K^*}\right)^a\right)^{\frac{b}{a}}} \tag{8}$$

where,

K* = transitional consistency index [Pa s^n]

a, b = adjustable parameters [−]

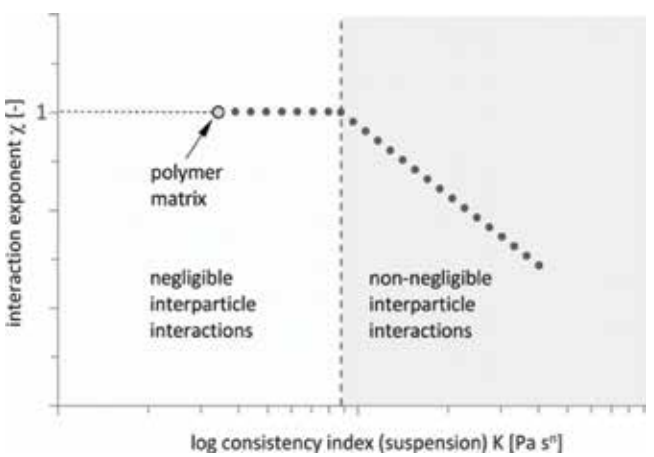

Figure 5. Interaction exponent of a suspension as a function of the consistency index.

The model parameter (K*) describes the transition from negligible interactions to non-negligible interactions, whereas (a) expresses the width of the transition. The intensity of interaction effects is considered by parameter (b). The model parameters of this empirical equation can be found by regression analysis to fit a given set of experimental data with regard to minimize the sum of the relative error squares. To quantify the quality of the approximation, the mean of the absolute relative error values is used. This procedure was applied to all regression analyses in this study.

2. Comparison of interaction effects in long-chain branched and linear polymeric matrices

Interparticle interactions take place when the filler concentration increases. This includes an increase of particles per unit volume, which come into contact during flow. Furthermore, the rotation and migration of particles during flow, as well as the formation and breaking of aggregates, produces additional dissipative effects, which lead to an increase in the viscosity [1]. The mathematical consideration of interaction effects, which are dependent on the size, size distribution and morphology of the filler particles, as well as the filler volume concentration and the applied shear rate or shear stress, which is affected by volume output and the flow channel geometry in one general approach that describes the flow behavior of suspensions, is subject of this chapter. In addition to the particle properties and process conditions, the molecular structure of the matrix polymer has an influence on the formation of interparticle interaction effects and thus also on the flow behavior of the suspension. Linear and long-chain branched polymers differ in both shear thinning flow behavior and nonlinear, steady-state viscoelastic melt properties. The elastic melt properties, defined as the ratio of normal stress difference and shear stress, influence the particle migration during flow. The resulting differences in flow behavior are illustrated below using a long-chain branched LDPE and a linear PP as polymer matrices. In order to characterize the rheological properties of the particle-filled polymer melts, the fillers must be uniformly dispersed into the polymer matrix by means of suitable compounding techniques. The fillers mentioned in this chapter (**Figure 6**) can be classified based on their geometrical shape into the following categories:

- Spherical → glass beads, wood flour (small fraction)
- Plate-like → natural graphite
- Fibrous → wood flour (big fraction), wood fibers

The particle size distribution was determined using the Mastersizer 3000 (Malvern Instruments GmbH) via laser diffraction. The preparations of all formulations as shown in the following section were carried out by compounding on a corotating twin screw extruder (Brabender DSE 20) with a mass temperature of 190°C and mass output of 5 kg/h. Temperature profile: feed zone 170°C; plastification zone 180°C; conveying zone 185°C; mixing zone 185°C; extrusion zone 190°C.

2.1. Low-density polyethylene

The polymer matrix of all following compounds in this section is a low-density polyethylene (LDPE), which is highly branched and exhibits shear thinning flow behavior.

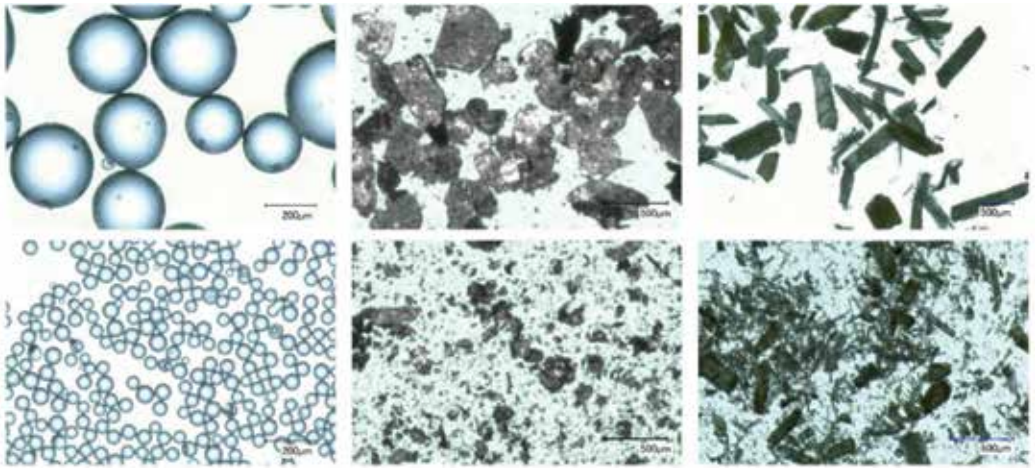

Figure 6. Light transmitted microscopy of spherical, plate-like and fibrous particles.

Figure 7 shows the flow functions (shear stress as a function of shear rate) of unfilled LDPE and LDPE filled with different volumetric concentrations of wood fibers. The volume concentrations correspond to typical mass fractions and have been discussed in previous studies [14].

All flow functions exhibit shear thinning flow behavior, which can be mathematically described by the power law of Ostwald/de Waele. With increasing volumetric content of the wood fibers, the level of the flow functions is shifted to higher values. Accordingly, the consistency indices (K) increase with the increasing volume fraction of the filler particles. The extent of the consistency increase depends on the size and geometrical shape of the filler particles. **Figure 8** shows flow functions of various filled LDPE systems at a fixed loading of 46 vol% to illustrate the impact of the filler morphology on the flow behavior. At low shear rates, the relative increase

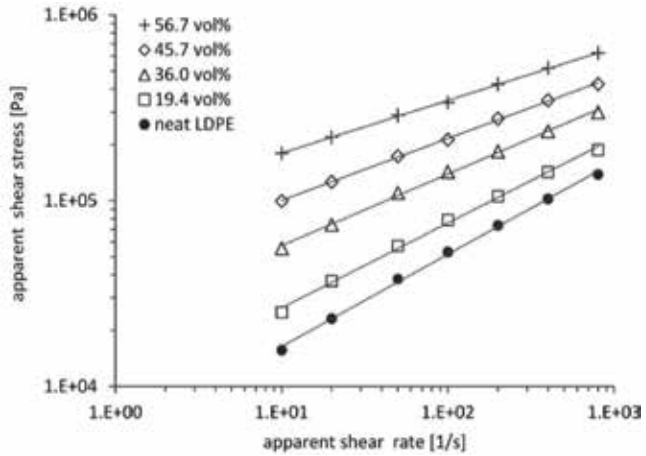

Figure 7. Flow functions of LDPE filled with varying volume fractions of wood fibers (d50 = 527 μm).

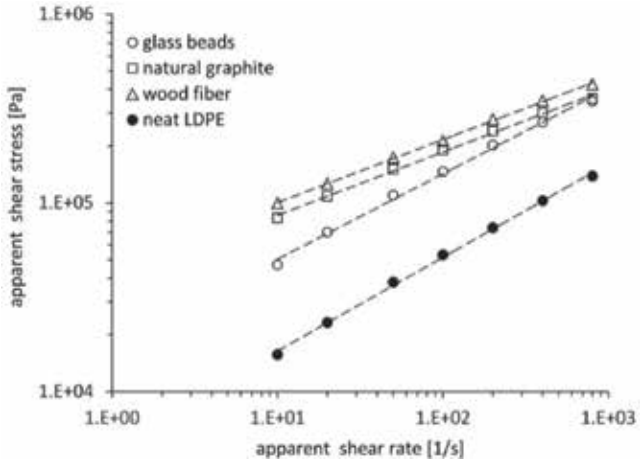

Figure 8. Flow functions of LDPE filled with 46 vol% of different fillers; glass beads (d50 = 346 μm), natural graphite (d50 = 267 μm), wood fibers (d50 = 527 μm) in comparison with the unfilled LDPE (T = 190°C).

in shear stress of the suspension to the shear stress of the polymer matrix is the highest for the fibrous particles (*wood fibers*), slightly lower for the plate-like particles (*natural graphite*), and the lowest for the spherical particles (*glass beads*). With increasing shear rates, the impact of the filler morphology on the flow behavior decreases.

In order to describe the impact of the volumetric filler concentration on the consistency index of particle-filled LDPE for various fillers in different size fractions, Eq. (7) has been used. **Figure 9** shows that experimental data (*symbols*) can be excellently fitted (*lines*) on the basis of this equation.

At low filler concentrations up to approx. 20 vol%, the particle properties, for example, particle size and morphology, have no significant impact on the extent of the consistency index

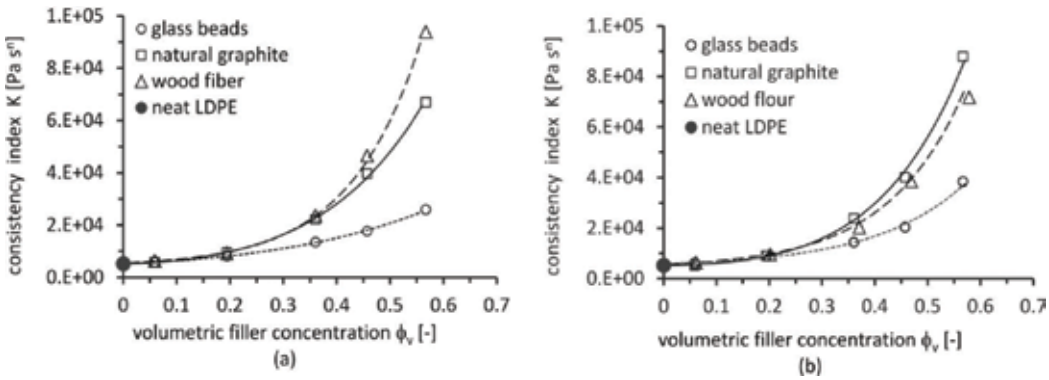

Figure 9. Consistency index as a function of volumetric filler concentration for LDPE filled with various fillers with different particle sizes, (T = 190°C); (a) glass beads (d50 = 346 μm), natural graphite (d50 = 267 μm), wood fibers (d50 = 527 μm); (b) glass beads (d50 = 60 μm), natural graphite (d50 = 77 μm), wood flour (d50 = 110 μm).

increase. At higher filler concentrations, the differences between the filler types are substantial. High aspect ratio particles such as wood fibers and natural graphite, regardless of their size, have a significantly greater impact on the consistency index than the spherical glass beads. Generally, the viscosity of a suspension and thus the consistency index exhibit higher values with decreasing particle size at a constant filler volume fraction. An exception can be observed here with the wood fillers. The small particle fraction contains a considerable amount of wood dust, which has a much lower aspect ratio as compared to the larger wood fibers. Since the impact of the aspect ratio on the consistency index increase is stronger in comparison with the particle size, the larger fibrous wood fillers cause a higher increase in consistency than the smaller particles of wood flour.

The *generalized interaction function* (Eq. (8)) is used in order to describe the interaction exponent as a function of the consistency index, taking into account the transition from negligible interparticle interactions to the domain of non-negligible interactions. **Figure 10** shows that experimental data (symbols) can be fitted (lines) on the basis of this equation with high accuracy.

The interaction function illustrates that glass beads in LDPE exhibit less interparticle interactions in comparison with particles with larger aspect ratio. In particular, large glass beads even show a range of negligible interparticle interactions with a transition to non-negligible interactions. Regardless of type and size, high aspect ratio particles have a characteristic relationship between consistency index and interaction exponent, which is distinctive of the polymer matrix LDPE.

Based on the *generalized interaction function* (Eq. (8)) and the relationship between consistency and volumetric filler concentration (Eq. (7)), the shift factor B can be derived as a function of the volume fraction for variable shear stresses (Eq. (6)). **Figure 11** comparatively illustrates the influence of the filler volume concentration and the applied shear stress for various fillers in

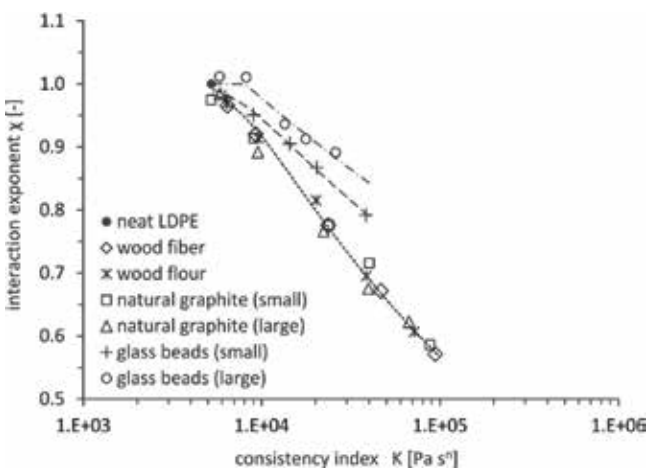

Figure 10. Interaction exponent as a function of consistency index of LDPE filled with various fillers (T = 190°C).

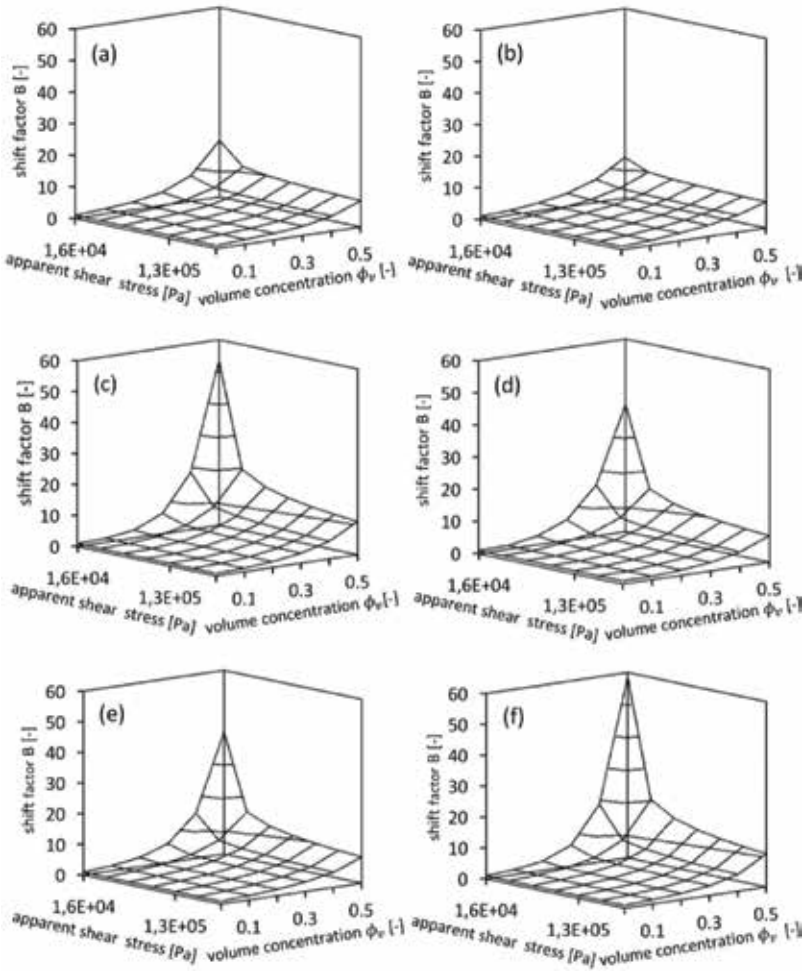

Figure 11. Shift factor B as a three-dimensional function of filler content and applied shear stress for LDPE filled with various fillers; (a) glass beads (d50 = 60 μm), (b) glass beads (d50 = 346 μm), (c) natural graphite (d50 = 77 μm), (d) natural graphite (d50 = 267 μm), (e) wood flour (d50 = 110 μm), (f) wood fibers (d50 = 527 μm).

different size fractions on the shift factor B. On the basis of the shift factor B, the flow behavior of polymer suspensions can be estimated for arbitrary volume concentrations and shear stresses or shear rates on the basis of the following equation:

$$\tau_c = B^{n_0} \cdot \tau_0 = B^{n_0} \cdot K_0 \cdot \dot{\gamma}^{n_0} \tag{9}$$

2.2. Polypropylene

The polymer matrix of all following compounds in this section is a polypropylene (PP), which exhibit a linear molecular structure and shear thinning flow behavior.

Figure 12 shows the flow functions (shear stress as a function of shear rate) of PP filled with different volumetric concentrations of wood flour, as well as of the unfilled polymer matrix.

As with particle-filled LDPE, all PP-based flow functions exhibit shear thinning flow behavior. In the observed shear rate range, the flow behavior can also be described very well by the power law. Compared to the LDPE-based compounds, the flow behavior index (n) of the PP-based formulations has slightly smaller values and thus a higher pseudoplasticity.

The influence of the filler morphology on the flow behavior of PP filled with different filler types at a fixed loading of 46 vol% is shown in **Figure 13**. Compared to long-chain branched LDPE, the impact of filler type on the flow function of linear PP is lower. Furthermore, it is obvious that the flow behavior index is only slightly affected by the different aspect ratio of the filler types.

On the basis of (Eq. (7)), the impact of the volumetric filler concentration on the consistency index of particle-filled PP has been described. **Figure 14** shows that experimental data (*symbols*) can be excellently fitted (*lines*).

Over the entire range of volume fraction, the differences between the filler types are substantial regarding the impact on the consistency index increase. Basically, a strong influence can be observed of the aspect ratio of the filler particles on the consistency increase. High aspect ratio particles such as wood fibers and natural graphite, regardless of their size, have a significantly greater impact on the consistency index than the spherical glass beads, especially at high filler contents.

Figure 15 presents the correlation between interaction exponent and consistency index, which have been mathematically described by the *generalized interaction function* (Eq. (8)). This contains all fillers; wood fibers/flour, natural graphite and glass beads, in the entire concentration range from 6 to 56 vol%, in each case in two particle size fractions.

It is a remarkable fact that there is a characteristic relationship between interaction exponent and consistency index for all PP-based compounds, regardless of filler type, size and volume

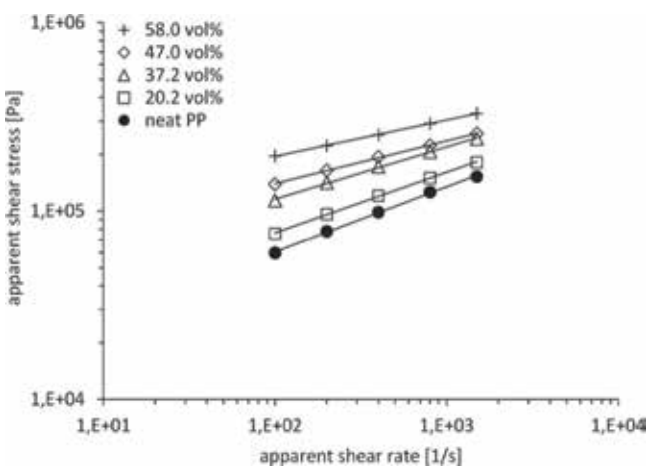

Figure 12. Flow functions of PP filled with varying volume fractions of wood flour (d50 = 110 μm), (T = 200°C).

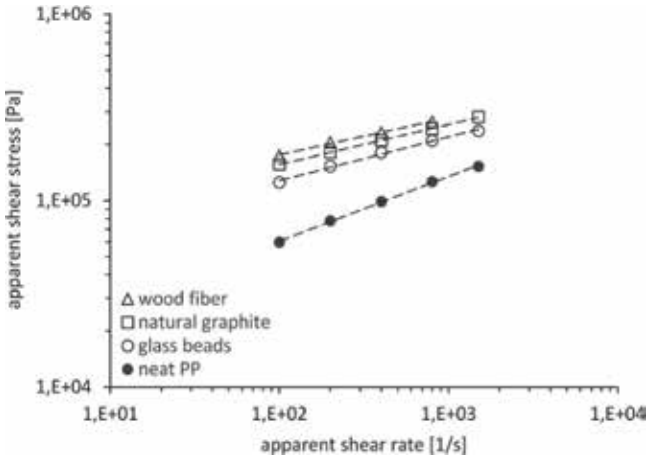

Figure 13. Flow functions of PP filled with 46 vol% of different fillers; glass beads (d50 = 346 μm), natural graphite (d50 = 267 μm), wood fibers (d50 = 527 μm) in comparison with the unfilled LDPE (T = 200°C).

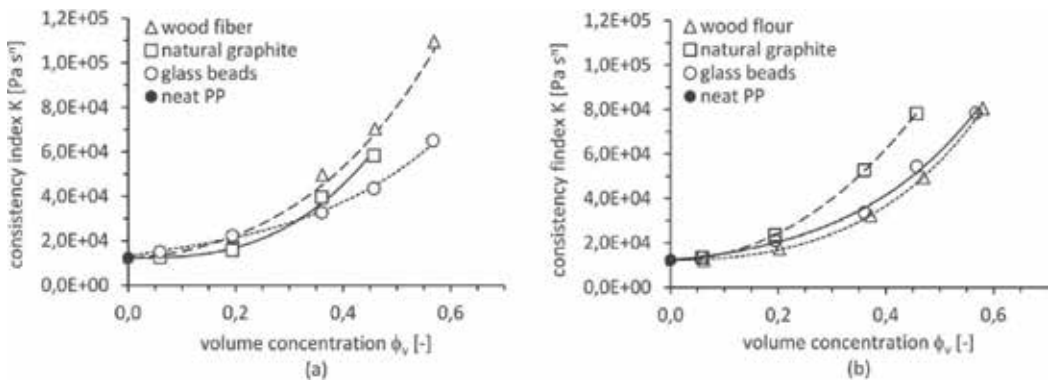

Figure 14. Consistency index as a function of volumetric filler concentration for PP filled with various fillers with different particle sizes, (T = 200°C); (a) glass beads (d50 = 346 μm), natural graphite (d50 = 267 μm), wood fibers (d50 = 527 μm); (b) glass beads (d50 = 60 μm), natural graphite (d50 = 77 μm), wood flour (d50 = 110 μm).

fraction. On the basis of this characteristic correlation, interparticle interactions in PP-based suspensions can be universally described with only one set of parameters of the generalized interaction function. The parameters that are generally valid for particle-filled PP to describe the interaction exponent as a function of consistency (Eq. (8)) index are:

$$K^* = 16706 \text{ Pa s}^n$$

$$a = 4.076$$

$$b = 0.385$$

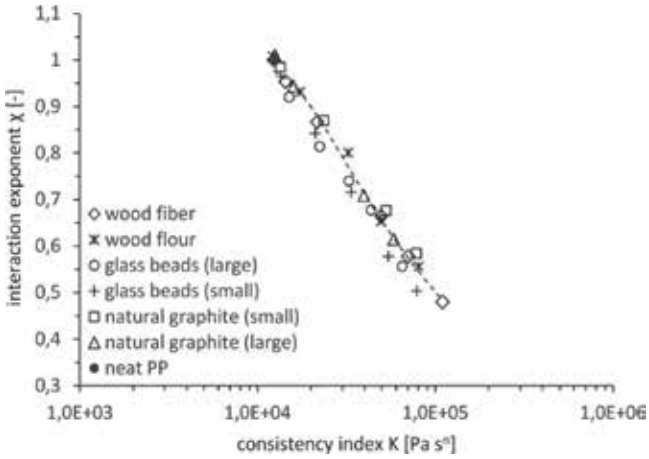

Figure 15. Interaction exponent as a function of consistency index of PP filled with various fillers (T = 200°C).

On the basis of these parameters, the flow curves of particle-filled PP can be estimated, regardless of the filler type, particle size, and volume fraction. **Figure 16** exemplarily illustrates this on different formulations. The experimental data (symbols) have been excellently fitted (lines), using that generally valid parameter set of the interaction function.

Figure 17 comparatively illustrates the influence of the filler volume concentration and the applied shear stress for various fillers in different size fractions on the shift factor B, which has been derived on the basis of (Eq. (6)). On the basis of the shift factor B, the flow behavior of polymer suspensions can be estimated for arbitrary volume concentrations and shear stresses or shear rates, respectively.

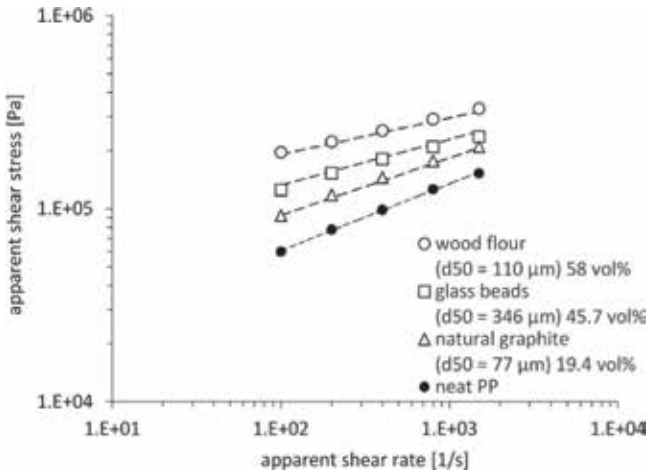

Figure 16. Comparison of experimental data (symbols) to predicted flow curves (lines) for PP filled with various fillers by using just one parameter set of the interaction function ($K^* = 16{,}706$ Pa s^n, a = 4.076, b = 0.385), (T = 200°C).

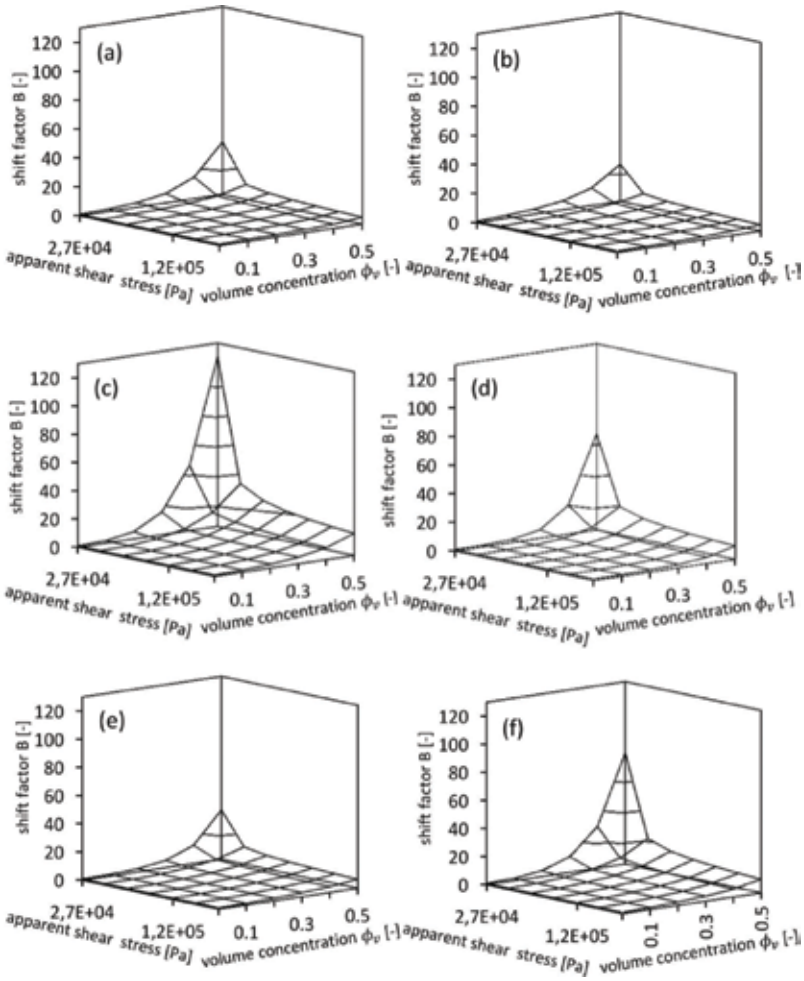

Figure 17. Shift factor B as a three-dimensional function of filler content and applied shear stress for PP filled with various fillers; (a) glass beads (d50 = 60 μm), (b) glass beads (d50 = 346 μm), (c) natural graphite (d50 = 77 μm), (d) natural graphite (d50 = 267 μm), (e) wood flour (d50 = 110 μm), (f) wood fibers (d50 = 527 μm).

3. Conclusion

In this chapter, new mathematical models describing interparticle interaction effects in long-chain branched and linear polymer matrices have been presented. In the context of studies with variable volumetric filler concentrations, the influence of filler type (morphology and aspect ratio) and particle size on interparticle interactions has been compared.

On the basis of the *generalized interaction function*, the correlation between interaction exponent and consistency index of particle-filled polymer melts can be mathematically described with high accuracy to experimental data. This correlation is characteristic and valid for each individual polymer matrix.

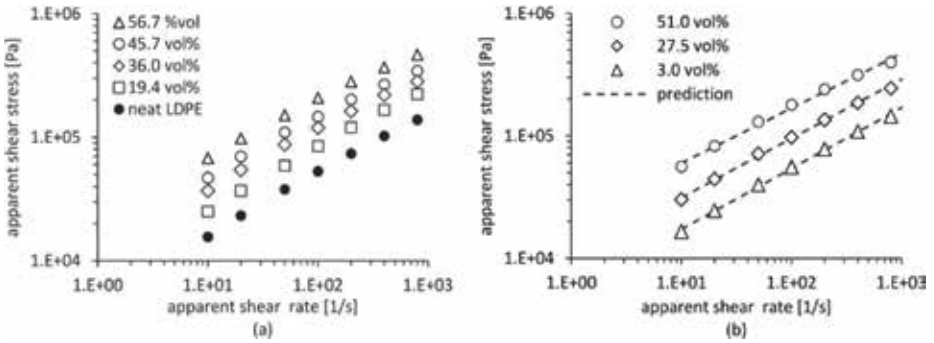

Figure 18. Flow functions of LDPE filled with varying volume fractions of glass beads (d50 = 60 μm), (T = 190°C); (a) measured values; (b) comparison of experimental data (symbols) to predicted flow curves (lines).

Based on the *generalized interaction function*, the shear thinning flow behavior of polymer suspensions can be estimated with high accuracy, regardless of filler type, particle size and volume fraction. The procedure for this is illustrated below using the example of LDPE filled with glass beads (d50 = 60 μm):

1. analysis of the flow functions for different filler concentrations (**Figure 18a**)
2. determination of the functional relationship between consistency index and volumetric filler concentration (Eq. (7))
3. determination of the functional parameters of the generalizes interaction function (Eq. (8))
4. derivation of the shift factor B (Eq. (6))
5. estimation of the flow functions for arbitrary volumetric filler concentrations (Eq. (9); **Figure 18b**)

Author details

Nico Laufer[1]*, Harald Hansmann[2], Christian Boss[1] and Stefan Ofe[1]

*Address all correspondence to: laufer@ipt-wismar.de

1 Institute for Polymer Technologies e. V., Wismar, Germany

2 Department of Mechanical Engineering, Hochschule Wismar University of Applied Sciences, Technology, Business and Design, Wismar, Germany

References

[1] Shenoy A. Rheology of Filled Polymer Systems. Dordrecht: Kluwer Academic Publishers; 1999 475 p. ISBN: 0-412-83100-7

[2] Einstein A. Eine neue Bestimmung der Moleküldimensionen. Annals of Physics. 1906;**324**:289-306. DOI: 10.1002/andp.19063240204

[3] Einstein A. Berichtigung zu meiner Arbeit: Eine neue Bestimmung der Moleküldimensionen. Annals of Physics. 1911;**339**:591-592. DOI: 10.1002/andp.19113390313

[4] Osswald T, Rudolph N. Polymer Rheology – Fundamentals and Applications. Munich: Carl Hanser Verlag; 2015. 225 p. ISBN: 978-1-56990-517-3

[5] Mueller S, Llewellin EW, Mader HM. The rheology of suspensions of solid particles. Proceedings of the Royal Society of London A. DOI: 10.1098/rspa.2009.0445

[6] HJH B. Viscosity of a concentrated suspension of rigid monosized particles. Physical Review E. 2010;**81**(5):051402-1/11. http://dx.doi.org/10.1103/PhysRev.81.1

[7] Hochstein B. Rheologie von Kugel- und Fasersuspensionen mit viskoelastischen MatrixflŸssigkeiten [Ph.D. Thesis]. UniversitŠt Fridericiana Karlsruhe: Karlsruhe; 1997

[8] Tadros TF. Rheology of Dispersions: Principles and Applications. Wiley: Weinheim; 2010. 199 p 978-3-527-32003-5

[9] Pasquino R. Rheology of viscoelastic suspensions [Ph.D. thesis]. Napoli: University of Naples Federico II; 2008

[10] Kitano T, Kataoka T, Shirota T. An empirieal equation of the relative viscosity of polymer melts filled with various inorganic fillers. Rheologica Acta. 1981;**20**:207-209. DOI: https://doi.org/10.1007/BF01513064

[11] Barnes HA. A Review of the Rheology of Filled Viscoelastic Systems. Rheology Reviews. 2003:1-36

[12] Hinkelmann B. Zur analytischen Beschreibung des Füllstoffeinflusses auf das Fließverhalten von Kunststoff-Schmelzen. Rheologica Acta. 1982;**21**:491. DOI: https://doi.org/10.1007/BF01534327

[13] Pahl M, Gleißle W, Laun H. Praktische Rheologie der Kunststoffe und Elastomere. VDI-Verlag GmbH: Düsseldorf; 1995. 448 p. ISBN: 3-18-234192-8

[14] Hansmann H, Laufer N, Kühn S. Investigation on the Flow Behavior of WPC Melts. In: 9th WPC, Natural Fibre and other innovative Composites Congress and Exhibition; 19-20 June 2012; Hanser, München: 2012. pp. A6-1–A6-11

[15] Khodakov GS. On suspension rheology. Theoretical Foundations of Chemical Engineering. 2004;**38**(4):430-439. DOI: https://doi.org/10.1023/B:TFCE.0000036973.95412.a3

[16] Laufer N, Koch M, Hansmann H, Boss C, Ofe S. Effects of Interparticle Interactions on the Flow Behaviour of Low Density Polyethylene Filled with Various Fillers. In: Europe Africa Conference 2017 of the Polymer Processing Society (PPS); 26-29 June 2017; Dresden

[17] Laufer N, Hansmann H, Koch M, Boss C, Ofe S, Düngen M. Influence of interparticle interaction effects on the rheological properties of low density polyethylene filled with glass beads. Polymer Testing. 2017;**62**:440-446. DOI: https://doi.org/10.1016/j.polymertesting.2017.07.019

[18] Laufer N, Hansmann H, Boss C, Ofe S. Effects of Volume Fraction, Size and Geometry of Different Fillers on Interparticle Interactions in LDPE Melts. In: 3rd International Conference on Rheology and Modeling of Materials; 02-06 October 2017; Miskolc-Lillafüred

Chapter 8

Rheology of Highly Filled Polymers

Christian Kukla, Ivica Duretek,
Joamin Gonzalez-Gutierrez and Clemens Holzer

Additional information is available at the end of the chapter

http://dx.doi.org/10.5772/intechopen.75656

Abstract

In many applications and/or manufacturing processes, highly filled polymers are necessary. One of these fields is powder metallurgy, where polymers or polymer mixtures are used to enable the shaping process within the production of the parts. Metal and also ceramic powders are mixed with different polymeric substances with a powder content of more than 50 vol%. Within the production, this mixture, called feedstock, has to flow into the final shape. Thus, for a proper understanding of the production processes, fundamental knowledge on the flow behavior of the feedstocks is required. For the rheology of polymers, several techniques together with the proper equipment are available. In the case of high viscosities, rotational and high-pressure capillary rheometers (HPCRs) are used. To gain reliable data, a proper measurement procedure is essential, which means that the operator has to have a deeper physical understanding of the material and the effects arising during the measurements. Therefore, this chapter gives an insight into rotational and high-pressure capillary rheometry with special emphasis on the behavior of polymers highly filled with stiff particles. Based thereon important remarks on the measurement equipment, procedure and evaluation of the measured data are provided.

Keywords: rheology, polymer, highly filled, feedstock, plate-plate rheometer, high-pressure capillary rheometer, yield stress, powder loading, Bagley correction

1. Introduction

The addition of inorganic or organic fillers into polymeric materials is an effective way to attain certain desirable properties for different applications [1].The rheological behavior is dependent on the amount of fillers in the liquid polymer. Other factors influencing the viscosity of the highly filled polymers are the particle size and shape, the particle size distribution,

the nature of the filler and the polymer matrix, as well as the use of coupling agents or compatibilizers. A detailed description of these influencing factors is given in [1].

For very dilute systems, the fillers are sufficiently apart that the interaction between them is negligible, and their rheological behavior is drastically changed when the concentration increases beyond 15 vol%, approaching a solid-like behavior [2]. However, the critical volume fraction, at which the solid-like behavior is observed, is a function of the particle shape and size distribution [1]. In this chapter, we discuss the flow behavior of filled polymers with a particle concentration well above 15 vol%, where the interparticle interaction cannot be ignored; these materials are referred at as highly filled polymers. Highly filled polymers have found applications in many industries including the adhesive, dental, battery, ceramic, metallurgy, electronics packaging, and solid propellant industries; therefore, understanding their flow behavior is crucial for many industrial applications [1].

In the literature, a wide variety of models to describe the dependence of the viscosity of mainly the volume concentration of the filler ϕ_P is available [3–12]. Other parameters like shape factors or interactions between the particles are also taken into account [1, 13]. Einstein was the first to address the suspension behavior in the dilute limit theoretically ([4], corrected 1911 [5]). Later on, further models have been developed. Regarding the concentration of the filler as the main parameter, these models can be structured into two groups [13]:

- Exponential models (Mooney [10] type) and
- Power-law models (Krieger [9] type)

In addition to [1, 13], we show in this chapter some models with a flow behavior integrating a yield strength.

Particular applications of highly filled polymers in the ceramic and metallurgy industries are ceramic injection molding (CIM), metal injection molding (MIM), and fused filament fabrication (FFF) [14, 15]. FFF is a special variant of material extrusion (ME) additive manufacturing (AM). In CIM, MIM, and FFF, a polymeric blend is used as a carrier or binder material for stiff powders during the fabrication of ceramic and metallic parts with complex geometry. Since the final part obtained at the end of these processes must be metal or ceramic, the filler content should be larger or equal to 50 vol% [15]. Measuring the rheological behavior of these materials is crucial to ensure that the correct processing conditions (e.g., for injection molding or extrusion) are used. Thus, it is one of the main motivations and backgrounds for preparing this chapter.

In this chapter, the methods used to measure the rheological properties of highly filled polymers with stiff fillers together with special issues or features of the rheological behavior of highly filled polymers are discussed in Section 2, and models used to describe the viscosity of highly filled polymers are explained in Section 3.

2. Measurement methods

Rheometers can be divided into two groups. In the first group, a material is dragged along a moving wall (like rotational rheometers), while in the second group, the sample is forced

through a channel, cylindrical pipe, or slit by means of pressure (like high-pressure capillary rheometers (HPCRs)) [2]. In this section, the specific details of performing rheometry on highly filled polymers with both types of rheometers are presented. It is important to remember that in order to have a complete rheological characterization of highly filled polymers both rheometers are needed to cover the range of shear rates that could occur during different processing operations [16].

2.1. Rotational rheometer

A rotational rheometer consists of a rotating or oscillating geometry and a fixed geometry; between these two geometries, the sample is sheared by a known torque when using a controlled shear stress (CSS) rheometer or a known deformation rate when using a controlled strain rate (CSR) rheometer. Several measuring geometries are available for rotational rheometers of polymeric materials; the most common examples are concentric cylinders (Couette or Searle Type), cone plates, and parallel plates (or disks) [2]. For highly filled polymers, parallel plates are the preferred measuring geometry (**Figure 1**). The main reason for using parallel plates is that the measuring gap can be adjusted. The high content of solid rigid particles in highly filled polymers could prevent reaching gaps smaller than 0.5 mm, which are required when using truncated cone-plate geometries and certain types of concentric cylinders. It is recommended that the measuring gap be at least 10 times larger but not larger than 50 times than the largest particle inside a suspension [2].

In order to satisfactorily measure rheological data in a rotational rheometer, two conditions need to be satisfied:

i. the sample must adhere to the plate surface and

ii. the flow must be laminar.

For highly filled polymers, adhesion to the plate surface can be complicated since the filler particles may be in direct contact with the plate surface and thus reduce the friction. Over time also particle migration or sedimentation might contribute to the formation of a low-viscosity depleted layer between the plate surface and the bulk of the fluid. Both conditions could lead to slip effects. In order to prevent slip from happening, it is recommended to use serrated plates (instead of smooth plates), as shown in **Figure 2**. The serrated plates provide enough grip between the sample and the measuring plates; thus, the sample is

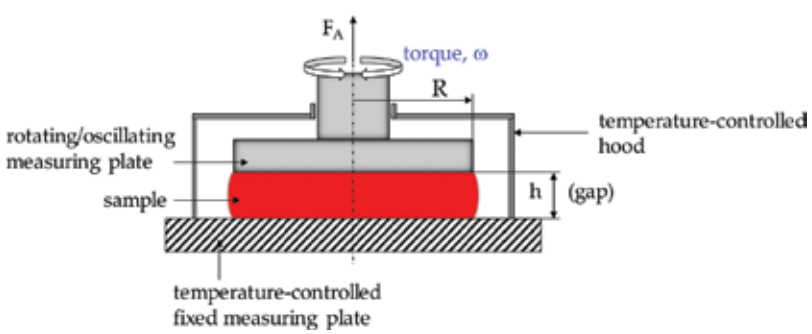

Figure 1. Schematic drawing of the parallel plate rheometer.

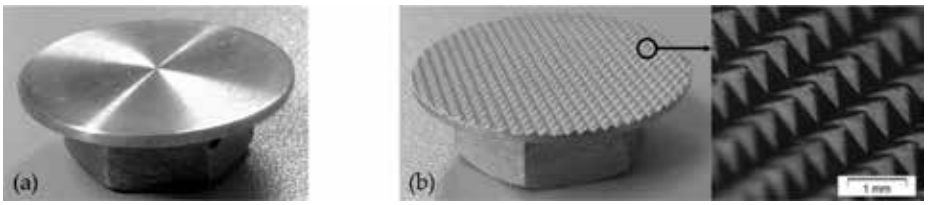

Figure 2. Measuring plate geometries: smooth (a) and serrated (b).

homogeneously sheared throughout its bulk, satisfactorily preventing slip. Using deep channels or smaller features on the plate is not sufficient to prevent slip during rotational rheometry measurements as it has been shown elsewhere [16].

For highly filled polymers, it is recommended to use a measuring gap between 0.5 and 1.5 mm and serrated plates with a diameter between 20 and 25 mm. The sample should be prepared by pressing the highly filled polymeric pellets into disks of slightly larger dimensions than the selected measuring plate and the desired gap, in order to ensure reaching the selected gap without air gaps in the highly viscous sample. Once the measuring temperature is selected and the measuring chamber has reached the set temperature, the sample can be introduced. When it has reached the measuring temperature, the movable plate is slowly brought to the measuring gap. It is important to remove the excess material coming out from between the measuring plates and that the normal force is zero before starting the measurement in order to prevent artificially increasing the measured viscosities. In a previous investigation, it was observed that a tenfold increased normal force leads to a viscosity increase of one order of magnitude [16].

Viscosity measurements of highly filled polymers are usually performed in constant rotational mode and not in the oscillatory mode because the Cox-Merz rule [17] is not valid for highly filled polymers (see also Section 2.6). The shear rate range for highly filled polymers is also quite narrow (10^{-4} to 10^{-1} s^{-1}). The large amount of fillers leads to a yield stress near the zero shear stress limit, and therefore, a high viscosity value is observed at low shear rates [18]. Once the rotating plate starts to move, the filler particles start to orient in the direction of flow and therefore a clear shear thinning behavior is observed for most highly filled polymers. Continuously shearing the sample eventually leads to melt fracture and sample expulsions, which lead to an abrupt and irreversible drop in the viscosity; therefore, only the viscosity measurements before melt fracture should be considered [2]. Sample expulsion is very common and can occur already at shear rates of 10^{-1} s^{-1}, but this depends on the filler content and the type of polymer.

When measuring highly filled polymers, preshear should be applied. This is especially important for thixotropic materials and those materials that show a yield stress. This can be used to set the initial state of the sample and increase the repeatability of rheological measurements of highly filled polymers [2].

Finally, care should also be taken when selecting the time of the experiment, since prolonged exposure to temperatures above the melt temperature of the suspending polymers could lead to chemical changes in the sample [2]. Furthermore, it is always recommended to perform rotational rheometry measurements in an oxygen-free atmosphere and not to use high shear rates.

2.2. High-pressure capillary rheometer

The high-pressure capillary rheometer (HPCR) allows the routine analysis of the flow and viscosity of polymer melts at shear rates from 10 to 10^6 s^{-1}. The realizable shear rate range depends on the viscosity of the tested material, the measurement temperature, and the used die geometry (e.g., round die or slit die).

The HPCR comprises a temperature-controlled test barrel and an exchangeable die at its end. The geometry of the die is variable. The melt inside the test barrel is pressed through the round or slit die by means of a test piston. When all test parameters are defined and the system reaches the test temperature, the test barrel can be filled with polymer granulate. In order to fill it bubble free, the material should be filled in portions. After each portion, the material should be pressed manually with a tamper or with the test piston. The measurement is ready to begin when the test barrel is full. Then, the preheat time (or melting time) starts. At the end of the preheat time, the test starts automatically by the movement of the piston with the first preselected feed rate. The melt pressure is measured by using mounted pressure transducers before the round die or along the slit length of the slit die (**Figure 3**). As soon as the pressure varies exactly within the tolerance limit, the speed of the piston is recorded. Therefrom, the apparent viscosity data are calculated immediately. At the same time, the piston speed is increased to the next value. In this way, the whole speed program is run step by step.

In the following section, the two types of dies used for HPCR are presented together with a discussion of important points one should be aware of when measuring viscosities with them.

2.2.1. Round die

High-pressure capillary rheometers with round dies (**Figure 3**, left) are widely used in polymer melt rheometry. Round dies exist in different lengths with the same diameter (e.g.,

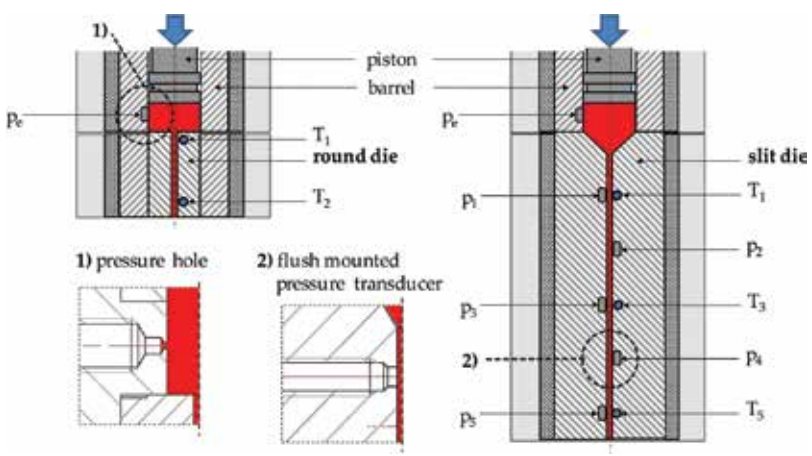

Figure 3. Schematic drawing of the high-pressure capillary rheometer with the round and slit die; p—Pressure transducers and T—Thermocouple (wall temperature).

L/D = 10, 20, and 30). The entrance angle of a round die is 180°. To measure the temperature near the die wall, thin thermocouples can be attached to the die as shown in **Figure 3**.

From geometrical data, the speed of the piston, and the related pressure drop, the so-called apparent viscosity is calculated [19]. In order to obtain the correct viscosity of polymeric materials, two corrections are commonly applied to round dies data: the Bagley correction [20] and the Weissenberg-Rabinowitsch correction [21]. The Bagley correction takes care of the nonideality arising from viscoelastic effects at the entrance of the die. During the melt flow in the die inlet, outlet pressure losses develop. For the correction of these inlet and outlet pressure losses, the Bagley correction can be used. Therefore, several measurements with capillaries with the same diameter but with different lengths have to be done.

The plotted measured pressures (p_{meas}) in front of the die versus L/D ratio in general can be described by a linear function for each individual shear rate. The extrapolation of these straight lines to the L/D ratio = 0 provides the pressure correction value p_{en} mentioned in Eq. (1) [21].

$$\tau_{\bigcirc} = \frac{(p_{meas} - p_{en}) \cdot R}{2 \cdot L} \tag{1}$$

where $\tau_{\bigcirc}$ is true shear stress, p_{en} is entrance pressure loss, and R is die radius.

The apparent shear rate for round die $\dot{\gamma}_{app,\bigcirc}$ is calculated by using Eq. (2) [19].

$$\dot{\gamma}_{app,\bigcirc} = \frac{4 \cdot \dot{V}}{\pi \cdot R^3} \tag{2}$$

with $\dot{V}$ as the volumetric flow rate.

The Weissenberg-Rabinowitsch correction for the round die (Eq. (3)) considers the fact that the shear rate mentioned in Eq. (2) is only valid for Newtonian fluids and provides the true shear rate at the capillary wall for them [22].

$$\dot{\gamma}_{\bigcirc} = \frac{\dot{\gamma}_{app,\bigcirc}}{4}\left(3 + \frac{d \log \dot{\gamma}_{app,\bigcirc}}{d \log \tau_{\bigcirc}}\right) \tag{3}$$

Finally, the true viscosity is calculated from Eq. (4).

$$\eta = \frac{\tau_{\bigcirc}}{\dot{\gamma}_{\bigcirc}} \tag{4}$$

2.2.2. Slit die

In the slit die, the pressure gradient, which is used to calculate the viscosity, is measured by using a series of pressure transducers along the length of the slit. **Figure 3**, right, gives a schematic drawing of the HPCR with slit die. The pressure profile along the slit die is measured by melt pressure transducers p_1 to p_5. The pressure transducer p_e gives the pressure at the die entrance. The temperature at the die wall is recorded by using thermocouples, which are fixed very near to the inner wall of the slit. The slit die has the rectangular channel of width (B) and height (H).

The pressure drop Δp can be determined by taking the difference of two pressures measured along the flow length and the corresponding distance ΔL between the pressure transducers. Thus, no Bagley correction is necessary when the pressure drop is measured along the slit. However, a so-called shape factor F_p [23] in Eq. (7) might be employed to account for the influence of the width in the rectangular flow channel [19]. The true shear stress $\tau_\square$ can be calculated from the measured pressures along the slit length and geometrical parameters of slit die, by using Eq. (5) [24].

$$\tau_\square = \frac{\Delta p \cdot H}{2 \cdot \Delta L} \tag{5}$$

Eq. (5) is applicable when the ratio B/H is greater than 40; in other cases, $\tau_\square$ is given by [19]

$$\tau_\square = \frac{\Delta p \cdot (B \cdot H)}{2 \cdot \Delta L \cdot (B + H)} \tag{6}$$

The apparent shear rate $\dot{\gamma}_{app,\square}$ is given by Eq. (7) [23].

$$\dot{\gamma}_{app,\square} = \frac{6 \cdot \frac{\dot{V}}{F_p}}{B \cdot H^2} \tag{7}$$

The Weissenberg-Rabinowitsch correction (Eq. (8)) adjusts the shear rate at the wall for the non-Newtonian liquids. The true shear rate at the wall for a slit die ($\dot{\gamma}_\square$) is calculated by [22]:

$$\dot{\gamma}_\square = \frac{\dot{\gamma}_{app,\square}}{3}\left(2 + \frac{d \log \dot{\gamma}_{app,\square}}{d \log \tau_\square}\right) \tag{8}$$

Finally, the true shear viscosity is calculated by using Eq. (9).

$$\eta = \frac{\tau_\square}{\dot{\gamma}_\square} \tag{9}$$

Figure 4 summarizes the calculation of the viscosity from measurements using round or slit dies in the form of a flowchart.

2.2.3. Remarks on Bagley correction

In general, the pressure curves show straight lines with a certain negligible nonlinearity in **Figure 5**, left. Highly filled polymers like some MIM feedstocks can exhibit nonlinear Bagley curves that give negative entrance pressure losses when linearized, which has no physical meaning.

Figure 5, right, shows the results of the Bagley extrapolation on an MIM feedstock. The linear approximation of the measured values results in negative entrance pressure losses. The reasons for this can be the pressure dependence of the viscosity [25] and errors in the pressure measurement by using of pressure holes, especially in the low pressure range. A pressure hole is generally used when using round dies (insert 1 in **Figure 3**) since it is not possible to

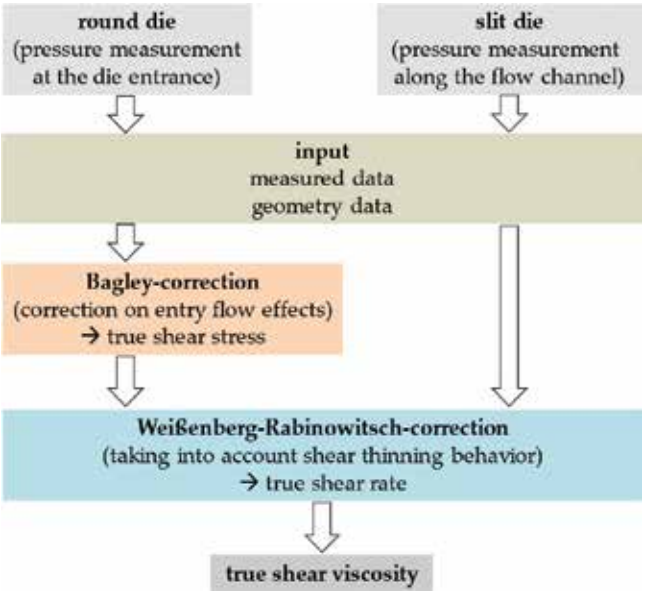

Figure 4. Flowchart of the process used to calculate the true viscosity.

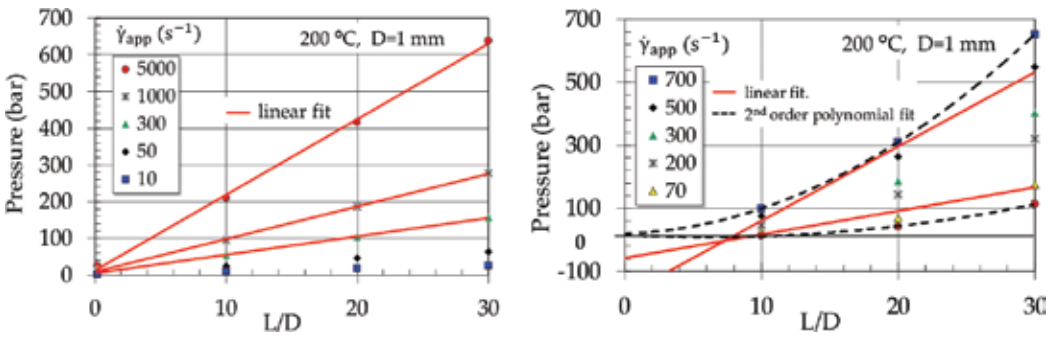

Figure 5. Bagley diagram. IN718 feedstock (left) and 316LS feedstock [28] (right).

mount a pressure transducer flush to the wall of a round die as in a slit die (insert 2 in **Figure 3**). The occurrence of wall slip and different particle distributions can also lead to nonlinear Bagley plots. Nyborg [26] and Bilovol [27] also reported negative entrance pressure losses from measurements on MIM feedstocks.

2.2.4. 'Pressure hole effect'

The comparison of the viscosities of an MIM feedstock measured with round and slit dies at a temperature of 200°C is shown in **Figure 6**. The viscosity measured with the round die (D = 1 mm) is about 16% higher than that of the slit die (H = 1 mm). The cause of this difference may be related to anisotropic pressure propagation in the pressure measurement when

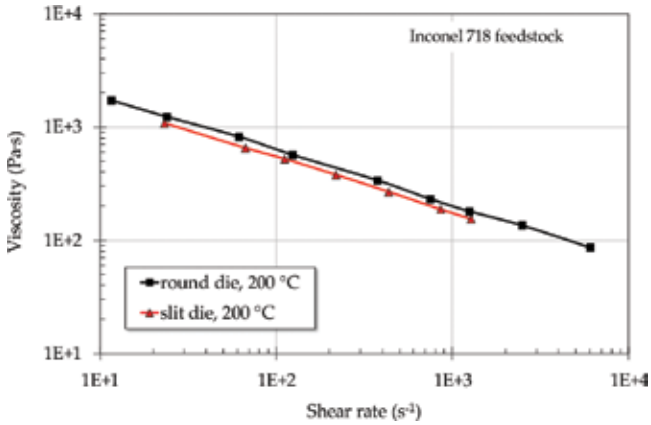

Figure 6. Comparison of the viscosity measured with round and slit die for IN718 feedstock; measurement at the high-pressure capillary rheometer.

using a pressure hole (insert 1 in **Figure 3**). We are dealing with highly filled polymers with more than 50 vol% of powder, and a network of powder grains is no good means for pressure propagation. This refers to the potential source of error termed "pressure hole effect" [29–31].

2.2.5. Pressure fluctuations

Pressure is one of the most important parameters in viscosity calculation. In rheological measurements, the pressure is determined in such a way that for each shear rate, the disturbances in the pressure values must be less than 1%. Usually, these pressure fluctuations are higher in highly filled compounds. They are dependent on the filler content and particle size.

The pressure profile measured with the slit die (H = 1 mm) on PE compound with flame retardant Al(OH)3 shows considerable pressure fluctuations up to ±50 bar (± 14%) and more (**Figure 7**, left). The melt strand coming out of the slit die showed a cyclic change between smooth and wrinkled (**Figure 7**, left, inserted photo) and the measured pressure is clearly unsteady (**Figure 7**, left, inserted diagram). This can be attributed to the stick-slip effect. The pressure profile measured with the slit die on a titanium feedstock also shows considerable pressure fluctuations up to ±20 bar and more (**Figure 7**, right).

2.2.6. Influence of preshearing history on viscosity and homogeneity

Earlier rheological investigations [33–35] showed that the shearing in the plasticizing cylinder of the injection molding machine has a significant influence on the flow behavior of MIM feedstocks.

Figure 8 shows the viscosities of 316LA MIM feedstock measured with the same slit die on the high-pressure capillary rheometer and on the injection molding machine rheometer at three temperatures. The slit die of the capillary rheometer was mounted on the injection molding machine (IMM) with the appropriate adapter [35]. As expected, both measurements give the

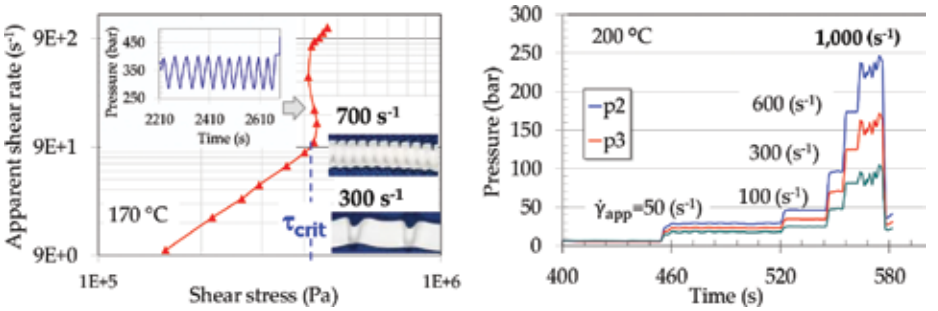

Figure 7. Stick and slip effect. PE compound with flame retardant Al(OH)3 [32] (left) and Ti feedstock (right).

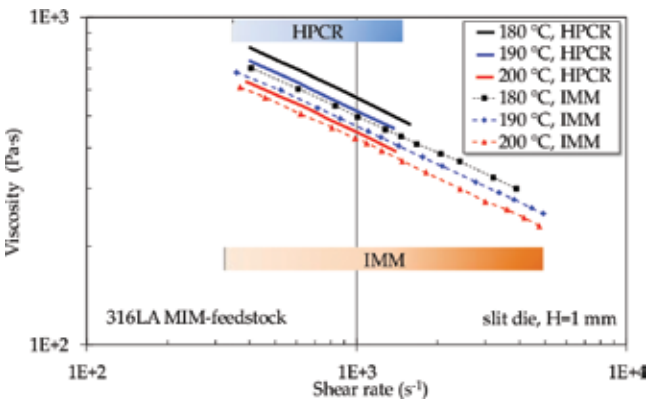

Figure 8. Comparison of viscosity measurements on high-pressure capillary rheometer (HPCR) and injection molding machine (IMM) [35].

similar slope of viscosity curves but at different levels. The viscosities measured at the injection molding machine are lower than those at HPCR. The most likely reason is preshearing of the melt by the screw during plasticization. This leads to better homogenization of the feedstock. Furthermore, the temperature distribution within the melt in the plasticizing cylinder of the IMM could also have an influence.

2.3. Yield stress

In contrast to unfilled thermoplastics for highly filled polymers at very low shear rates, no Newtonian plateau is observed but instead the viscosity increases strongly. This indicates the possible presence of the limiting shear stress also known as yield stress or yield point. The yield stress is classically defined as the minimum shear stress that must be applied to the material to initiate flow. In addition, yield stress is generally denoted as the transition stress at which a material behaves either as elastic solid-like or viscous liquid-like. This transition usually occurs within a range of stresses, in which the material exhibits viscoelastic behavior [36, 37]. Moreover yield stress can be defined as the force per unit area necessary to overcome interparticle interactions and its magnitude is determined by the overall strength of

the interparticle network. When the stress exceeds the yield stress, the fluid will flow like a viscous fluid with a finite viscosity.

The most common way for determining the yield stress is from a flow curve measured on a rheometer. It involves the extrapolation of the flow curve to zero shear rate using mathematical models such as Bingham, Herschel-Bulkley, Cross-Herschel-Bulkley, or CARPOW.

When using models based on measurements with the HPCR only, accuracy could be not satisfying, because the HPCR gives data only at higher shear rates, which have to be extrapolated to zero.

A better method for the yield point determination is by the rotational rheometer, preferably in the controlled shear stress (CSS) mode. Here, by plotting deformation γ versus shear stress τ in a double logarithmic scale, two regions with different slopes exist (**Figure 9**, right). The first one (lower slope) is the elastic deformation region, while the second one (steeper slope) is the viscous flow region. The yield stress can be detected as the transition point in the slope of the two power law regressions [38].

CSS is more sensitive and provides more accurate results of yield stress than CSR. Better results are obtained by a combination of CSS measurements (low shear rates) and high-pressure capillary rheometer measurements (high shear rates).

It is evident that the choice of the method or model yields different values of yield stress. However, the accuracy depends on the sensitivity of the equipment and the skills of the operator. The previous investigations [39] show there is no single best method to measure yield stress of highly filled polymers, such as MIM feedstock.

2.4. Powder loading

A second important point for highly filled polymers is that the viscosity is a function of the characteristics of the powder and of the volume powder content ϕ_p. It has been observed that the viscosity of concentrated suspensions, including MIM and CIM feedstocks, increases rapidly and nonlinearly as the solid content increases [8].

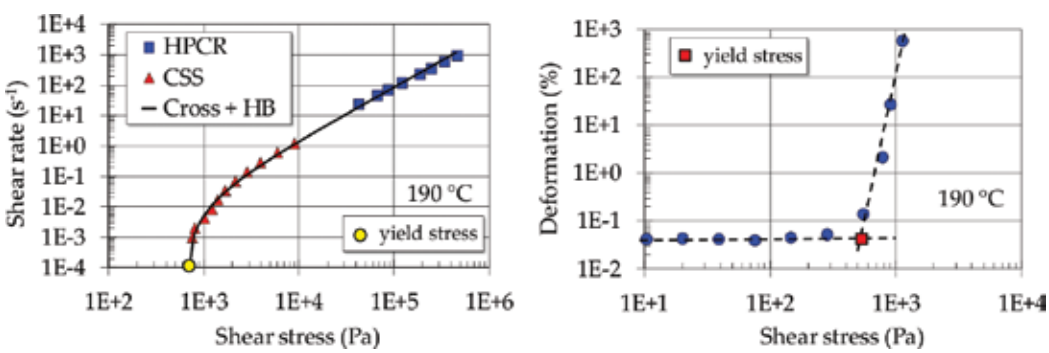

Figure 9. Flow curve measured with rotational (CSS) and high-pressure capillary rheometer (HPCR) for 316 L feedstock: fitting the experimental curves using Cross-Herschel-Bulkley model (left) and determination of the yield stress with rotational rheometer, CSS (right) [40].

Figure 10 shows the comparison of the measured to the calculated increase in viscosity by increasing φ_p of the feedstock at shear rate of 100 s^{-1}. Here the relative viscosity η_r is used, which is the ratio of the viscosity of the feedstock with a certain powder loading to the viscosity of the polymeric binder system at a given shear rate and temperature. For lower powder loadings, the Frankel-Acrivos model [6] provides a better fit to the measured data; for higher powder loadings, the Krieger-Dougherty model [9] is better. It has to be emphasized that the fit is dependent also on the shear rate at which the data were measured and other models available in the literature might fit better [12].

Most of the models in the literature and also the ones used in **Figure 10** are shifting the viscosity curve along the y-axis in a double logarithmic viscosity-shear rate diagram as the powder content increases (**Figure 11**, green arrow). This does not describe the behavior of feedstocks in a proper way. One main point is the shear rate at which the transition from Newtonian to shear thinning behavior takes place. This shear rate is a function of the powder loading ϕ_p and cannot be described by the models mentioned before [12]. Geisbüsch [42] used a model which is based on the fact that the binder is sheared more when more powder is in the feedstock. This model is based on the fact that the powder can be regarded as rigid. Thus the deformation in a shear field has to be taken by the binder (**Figure 11**, right), which means that the binder is sheared more, resulting in a lower viscosity of the binder (due to the shear thinning behavior of a polymer [43]). All together the viscosity is shifted to higher values by higher powder loading and somewhat decreased by higher dissipation inside the polymer due to enhanced shear strain (**Figure 11**, red arrow).

2.5. Temperature influence

One generally neglected effect on the measured viscosity data is the rise of the temperature due to dissipation. In a standard measurement setup of a high-pressure capillary rheometer, a temperature is chosen and set in the control unit. Usually there is no temperature transducer mounted inside the flow channel. Thus, the set temperature value is assigned to the derived viscosity curve.

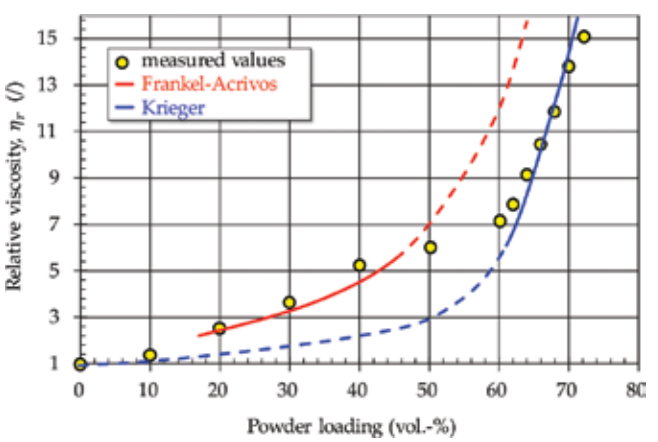

Figure 10. Comparison of measured with predicted values of relative viscosity η_r [41].

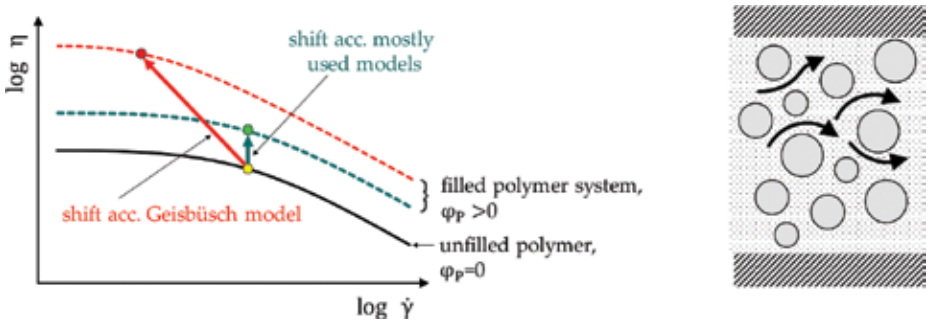

Figure 11. Schematic viscosity diagram of a filled polymer system; shift acc. Geisbüsch and mostly used model (left), shear enhancement in the binder (right).

But in reality, a certain heat dissipation takes place. The assumption of isothermal conditions is only applicable if the related rise in temperature is small. For unfilled polymers, this effect cannot be neglected at very high shear rates only (10^5 to 10^6 s^{-1}). In our case of stiff fillers (between 50 and 60 vol% of filler), nearly all the dissipated heat is generated in the matrix, since the stiff filler is more or less just 'swimming' with the flow of the polymer (**Figure 11** right). As reported previously [44], at a shear rate above 100 s^{-1}, nearly all dissipated heat will stay in the polymer resulting in a higher temperature and at the same time a lower viscosity of the polymer. Therefore, the actual temperature, which should be assigned to a specific value of viscosity, is higher than the normally used one. Using the actual temperature data gives in the end a flatter viscosity curve.

2.5.1. Temperature development in the slit die and temperature correction

Rheological measurements on unfilled polymers [45–47] and on MIM feedstocks [33, 35, 44] show an initial increase of the measured die wall temperature.

Figure 12 shows, as an example, the measured temperature profiles of the die wall temperatures for 316 L MIM feedstock from experimental measurements with the slit die on HPCR at 190°C.

The analysis clearly shows (**Figure 12**) the increase of the temperature due to shear dissipation from an apparent shear rate up to approximately 7 K at the highest shear rate of 10^3 s^{-1}. Thus, the measured data needs to be corrected with respect to temperature. So the melt temperature rise due to dissipative heating and compression heat was taken into account by applying a special temperature correction procedure [45]. For this purpose, a thermodynamic dimensionless number, the so-called Cameron number [48], is used, and the temperature corrected viscosity is obtained. Utilizing a modified Agassant method [45, 49], the average melt temperature inside the flow channel is calculated and applied to adjust the viscosity. The shear viscosities obtained under varying temperatures can be transformed into a single master curve by applying the time-temperature superposition principle [45, 49].

Estimation of temperature rise in a polymer highly filled with stiff powders and the related viscosity correction.

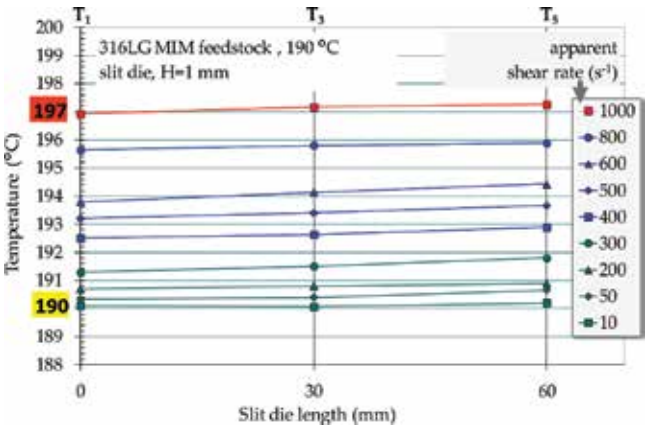

Figure 12. Temperature profiles at different shear rates (slit die) [35].

In injection molding of highly filled polymers, high shear rates occur. Since the fillers are stiff, all the shear has to be taken up by the polymer system. In case of high shear rates, one has to consider whether due to the short times the generated heat stays to a high extent in the polymer or it is conducted into the powder. Therefore, we evaluated the contribution of viscous dissipation over the heat conduction normal to the direction of flow by calculating the Griffith number (Gr). The calculation of Gr showed that at high shear rates (higher than 100 s^{-1}), the heat generated in the binder due to viscous dissipation is larger than the heat transmitted by conduction to the metal particles (i.e., Gr > 1), and thus, the binder will have higher temperature than the filler particles [44].

Using the estimated temperature rise, one can correct the viscosity at high shear rates and use the model proposed by Geisbüsch [42] to predict the measured data. This is shown in **Figure 13** for the particular example of 60 vol% MIM feedstock. The viscosity values were shifted by using the Arrhenius equation, and it can be seen that the prediction from the model has improved at the higher shear rates [44].

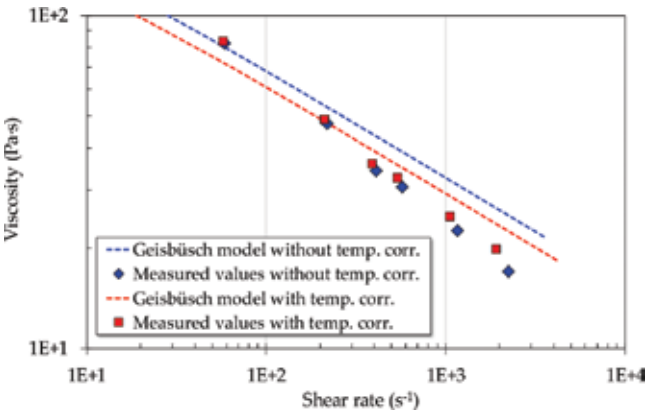

Figure 13. Viscosity corrections due to temperature increase at high shear rates and predictions by the Geisbüsch model for 60 vol% feedstock [44].

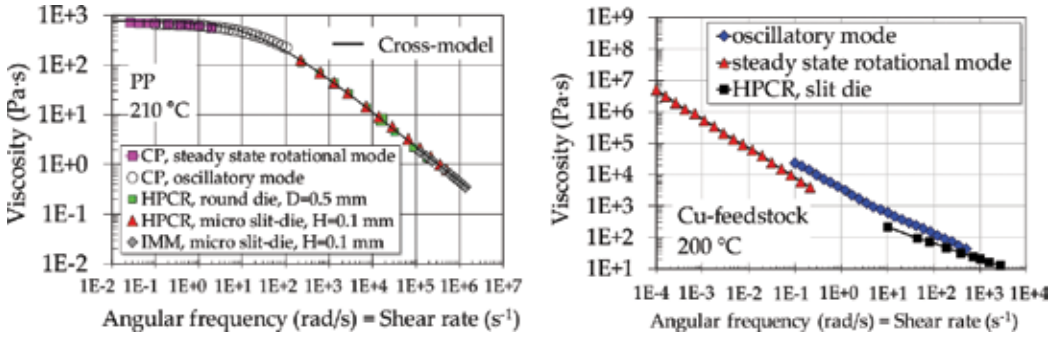

Figure 14. Cox-Merz rule as an example for unfilled polypropylene [49, 50] (left) and for highly filled Cu feedstock (right); CP—Cone-plate rheometer, HPCR—High-pressure capillary rheometer, and IMM—Injection molding rheometer.

2.6. Cox-Merz rule and highly filled polymers

The rheological behavior of highly filled polymers is a complex function of its physical properties and the processes that occur at the scale of the suspended particles. Therefore, there are special considerations that do not apply to highly filled polymers but are applicable to unfilled polymers. For example, the Cox-Merz rule [17], which states that the viscosity measured in oscillatory mode is equivalent to the viscosity measured in steady-state rotational mode or in a capillary rheometer (**Figure 14**, left). The Cox-Merz rule is quite useful to extend the range of shear rates or angular frequencies, where the viscosity can be measured without sample fracture, secondary flows, and material expulsion. However, for highly filled systems, it does not apply as shown in **Figure 14**, right. In oscillatory mode, the viscosity values (complex viscosity) tend to be overestimated with respect to the measurements obtained in steady-state rotational mode or by high-pressure capillary rheometry.

3. Viscosity models

The mathematical model describing quantitatively the relation between shear stress and the shear strain during flow of the polymeric fluids is called the constitutive equation. Even though the molecular structure and viscoelasticity of polymeric materials are quite complicated, various forms of constitutive equations have been proposed.

In order to describe, for example, the injection molding process, a viscosity function is necessary, which is valid over the whole process range. The viscosity as a function of temperature, shear rate, and pressure is needed for the calculation of the filling and holding pressure phase; it has an effect on the pressure calculation and the holding pressure efficiency.

For the injection molding simulation, it is very important to describe the viscosity, as the shear rate approaches zero, as accurately as possible. This behavior is significant in the post-pressure phase because here the melt speeds are very small overall. In addition, even during the faster filling phase, due to a symmetrical velocity profile, the shear rate in the middle of the channel is zero. For highly filled polymers at low shear rates (<0.1 s^{-1}), the viscosity increases and a yield point can occur (**Figure 15**). This means that viscous flow is only observed above a

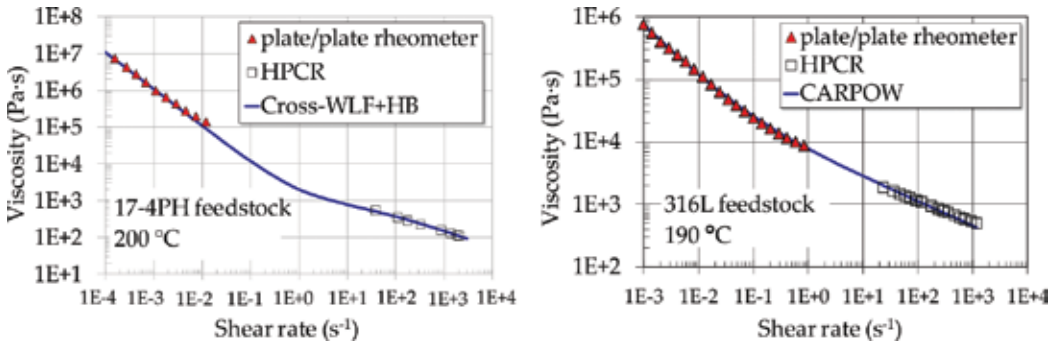

Figure 15. Approximation of the viscosity curve of two different feedstocks using Cross-WLF model with Herschel-Bulkley (HB) extension (left) and CARPOW model (right).

Model	Equation of the model	
Cross-WLF with Herschel-Bulkley extension	$\eta = \frac{\eta_0}{1+\left(\frac{\eta_0 \cdot \dot{\gamma}}{D_4}\right)^{(1-n)}} + \tau_\gamma \cdot \left(\frac{1-e^{(-\alpha \cdot \dot{\gamma})}}{\dot{\gamma}}\right)$ [51]	(10)
	$\eta = \frac{\eta_0}{1+\left(\frac{\eta_0 \cdot \dot{\gamma}}{D_4}\right)^{(1-n)}} + \frac{\tau_{y0} \cdot e^{\left(\frac{T_y}{T}\right)}}{\dot{\gamma}}$ [52]	(11)
	$\eta_0 = D_1 \cdot e^{\left[\frac{-A_1(T-T_S)}{A_2+(T+T_S)}\right]}, T_S = D_2 + D_3 \cdot p, \quad A_2 = \tilde{A}_2 + D_3 \cdot p$	
CARPOW	$\eta = \frac{d_c \cdot a_T}{(a_T \cdot b_1 + \dot{\gamma})^{n_1}} + \frac{A \cdot a_T}{(1+\dot{\gamma} \cdot B \cdot a_T)^C}$ [53]	(12)

where D_1, D_2, D_3, D_4—cross coefficients, η_0—zero shear viscosity, τ_γ, α and τ_{y0}, T_y—coefficients of Herschel-Bulkley extension, $\dot{\gamma}$—shear rate, $A_1, A_2, \tilde{A}_2$—Williams-Landel-Ferry (WLF) coefficients, p—pressure, T—temperature, T_S—reference temperature, a_T—temperature shift factor acc. Arrhenius or WLF, d_c—consistency parameter (toughness of the highly filled system), b_1—turning point of the viscosity curve, n_1—flow exponent of low shear rate range, and A, B, C—Carreau coefficients.

Table 1. Selected models to describe shear rate and temperature dependents of viscosity.

minimum wall shear stress. As mentioned before, the cause of this phenomenon is an interaction of the filler particles with each other or with the polymer matrix. Due to the increase in viscosity at low shear rates, the behavior of highly filled polymers in the low shear rate range resembles that of a solid rather than a polymer melt.

For the description of the temperature-dependent flow behavior in a wide shear rate range of unfilled and little-filled polymers, a number of viscosity models have been published, such as the well-known Carreau model and Cross model [43, 48]. The flow behavior of highly filled polymer compounds like MIM feedstocks can be described with the models shown in **Table 1**. These viscosity models offer the opportunity to approximate the measured viscosity data at low shear rates with yield stress and the viscosity at high shear rates with shear thinning behavior. Examples of the fit of these models are given in **Figure 15**.

4. Conclusion

Good rheological data are necessary for a proper optimization of the production using highly filled polymers and also for good simulations of the related production processes. Since simulation of a production process needs a good virtual model of this process, the correct understanding of the occurring physical effects is vital.

Rheology of highly filled polymers is the tool in place to gain such a deeper understanding. On the other hand, it is essential to have this understanding when measuring reliable rheological data of such materials, which show special and characteristic behavior like yield stress or dependency on the powder loading and shear rate.

Acknowledgements

The researchers acknowledge the Polymer Competence Center Leoben (PCCL) for providing the rotational rheometer for measurements.

Author details

Christian Kukla[1]*, Ivica Duretek[2,3], Joamin Gonzalez-Gutierrez[2] and Clemens Holzer[2]

*Address all correspondence to: christian.kukla@unileoben.ac.at

1 Industrial Liaison Department, Montanuniversitaet Leoben, Leoben, Austria

2 Department of Polymer Engineering and Science, Montanuniversitaet Leoben, Leoben, Austria

3 Polymer Competence Center Leoben GmbH, Leoben, Austria

References

[1] Rueda MM, Auscher M-C, Fulchiron R, Périé T, Martin G, Sonntag P, Cassagnau P. Rheology and applications of highly filled polymers: A review of current understanding. Progress in Polymer Science. 2017;**66**:22-53. DOI: 10.1016/j.progpolymsci.2016.12.007

[2] Mewis J, Wagner NJ. Colloidal Suspension Rheology. Cambridge, UK: Cambridge University Press; 2011. 393 pp

[3] Eilers H. Die Viskosität von Emulsionen hochviskoser Stoffe als Funktion der Kontzentration. Kolloid-Zeitschrift. 1941;**97**:313-321. DOI: 10.1007/BF01503023

[4] Einstein A. Eine neue Bestimmung der Moleküldimensionen [Dissertation]. Zürich: Universität Zürich; 1906

[5] Einstein A. Berichtigung zu meiner Arbeit. Annals of Physics. 1911:591-592. DOI: 10.1002/andp.19113390313

[6] Frankel NA, Acrivos A. On the viscosities of a concentrated suspension of solid spheres. Chemical Engineering Science. 1967;**22**:847-853. DOI: 10.1016/0009-2509(67)80149-0

[7] Janardhana Reddy J, Ravi N, Vijayakumar M. A simple model for viscosity of powder injection moulding mixes with binder content above powder critical binder volume concentration. Journal of the European Ceramic Society. 2000;**20**:2183-2190. DOI: 10.1016/S0955-2219(00)00096-0

[8] Kate KH, Enneti RK, Park SJ, German RM, Atre SV. Predicting powder-polymer mixture properties for PIM design. Critical Reviews in Solid State and Materials Sciences. 2014;**39**:197-214. DOI: 10.1080/10408436.2013.808986

[9] Krieger IM, Dougherty TJ. A mechanism for non-Newtonian flow in suspensions of rigid spheres. Transactions of the Society of Rheology. 1959;**3**:137-152. DOI: 10.1122/1.548848

[10] Mooney M. The viscosity of a concentrated suspension of spherical particles. Journal of Colloid Science. 1951;**6**:162-170. DOI: 10.1016/0095-8522(51)90036-0

[11] Mueller S, Llewellin EW, Mader HM. The rheology of suspensions of solid particles. Proceedings of the Royal Society A: Mathematical, Physical and Engineering Sciences. 2010;**466**:1201-1228. DOI: 10.1098/rspa.2009.0445

[12] Gonzalez-Gutierrez J, Duretek I, Kukla C, Poljšak A, Bek M, Emri I, Holzer C. Models to predict the viscosity of metal injection molding feedstock materials as function of their formulation. Metals. 2016;**6**:129. DOI: 10.3390/met6060129

[13] Pabst W. Fundamental considerations on suspension rheology. Ceramics − Silikáty. 2004; **48**(1):6-13

[14] Gonzalez-Gutierrez J, Godec D, Guran R, Spoerk M, Kukla C, Holzer C. 3D printing conditions determination for feedstock used in fused filament fabrication (FFF) of 17-4PH stainless steel parts. Metallurgia. 2018;**57**:117-120

[15] Gonzalez-Gutierrez J, Stringari GB, Emri I. Powder injection molding of metal and ceramic parts. In: Wang J, editor. Some Critical Issues for Injection Molding. Rijeka, Croatia: InTech; 2012. pp. 65-86. DOI: 10.5772/38070

[16] Kukla C, Duretek I, Gonzalez-Gutierrez J, Holzer C. Rheology of PIM feedstocks. Metal Powder Report. 2017;**72**:39-44. DOI: 10.1016/j.mprp.2016.03.003

[17] Cox WP, Merz EH. Correlation of dynamic and steady flow viscosities. Journal of Polymer Science. 1958;**28**:619-622. DOI: 10.1002/pol.1958.1202811812

[18] Stickel JJ, Powell RL. Fluid mechanics and rheology of dense suspensions. Annual Review of Fluid Mechanics. 2005;**37**:129-149. DOI: 10.1146/annurev.fluid.36.050802.122132

[19] Pahl M, Gleißle W, Laun H-M. Praktische Rheologie der Kunststoffe und Elastomere. Dusseldorf, Germany: VDI-Verlag; 1991. 454 pp

[20] Bagley EB. End corrections in the capillary flow of polyethylene. Journal of Applied Physics. 1957;**28**:624-627. DOI: 10.1063/1.1722814

[21] Eisenschitz R, Rabinowitsch B, Weissenberg K. Zur Analyse des Formveraenderungswiderstandes. Mitteilungen der deutschen Materialspruefungsanstalten. 1929;**9**:91-94. DOI: 10.1007/978-3-642-92045-5_11

[22] Wales JLS, den Otter JL, Janeschitz-Kriegl H. Comparison between slit viscometry and cylindrical capillary viscometry. Rheologica Acta. 1965;**4**:146-152. DOI: 10.1007/BF01984712

[23] Tadmor Z, Klein I. Engineering Principles of Plasticating Extrusion. New York: Van Nostrand Reinhold; 1970. 500 pp

[24] Eswaran R, Janeschitz-Kriegl H, Schijf J. A slit viscometer for polymer melts. Rheologica Acta. 1963;**3**:83-91. DOI: 10.1007/BF01979457

[25] Laun HM. Polymer melt rheology with a slit die. Rheologica Acta. 1983;**22**:171-185. DOI: 10.1007/BF01332370

[26] Nyborg L, Johansson E, Niederhauser S. Assessment of rheology and related properties of PIM feedstock material. In: Euro PM200 Proceedings. 2nd European Symposium on Powder Injection Moulding; 18-20 October, Munich. Shrewsbury, UK: EPMA; 2000. pp. 67-74

[27] Bilovol VV. Mould filling simulations during powder injection moulding [PhD thesis]. Delft, The Netherlands: Delft University of Technology; 2003

[28] Friesenbichler W, Duretek I. Rheologische Charakterisierung hochgefüllter PIM-Feedstocks und Holzcompounds. In: Tagungshandbuch zum 17. Leobener Kunststoffkolloquium. 17. Leobener Kunststoffkolloquium; 20-21 November, Leoben, Austria. Leoben, Austria: Montanuniversitaet Leoben; 2003. pp. XIX-1-XIX-24

[29] Han CD. On intrinsic errors in pressure-hole measurements in flow of polymer melts. AIChE Journal. 1972;**18**:116-121. DOI: 10.1002/aic.690180121

[30] Walters K. Rheometry. New York: John Wiley & Sons Inc; 1975. 278 pp

[31] Chastagner MW. Slit die rheology of HDPE and ABS based wood plastic composites [master thesis]. Pullman, WA, USA: Washington State University; 2005

[32] Feldbacher G. Rheologische und thermodynamische Stoffdatenerfassung von zwei Thermoplasten für die FEM Werkzeugauslegung [bachelor thesis]. Leoben, Austria: Montanuniversitaet Leoben; 2003

[33] Atakan Y. Ermittlung der Fließfähigkeit und Plastifizierarbeit von handelsüblichen MIM-Feedstocks [master thesis]. Leoben, Austria: Montanuniversitaet Leoben; 2008

[34] MATLAW Consortium. Final Report MATLAW: New material laws for metal filled injection moulding feedstocks [Internet]. 15.01.2009. Available from: http://cordis.europa.eu/publication/rcn/11893_en.html [Accessed 2018-01-23]

[35] Duretek I. Untersuchungen zum Fließverhalten von Metall-, Keramik- und Holz-Kunststoffverbunden [PhD thesis]. Leoben, Austria: Montanuniversitaet Leoben; 2013

[36] Liddell PV, Boger DV. Yield stress measurements with the vane. Journal of Non-Newtonian Fluid Mechanics. 1996;**63**:235-261. DOI: 10.1016/0377-0257(95)01421-7

[37] Sun A, Gunasekaran S. Yield stress in foods: Measurements and applications. International Journal of Food Properties. 2009;**12**:70-101. DOI: 10.1080/10942910802308502

[38] Dapčević T, Dokić P, Hadnađev M, Pojić M. Determining the yield stress of food products: Importance and shortcomings. Food Processing, Quality and Safety. 2008;**35**:143-149

[39] Duretek I, Kukla C, Langecker GR, Holzer C. Measurement of the yield stress of a stainless steel feedstock. In: Euro PM2013 Proceedings. Euro PM2013 Congress & Exhibition; 15-18 September, Gothenburg, Sweden. Bellstone: EPMA; 2013

[40] Kukla C, Duretek I, Holzer C. Controlled shear stress method to measure yield stress of highly filled polymer melts. AIP Conference Proceedings. 2016;**1779**:070006-1 to 070006-5. DOI: 10.1063/1.4965538

[41] Kukla C, Duretek I, Holzer C. Modelling of rheological behaviour of 316L feedstocks with different powder loadings and binder compositions. In: Euro PM2014 Proceedings. Euro PM2014 Congress and Exhibition; 21-24.09; Salzburg, Austria. Bellstone: EPMA; 2014. pp. 1-6

[42] Geisbüsch P. Ansätze zur Schwindungsberechnung ungefüllter und mineralisch gefüllter Thermoplaste [PhD thesis]. Aachen: RWTH Aachen; 1980

[43] Osswald TA, Hernandez-Ortiz JP. Polymer Processing: Modeling and Simulation. Munich: Carlo Hanser Verlag; 2006. 597 pp

[44] Kukla C, Duretek I, Schuschnigg S, Gonzalez-Gutierrez J, Gooneie A, Holzer C. Study of rheological behaviour of stainless steel feedstock taking into account the thermal effects. In: Rasteiro MG, editor. Ibereo 15: Conference Proceedings; Coimbra, Portugal: University of Coimbra. 2015. pp. 46-49

[45] Friesenbichler W, Langecker GR, Duretek I, Schuschnigg S. Polymer melt rheology at high shear rates using a new micro-rheology technique. In: Proceedings of 21st Annual Meeting of the Polymer Processing Society. 6.1-1-6.1-15

[46] Duretek I, Friesenbichler W, Schuschnigg S, Rajganesh J, Langecker GR. Study on rheological behaviour of polymer melts at high shear rates using a new micro-rheology technique. In: Proceedings of Past and Future of Polymer Processing, Technology and Science; 27-28 April; Zagreb, Croatia. 2006

[47] Friesenbichler W, Duretek I, Rajganesh J, Selvasankar RK. Measuring the pressure dependent viscosity at high shear rates using a new rheological injection mould. Polimery. 2011;**56**(1):58-62

[48] Agassant JP, Sergent P, Avenas JF, Carreau PJ. Polymer Processing: Principles and Modelling. Cincinnati, OH, USA: Hanser Gardner; 1991. 846 pp

[49] Schuschnigg S. Rheologische Untersuchungen bei hohen Schergeschwindigkeiten mit Hilfe eines Mikrorheologie-Schlitzdüsen Messsystems [master thesis]. Leoben, Austria: Montanuniversitaet Leoben; 2004

[50] Cramer A, Michaeli W, Friesenbichler W, Duretek I. Simulation des Spritzgießprozesses von Mikrobauteilen. Zeitschrift Kunststofftechnik Journal of Plastics Technology. 2007:1-26

[51] SIGMA Engineering. SIGMASOFT 5.0+: Manual. SIGMA Engineering GmbH: Aachen, Germany; 2013

[52] CoreTech System. Moldex3D R15.0: Manual. New Taipei City, Taiwan: CoreTech System Co., Ltd; 2017

[53] Erb T, Geiger K, Bonten C. Mixing processes—Influence of the viscosity model on flow calculations. AIP Conference Proceedings. 2014;**1593**:549-555. DOI: 10.1063/1.4873841

Edited by Luis Rivera-Armenta and Beatriz Adriana Salazar Cruz

Rheology is the science that studies the behavior of the flow of matter in a liquid state or soft solids under the application of stress or deformation to obtain a response to an applied force. In polymers, rheology is an important tool to understand behavior under processing conditions and to design equipment. Another application for rheology in the polymer field is to understand structure–property relationships by means of molecular weight, molecular weight distribution, stereochemistry, morphology, melt degradation, and performance under processing. This book covers the essential criteria for selecting the best test types for various applications and new developments, for accurately interpreting results, and for determining other areas where rheology and rheological phenomena may be useful in your work.

Published in London, UK

IntechOpen

ISBN 978-1-83881-657-5
9 781838 816575